The Topochemical Reduction of Some Rhodium-containing Complex Oxides

Zheying Xu

Exeter College

March 2022



A thesis submitted to the

Board of the Faculty of Physical Sciences

in partial fulfilment of the requirements

for the degree of Doctor of Philosophy

The Topochemical Reduction of Some Rhodium-containing Complex Oxides

This work focuses on topochemical reduction reactions of rhodium-containing complex transition-metal oxides using Zr as an oxygen getter to form metastable anion-deficient reduced oxide phases.

Building on the work of topochemical deintercalation of oxide ions from ruthenium-containing complex oxides using CaH_2 and Zr as reducing agents, the rhodium-containing analogues n = 1 Ruddlesden-Popper phases $LaSrM_{0.5}Rh_{0.5}O_4$ (M = Co, Ni) were prepared via a ceramic method and their topochemical reduction reactions were explored. The initial investigation of the reactivity of $LaSrM_{0.5}Rh_{0.5}O_4$ (M = Co, Ni) was performed by treating them with Zr powder in sealed silica ampoules and heating them in the temperature range $450 \leq T/^{o}C \leq 520$. The reactions resulted in the formation of distinct phases $LaSrM_{0.5}Rh_{0.5}O_{3.25}$ (M = Co, Ni). $LaSrM_{0.5}Rh_{0.5}O_{3.25}$ (M = Co, Ni) have structures with lower symmetry (*Immm*) than parent phases $LaSrM_{0.5}Rh_{0.5}O_4$ (M = Co, Ni) (*I4/mmm*), with ¼ of the oxide ions which originally reside in 'equatorial' anion sites being deintercalated. This selective deintercation of oxygen atoms led to a structural arrangement of a 1:1 ratio of C_{4v}:D_{4h} transition-metal sites. The X-ray powder diffraction data and magnetic data and X-ray photoelectron spectroscopy data indicate the disproportionation of rhodium centres. The rhodium centres are found to be disproportionated into a 1:1 ratio of Rh^{I}: Rh^{III} with Rh^{I} located in D_{4h} sites and Rh^{III} located in C_{4v} sites, making the resulting phases the first reported extended solids containing Rh^{I}.

Doping chemistry of $LaSrCo_{0.5}Rh_{0.5}O_4$ was investigated by manipulating the ratio between La and Sr. The doped parent oxide phases can be reduced to the corresponding oxide phases, $La_xSr_{2-x}Co_{0.5}Rh_{0.5}O_{3.25}$ ($0.90 \leq x \leq 1.10$), with the same oxygen deficiency, suggesting that the transition-metal oxidation states and the oxygen deficiency are not coupled.

The topochemical reduction chemistry of rhodium-containing Ruddlesden Popper phases can be extended to the perovskite analogue La_2MRhO_6 (M = Co, Ni) and $LaSrMnRhO_6$. Topochemical reduction of these parent phases with Zr yields $La_2MRhO_{4.5}$ (M = Co, Ni) and $LaSrMnRhO_{4.5}$. Analogous to $LaSrM_{0.5}Rh_{0.5}O_{3.25}$, these reduced perovskite phases have a 1:1 ratio of C_{4v}:D_{4h} transition metal sites and are confirmed to be mixed valence $Rh^{I/III}$ compounds as Ruddlesden-Popper analogues.

No magnetic ordering at low temperature is observed in $La_2NiRhO_{4.5}$ and $LaSrMnRhO_{4.5}$, while $La_2CoRhO_{4.5}$ exhibits complicated magnetic ordering behaviour. For $La_2CoRhO_{4.5}$, two antiferromagnetic orderings with moments pointing at different directions (G-type antiferromagnetic ordering with moments pointing out-of-plane and A-type antiferromagnetic ordering with moments pointing in-plane) were observed and each order responds separately to temperature.

Declaration

The work described in this thesis was carried out at the Inorganic Chemistry Laboratory at the University of Oxford between October 2018 and February 2022 under the supervision of Professor Michael A. Hayward. All of the work presented in this thesis is my own, except where I have either given reference to a published source or acknowledged help from a named person. None of the work has been submitted by the author for any other degree at any other university.

Zheying Xu

March 2022

拙作敬献庄尧珠女士

Acknowledgements

First, I would like to thank my supervisor Professor Michael A. Hayward for offering me the opportunity to come to Oxford for Dphil study. Your expertise and dedication into scientific research has inspired me not only in the Dphil project but also in my future career.Without the guidance and the feedback throughout this project from you, I would not have completed this work.

I would like to thank my mom and dad for funding me to study in Oxford and complete my Dphil study.

Also, I need to thank all the researchers who contributed to this work: Prof. Robert Palgrave from University College London for XPS measurement and analysis; Dr. Simon Cassidy for the assistance in collecting SQUID data and synchrotron XRD data; Dr. Robert Jacobs and Dr. Amber Thompson for TGA and XRD training; Dr. Ron Smith and Dr. Emanuelle Suard for the assistance in collecting the neutron powder diffraction data; the Clarke and Goodwin groups and the I11 beam scientists at Diamond Light Source for helping to collect the synchrotron X-ray powder diffraction data.

Finally, I would like to thank all the members of MAH group that I have worked with over the past three years, specifically Dr. Lun Jin and Dr. Tong Zhu for teaching me all the research and practical skills; Dr. Xabier Martínez de Irujo-Labalde for the academic advice and all the other group members for keeping me accompanied.

Table of Contents

The Topochemical Reduction of Some Rhodium-containing Complex Oxides **I**

Declaration **III**

Acknowledgements **VII**

Table of Contents **IX**

Chapter 1 Introduction.....1

1.1. Complex Transition-metal Oxides.....1

1.2. Perovskites and Related Structures.....2

1.2.1. Perovskite Structure and Tolerance Factor.....2

1.2.2. Glazer Tilt Notations.....5

1.2.3. *B*-Site Disordered Perovskites and Ordered Double Perovskites.....6

1.2.4. Ruddlesden-Popper Structure.....7

1.3. Electronic States of Atoms in Transition-metal Oxides.....8

1.3.1. Spin-state of Transition Metals in Complex Oxides.....8

1.4. Magnetic Interactions in Transition-metal Oxides.....10

1.4.1. Correlated Magnetic Behaviour and Magnetic Ordering.....10

1.4.2. Coupling Mechanisms and the Goodenough-Kanamori Rule.....11

1.5. Synthesis and Topochemical Reduction of Transition-metal Oxides.....12

1.5.1. Traditional Synthesis of Crystalline Solids and its Disadvantages.....12

1.5.2. Topochemical Reduction.....13

1.5.2.1. Topochemical Reduction Using Binary Metal Hydrides.....14

1.5.2.2. Topochemical Reduction Using Finely Divided Electropositive Metals.....15

1.6. The Motivation of the Work.....16

Chapter 2 Experimental Methods and Techniques.....19

2.1. Synthesis of Starting Materials: Ceramic Method.....19

2.2. Synthesis of Topochemical Reduced Materials.....20

2.2.1. Zirconium Getter Reductions.....20

2.2.2. Handling Air-sensitive Reactions and Compounds.....22

2.2.2.1. Argon-filled Glove Box.....22

2.2.2.2. Air-sensitive X-ray Powder Diffraction.....23

2.3. Powder Diffraction....24
2.3.1. X-ray Powder Diffraction....26
2.3.1.1. Cu-sourced Instruments: Panalytical Empyrean, Panalytical X'Pert and Bruker D8....26
2.3.1.2. Mo-sourced Instrument:Panalytical Empyrean with PheniX Cryostat....27
2.3.1.3. Synchrotron X-ray Powder Diffraction....27
2.3.2. Neutron Powder Diffraction....28
2.3.2.1. POLARIS Diffractometer....30
2.3.2.2. D2B and D1B Diffractometers....32
2.4. Rietveld Refinement....34
2.5. SQUID Magnetometry....35
2.5.1. Sample Preparation for SQUID Measurements....36
2.5.2. Standard Measurements....37
2.5.3. Ferrosubtraction Measurements....37
2.6. Magnetism....38
2.6.1. The Curie-Weiss Law....38
2.7. Thermogravimetric Analysis (TGA)....41
2.8. X-ray Photoelectron Spectroscopy....42
2.8.1. The Principles of XPS....42
2.8.2. Standard XPS Measurement....43

Chapter 3 Synthesis and Characterisation of *n* = 1 Rh-containing Ruddlesden-Popper Phases....45
3.1. Introduction....46
3.2. Experimental....46
3.2.1. Synthesis of $LaSrCo_{0.5}Rh_{0.5}O_4$....46
3.2.2. Synthesis of $LaSrNi_{0.5}Rh_{0.5}O_4$....47
3.2.3. Synthesis of $La_{0.5}Sr_{1.5}Fe_{0.5}Rh_{0.5}O_4$....47
3.3. Results....48
3.3.1. Structural Characterisation of $LaSrCo_{0.5}Rh_{0.5}O_4$....48
3.3.2. Structural Characterisation of $LaSrNi_{0.5}Rh_{0.5}O_4$....50
3.3.2.1. Synchrotron X-ray Powder Diffraction....50
3.3.2.2. Neutron Powder Diffraction....51
3.3.3. Structural Characterisation of $La_{0.5}Sr_{1.5}Fe_{0.5}Rh_{0.5}O_4$....55
3.3.3.1. Synchrotron X-ray Powder Diffraction....55
3.3.3.2. Neutron Powder Diffraction....55

3.3.4. Magnetic Characterisation of $LaSrCo_{0.5}Rh_{0.5}O_4$ 60
3.3.5. Magnetic Characterisation of $LaSrNi_{0.5}Rh_{0.5}O_4$ 61
3.3.6. Magnetic Characterisation of $La_{0.5}Sr_{1.5}Fe_{0.5}Rh_{0.5}O_4$ 62
3.4. Discussion 63
3.4.1. Cation Disorder in Rh-containing n = 1 Ruddlesden-Popper Phases 63
3.4.2. Spin States and Oxidation States of Transition Metals in Rh-containing n = 1 Ruddlesden-Popper Phases 64
3.4.2.1. $LaSrCo_{0.5}Rh_{0.5}O_4$ 64
3.4.2.2. $LaSrNi_{0.5}Rh_{0.5}O_4$ 66
3.4.2.3. $La_{0.5}Sr_{1.5}Fe_{0.5}Rh_{0.5}O_4$ 68
3.5. Conclusion 70

Chapter 4 Synthesis and Characterisation of $LaSrM_{0.5}Rh_{0.5}O_{3.25}$ (M = Co, Ni) 71
4.1. Introduction 71
4.2. Experimental 71
4.3. Results 72
4.3.1. Initial Investigation of Reactivity of $LaSrM_{0.5}Rh_{0.5}O_4$ (M= Co, Ni) with Zr 72
4.3.2. Structural and Chemical Characterisation of $LaSrM_{0.5}Rh_{0.5}O_{3.25}$ (M = Co, Ni) 74
4.3.2.1. Thermogravimetric Analysis of $LaSrM_{0.5}Rh_{0.5}O_{3.25}$ (M = Co, Ni) 74
4.3.2.2. Synchrotron X-ray Powder Diffraction of $LaSrM_{0.5}Rh_{0.5}O_{3.25}$ (M = Co, Ni) 76
4.3.2.3. Neutron Powder Diffraction of $LaSrM_{0.5}Rh_{0.5}O_{3.25}$ (M = Co, Ni) 79
4.3.3. X-ray Photoelectron Spectroscopy of $LaSrM_{0.5}Rh_{0.5}O_{3.25}$ (M = Co, Ni) 90
4.3.4. Magnetic Characterisation of $LaSrM0.5Rh_{0.5}O_{3.25}$ (M = Co, Ni) 92
4.4. Discussion 96
4.4.1. Structure Analysis of $LaSrM_{0.5}Rh_{0.5}O_{3.25}$ (M = Co, Ni) 96
4.4.2. Disproportionation of Rh^{II} in $LaSrM_{0.5}Rh_{0.5}O_{3.25}$ (M = Co, Ni) 97
4.5. Conclusion 103

Chapter 5 A-site Doping of $La_xSr_{2-x}Co_{0.5}Rh_{0.5}O_4$ Series 105
5.1. Introduction 105
5.2. Experimental 105
5.3. Results 106
5.3.1. Structural Characterisation of $La_xSr_{2-x}Co_{0.5}Rh_{0.5}O_4$ ($0.85 \leq x \leq 1.15$) 106

5.3.2. Magnetic Characterisation of $La_xSr_{2-x}Co_{0.5}Rh_{0.5}O_4$ ($0.85 \leq x \leq 1.15$) 108
5.4. Discussion 110
5.5. Conclusion 113

Chapter 6 *A*-site Doping of $La_xSr_{2-x}Co_{0.5}Rh_{0.5}O_{3.25}$ Series 115
6.1. Introduction 115
6.2. Experimental 115
6.2.1. Synthesis of $La_xSr_{2-x}Co_{0.5}Rh_{0.5}O_{3.25}$ ($0.85 \leq x \leq 1.15$) 115
6.2.2. Preparation for Sintered Pellet Phase of $La_xSr_{2-x}Co_{0.5}Rh_{0.5}O_{3.25}$ ($0.85 \leq x \leq 1.15$) for Resistance Measurements 116
6.3. Results 117
6.3.1. Structural Characterisation of $La_xSr_{2-x}Co_{0.5}Rh_{0.5}O_{3.25}$ ($0.85 \leq x \leq 1.15$) 117
6.3.1.1. Thermogravimetric Analysis of $La_xSr_{2-x}Co_{0.5}Rh_{0.5}O_{3.25}$ ($0.85 \leq x \leq 1.15$) 117
6.3.1.2. Synchrotron X-ray Powder Diffraction of $La_xSr_{2-x}Co_{0.5}Rh_{0.5}O_{3.25}$ ($0.85 \leq x \leq 1.15$) 119
6.3.2. Magnetic Characterisation of $La_xSr_{2-x}Co_{0.5}Rh_{0.5}O_{3.25}$ ($0.85 \leq x \leq 1.15$) 122
6.3.3. Conductivity Measurement of $La_xSr_{2-x}Co_{0.5}Rh_{0.5}O_{3.25}$ ($0.85 \leq x \leq 1.15$) 125
6.4. Discussion 126
6.4.1. Doping Limits of $La_xSr_{2-x}Co_{0.5}Rh_{0.5}O_{3.25}$ ($0.85 \leq x \leq 1.15$) 126
6.4.2. Magnetic Behaviour of $La_xSr_{2-x}Co_{0.5}Rh_{0.5}O_{3.25}$ ($0.85 \leq x \leq 1.15$) 127
6.5. Conclusion 129

Chapter 7 Synthesis and Characterisation of $La_2NiRhO_{4.6}$ and $LaSrMnRhO_{4.5}$ 131
7.1. Introduction 131
7.2. Experimental 131
7.2.1. Synthesis of La_2MRhO_6 (M = Mn, Ni) and $LaSrMnRhO_6$ 131
7.2.2. Synthesis of $La_2MRhO_{6-\delta}$ (M = Mn, Ni) and $LaSrMnRhO_{6-\delta}$ 132
7.3. Results 133
7.3.1. Structural Characterisation of 'parent oxides' 133
7.3.1.1. X-ray Powder Diffraction of La_2NiRhO_6 133
7.3.1.2. Synchrotron X-ray Powder Diffraction of La_2MnRhO_6 and $LaSrMnRhO_6$ 135
7.3.2. Initial Investigation of Reactivity of La_2MRhO_6 (M = Ni, Mn) and $LaSrMnRhO_6$ with Zr 138
7.3.2.1. Initial Investigation of Reactivity of La_2NiRhO_6 with Zr 138
7.3.2.2. Initial Investigation of Reactivity of La_2MnRhO_6 and $LaSrMnRhO_6$ with Zr 139

7.3.3. Structural and Chemical Characterisation of $La_2NiRhO_{6-\delta}$ and $LaSrMnRhO_{6-\delta}$ .141
7.3.3.1. Thermogravimetric Analysis of $La_2NiRhO_{6-\delta}$ and $LaSrMnRhO_{6-\delta}$ 141
7.3.3.2. Space Group Determination of $La_2NiRhO_{4.6}$ and $LaSrMnRhO_{4.5}$ 144
7.3.3.3. Neutron Powder Diffraction of $La_2NiRhO_{4.6}$ and $LaSrMnRhO_{4.5}$.....148
7.3.4. Magnetic Characterisation of $La_2NiRhO_{4.6}$ and $LaSrMnRhO_{4.5}$ 152
7.3.4.1. Magnetic Characterisation of $La_2NiRhO_{4.6}$ 152
7.3.4.2. Magnetic Characterisation of $LaSrMnRhO_{4.5}$.....154
7.4. Discussion.....156
7.5. Conclusion 160

Chapter 8 Synthesis and Characterisation of $La_2CoRhO_{4.5}$ 161
8.1. Introduction.....161
8.2. Experimental.....161
8.2.1. Synthesis of La_2CoRhO_6.....161
8.2.2. Synthesis of $La_2CoRhO_{6-\delta}$.....162
8.3. Results.....162
8.3.1. Structural Characterisation of La_2CoRhO_6 162
8.3.2. Initial Investigation of Reactivity of La_2CoRhO_6 with Zr 164
8.3.3. Structural and Chemical Characterisation of $La_2CoRhO_{6-\delta}$.....165
8.3.3.1. Thermogravimetric Analysis of $La_2CoRhO_{6-\delta}$.....165
8.3.3.2. Neutron Powder Diffraction of $La_2CoRhO_{4.5}$ 167
8.3.3.2.1. Space Group Determination of $La_2CoRhO_{4.5}$ 167
8.3.3.2.2. Magnetic Ordering Determination of $La_2CoRhO_{4.5}$ 170
8.3.3.3. Variable-temperature Measurement of $La_2CoRhO_{4.5}$ 175
8.3.3.3.1. Variable-temperature Neutron Powder Diffraction Data.....175
8.3.3.3.2. Magnetic Characterisation of $La_2CoRhO_{4.5}$.....177
8.3.3.3.3. Variable-temperature Synchrotron X-ray Powder Diffraction of $La_2CoRhO_{4.5}$ 179
8.3.3.3.4. Serial Magnetic Refinement of $La_2CoRhO_{4.5}$ over Temperature 181
8.3.3.3.5. Conclusion of the Magnetic Transition of $La_2CoRhO_{4.5}$ over Temperature 182
8.4. Discussion.....184
8.5. Conclusion 190

Chapter 9 Conclusions.....191
Appendix 1 Table of Figures.....195

Appendix 2 Additional Data for Chapter 5-8.....211
Appendix 3 Bibliography 229

Chapter 1

Introduction

1.1. Complex Transition-metal Oxides

Complex transition-metal perovskite oxides have been a subject of intense study in a large number of scientific disciplines. A huge variety of transition metal cations is able to be incorporated within perovskite frameworks and their analogues. This flexible chemistry enables perovskite oxides to be an ideal playground to explore a diverse range of different physical and chemical phenomena.

In complex oxides, transition metal centres can adopt variable oxidation states and spin states based on the surrounding chemical environment, hence stable electronic configurations with partial filling of the *d* orbitals occur in these systems. In these solid-state oxides, transition metal centres are normally organised into regular arrays linked via shared anions as bridging ligands (O^{2-}, H^-, etc.). The electrons in partially filled *d* orbitals on neighbouring transition-metal centres can interact via direct exchange couplings or through super-exchange couplings with the anion link involved as a bridge. This cooperative behaviour of the *d* electrons localised at transition metal centres can lead to strong inter-cation electronic couplings which can be propagated through the material and then result in macroscopic properties.

These cooperative macroscopic properties include long-range magnetic ordering[1], magnetoresistance[2,3], high-temperature superconductivity[4,5], multiferroicity[6–9] and photocatalytic behaviour[10]. The application of these unusual behaviours enables the complex oxides to make significant contributions to the area of functional materials such as photocatalysts, ionic conductors, superconductors, catalysts, photovoltaics, etc[1,5,10,11].

These macroscopic properties typically show high sensitivity to small adjustments in transition metal oxidation states, coordination geometries and anion lattices. Thus, the fine modification of the compositional and structural chemistry of complex oxides have been utilised to design materials with original electronic and magnetic properties.

1.2. Perovskites and Related Structures

1.2.1. Perovskite Structure and Tolerance Factor

One of the most common frameworks that complex transition-metal oxides adopt is the perovskite structure, which has a general chemical formula of ABO_3, with *A* being an alkaline earth metal and/or lanthanide, and *B* being a transition metal[12]. The structure can be described as a three-dimensional network of corner-sharing BO_6 octahedra, with the *A*-site cations sitting in 12-coordinate sites formed by this network, as shown in Figure 1-1 (a).

The geometry and stability of a perovskite framework is highly dependent on the size of the *A* and *B* cations. For an ideal cubic perovskite, $SrTiO_3$[13] for example (Figure 1-1 (a)), the combination of Sr and Ti cations allows the Ti-O-Ti bond angles to be 180° in the framework, maximising the overlap of transition-metal 3d orbitals and O 2p orbitals, and hence forming a structure with $Pm\bar{3}m$ symmetry. In this ideal scenario, the *A* - O bond length is $\frac{a}{\sqrt{2}}$ and the *B* - O bond length is $\frac{a}{2}$, where *a* is the cubic unit cell parameter. This leads to a relationship of $< A-O > = \sqrt{2} < B-O >$. Therefore, a Goldschmidt tolerance factor (*t*)[14] is defined to describe the flexibility of perovskite structures based on the size of *A* and *B* cations:

$$\boldsymbol{t} = \frac{< A-O >}{\sqrt{2} < B-O >} = \frac{r_A + r_O}{\sqrt{2}(r_B + r_O)}$$

where $< A - O >$ and $< B - O >$ correspond to the average bond lengths between *A*-/*B*-site cations and oxygen ions; r_A, r_B and r_O are the radii of *A*-site cation, *B*-site cation and oxygen anion, respectively.

For the perfect scenario mentioned above, the tolerance factor, *t*, is equal to 1. However, when there is a mismatch in the sizes of the *A*- and *B*- cations ($t \neq 1$), the perovskite framework can distort, as described below, to accommodate a range of $< A - O > : < B - O >$ radius ratios, enabling a wide variety of *A* and *B* cation combinations to form thermodynamically stable perovskite phases.

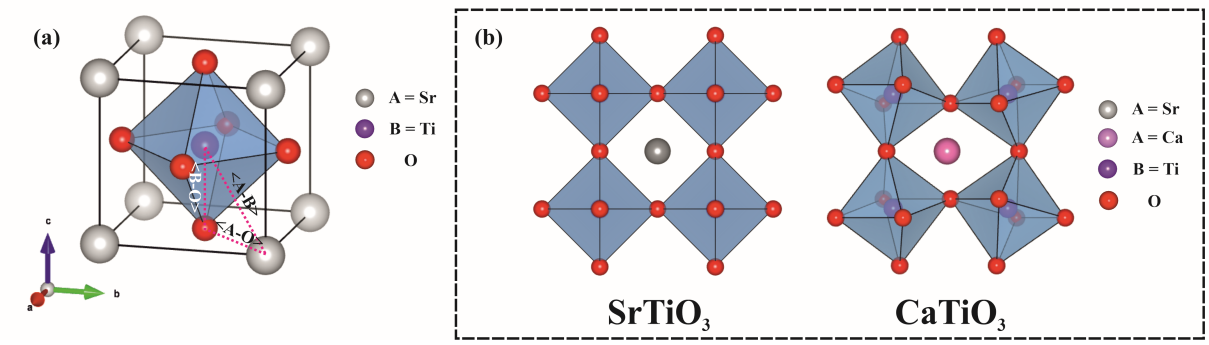


Figure 1-1 (a) a cubic $Pm\bar{3}m$ unit cell of $SrTiO_3$[13]; the pink dashed lines represent *A*-O, *B*-O, *A*-*B* bond distances. (b) a schematic presentation of the cooperative rotations of BO_6 octahedra to fit to $t < 1$ scenario in $CaTiO_3$ phase (Undistorted $SrTiO_3$ is plotted as a reference)[15].

In $t < 1$ scenarios, the *A*-site cation is smaller than the ideal size for the 12-coordinatie sites and this drives tilts and twist of BO_6 octahedra to lower the *B* – O – *B* bond angle, which in turn decreases the $< A - O >$ bond length. For instance, compared to ideal structure of $SrTiO_3$, a twisted, corner-shared array of TiO_6 octahedra with 154.5° Ti – O – Ti bond angle is adopted by $CaTiO_3$ as shown in Figure 1-1 (b). This structural distortion compensates for the size mismatch between the Ca^{II} and Ti^{IV} cations. As shown in Figure 1-2, the distortion of BO_6 octahedra can result in a lowering of symmetry from cubic to orthorhombic[15], rhombohedral[16], trigonal[17] or even monoclinic[18].

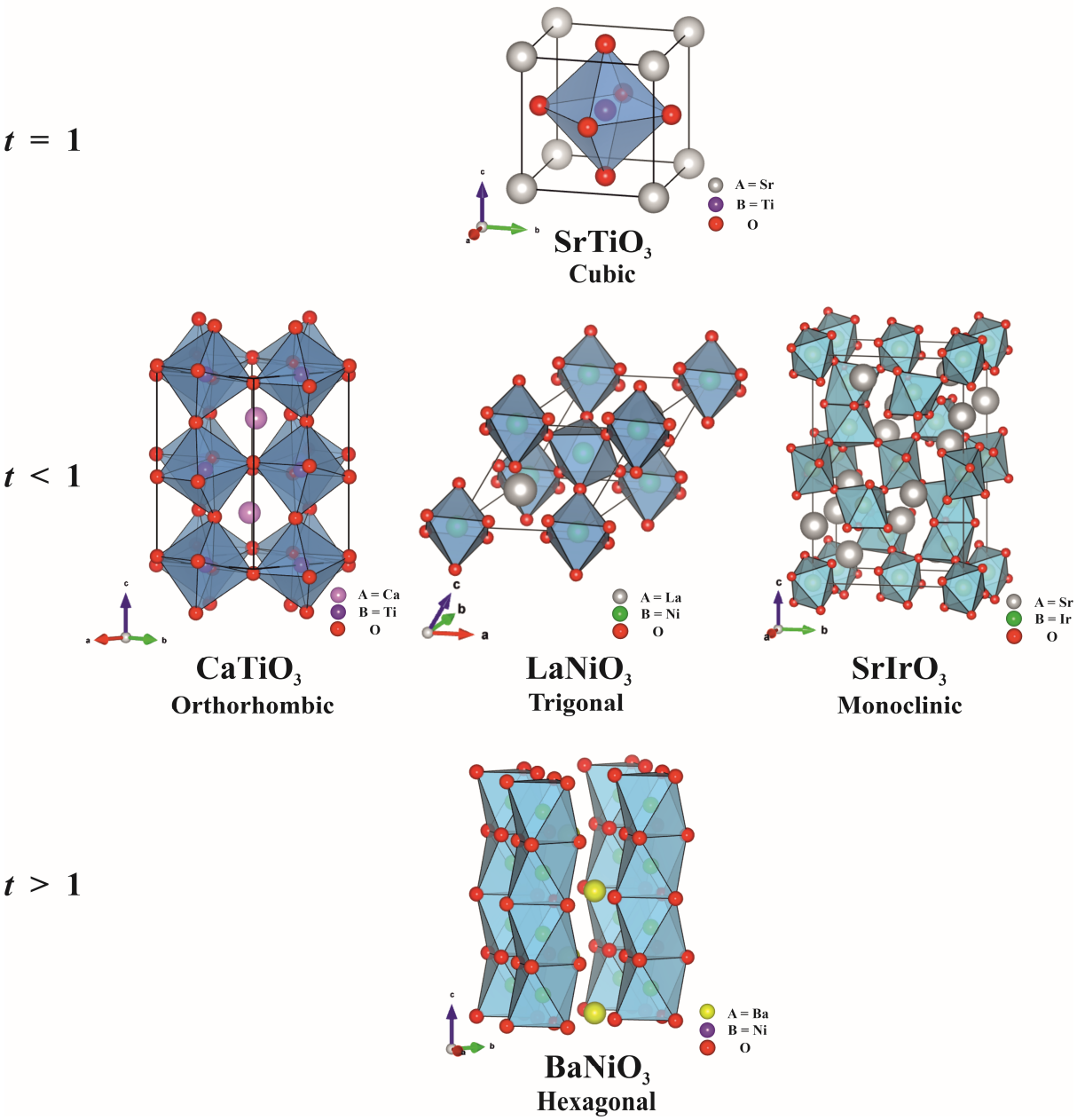


Figure 1-2 The ABO_3 perovskite-related structure of ($t = 1$): $SrTiO_3$ cubic $Pm\bar{3}m$ [13]; ($t < 1$): $CaTiO_3$ orthorhombic $Pbnm$[15], $LaNiO_3$ trigonal $R\bar{3}c$[17], $SrIrO_3$ monoclinic $C2/c$[18]; ($t > 1$): $BaNiO_3$ hexagonal $P6_3/mmm$[19].

In $t > 1$ scenarios, the A-site cation is larger than the ideal size for the 12-coordinate sites created by the BO_6 octahedra. This leads to a change in the connectivity of the BO_6 units from corner-sharing to face-sharing, leading to the formation of hexagonal polytype perovskite frameworks[19], as shown in Figure 1-2.

1.2.2. Glazer Tilt Notations

As mentioned in Section 1.2.1, the corner-linked BO_6 octahedra will tilt to accommodate the large *B*-site cations and small *A*-site cations. The numerous types of tilting can be described by Glazer tilt notations[20]. This classification considers the combination of rotations of an octahedron along three 4-fold axes (shown in Figure 1-3 (a)) and is given by a three-letter symbol. As we can see in Figure 1-3(b), in the corner-linked octahedra network, rotating an octahedron clockwise naturally requires its in-plane neighbours to rotate anticlockwise. However, the choice of rotation cannot effect the octahedra in the neighbouring planes (above or below). Thus, the octahedra in the neibouring planes are free to rotate in either the same or the opposite sense, described by superscript + (in-phase tilting) and – (out-of-phase tilting), separately.

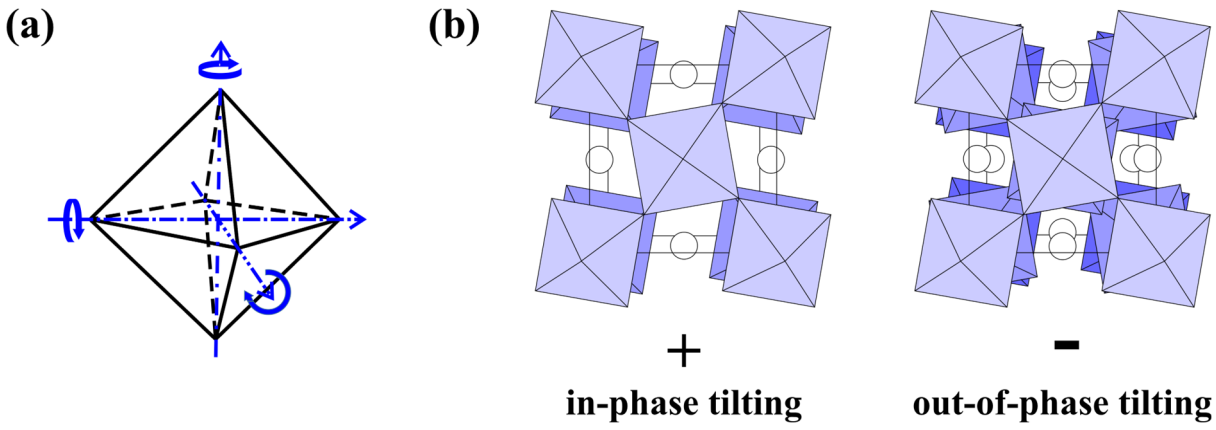


Figure 1-3 (a) A schematic presentation of an octahedron and its possible rotation along three 4-fold axes (shown as blue arrows). (b) A schematic presentation of in -phase uniaxial rotation (left) and out-of-phase uniaxial rotation (right).

In the three-letter symbol, equal rotations along different 4-fold axes of an octahedron are symbolized by the same letters. Thus, the none rotation is denoted with $a^0a^0a^0$. A uniaxial rotation is described as $a^0a^0c^+$ or $a^0a^0c^-$, depending on whether the adjacent octahedra layers rotate in the same sense ($a^0a^0c^+$) or the opposite sense ($a^0a^0c^-$). for biaxial and triaxial rotations, the letter *b* is added into the symbol.

This classification gives 23 tilt systems in total, while only a small number of them can form in reality[21]. Among these tilting systems, $a^0a^0a^0$ with $Pm\bar{3}m$ symmetry for cubic perovskites, $a^-a^-a^-$ with $R\bar{3}c$ symmetry for rhombohedral perovskites and $a^+b^-b^-$ with *Pnma* symmetry for orthorhombic perovskites are particularly frequent.

1.2.3. *B*-Site Disordered Perovskites and Ordered Double Perovskites

Among all the methods of ABO_3 perovskite modification, the chemical substitution of *B*-site cations is of enduring interest, especially for the situations in which the *B*-sites are equally occupied by a 1:1 ratio of *B*- and *B'*- cations. In these situations, samples have a composition of $A_2BB'O_6$. These $A_2BB'O_6$ perovskite phases can adopt schemes in which *B* and *B'* cations are either ordered or disordered.

It has been generally observed that $A_2BB'O_6$ perovskite phases only adopt ordered structures if *B*- and *B'*- cations differ significantly in size and/or charge, with a 3-unit-charge difference typically being required to stabilize ordered structures[22,23]. For example, $Sr_2Ni^{II}W^{VI}O_6$[24] adopts an ordered array of transition-metal cations to minimise the structural strain[21].

However, if the two *B*-site cations are similar in size and/or have a charge difference smaller than two, the *B*-site cations tend to be randomly distributed and hence result in a disordered solid solution with the chemical formula better described as $AB_{0.5}B'_{0.5}O_3$ such as $LaCr^{III}_{0.5}Fe^{III}_{0.5}O_3$[23] or $SrFe^{III}_{0.5}Mo^{V}_{0.5}O_3$[25]. These solid solutions with a high level of chemical disorder usually have complicated magnetic interactions between transition-metal sites when the system has multiple unpaired electrons and are al so more likely to be insulators.

1.2.4. Ruddlesden-Popper Structure

In addition to the ABO_3 perovskite structure, some other perovskite-related structures such as layered Ruddlesden-Popper phases are also hot research topics[26]. The Ruddlesden-Popper structure is a layered variant of perovskite structure found by S. N. Ruddlesden and P. Popper in 1957 and 1958[27,28]. The structure consists of layers of two-dimensional ABO_3 perovskite slabs and intercalated cations forming AO rock-salt layers. Hence, a general formula of $A_{n+1}B_nO_{3n+1}$ can be generated where A is an alkaline earth metal and/or a lanthanide, B is a transition metal and n is the number of layers of corner-shared BO_6 octahedra stacked in the perovskite slabs. The general formula can also be regarded as $(AO)(ABO_3)_n$ with the $n = \infty$ phase being the three-dimensional perovskite structure.

Typical Ruddlesden-Popper structures are plotted in Figure 1-4, based on the structure of $Sr_{n+1}Ru_nO_{3n+1}$ family (n = 1, 2, 3)[29]. In the $n > 1$ Ruddlesden-Popper structure, the A-site cations sit in two different sites, the 12-coordinate sites residing in the ABO_3 slabs and the 9-coordinate sites residing in the AO layers, as circled in Figure 1-4, while the B-site cations are only located in the 6-coordinate sites.

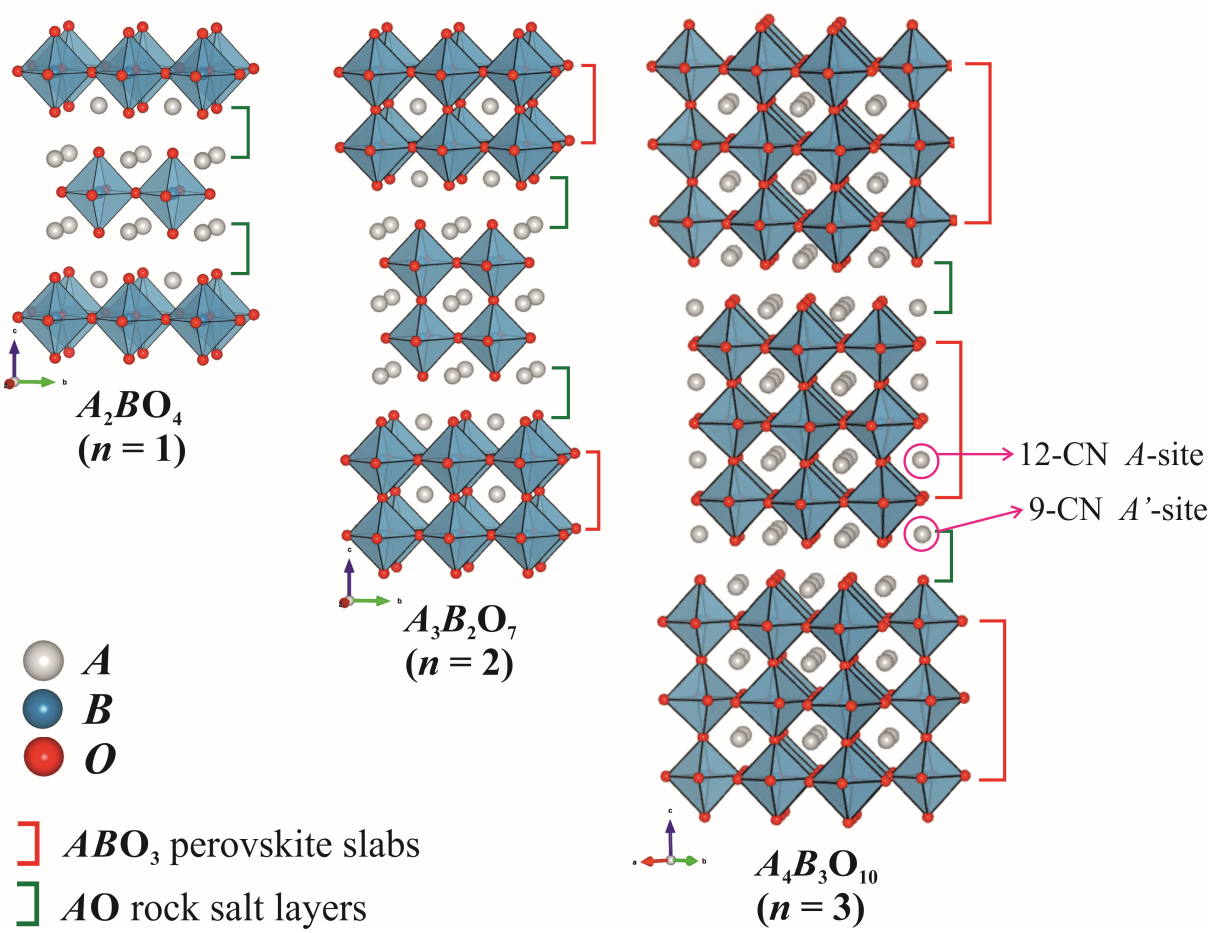


Figure 1-4 Ruddlesden-Popper phases $A_{n+1}B_nO_{3n+1}$ with n = 1,2,3[29]. The red and green brackets present the perovskite slabs and the rock salt layers, respectively. The pink circles present two different A-site positions.

1.3. Electronic States of Atoms in Transition-metal Oxides

1.3.1. Spin-state of Transition Metals in Complex Oxides

The spin states of transition-metals tend to vary between high-spin (HS) and low-spin (LS) configurations. Factors governing which state is adopted can be understood using crystal field theory and ligand field theory, which is discussed as follows, with 6-coordinate $3d^6$ Co^{III} used as an example.

The spin-state adopted by a Co^{III} atom depends on the magnitude of the crystal field splitting energy (Δ) and the intraatomic exchange energy (J_{ex}). The value of J_{ex} depends on the identity

and oxidation state of the metal but little on the chemical environment. In contrast, the value of Δ depends strongly on the chemical environment of the metal center.

Figure 1-5 shows three possible states (low-, high- and intermediate-spin) that 6-coordinate Co^{III} cations can adopt. In a low-spin configuration shown on the left, *d* electrons fill the t_{2g} symmetry orbitals before any electrons are placed in e_g symmetry orbitals. In a high-spin configuration shown in the middle, *d* electrons 'singly' fill all of the *d* orbitals before pairing. As shown in Figure 1-5, if $\Delta > 2J_{ex}$ then an LS configuration is adopted, while if $2J_{ex} > \Delta$, an HS state is more stable. As shown on the right, there is a third possible spin-state for Co^{III}, the $S = 1$ intermediate-spin (IS) state. In isolated molecules, an intermediate-spin state is not accessible since it can never be more stable than both HS and LS states. However, there is some evidence for the intermediate-spin state in $LaCoO_3$[30], which is stabilized by the formation of strong interactions via the filling of σ^* bonds formed from the Co^{III} e_g symmetry orbitals.

The spin states of Co^{III} can be affected by the nature of ligands to which the metal center is bonded as they modify the value of Δ. With ligands enlarging the value of Δ (i.e. $Co^{III}(NH_3)_6$), Co^{III} sites tend to become low spin. Conversely, Co^{III} sites tend to become high spin when ligands reduce the value of Δ (i.e. $Co^{III}F_6$).

In an intermediate regime, $Co^{III}O_6$ units have a ligand field close to the 'critical value' between HS and LS states. The relative magnitude of J_{ex} and Δ in a $Co^{III}O_6$ unit are such that the existence of systems with both HS and LS states is possible, with the particular spin-state strongly dependent on the local bonding and/or temperature.

LS Co^{III} has been found in many phases such as the layered oxide $LiCoO_2$[31] and the $n = 1$ Ruddledsden-Popper phase $La_2Li_{0.5}Co_{0.5}O_4$[32]. HS Co^{III} has been found in phases such as Sr_2CoO_3Cl[33] and $BiCoO_3$[34], which contain 100% HS Co^{III} at room temperature. A mixture

of HS/LS/IS Co^{III} can be found in systems such as $LnBaCo_2O_{5.4}$ (Ln = Eu, Gd)[35], $Sr_{1-x}Y_xCoO_{3-\delta}$[36], $LaCo_{1-x}Rh_xO_3$ [37][38][39] and $LaCoO_3$[40,41].

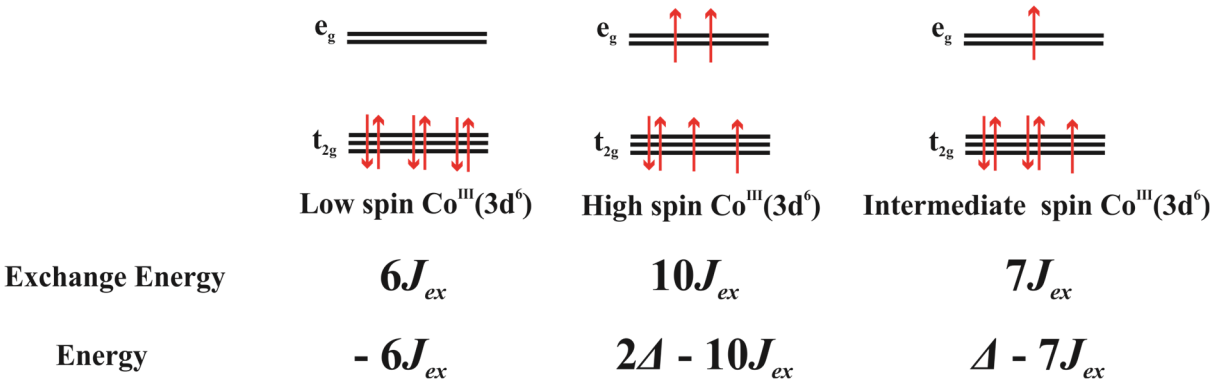


Figure 1-5 A schematic diagram of the spin state of trivalent Co ions: (left) low spin, $t_{2g}^6e_g^0$ Co^{III} with energy of -6 J_{ex} (J_{ex}: intra-atomic exchange energy); (middle) high spin, $t_{2g}^4e_g^2$ Co^{III} with energy of 2Δ-10J_{ex} (Δ: crystal field splitting energy); (right) intermediate spin, $t_{2g}^5e_g^1$ Co^{III} with energy of Δ-7J_{ex}.

1.4. Magnetic Interactions in Transition-metal Oxides

1.4.1. Correlated Magnetic Behaviour and Magnetic Ordering

For systems in which strong magnetic interactions occur between electron spins, correlated magnetic behaviour can be observed, including ferromagnetism, antiferromagnetism, canted-antiferromagnetism, ferrimagnetism, etc.

Ferromagnetism arises when the localised magnetic moments tend to align parallel to each other and hence results in a net magnetic moment. Alternatively, antiferromagnetism occurs when localised magnetic moments align anti-parallel to each other and hence results in zero net magnetic moment. In some antiferromagnetic materials, non-zero magnetic moments can be observed due to spin canting, in which spins are tilted and the angle between spins is not 180°. In a ferrimagnetic material, the system has opposing localised magnetic moments as in the antiferromagnetic material while these opposing moments are not equal in magnitude, which results in a net magnetic moment.

1.4.2. Coupling Mechanisms and the Goodenough-Kanamori Rule

The interactions between neighboring metal centers can be mediated by different types of couplings.

M - *M* direct exchange coupling arises when two transition metal atoms have direct orbital overlap. However, in complex oxides, the distance between transition-metal centers are usually too great to allow direct orbitals overlap.

Compared to *M* - *M* direct exchange couplings, *M* - O - *M* super-exchange interactions, in which an oxygen atom acts as a bridge to mediate the magnetic coupling of spins, are stronger and more common. In this interaction, the virtual hoping of electrons in O 2*p* orbitals couples the magnetic moments on adjacent metal cations. The strength of this interaction depends on many factors such as *M*-O-*M* bond angle, *M*-O-*M* bond length and the energy match between metal *d* orbital and the oxygen *p* orbitals. The magnetic behavior mentioned in Section 1.4.1 can be inferred from the predicted sign of the super-exchange coupling based on the geometry of the *M*-O-*M* bond and the orbital filling. A semi-empirical set of rules called Goodenough-Kanamori rules[42] is summarized based on Anderson's work[43] and can be used to predict the sign of magnetic coupling between metal centers based on orbital filling and bond geometry. According to the Goodenough-Kanamori rules, a 180º *M*-O-*M* super-exchange interaction between ½ filled orbitals results in a strong antiferromagnetic coupling (Figure 1-6 (left)) while a 90º *M*-O-*M* super-exchange interaction between ½ filled orbitals results in a weak ferromagnetic coupling (Figure 1-6 (right)).

In the complex oxides presented in this thesis, 180° *M*-O-*M* super-exchange interactions are more common than 90° *M*-O-*M* super-exchange interactions. According to the Goodenough-Kanamori rules, for 180° *M*-O-*M* super-exchange interactions, ½ filled orbital - filled orbital interactions and ½ filled orbital - empty orbital interactions favor ferromagnetic coupling while

½ filled orbital - ½ filled orbital and filled orbital - empty orbital interactions favors antiferromagnetic coupling.

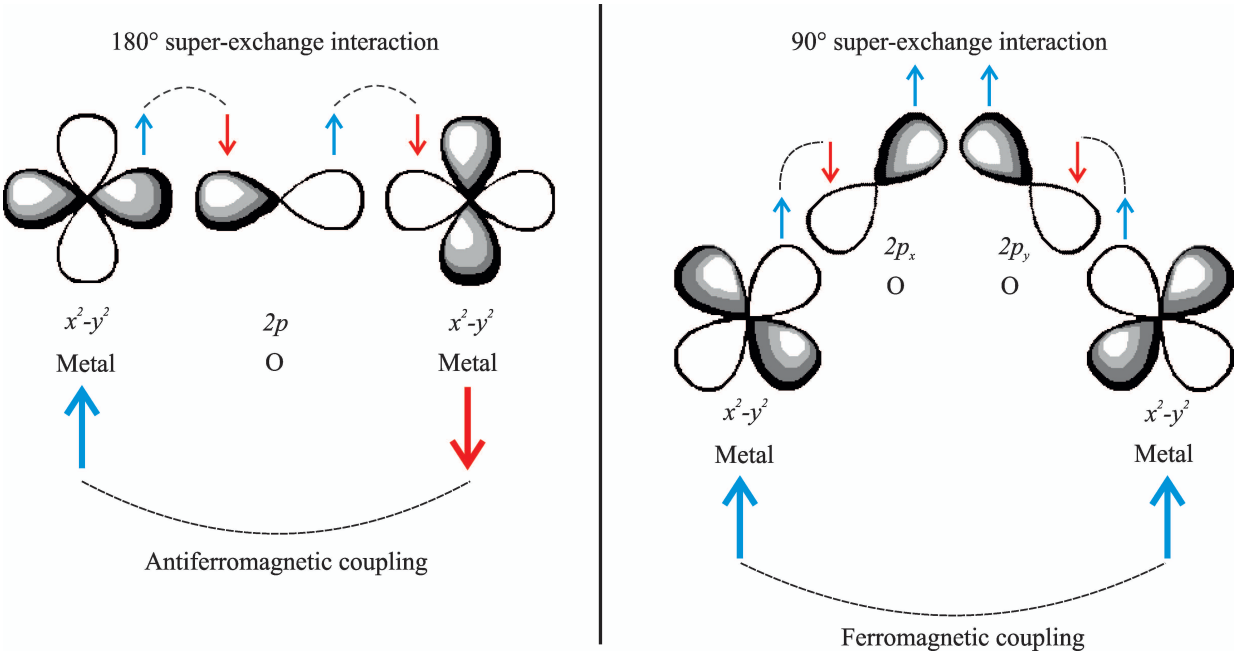


Figure 1-6 A schematic representation of super-exchange interactions of *M*-O-*M* in 180° (left) and 90° (right) arrangements.

1.5. Synthesis and Topochemical Reduction of Transition-metal Oxides

1.5.1. Traditional Synthesis of Crystalline Solids and its Disadvantages

In crystalline solids, the mobility of ions in the lattice is extremely low. Thus, traditional solid-state synthesis methods such as the ceramic method require high temperatures ($T \geq 1000$ °C) to overcome large energetic barriers to ion diffusion. As a result, the application of traditional solid-state synthesis methods generally achieves preparation of the most thermodynamically stable phases. To pursue metastable complex oxide phases mentioned in the thesis, traditional solid-state synthesis methods are not appropriate because of their thermodynamic control, so the synthetic routes that have access to kinetic control are then proposed and utilised in the thesis.

1.5.2. Topochemical Reduction

To prepare complex oxides containing metals with novel oxidation states and coordination geometries, one of the most common approaches is the modification of anion lattices, either by introducing anion vacancies or replacing them with non-oxide hetero-anions.

A series of low temperature techniques using kinetic control have been developed to prepare metastable solid phases[44]. These topochemical methods make use of the different ion mobilities in a crystalline solid to alter selective features in the framework of 'parent' phases while maintaining the structural lattice. These methods allow access to metastable phases which are inaccessible using traditional thermodynamic methods[45]. In the anion lattice modification using topochemical methods, the most commonly used reducing agents include solid state binary metal hydrides, flowing H_2 gas and finely divided electropositive metals. The choice of the reducing agent depends on the nature of 'parent' phases, the chemical composition of targeted phases and the desired reaction temperature regime.

However, thermodynamic instability is the main difficulty in preparing topochemically reduced phases from perovskite-related structures. The $M^{2+} + 2e^- \rightarrow M$ redox potential of 4d and 5d transition metals tend to take small positive values[46]. This means on topochemical reduction via anion deintercalation, most complex oxides containing only 4d or 5d metals (e.g. $SrRuO_3$) decompose to form the corresponding elemental metal, e.g. $SrRuO_3 \rightarrow SrO + Ru$[47]. Previous studies of the topochemical reduction of 4d/5d oxides have shown that 3d transition metals are able to covalently stabilize the frameworks and prevent complex oxides from being reduced all the way to their elemental states. For example, the $n = \infty$, 1, and 2 members of the $(La_{x/2}Sr_{1-(x/2)})_n(Ni_{0.5}Ru_{0.5})_nO_{3n+1}$ compositional series ($La_xSr_{2-x}NiRuO_6$, $La_xSr_{4-x}NiRuO_8$, $La_xSr_{3-x}NiRuO_7$) can be topochemically reduced using reducing agents such as binary metal hydrides and finely divided electropositive metals[48]. Reduction reactions yield $(La_{x/2}Sr_{1-(x/2)})_nSr(Ni_{0.5}Ru_{0.5})_nO_{3n-1}$ compounds ($La_xSr_{2-x}NiRuO_4$, $La_xSr_{4-x}NiRuO_6$,

$La_xSr_{3-x}NiRuO_5$), containing Ni^I and Ru^{II} cations in square-planar coordination, while the reduction of complex oxides containing only Ru as *B*-site cation leads to decomposition. Therefore, the topochemical reduction of complex oxides containing both 3d and 4d transition metals are investigated in this thesis.

1.5.2.1. Topochemical Reduction Using Binary Metal Hydrides

Binary metal hydrides (NaH, CaH_2 and LiH) can be used as reducing agents for topochemical reduction reactions. Reactions using metal hydrides typically lead to either oxide ion deintercalation or hydride ion incorporation.

The reduction of samples such as $LaNiO_3$ and $SrFeO_3$ using metal hydrides are reported to yield reduced complex oxides $LaNiO_2$[44] and $SrFeO_2$[49]. The reduction of samples such as $BaTiO_3$, $Sr_{n+1}V_nO_{3n+1}$ and $LaSr_3NiRuO_8$ with CaH_2 lead to hydride ion incorporation and yield the oxyhydride phases $BaTiO_xH_y$[50], $Sr_{n+1}V_nO_{3n-1}H_n$[51] and $LaSr_3NiRuO_4H_4$[52]. As shown in Figure 1-7, the $(Ni/Ru)O_6$ octahedra in the $LaSr_3NiRuO_8$ phase have been converted to $(Ni/Ru)O_4H_2$ units after the reduction using CaH_2 as a reducing agent.

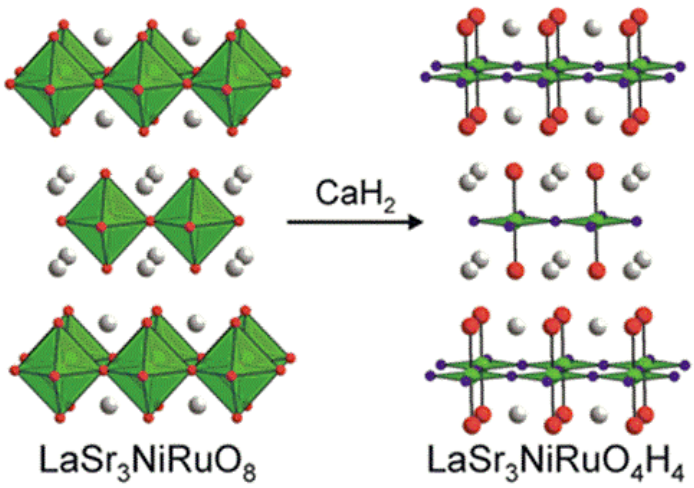


Figure 1-7 A schematic presentation of the Ruddlesden–Popper phase $LaSr_3NiRuO_8$ transformed topochemically into the oxide–hydride $LaSrNiRuO_4H_4$ phase by the action of CaH_2 at 450 °C. (La/Sr gray, Ni/Ru green, O red and H blue)[52].

1.5.2.2. Topochemical Reduction Using Finely Divided Electropositive Metals

An alternative method for anion deintercalation of complex transition-metal oxides utilizes finely divided electropositive metals such as Zr and Al as oxygen getters.

When heating complex oxides at a suitable temperature, the oxygen anions in the lattice gain mobility and samples tend to release oxygen. This oxygen release process reaches an equilibrium with O_2 partial pressure in contact with the solid surface, as described as the following equation:

$$MO_n \leftrightarrow MO_{n-2\delta} + \delta O_2\,(g)$$

The equilibrium can be driven to the right to form metastable reduced oxide phases by lowering O_2 partial pressure. Thus, an oxygen getter (Zr, Al) is added in the system to react rapidly with the released O_2 and form thermodynamically stable by-products such as ZrO_2 and Al_2O_3. In this method, metal oxides and an oxygen getter are placed separately in a sealed silica glass ampoule to avoid unnecessary contamination. For example, distinct phases of $La_2Co_2O_5$ and $La_3Co_3O_8$ are formed by isothermal reduction of $LaCoO_3$ using chips of Zr.[53],[54] The reaction equation is shown as follows:

$$LaCoO_3 \leftrightarrow LaCoO_{3-\delta} + O_2 + Zr \rightarrow La_nCo_nO_{3n-1} + ZrO_2$$

Figure 1-8 shows the reduced phases $La_nCo_nO_{3n-1}$ (n = 2,3) which have structures which consist of CoO_6 octahedra in sheets stacked in an alternating sequence with CoO_4 tetrahedra sheets[53][54].

Other getters such as Al are not as widely used as the Zr getter, but a range of oxygen-deficient phases $LaNiO_{3-x}$ ($0 \leq x \leq 1$) is reported to form by using aluminium as the oxygen getter[55,56].

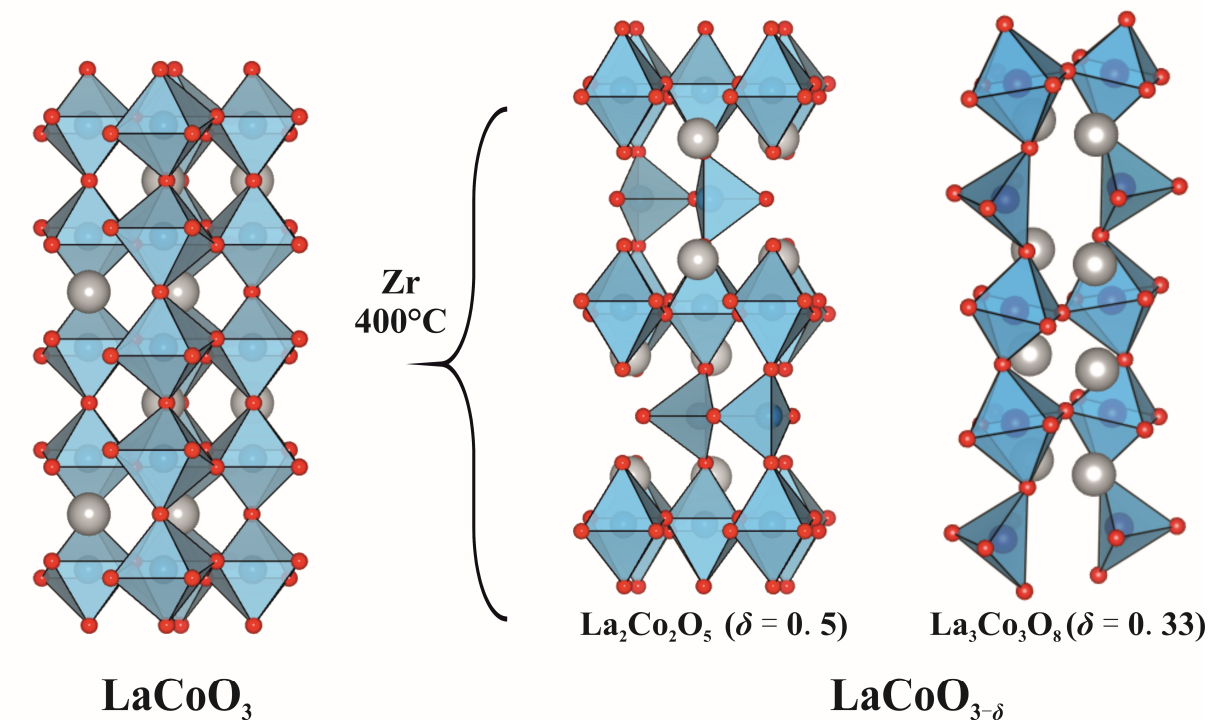


Figure 1-8 Topochemical reduction of $LaCoO_3$ with Zr getter to form reduced phases $La_nCo_nO_{3n-1}$ (n = 2,3)[53][54].

1.6. The Motivation of the Work

Perovskite-related oxide phases containing 4d/5d transition metals have shown a rich reduction chemistry.

Topochemical deintercalation of oxide ions from ruthenium-containing complex oxides has been well explored. For example, reduction reactions of $Sr_2Fe_{0.5}Ru_{0.5}O_4$ and $Sr_3(Fe_{0.5}Ru_{0.5})_2O_7$ with CaH_2 have been reported and both square-planar MO_4 coordination sites and square-based pyramidal MO_5 coordination sites (M = Fe, Ru) were found in the resulting phases $Sr_2Fe_{0.5}Ru_{0.5}O_{3.35}$ and $Sr_3(Fe_{0.5}Ru_{0.5})_2O_{5.68}$[57]. In addition, the reduction of the n = ∞, 1, and 2 members of the $(La_{x/2}Sr_{1-(x/2)})_nSr(Ni_{0.5}Ru_{0.5})_nO_{3n+1}$ compositional series have been reported to yield corresponding topochemically reduced $(La_{x/2}Sr_{1-(x/2)})_nSr(Ni_{0.5}Ru_{0.5})_nO_{3n-1}$ compounds ($La_xSr_{2-x}NiRuO_4$, $La_xSr_{4-x}NiRuO_6$ and $La_xSr_{3-x}NiRuO_5$) using CaH_2 and Zr as reducing agents, which contain Ni and Ru cations in square-planar coordination sites [48].

Compared to the studies of ruthenium-containing complex oxides, the reduction chemistry of rhodium-containing complex oxides have not been well developed. Thus, building on the advance of previous studies, topochemical reduction of rhodium-containing complex oxides is investigated.

Chapter 2

Experimental Methods and Techniques

2.1. Synthesis of Starting Materials: Ceramic Method

The thermodynamically stable starting materials in this thesis are prepared via a ceramic method. The ceramic method is one of the most common methods utilized for the preparation of solid-state compounds. In a typical ceramic method synthesis, stoichiometric quantities of precursors such as metal oxides, metal carbonates and elemental metals are prepared and ground together using an agate mortar and pestle to achieve a homogenous mixture of reactants. The mixed powders containing carbonates are then transferred into an alumina crucible, heated in air at a rate of 5 °C min^{-1} to 1000 °C for carbonate decomposition. After carbonate decomposition, samples are then reground and pressed into pellets (diameter 13mm) under 5.5 tonnes of force in order to increase the number of crystallites in contact. After pelletizing, samples are heated in an alumina crucible at suitable temperatures in a muffle furnace. High temperatures (above 1000 °C) are usually required to speed up the diffusion with solids. Specific atmospheres (air, Ar, O_2, H_2 etc.) are applied to high-temperature reactions as protection gas or reagent gas to aid pure phase formation. The reaction temperatures and selected atmospheres for the synthesis of specific phases are detailed in the related chapters. After each cycle of heating, samples are reground and re-pressed into pellets to create fresh surfaces in contact. Multiple (3 ~ 4 times) heating periods (~ 50 hours each) with grindings in between are normally required to reach a homogeneous single phase. Reaction progress was monitored by laboratory X-ray powder diffraction. When no obvious change is observed in XRD pattern from the subsequent heating reaction, the reaction is deemed complete. Synchrotron X-ray powder diffraction data and neutron powder diffraction data are then collected from the resulting phase.

2.2. Synthesis of Topochemical Reduced Materials

2.2.1. Zirconium Getter Reductions

Zirconium getter reduction is an effective method for performing topochemical anion deintercalation reactions on complex transition-metal oxides. This method is based on the oxygen release process of complex metal oxides. Above a certain temperature, the oxygen content of complex metal oxides and the O_2 partial pressure in contact with the solid surface reach an equilibrium, which can be described as the following equation:

$$MO_n \leftrightarrow MO_{n-2\delta} + \delta O_2\,(g)$$

The oxygen release equilibrium can be driven to the right by raising the temperature or by lowering the O_2 partial pressure in the system, allowing the formation of metastable reduced oxide phases. Thus, zirconium powder is used in those reactions as an oxygen getter to react rapidly with the released O_2 to form ZrO_2 which is highly thermodynamically stable. To avoid unnecessary contamination, metal oxides and the Zr oxygen getter are placed separately in a sealed silica glass ampoule. For example,as mentioned in Section 1.5.2.2, $La_2Co_2O_5$ and $La_3Co_3O_8$ were formed by isothermal reduction of $LaCoO_3$ in which the samples were held in an alumina crucible in the glass ampoules separated from Zr chips.[53],[54].

In this thesis, the Zr getter method is chosen for most of the topochemical anion deintercalation reduction reactions. As shown in Figure 2-1, dented open silica glass ampoules are prepared for Zr getter reactions, with the dent being ~ 1 cm from the bottom of a silica tube. In an argon-filled glove box, 2 mole equivalents of zirconium powder (compared to the parent oxide) are weighed and transferred to the bottom of the special silica glass tubes (Figure 2-1) using a funnel. The sample to be reduced is placed in a smaller silica tube and loaded into the dented silica tube after transferring the zirconium powder so that the two powders share an atmosphere but are not in physical contact. To avoid exposure of oxygen, the whole apparatus is then sealed

using a Young's tap, evacuated and sealed under vacuum using a methane blow torch to form a sealed silica ampoule.

The sealed silica ampoule is then placed in a low temperature furnace and heated to a specific temperature at a ramp rate of 1 °C/min to avoid overshooting the desired temperature. After one cycle of heating, the ampoule is opened inside the glovebox. The reduced sample is reground and fresh Zr powder is added at the bottom of a new silica tube. Reaction progress is monitored by air-sensitive laboratory X-ray Powder Diffraction (Section 2.2.2.2). The optimum temperature for topochemical reduction is screened via X-ray Powder Diffraction analysis. Typically, the Zr getter reduction can be completed by being heated at the optimum temperature for 3 periods of 4 days, with the sample being reground between heating periods.

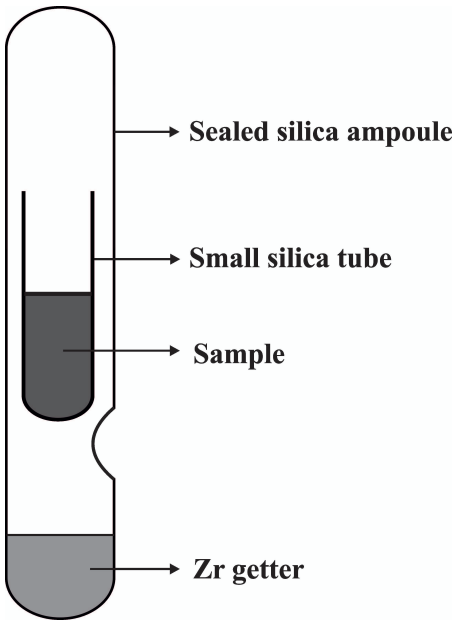


Figure 2-1 A schematic graph of a sealed silica ampoule for zirconium getter reactions.

2.2.2. Handling Air-sensitive Reactions and Compounds

Many reducing reagents mentioned in this thesis exhibit high sensitivity to both air and moisture. For example, binary metal hydrides and elemental zirconium powder can react rapidly with O_2 and H_2O in air. In addition, all of the reduced oxide phases mentioned in following chapters slowly react with O_2 in air. Some of the reduced oxide phases will be re-oxidised back to starting materials after long exposure in air. Some of the mixed-powder reduced phases and hydrides will react rapidly with H_2O to form hydroxides, which will contaminate the reduced phases. Thus, during the whole process of these air-sensitive reduction reactions and related characterization involving any of these air-sensitive chemicals, samples need to be kept under an inert atmosphere at all times, air-and-moisture-free reaction apparatus and characterisation techniques are needed.

2.2.2.1. Argon-filled Glove Box

The inert atmosphere for the preparation of topochemical reductions and the air-sensitive sample storage is provided by an argon-filled glove box, as shown in Figure 2-2. In this thesis, a UNIlab plus glovebox workstation from MBRAUN was used. The glovebox is filled with argon with the partial pressure of O_2 and H_2O both below 0.1 ppm. The solvent vapors and oxygen in the internal atmosphere can be removed by continuous circulation of the working gas argon through a gas purifier. Thus, the air-and-moisture-sensitive reducing reagents and reduced samples can be transferred through the antechamber of the glovebox and stored inside the glovebox to avoid deterioratation. All the activities that took place in the glovebox were carried out using the Butyl gloves fixed on gloveports (shown in Figure 2-2) in the box window.

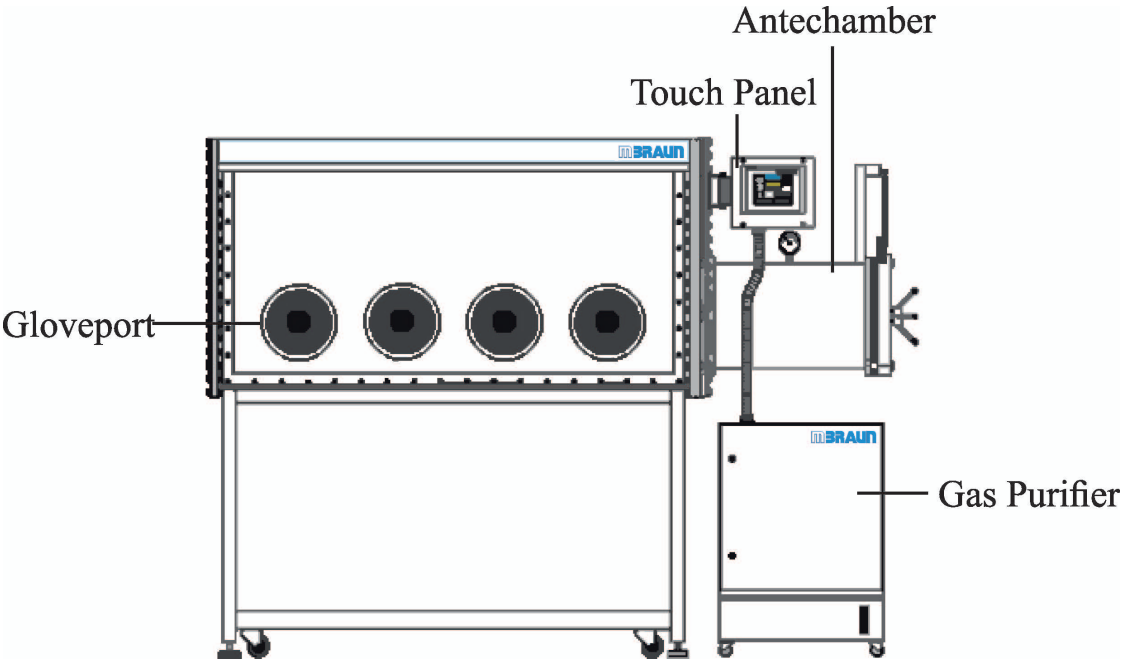


Figure 2-2 A schematic graph of an argon-filled glovebox[58]

2.2.2.2. Air-sensitive X-ray Powder Diffraction

The inert atmosphere is also needed during the characterization of air-sensitive samples. Thus, air-sensitive sample holders are used when collecting X-ray powder diffraction data from these air-sensitive samples. As shown in Figure 2-3, a thin layer of Dow Corning high vacuum grease is applied to a glass slide. A small amount of air-sensitive powder is evenly distributed on the grease layer. The slide is then transferred into the chamber with an acetate window in the air-sensitive sample holder. In order to form an air-tight environment, the whole set is sealed by screwing on a brass lid and compressing an O-ring between the lid and the rest of the sample holder. The preparation of sealed glass slides with samples in an air-sensitive sample holder is carried out in an argon-filled glovebox.

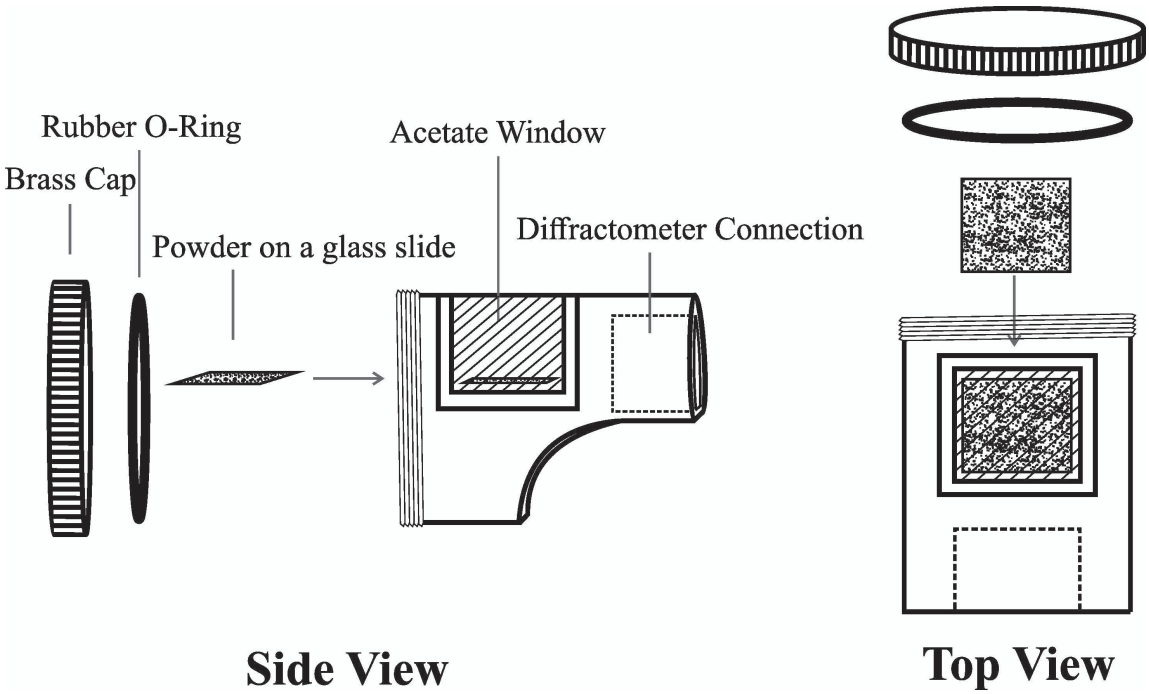


Figure 2-3 A schematic graph of an air-sensitive X-ray sample holder.

2.3. Powder Diffraction

In solid state chemistry, powder diffraction techniques are among the most commonly used methods for the structural characterisation of crystalline materials. In this thesis, X-ray powder diffraction and neutron powder diffraction are utilized for the structure analysis of the materials.

Diffraction phenomena occur when a wave encounters scattering obstacles of comparable size to the wavelength of the radiation. For crystallized solid phases, the periodically arranged atoms form an array of lattice planes with spacings, which are comparable to the wavelengths of X-rays and neutron radiations. The relation between the wavelength and the scattering angle for a crystal lattice is given by Bragg's Law[59]:

$$\boldsymbol{n\lambda = 2d_{hkl}\sin(\theta)}$$

where n is an integer; λ is the wavelength of the incident beam, d_{hkl} is the interplanar distance between planes of atoms that contribute to diffraction peaks; θ is the angle between the beam

and the lattice planes (as shown in Figure 2-4). At the points where atoms form lattice planes with an interplanar distance d_{hkl}, waves interfere constructively and destructively and produce a diffraction peak when the path-length difference $2d_{hkl}\sin\theta$ is equal to integer multiples of the wavelength. Therefore, the lattice-plane spacings can be characterized based on the wavelength and the scattering angle.

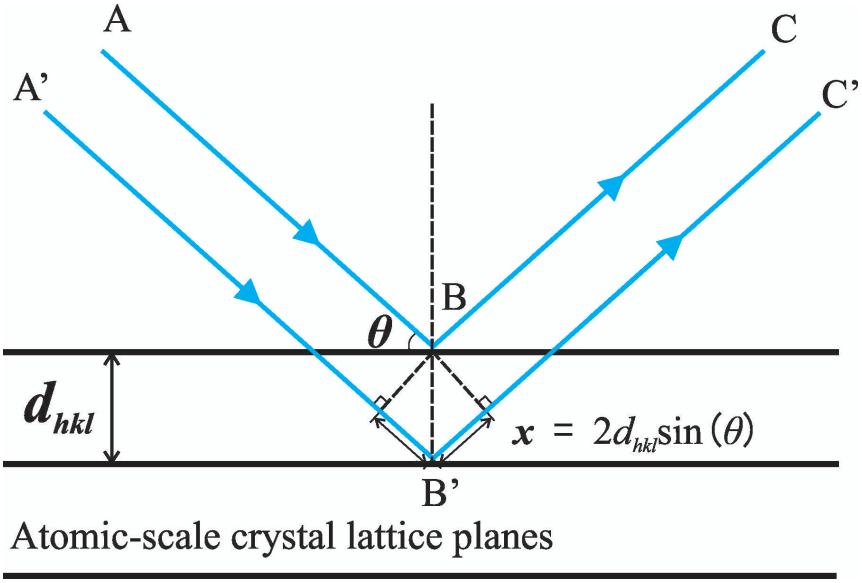


Figure 2-4 Bragg's Law Reflection. The constructive interference occurs when the distance difference *x* between paths ABC and A'B'C' equals to an integer number of wavelengths.

The intensity of the given reflection (I_{hkl}) is defined as follows:

$$\boldsymbol{I_{hkl} \propto LmA|F_{hkl}|^2}$$

In this equation, L is the Lorentz-polarisation function constant; m is the reflection multiplicity; A is the absorption factor; F_{hkl} is the structure factor. The structure factor, F_{hkl}, describes how individual contents of the unit cell influences the intensity of a reflection, I_{hkl}. The detailed relationship that defines the structure factor F_{hkl} is listed as follows:

$$\boldsymbol{F_{hkl} = \sum_n f_n(\theta)\exp\left[2\pi i(hx_n + ky_n + lz_n)\right]\exp\left[\frac{-8\pi^2 U_{iso_n}\sin^2\theta_{hkl}}{\lambda^2}\right]}$$

In this equation, f_n is the atomic scattering factor; x_n, y_n, z_n are the fractional coordinates of the atoms in the unit cell; U_{iso_n} is the isotropic thermal displacement factor.

2.3.1. X-ray Powder Diffraction

2.3.1.1. Cu-sourced Instruments: Panalytical Empyrean, Panalytical X'Pert and Bruker D8

In this thesis, X-ray powder diffraction data are mainly collected using Panalytical Empyrean, Panalytical X'pert and Bruker D8 Eco diffractometers. All the diffractometers are configured in Bragg-Bretano focussing geometry. The three diffractometers differ in incident beams. Both Cu $K_{\alpha 1}$ and $K_{\alpha 2}$ radiations are present in the incident beam in Bruker D8 instrument, while for the Panalytical Empyrean and Panalytical X'pert instruments, a Ge (111) monochromator is installed so that only Cu $K_{\alpha 1}$ radiation is present in the incident beam.

Based on their relative advantages, in this thesis, Bruker D8 diffractometer was used for a quick check of crystallized phases; Panalytical Empyrean diffractometer was used for reaction progress monitoring; Panalytical X'pert diffractometer was used for detailed characterisation of crystal structures after the reaction is deemed complete.

The sample preparation required for XRD measurements is the same for the different diffractometers. The assembly of air-sensitive samples holder has been described in Section 2.2.2.2. For non-air-sensitive samples, a silicon wafer sample holder is used for XRD measurement. The silicon wafer is covered with a thin layer of Dow Corning high vacuum grease. Non-air-sensitive samples are evenly distributed on the greasy side of the silicon wafer. The wafer is then installed on a spinning stage in the diffractometer which rotates during the measurement to avoid any possible influence from uneven sample distribution. The silicon wafer sample holder is cleaved along the [110] plane, so it exhibits no diffraction peaks. Therefore, the sample holder won't interfere with diffraction pattern collected from samples.

2.3.1.2. Mo-sourced Instrument:Panalytical Empyrean with PheniX Cryostat

The PheniX apparatus is a closed cycle helium cyrostat designed for low temperature X-ray powder diffraction measurement in the temperature range $12 \leq T/\mathrm{K} \leq 298$. The cryostat is mounted onto a vertical goniometer in a Mo-sourced Panalytical Empyrean diffractometer. Air-sensitive samples are loaded onto a silicon wafer sample holder and kept under a dynamic vacuum to avoid exposure to air.

2.3.1.3. Synchrotron X-ray Powder Diffraction

A synchrotron is a particular type of cyclic particle accelerator which accelerates beams of electrons through a fixed closed-loop path. A synchrotron light source can produce X-ray beams with much higher brilliance than the X-ray beam from a laboratory source, which is the most important advantage of synchrotron radiation over a laboratory X-ray source. With high-energy X-ray beams generated by synchrotron sources, we can get high-resolution and high-signal-to-noise-ratio X-ray powder diffraction data for nuclear structure studies of complex transition metal oxides[60].

The synchrotron X-ray powder diffraction data in this thesis were collected using the I11 beamline at the Diamond Light Source Facility in Didcot, Oxfordshire, U.K. The I11 beamline is able to produce X-rays at energies from 5 to 30 keV. The schematic representation of I11 X-ray source and the diffractometer is shown in Figure 2-5[61],[62].

In the experimental hutch in Figure 2-5, samples sealed in borosilicate capillaries (diameters range from 0.3mm to 0.7mm) are placed in brass holders and installed by a robotic arm into a magnetic spinner stage which is pre-aligned to the centre of the diffractometer. Noncontact sample environments (N_2 cryocooler and hot gas blower) mounted on the large motorized sample table can provide variable-temperature measurement (80K -1000K).

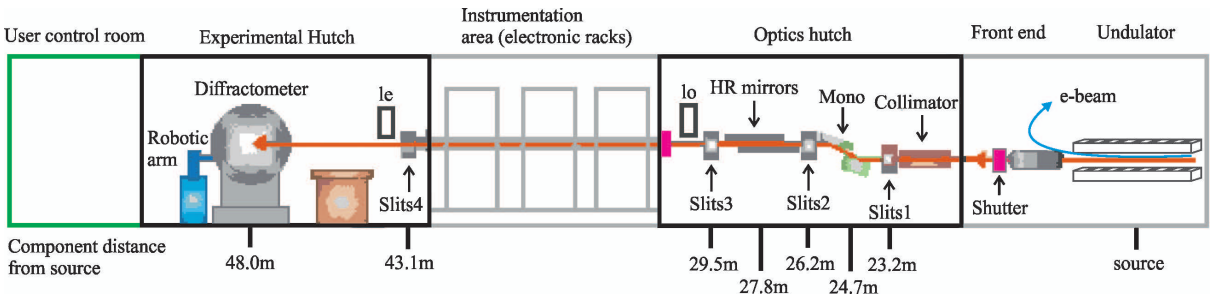


Figure 2-5 A Schematic representation of Beamline I11 showing the main components and their approximate distances from the IVU (X-ray source)[61].

2.3.2. Neutron Powder Diffraction

Neutron powder diffraction is also commonly used for the characterisation and structure analysis of crystallized phases. The basic difference between X-ray powder diffraction and neutron powder diffraction is that X-ray radiation interacts with the electron density of atoms in the lattice while the neutron radiation interacts with the nuclei of the atoms.

Based on different interaction mechanism, neutron powder diffraction has several advantages over X-ray powder diffraction, which are listed as follows. Firstly, as the scattering of X-rays is dependent on the number of electrons an atom has, light atoms (e.g. oxygen) make only small contributions to the diffraction pattern when heavier atoms (e.g. lanthanum) are present as well. In contrast, neutron scattering lengths of atoms do not follow a linear relationship with the atomic number[63], therefore the locations and occupancies of light elements can be investigated much more accurately in samples containing both light and heavy elements if neutron diffraction is used. Secondly, unlike the X-ray scattering form factor, the neutron scattering form factor is almost independent of the scattering angle. Thus, high angle neutron diffraction peaks maintain a high intensity, bringing structural information with higher reliability in the area of small d-spacings compared to X-ray diffraction peaks, which helps determine crystal lattices with higher accuracy. Finally, interactions with electron spins are allowed in neutron

diffraction since neutrons are half-integer spin particles. Thus, when neutrons are scattered by a lattice of ordered magnetic moments, the magnetic structure of the phases can be determined.

For an unpolarised neutron source, the total scattered intensity is the sum of nuclear and magnetic scattering. The magnetic structure factor (F_{mag}^{hkl}) can be described as follows[64]:

$$\boldsymbol{F_{mag}^{hkl}} = \sum_j q_j p_j e^{2\pi i h x_j}$$

where q_j is the magnetic interaction vector, p_j is the magnetic form factor, h is the magnetic scattering vector and x_j is the position vector of magnetic atoms in the unit cell.

The observed intensity of a magnetic reflection (I_{mag}^{hkl}) is proportional to the square of the projection of the magnetic structure factor onto the scattering vector[64]:

$$\boldsymbol{I_{mag}^{hkl}} = \left|F_{mag}^{hkl}\right|^2 \cos^2 \alpha$$

where α is the angle between the magnetic scattering structure and the relevant lattice plane. Large-scale samples (> 1 g) are required for neutron diffraction measurements due to the weak neutron scattering interaction. In this thesis, 2 - 4 g of an air-sensitive sample was loaded into a vanadium can in an argon-filled glove box and sealed with one indium washer and six screws. Vanadium exhibits a very low coherent scattering length of -0.3824 fm[63] and generally has a negligible contribution to neutron diffraction patterns, making it a good choice as the material for sample containers for neutron diffraction measurements.

The neutron powder diffraction data presented in this thesis were collected from these sources and diffractometers: POLARIS diffractometer at ISIS neutron facility, Rutherford Appleton Laboratory in Oxfordshire, U.K.; D2B and D1B diffractometers at the Institut Laue-Langevin (ILL) in Grenoble, France. We would like to thank Dr. E. Suard for assistance in collecting data at the ILL.

2.3.2.1. POLARIS Diffractometer

POLARIS instrument (Figure 2-6) is a high intensity, medium resolution powder diffractometer at ISIS Facility pulsed neutron source, an accelerator-based spallation source of neutrons. The POLARIS instrument is optimised for the rapid structural characterisation of small amounts of materials[65].

POLARIS utilizes the time-of-flight (TOF) neutron diffraction technique. In a TOF experiment, the time taken by a neutron to travel the flight path L from the moderator to the detector is measured, thus the de Broglie wavelength of the neutron can be obtained. With a fixed incident angle θ, the d-spacing of crystalline solid can then be calculated by the equation below:

$$\boldsymbol{n\lambda = \frac{h}{mv} = \frac{ht}{mL} = 2d_{hkl}\sin(\theta)}$$

where h is the Planck's constant, m is the mass of the neutron, t is the time taken by a neutron to travel the distance of L and θ is the fixed angle of detector banks of the POLARIS diffractometer. The POLARIS diffractometer have numerous detector elements at different angles. The detector elements are grouped into 5 separate banks, with each bank containing elements covering a similar d-spacing range. Bank 1 at a very low angle, bank 2 and 3 at low angles, bank 4 at 90° and bank 5 at backscattering angles are shown in Figure 2-6. The resolution of a POLARIS diffractometer varies dramatically with the detector angle. Thus, detector banks at high angles like bank 4 and bank 5 have higher resolustion and sharper diffraction peaks but only measure to relatively low maximum d-spacings, while detector banks at low angles such as bank 1 have poorer resolution and broader reflections but are able to measure a wider range of d-spacings. Hence, neutron powder diffraction data from each bank are complementary and data analysis is often conducted on the basis of a combination of data from multiple detector banks.

In this thesis, the POLARIS diffractometer was utilized to characterize the reduced phases $LaSrM_{0.5}Rh_{0.5}O_{3.25}$ (M = Co, Ni) as discussed in Chapter 4 and bank 3, 4 and 5 data were used and analysed.

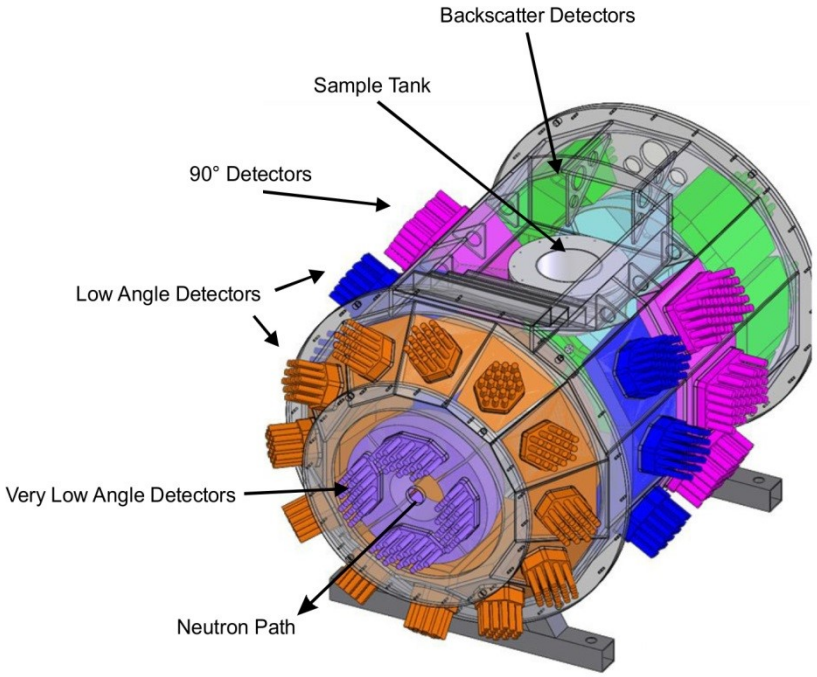


Figure 2-6 The POLARIS diffractometer at the ISIS Facility pulsed neutron source.[65]

2.3.2.2. D2B and D1B Diffractometers

The D2B and D1B instruments are neutron powder diffractometers at the ILL neutron source in France. The ILL neutron source provides neutrons with an extremely high intensity (energy in the meV range) from fission of ^{235}U. The fission process is sustained by lowering the energy of produced neutrons through a moderator filled with D_2O. The neutrons resulting from this moderation process are of suitable energies to perform diffraction experiments, with appropriate wavelengths which can be further discriminated by crystal monochromators in the instruments[66].

The D2B instrument (Figure 2-7) is a high-resolution powder diffractometer at ILL. In a measurement using the D2B diffractometer, scans are performed over the angle range $4° < 2\theta < 160°$ for multiple times and several scans are summed to give the diffraction pattern with a good signal-to-noise ratio, hence the diffraction pattern can accurately provide the structural information of the phases.

The D1B instrument (Figure 2-8) is another high intensity powder diffractometer at ILL. The D1B diffractometer is equipped with a position sensitive detector (PSD) covering the angular range from 0.8° to 128.8º and is optimised for high resolution at long d-spacings with an extremely high signal to noise ratio.

In this thesis, the magnetic and the nuclear structure of the reduced perovskite phase $La_2CoRhO_{4.5}$, $La_2NiRhO_{4.5}$ and $LaSrMnRhO_{4.5}$ are investigated using D1B diffractometer (λ = 2.52 Å) and D2B diffractometer (λ = 1.59 Å), with D1B conducting the low temperature neutron diffraction measurements and D2B conducting the ambient temperature neutron diffraction measurements. Details are discussed in Chapter 7 and Chapter 8.

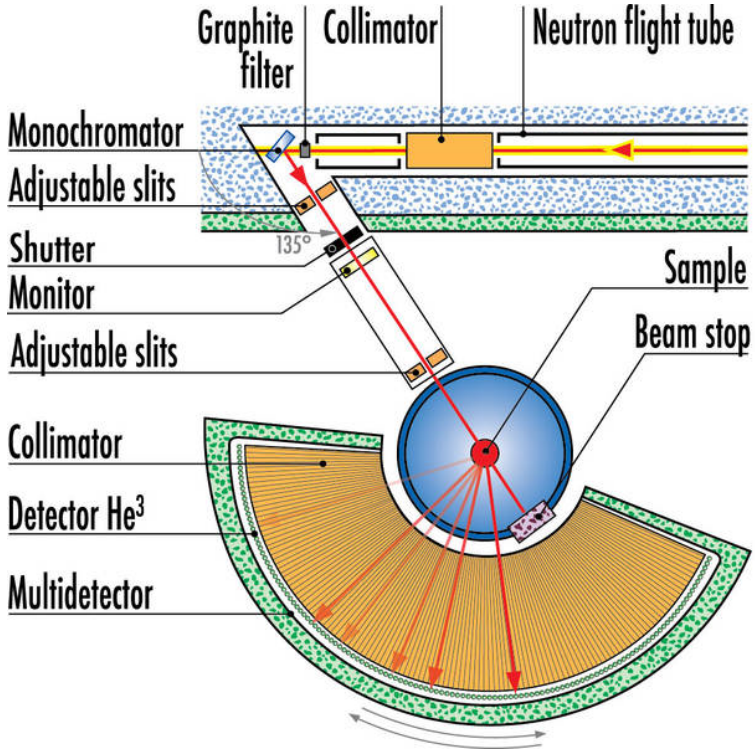


Figure 2-7 D2B diffractometer at ILL, Grenoble, France.[66]

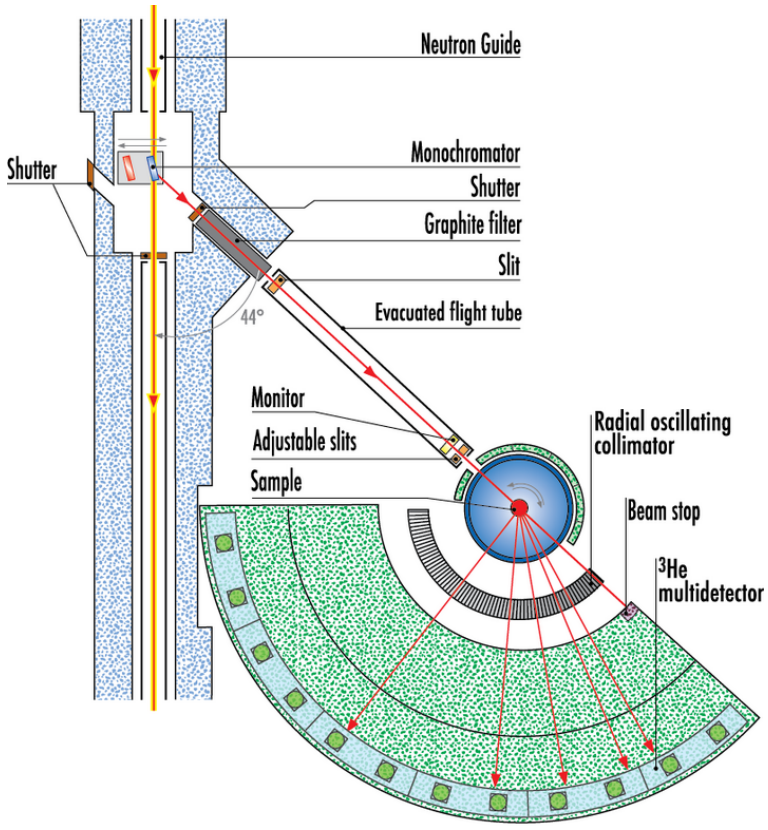


Figure 2-8 D1B diffractometer at ILL, Grenoble, France.[67]

2.4. Rietveld Refinement

Powder diffraction experiment gives a one-dimensional diffraction pattern extracted from the three-dimensional structure of a crystalline solid. As shown in Section 2.3, Miller planes with a specific d-spacing can contribute to a diffraction peak at a particular indicent angle which satisfies the Bragg's law. Miller planes with different *hkl* indices but similar d-spacings can contribute to diffraction peaks at similar angles, leading to overlapping reflections. This means that while it is easy to calculate the intensity of a peak from a known structure, the reverse - determining unknown structures from diffraction data - is much more challenging because it requires the deconvolution of the overlapping peaks.

To address this problem, the powder diffraction data in this thesis was analysed using the Rietveld refinement method[68]. The Rietveld method calculates a simulation of diffraction pattern from a proposed structural model, which is close to the real one, and then compares the simulation to the observed diffraction pattern. The crystallographic parameters of the proposed structural model are refined until the peak positions and intensities of the simulation matches with the observed data. The refinement goes with the aim of minimising the difference (*S*) between the experimental data and the model simulation using a least squares equation:

$$\boldsymbol{S} = \sum_i w_i \{y_i^{obs} - y_i^{calc}\}^2$$

In this equation, w_i is the weighting factor, y_i^{obs} is the observed intensity at point *i* in the diffraction pattern and y_i^{calc} is the calculated intensity at point *i*.

The Rietveld refinement is conduct using the General Structure Analysis System (GSAS) suite of programs[69]. The statistical fit of the model to the data is assessed using the following parameters: the goodness of fit, χ^2; the profile factor, R_p; the weighted profile factor, wR_p. The three parameters are defined as follows:

$$\chi^2 = \frac{\sum w_i (y_i^{obs} - y_i^{calc})^2}{n_{obs} - n_{var}}$$

$$R_p = \frac{\sum |y_i^{obs} - y_i^{calc}|}{\sum y_i^{obs}} \times 100\%$$

$$wR_p = \sqrt{\frac{\sum w_i (y_i^{obs} - y_i^{calc})^2}{\sum w_i (y_i^{calc})^2}} \times 100\%$$

where n_{obs} is the number of observations in all histograms and n_{var} is the number of variables in the least squares refinement. After the minimising the difference between the simulation and the observed data, structural information such as lattice parameters, atomic positions, site occupancy, displacement parameters and peak profiles can be obtained.

2.5. SQUID Magnetometry

The magnetic properties of samples in this thesis were measured using a Quantum Design MPMS 3 Superconducting Quantum Interference Device (SQUID). A SQUID magnetometer is extremely sensitive to small variations of magnetic flux by using Josephson effect. The SQUID contains a device known as a Josephson junction shown in Figure 2-9 (two pieces of superconducting materials separated by a thin insulating layer)[70].

In a Josephson junction, superconducting electrons are able to tunnel through the two junctions and maintain the phase coherence[71]. The Josephson junction has a maximum supercurrent (*Ic*) which is able to flow through it, depending on the junction size, the superconductor and the temperature.

As shown in Figure 2-9, for a direct-current SQUID, a current called bias current (I_{bias}) is applied to the superconducting ring and divides equally between the junctions. With the presence of a magnetic field through the ring, a screening current (I_s) is induced in the coil in order to produce a magnetic field which opposes the applied field. The induced current I_S is in

the same direction as I_{bias} in one of the branches of the coil, and opposite to the other branch. Thus, the total current in the two branches are $\frac{1}{2}I_{bias} + I_s$ and $\frac{1}{2}I_{bias} - I_s$. As long as any one of the branch current exceeds the critical current I_c of the Josephson junction, the tunnelling of cooper pairs through the Josephson junctions are then blocked, the superconductivity is lost and a voltage appears across the junction. Thus, a tiny magnetic flux signal can produce a corresponding voltage across the SQUID, which can be measured by conventional electronics.

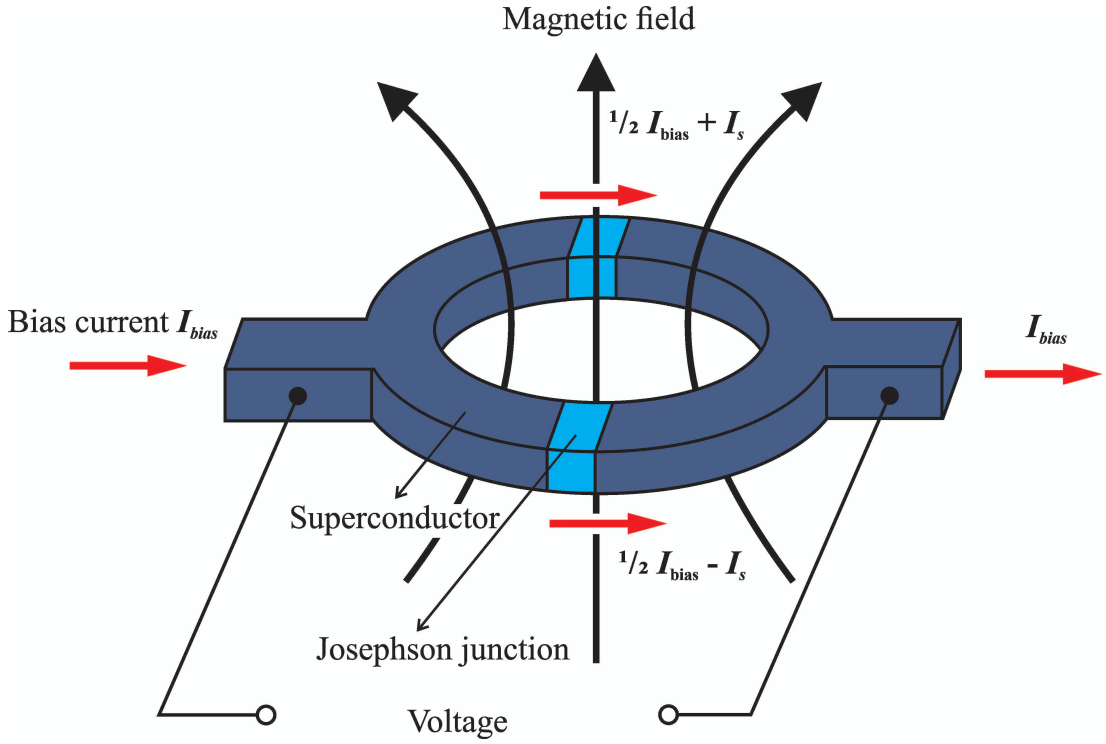


Figure 2-9 A schematic representation of the principal component in a SQUID magnetometer.

2.5.1. Sample Preparation for SQUID Measurements

In this thesis, a small mass of samples (20 - 50 mg) is weighed and loaded into in a gelatine capsule and placed inside a drinking straw, with 3 more empty capsules both above and below the sample capsule.The end capsules are covered with a layer of diamagnetic tape to fix their positions. After the capsules are loaded, the straw is then pierced with a needle multiple times to assist evacuation. The straw is then installed at the end of a long rod to be loaded into the SQUID magnetometer cryostat via a pumped antechamber.

2.5.2. Standard Measurements

Standard measurements were carried out to measure magnetic properties of all the starting materials in this thesis. Zero-field-cooled (ZFC) and field-cooled (FC) data were collected using an applied magnetic field of 100 Oe over the temperature range $5 \leq T/\mathrm{K} \leq 300$. Measurements as a function of field are usually conducted at both 300 K and 5 K over the field range of $-5 \leq H/\mathrm{T} \leq 5$.

2.5.3. Ferrosubtraction Measurements

Many of the topochemically reduced phases presented in this thesis contain ferromagnetic impurities. Thus, standard ZFC/FC measurements are not suitable as the ferromagnetic response from even a tiny amount of impurity is strong enough to mask out the magnetic response from the main phase. Thus, a ferrosubtraction technique is utilized in the magnetic measurements of these phases. In this technique, a large magnetic field (> 3T) is applied to saturate the magnetisation of the ferromagnetic impurities so that the ferromagnetic behaviour contributed by the impurities won't mask the magnetic behaviour of the bulk phase. Field-cooled isotherms are collected every 5 K over the temperature range $5 \leq T/\mathrm{K} \leq 300$. At each temperature, magnetisation-field isotherms are collected every 0.5 T over the field range $3 \leq H/\mathrm{T} \leq 5$. The resulting magnetisation data are plotted as a function of the applied field. A graphic representation of the plot is shown in Figure 2-10. The magnetisation-field data give a straight line if the ferromagnetic impurities have been saturated, with the gradient giving the paramagnetic susceptibility and the intercept giving the saturated ferromagnetic moment. A field-cooled plot can be made combining the calculated paramagnetic susceptibilities at each temperature.

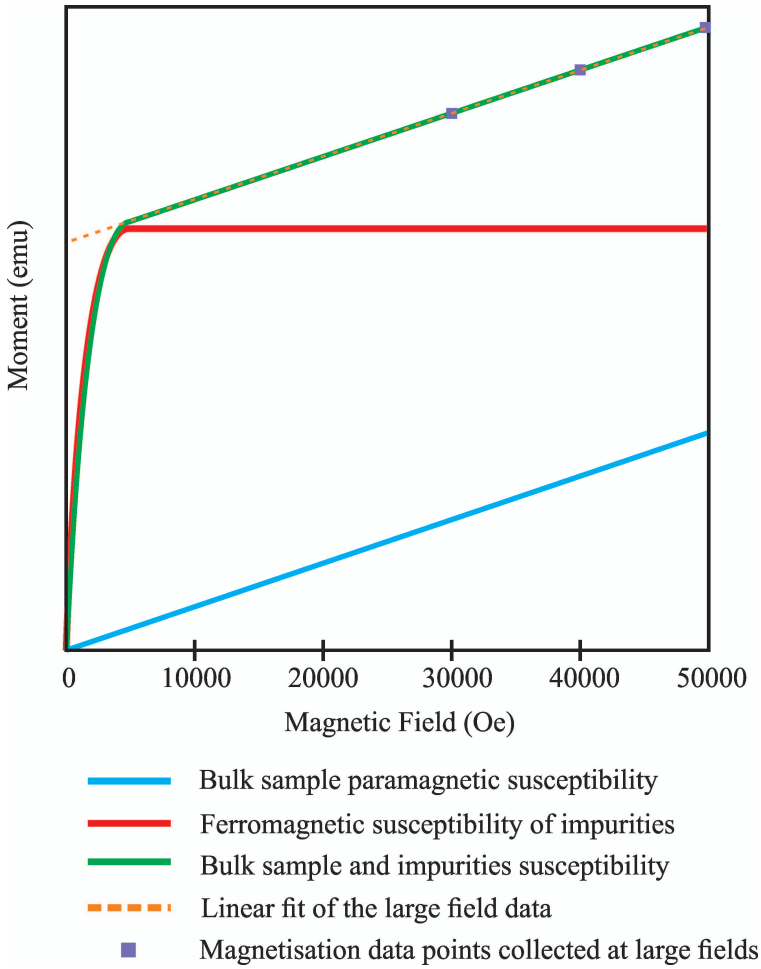


Figure 2-10 A schematic representation of the principles of ferrosubtraction measurements.

2.6. Magnetism

The magnetism of a solid arises from electron spins of individual atoms in the lattice. In this thesis, all of the samples exhibit non-diamagnetic behaviour due to the unpaired electrons in transition metal d orbitals. In the presence of an external magnetic field, the spins of these unpaired electrons tend to respond to the applied field and align along the field.

2.6.1. The Curie-Weiss Law

In an external magnetic field, the electron spins from a paramagnet respond weakly to the field and a small fraction of magnetic moments are deflected into the direction of the applied field. The density of these induced magnetic moments in the material can be quantified as the

magnetization (M). For paramagnets, the magnetization (M) and the applied field (H) have a relation, which can be described by the following equation:

$$\chi = \frac{dM}{dH}$$

where χ, paramagnetic susceptibility (χ), is a measure of how much a paramagnetic material becomes magnetized in an external field.

For a large number of paramagnetic spins in small applied fields, χ tends to be a constant, thus this equation can be simplified to:

$$\chi = \frac{M}{H}$$

However, the extent to which the electron spins align in the direction of the applied field goes against the thermal motions and χ decreases as the temperature increases. In a fixed value of applied field, the relationship between temperature and paramagnetic susceptibility can be described by the Curie Law:

$$\chi = \frac{\mathrm{C}}{T}$$

where C is the Curie constant and T is temperature. The Curie Law is proposed based on the ideal condition that individual magnetic moments do not interact with each other. However, in reality, the Curie Law can only hold for magnetically dilute materials but is not applicable in systems with interactions between spins. Thus, a corrected version of the Curie Law, the Curie-Weiss Law, is introduced for these systems:

$$\chi = \frac{\mathrm{C}}{T - \theta} + \mathrm{K}$$

where θ is Weiss constant, the magnitude of the strength of magnetic interactions; K is the constant to account for any temperature independent contribution to magnetic behaviour.

In the Curie-Weiss Law, the sign of Weiss constant θ indicates the sign of the coupling between spins. If $\theta < 0$, the system exhibits anti-ferromagnetic couplings; if $\theta > 0$, then the system exhibits ferromagnetic couplings.

By plotting the inverse magnetic susceptibility, $\frac{1}{\chi}$, against T (the equation shown as follows), the values of C and θ can be obtained from the calculation of the gradient and the intercept of the linear fit of the plot.

$$\frac{\mathbf{1}}{\boldsymbol{\chi} - \mathrm{K}} = \frac{T}{\mathrm{C}} - \frac{\theta}{\mathrm{C}}$$

The Curie constant is related to the magnetic moment of the material based on the following equation:

$$\boldsymbol{C} = \frac{\mathrm{N_A}\mu_\mathrm{B}^2\mu^2}{3\mathrm{k_B}}$$

where N_A is Avogadro's constant; μ_B is the Bohr magneton; k_B is the Boltzmann constant; μ is the magnetic moment.

For the transition-metal complex oxides discussed in this thesis, the spin-only formula is utilized to calculate the magnetic moment of the materials, which is described as follows:

$$\boldsymbol{\mu} = \mathrm{g}\sqrt{S(S+1)}$$

where g is the gyromagnetic ratio which is approximately 2; S is the sum of the spin quantum numbers of the electrons in the system.

Based on the Curie constant calculated from experimental data and the spin-only formula, the number of the unpaired electrons can be estimated and therefore spin states and oxidation states of transition metals can be predicted.

2.7. Thermogravimetric Analysis (TGA)

In this thesis, thermogravimetric analysis (TGA) is conducted to determine the oxygen content of the reduced phases after anion deintercalation. TGA is one of the most commonly used techniques for the measurement of thermal stability of materials. In this technique, changes of the sample weight are measured upon increasing temperature. A Mettler Toledo TGA/DSC 1 STARe system was utilized in this work, consisting of a balance with high sensitivity and a programmable furnace. To avoid possible perturbation, an inert atmosphere is created by a sealed box with venting system providing a flow of N_2. A small quantity of the reduced samples (20 mg - 60 mg) is weighed and transferred into a small alumina crucible and then loaded into the apparatus. The oxygen content of the reduced samples can be calculated based on the mass change and the known chemical compositions after heating.

Different TGA measurements are attempted under different scenarios. In this thesis, both reductive TGA and oxidative TGA were utilized. For a reductive TGA, a sample is heated under a steady flow of 10%/90% H_2/N_2 at a rate of 5 °C min^{-1} and held at 800 °C for 1 hour to complete the reaction before cooling. After the measurement, X-ray powder diffraction data are collected from the sample for chemical characterisation. Typically, a reductive TGA will lead to a decomposition to form metal oxides and/or elemental metal. For oxidative TGA, a sample is heated under a steady flow of O_2 at a rate of 5 °C min^{-1} and held at 1000 °C for 1 hour to complete the reaction before cooling. Typically, an oxidative TGA will lead to a re-oxidization of the sample back to its corresponding parent oxide. However, it's hard to confirm the full oxidation of the sample based on a post-TGA X-ray diffraction pattern. Thus, the reductive TGA is chosen for reduced-phase composition determination for higher accuracy.

2.8. X-ray Photoelectron Spectroscopy

2.8.1. The Principles of XPS

In this thesis, the oxidation states of transition metals are investigated using X-ray photoelectron spectroscopy (XPS). XPS is one of the photoemission spectroscopies used to conduct surface analysis by measuring the ejected electrons excited by the incident beam of X-rays.

As shown in Figure 2-11, the X-ray beam irradiates the sample with sufficient energy to excite the electrons in specific bound states in a ultrahigh vacuum condition. The photo-ejected electrons in the vacuum are then collected by an electron analyser which measures the kinetic energy of electrons. The XPS spectrum is then plotted as an energy spectrum of intensity (number of photo-ejected electrons versus time) against binding energy (Binding energy = Energy of the incident X-ray photon - Kintic energy of the ejected electron). Thus, chemical states and bonding environment from a specific element can be analysed from an XPS spectrum.

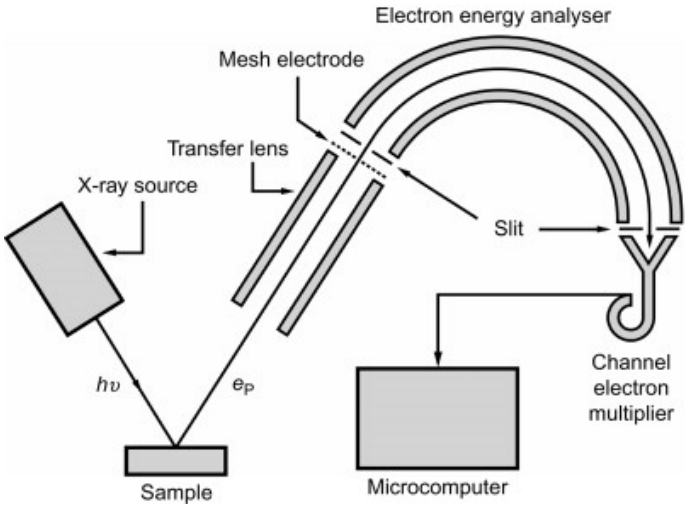


Figure 2-11 A schematic diagram of an XPS measurement system equipped with an electrostatic hemispherical analyser.[72]

2.8.2. Standard XPS Measurement

In this thesis, XPS analysis was performed using a Kratos Axis SUPRA XPS apparatus fitted with a monochromated Al Kα X-ray source. Survey scans were recorded at a pass energy of 160 eV, and high-resolution scans were recorded at a pass energy of 20 eV. Data were recorded at a pressure below 10^{-8} Torr and a room temperature of 294 K. The investigation of the oxidation states of transition-metal in $LaSrCo_{0.5}Rh_{0.5}O_{3.25}$ were carried out using XPS and is detailed in Chapter 4. We would like to thank Prof. R. Palgrave for the assistance in carrying out the XPS measurement at University College London.

Chapter 3

Synthesis and Characterisation of Rh-containing $n = 1$ Ruddlesden-Popper Phases

3.1. Introduction

The ABO_3 perovskite structure is adopted by a wide range of chemical compounds. This can be attributed to the many low-energy tilting distortions which can modify the average *A*-O bond lengths, whilst maintaining the *B*-O bond lengths, thus enabling a wide range of *A*:*B* radius ratios to be accommodated. However, the A_2BO_4, $n = 1$ Ruddlesden-Popper structure tends to be adopted by a narrower range of compounds, compared to the perovskite structure. This can be attributed to the limited number of tilting distortions exhibited by the framework, due to the presence of the *A*O rock salt layer, leading to a more restricted range of *A*:*B* radius ratios being favourable.

Rhodium is observed to exhibit oxidation states between Rh^{III} to Rh^{V} in thermodynamically stable oxide phases. Typically, the Rh^{III} oxidation state dominates, due to the stability of the d^6, t_{2g}^6 configuration in octahedral RhO_6 units, with Rh^{IV}-containing phases generally only preparable under high pressure conditions.

However, in mixed-metal perovskites, which contain two different transition metals on the octahedral *B*-sites, M^{III}/Rh^{IV} oxidation state combinations have been observed, as for example in the disordered perovskites $La_{0.5}Sr_{0.5}Mn^{III}_{0.5}Rh^{IV}_{0.5}O_3$ and $La_{0.5}Sr_{0.5}Fe^{III}_{0.5}Rh^{IV}_{0.5}O_3$[73]. These recent observations indicate that in the appropriate chemical setting, Rh^{IV} can be stablized in complex oxide phases at ambient pressure.

Thus, to extend the study to Ruddlesden-Popper phases, samples of the $n = 1$ Ruddlesden-Popper phases $LaSrCo_{0.5}Rh_{0.5}O_4$, $LaSrNi_{0.5}Rh_{0.5}O_4$ and $La_{0.5}Sr_{1.5}Fe_{0.5}Rh_{0.5}O_4$ are synthesized

and analysed. Details of the spin states and the oxidation states that these transition metals adopt is discussed in this chapter. The investigation of these rhodium-containing n = 1 Ruddlesden-Popper phases also acts as a prelude to the further topochemical reduction of related anion-deficient phases, which will be investigated and discussed in Chapter 4.

3.2. Experimental

3.2.1. Synthesis of $LaSrCo_{0.5}Rh_{0.5}O_4$

Samples of $LaSrCo_{0.5}Rh_{0.5}O_4$ were synthesized by a high-temperature ceramic method as described in Section 2.1. Suitable stoichiometric ratios of La_2O_3 (99.999%, dried at 900 °C), $SrCO_3$ (99.994%), Co_3O_4 (99.99%) and Rh_2O_3 (99.998%, dried at 850 °C for two hours) were ground together using an agate mortar and pestle, transferred into an alumina crucible and then heated in air at a rate of 5 °C min^{-1} to 1000 °C to decompose the carbonate. Samples were then reground and pressed into pellets (diameter 13mm) under 5.5 tonnes of force in order to increase the contact area of the starting materials. After that, the pellets were heated in an alumina boat for 3 periods of 50 hours at 1250°C in a steady pure O_2 flow with grinding and pelletisng between heating cycles. The high partial pressure of O_2 plays a significant role in isolating $LaSrCo_{0.5}Rh_{0.5}O_4$. Heating pellets in air resulted in a main phase with impurities such as $LaRhO_3$, Co_3O_4 and La_2O_3. Thus, an O_2 flow is needed as an oxidising agent for pure-phase formation. After heating, to make sure the samples are stoichiometric in oxide ions, the samples were cooled down relatively slowly and under flowing oxygen to avoid oxygen deficiency by fast cooling or lack of oxygen. The reaction progress was monitored by laboratory X-ray diffraction and once the reaction was regarded as complete, synchrotron X-ray powder diffraction (SXRD) data and neutron powder diffraction (NPD) data were collected from the resulting phase.

3.2.2. Synthesis of $LaSrNi_{0.5}Rh_{0.5}O_4$

Samples of $LaSrNi_{0.5}Rh_{0.5}O_4$ were synthesized by a high-temperature ceramic method as described in Section 2.1. Suitable stoichiometric ratios of La_2O_3 (99.999%, dried at 900 °C), $SrCO_3$ (99.994%), NiO (99.99%) and Rh_2O_3 (99.998%, dried at 850 °C for two hours) were ground together using an agate mortar and pestle, then transferred into an alumina crucible, heated in air at a rate of 1 °C min^{-1} to 1000 °C to decompose the carbonate. Samples were then reground and pressed into pellets (diameter 13mm) under 5.5 tonnes of force in order to increase the contact area of the starting materials. The pellets were heated for 3 periods of 50 hours at 1300°C in air, with grinding and pelleting between heating cycles. Unlike $LaSrCo_{0.5}Rh_{0.5}O_4$, no transition metal needs to be oxidized during the synthesis. Thus, isolating pure phase $LaSrNi_{0.5}Rh_{0.5}O_4$ can be achieved via heating in air. The reaction progress was monitored by laboratory X-ray diffraction and once the reaction was regarded as complete, SXRD data and NPD data were collected from the resulting phase.

3.2.3. Synthesis of $La_{0.5}Sr_{1.5}Fe_{0.5}Rh_{0.5}O_4$

Samples of $La_{0.5}Sr_{1.5}Fe_{0.5}Rh_{0.5}O_4$ were synthesized by a high-temperature ceramic method as described in Section 2.1. Suitable stoichiometric ratios of La_2O_3 (99.999%, dried at 900 °C), $SrCO_3$ (99.994%), Fe_2O_3 (99.99%) and Rh_2O_3 (99.998%, dried at 850 °C for two hours) were ground together using an agate mortar and pestle, transferred into an alumina crucible, heated in air at a rate of 1 °C min^{-1} to 1000 °C to decompose the carbonate. Samples were then reground and pressed into pellets (diameter 13mm) under 5.5 tonnes of force in order to increase the contact area of the starting materials. The pellets were heated for 3 periods of 50 hours at 1400°C in air, with grinding and pelleting between heating cycles. The reaction progress was monitored by laboratory X-ray diffraction and once the reaction was regarded as complete, SXRD data and NPD data were collected from the resulting phase.

3.3. Results

3.3.1. Structural Characterisation of $LaSrCo_{0.5}Rh_{0.5}O_4$

SXRD data (Section 2.3.1.3) were collected and analysed by the Rietveld method (Section 2.4). The SXRD data from $LaSrCo_{0.5}Rh_{0.5}O_4$ could be indexed on the basis of a body-centred tetragonal unit cell with a = 3.88(1) Å and c = 12.52(1) Å (shown in Figure 3-2). A structural model based on a n = 1, A_2BO_4 Ruddlesden-Popper phase with a 1:1 ratio of La: Sr solid-solution on A-site and a 1:1 ratio of Co:Rh solid-solution on B-site was then constructed. As shown in Figure 3-1, the refinement achieved a good fit with wRp = 4.41 %, confirming sample purity and quality. The detailed structural parameters are listed in Table 3-1, the selected bond lengths from A-site and B-site cations to oxygen ions are given in Table 3-2.

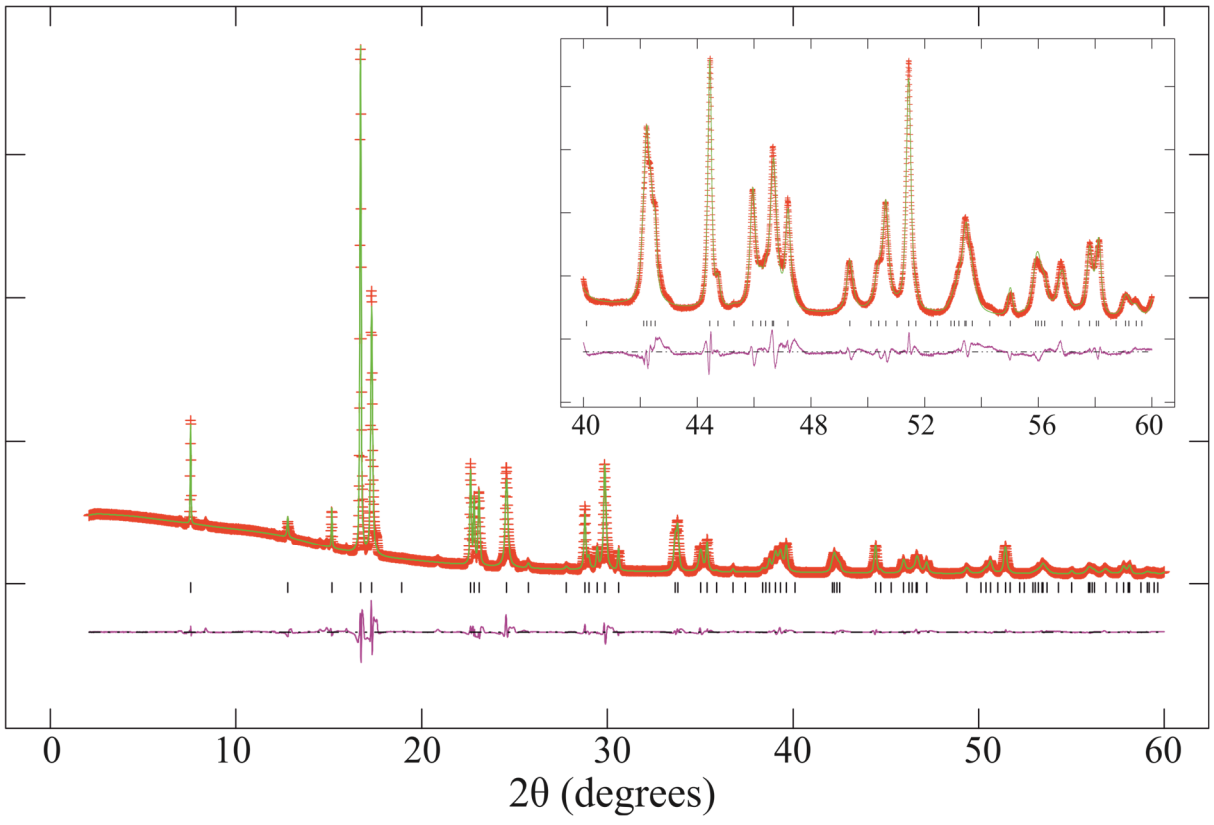


Figure 3-1 Observed (red), calculated (green) and difference plots (pink) from the Rietveld structural refinement of $LaSrCo_{0.5}Rh_{0.5}O_4$ using an *I4/mmm* model against SXRD data collected at room temperature.

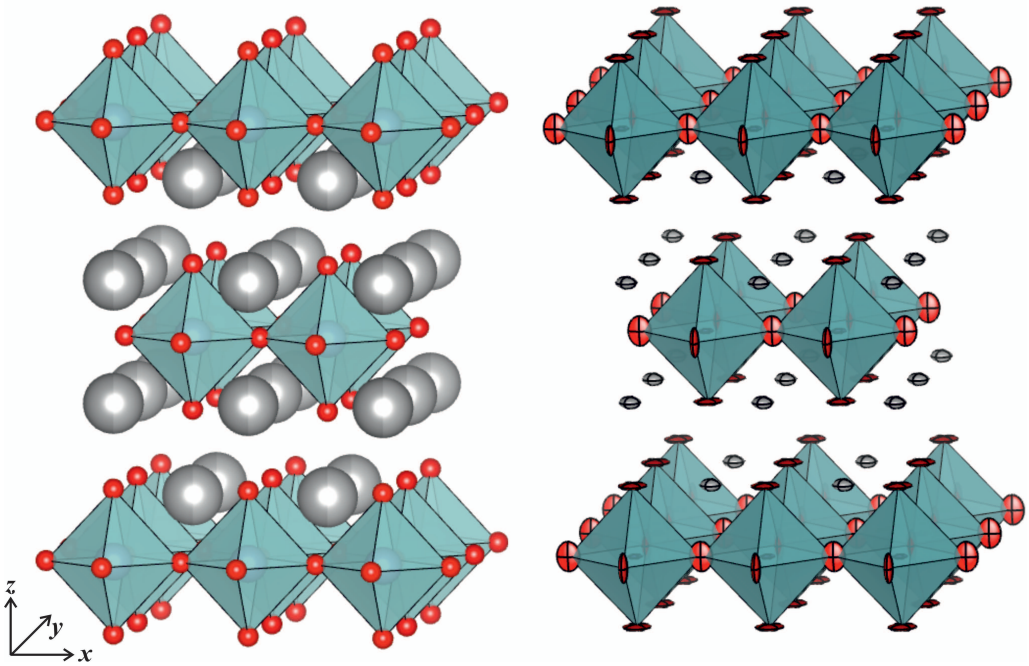


Figure 3-2 The crystal structure of $LaSrCo_{0.5}Rh_{0.5}O_4$ (left) with displacement ellipsoids (right).

Table 3-1 Structural parameters from the refinement of $LaSrCo_{0.5}Rh_{0.5}O_4$ against SXRD data collected at 298 K.

Atom	Wyckoff Position	*x*	*y*	*z*	Fraction	U_{11} (Å)
La/Sr	4*e*	0	0	0.35968(2)	0.5/0.5	0.0049(2)
Co/Rh	2*a*	0	0	0	0.5/0.5	0.0054(2)
O(1)	4*e*	0	0	0.1670(1)	1	0.0093(1)
O(2)	4*c*	½	0	0	1	0.0097(2)

$LaSrCo_{0.5}Rh_{0.5}O_4$ - space group *I*4/*mmm* (#139)
Formula mass: 371.45 g mol^{-1}, Z = 2
a = 3.87941(1) Å, *c* = 12.51885(5) Å, Volume = 188.407(2) $Å^3$
Radiation source: Synchrotron X-ray, λ = 0.8249 Å
Temperature: 298 K
χ^2 = 38.07; *wRp* = 4.41 %; *Rp* = 2.48 %.

Table 3-2 Selected bond lengths from the refined structure of $LaSrCo_{0.5}Rh_{0.5}O_4$.

Cation	Anion	Length (Å)
La/Sr	O (1)	2.4357(1) × 1
	O (1)	2.7571(1) × 4
	O (2)	2.6111(1) × 4
Co/Rh	O (1)	2.0618(1) × 2
	O (2)	1.9371(1) × 4

3.3.2. Structural Characterisation of $LaSrNi_{0.5}Rh_{0.5}O_4$

3.3.2.1. Synchrotron X-ray Powder Diffraction

SXRD data (Section 2.3.1.3) were collected and analysed by the Rietveld method (Section 2.4). The SXRD data from $LaSrNi_{0.5}Rh_{0.5}O_4$ could be indexed on the basis of a body-centred tetragonal unit cell with a = 3.88(1) Å and c = 12.56(2) Å. A structural model based on an n = 1, A_2BO_4 Ruddlesden-Popper phase with a 1:1 ratio of La: Sr solid-solution on A-site and a 1:1 ratio of Ni:Rh solid-solution on B-site was then constructed. As shown in Figure 3-3, the refinement achieved a good fit with wRp = 5.08 %, confirming sample purity and quality.

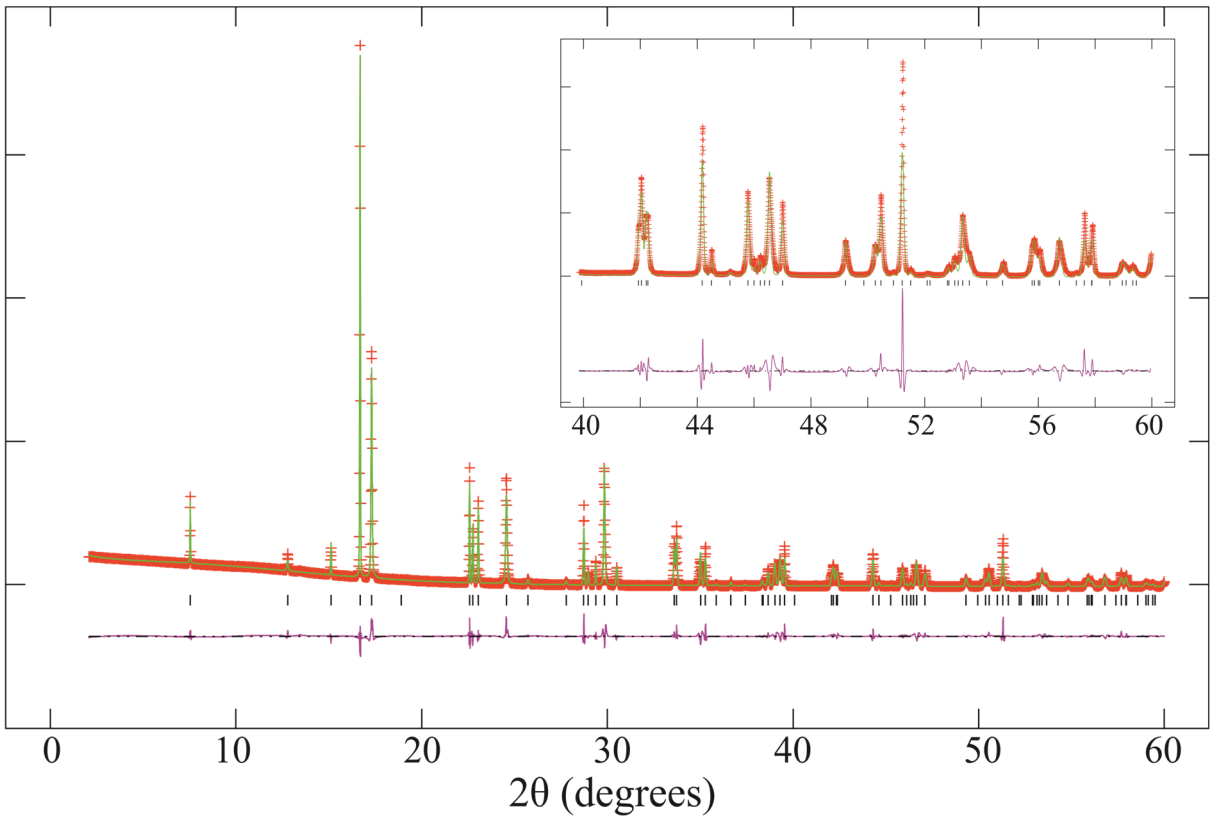


Figure 3-3 Observed(red), calculated(green) and difference plots(pink) from the Rietveld structural refinement of $LaSrNi_{0.5}Rh_{0.5}O_4$ using an *I4/mmm* model against SXRD data collected at room temperature.

3.3.2.2. Neutron Powder Diffraction

Time-of-flight NPD measurements were carried out at ambient temperature using the POLARIS diffractometer in ISIS (Section 2.3.2.1). A body-centred tetragonal unit cell with thermal ellipsoids shown in Figure 3-4 (space group *I*4/*mmm*) was used to refine the data. The refinement managed to achieve good statistical fits for both 298 K data and 5 K data with different anisotropic displacement parameters. As we can notice in Figure 3-4, the displacement parameters of the oxygen atoms are dynamic, changing with temperature, which indicates that the shape of the ellipsoid is due to the thermal motion rather than a static rotation of the disordered octahedra in the structure. Full details of the structural parameters are given in Table 3-3 and Table 3-4. The observed, calculated and difference plots of NPD data collected at 298 K are shown in Figure 3-5. Anisotropic displacement factors are given in Table 3-5 and selected bond lengths given in Table 3-6. Figure 3-6 indicates that there are no obvious additional magnetic diffraction features observed at 5 K and hence no long-range magnetic order in this system.

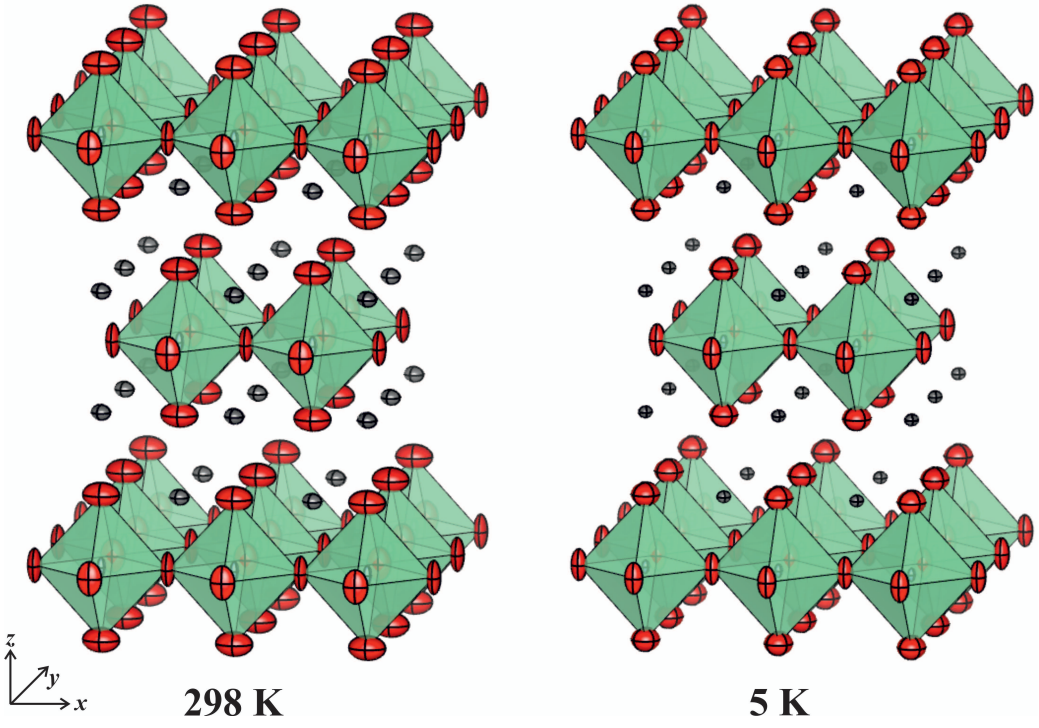


Figure 3-4 The crystal Structure of $LaSrNi_{0.5}Rh_{0.5}O_4$ with displacement ellipsoids at 298 K (left) and 5 K (right).

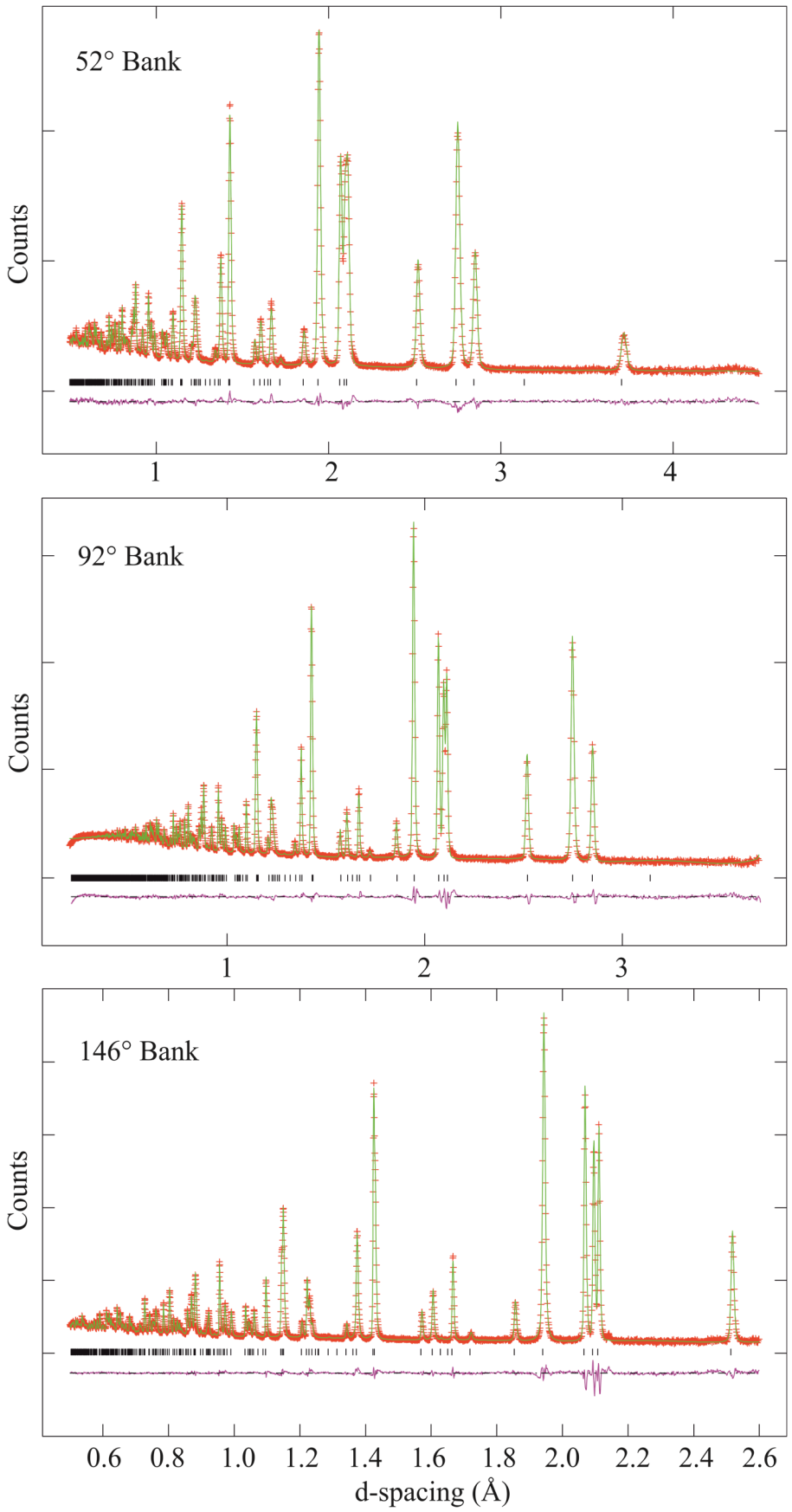


Figure 3-5 Observed, calculated and difference plots from the refinement of $LaSrNi_{0.5}Rh_{0.5}O_4$ against NPD data collected at 298 K.

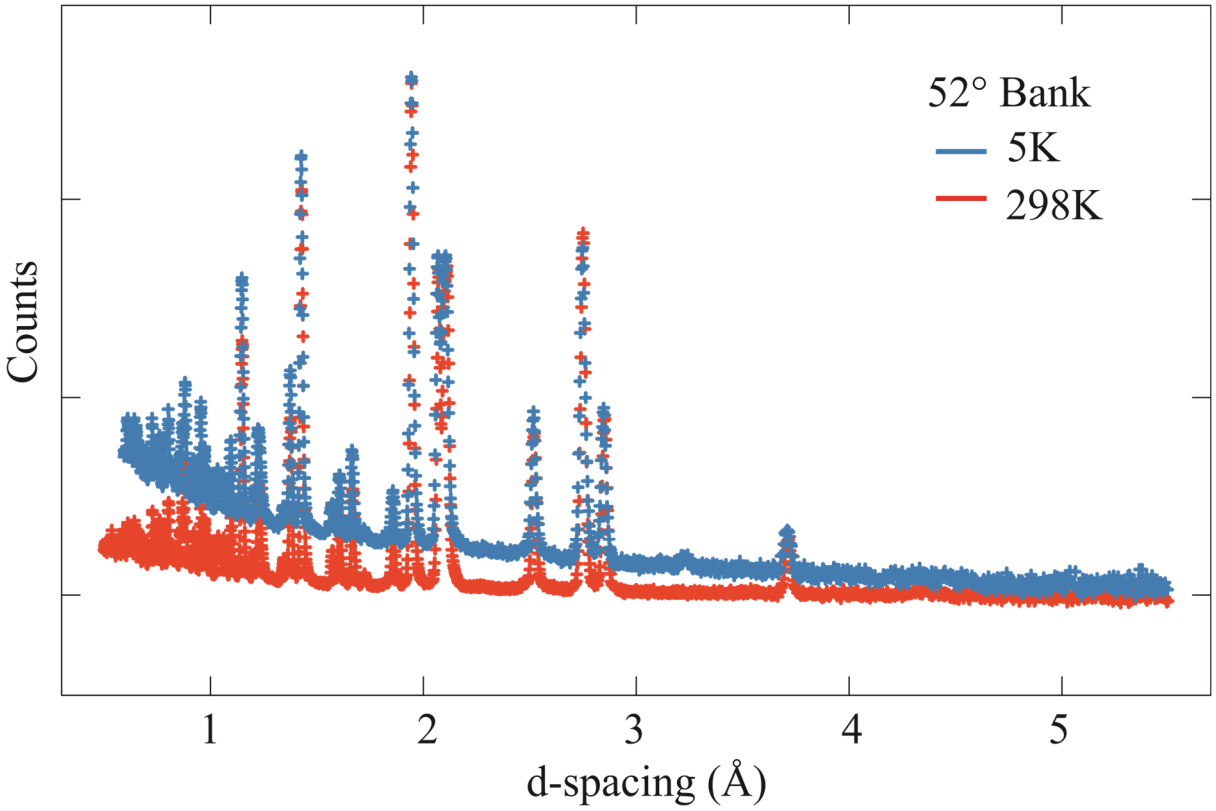


Figure 3-6 Comparison of low-angle NPD data collected from $LaSrNi_{0.5}Rh_{0.5}O_4$ at 298 K and 5 K.

Table 3-3 Structural parameters from the refinement of $LaSrNi_{0.5}Rh_{0.5}O_4$ against NPD data collected at 298 K.

Atom	Wyckoff Position	*x*	*y*	*z*	Fraction	U_{11} (Å)
La/Sr	4*e*	0	0	0.35959(4)	0.5/0.5	0.0073(1)
Ni/Rh	2*a*	0	0	0	0.5/0.5	0.0015(2)
O(1)	4*e*	0	0	0.16832(6)	1	0.0146(2)
O(2)	4*c*	½	0	0	1	0.033(2)

$LaSrNi_{0.5}Rh_{0.5}O_4$ - space group *I*4/*mmm* (#139)
Formula mass: 371.32 g mol^{-1}, Z = 2
a = 3.8840(1) Å, *c* = 12.5660(4) Å, Volume = 189.57(2) $Å^3$
Radiation source: Time-of-flight Neutron Powder Diffraction
Temperature: 298 K
χ^2 = 4.25; *wRp* = 3.41 %; *Rp* = 3.73 %.

Table 3-4 Structural parameters from the refinement of $LaSrNi_{0.5}Rh_{0.5}O_4$ against NPD data collected at 5K.

Atom	Wyckoff Position	*x*	*y*	*z*	Fraction	U_{11} (Å)
La/Sr	4*e*	0	0	0.35969(4)	0.5/0.5	0.0032(1)
Ni/Rh	2*a*	0	0	0	0.5/0.5	0.0014(2)
O(1)	4*e*	0	0	0.16856(7)	1	0.0152(2)
O(2)	4*c*	½	0	0	1	0.0042(2)

$LaSrNi_{0.5}Rh_{0.5}O_4$ - space group *I*4/*mmm* (#139)
Formula mass: 371.32 g mol^{-1}, Z = 2
a = 3.8807(1) Å, *c* = 12.5314(4) Å, Volume = 188.72(2) $Å^3$
Radiation source: Time-of-flight Neutron Powder Diffraction
Temperature: 5K
χ^2 = 1.78; *wRp* = 1.58 %; *Rp* = 2.60 %.

Table 3-5 Anisotropic displacement factors from refinements of $LaSrNi_{0.5}Rh_{0.5}O_4$ against NPD data collected at 298 K (top) and 5K (bottom).

Temperature: 298 K			
Atom	**U_{11}**	**U_{22}**	**U_{33}**
La/Sr	0.00731(13)	0.00731(13)	0.00407(16)
Ni/Rh	0.00154(11)	0.00154(11)	0.00672(26)
O (1)	0.01463(19)	0.01463(19)	0.01072(35)
O (2)	0.00329(21)	0.01061(26)	0.02116(36)
Temperature: 5 K			
Atom	**U_{11}**	**U_{22}**	**U_{33}**
La/Sr	0.00320(14)	0.00320(14)	0.00230(18)
Ni/Rh	0.00137(16)	0.00137(16)	0.00322(29)
O (1)	0.01528(20)	0.01528(20)	0.01000(41)
O (2)	0.00416(26)	0.00562(27)	0.01819(41)

Table 3-6 Selected bond lengths from the refined structure of $LaSrNi_{0.5}Rh_{0.5}O_4$ at 298 K (left) and 5 K (right).

Temperature: 298 K			**Temperature: 5 K**		
Cation	**Anion**	**Length (Å)**	**Cation**	**Anion**	**Length (Å)**
La/Sr	O (1)	2.394(1)	**La/Sr**	O (1)	2.389(1)
	O (1)	2.770(1)		O (1)	2.768(1)
	O (2)	2.624(1)		O (2)	2.618(1)
Ni/Rh	O (1)	2.125(1)	**Ni/Rh**	O (1)	2.119(1)
	O (2)	1.942(1)		O (2)	1.940(1)

3.3.3. Structural Characterisation of $La_{0.5}Sr_{1.5}Fe_{0.5}Rh_{0.5}O_4$

3.3.3.1. Synchrotron X-ray Powder Diffraction

SXRD data (Section 2.3.1.3) were collected and analysed by the Rietveld method (Section 2.4). The SXRD data from $La_{0.5}Sr_{1.5}Fe_{0.5}Rh_{0.5}O_4$ could be indexed on the basis of a body-centred tetragonal unit cell with a = 3.89(1) Å and c = 12.62(2) Å. A structural model based on an n = 1, A_2BO_4 Ruddlesden-Popper phase with a 1:3 ratio of La: Sr solid-solution on A-site and a 1:1 ratio of Fe: Rh solid-solution on B-site was then constructed. As shown in Figure 3-7, the refinement achieved a good fit with wRp = 2.24 %, confirming sample purity and quality.

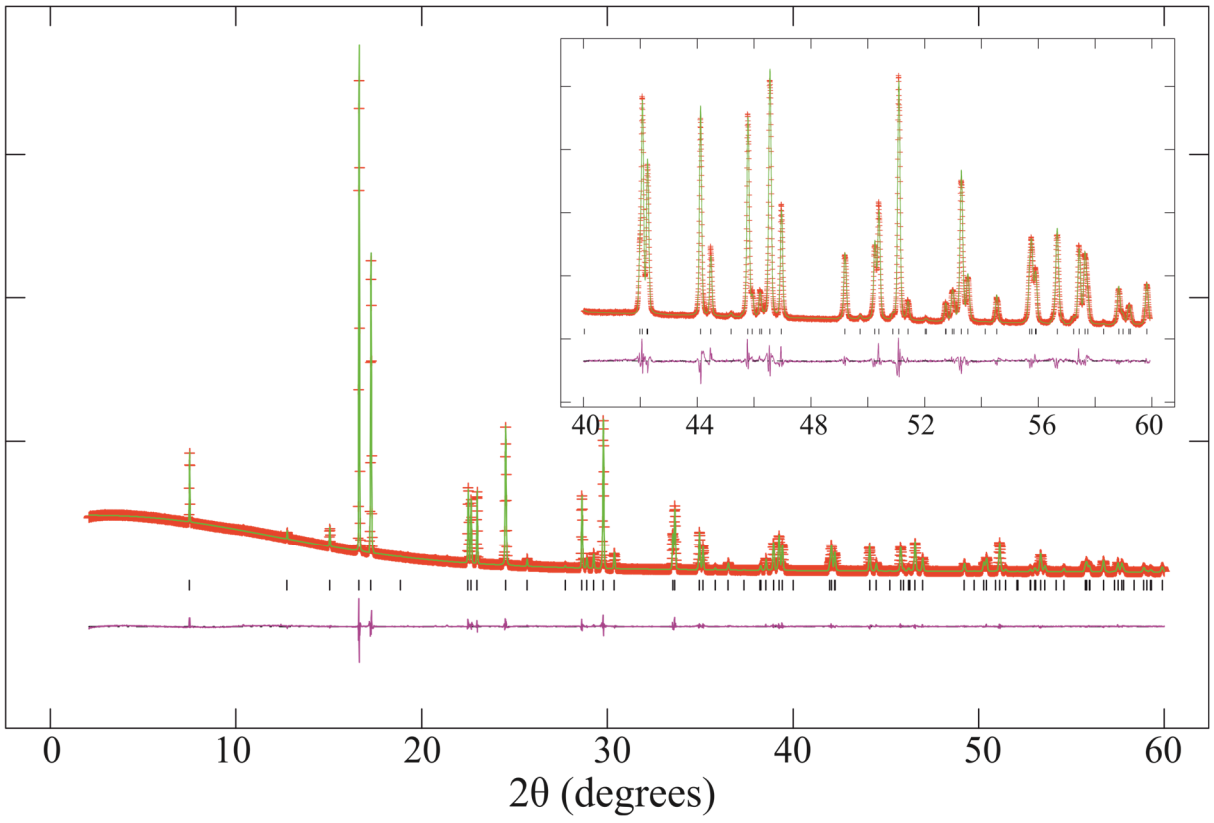


Figure 3-7 Observed(red), calculated(green) and difference plots(pink) from the Rietveld structural refinement of $La_{0.5}Sr_{1.5}Fe_{0.5}Rh_{0.5}O_4$ using an *I4/mmm* model against SXRD data collected at room temperature.

3.3.3.2. Neutron Powder Diffraction

Time-of-flight NPD measurements were carried out at ambient temperature using the POLARIS diffractometer in ISIS (Section 2.3.2.1). A body-centred tetragonal unit cell with thermal ellipsoids shown in Figure 3-8 (space group *I*4/*mmm*) was used to refine the data. The refinement managed to achieve good statistical fits for both 298 K data and 5 K data with different anisotropic thermal motion parameters. As in $LaSrNi_{0.5}Rh_{0.5}O_4$, we can also notice that the displacement parameters of the oxygen atoms in the structures are dynamic, changing with temperature, which indicates that the displacement parameter is due to the thermal motion rather than a static rotation of the disordered octahedra in the structure. Full details of the structural parameters are given in Table 3-7 and Table 3-8, anisotropic displacement factors are given in Table 3-9 and selected bond lengths are given in Table 3-10. The observed, calculated and difference plots of NPD data collected at 298 K are shown in Figure 3-9. As shown in Figure 3-10, the lack of difference between 5 K and 298 K NPD data indicates that there are no additional magnetic diffraction features observed at 5 K and hence no long-range magnetic order.

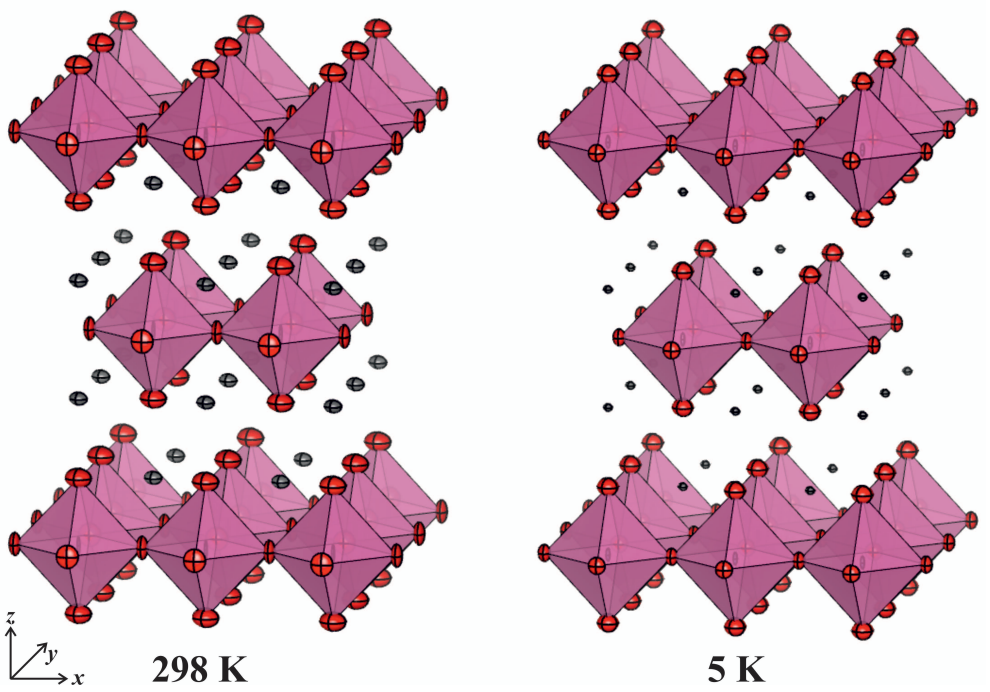


Figure 3-8 The crystal Structure of $La_{0.5}Sr_{1.5}Fe_{0.5}Rh_{0.5}O_4$ with displacement ellipsoids at 298 K (left) and 5 K (right).

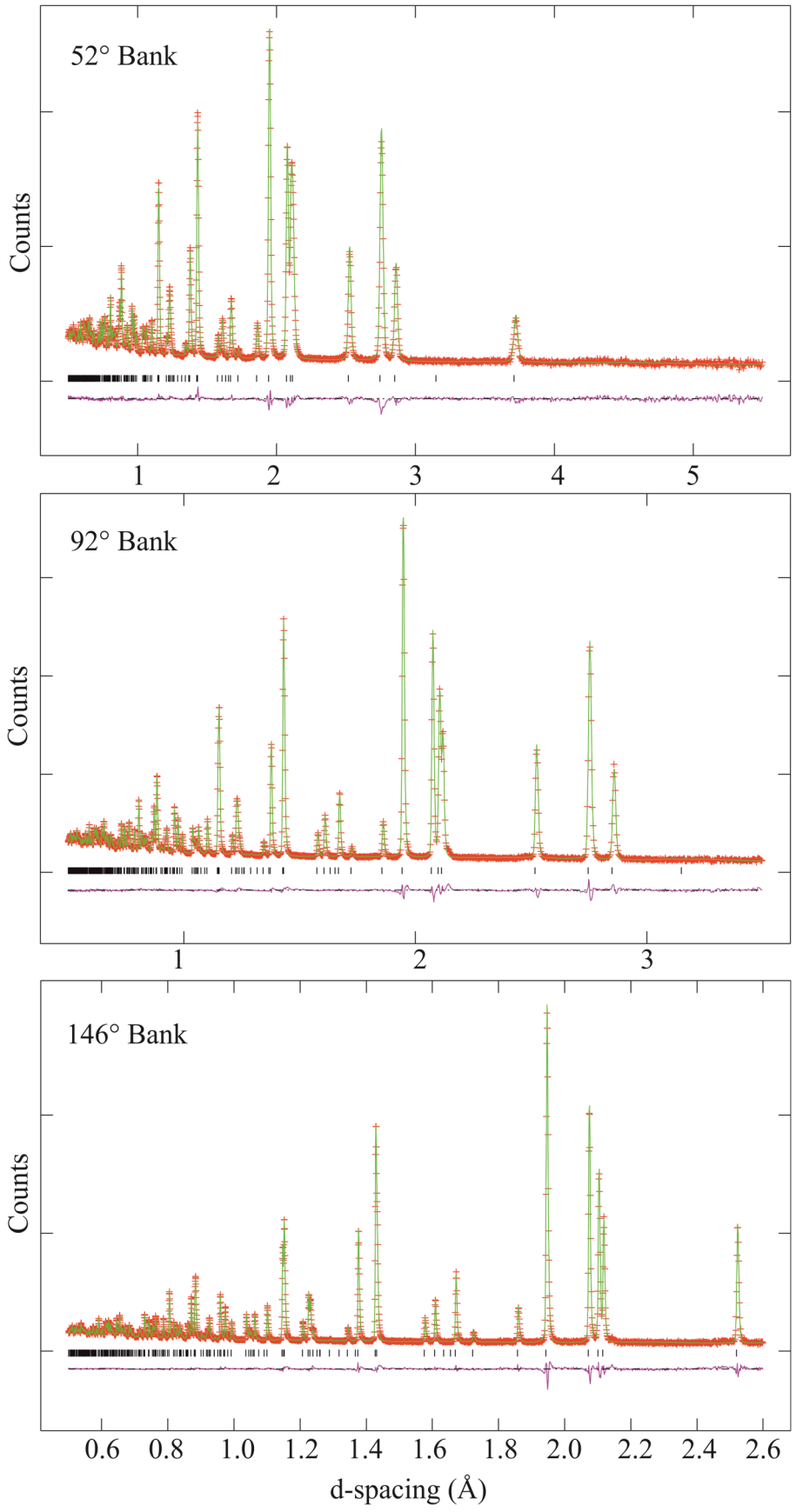


Figure 3-9 Observed, calculated and difference plots from the refinement of $La_{0.5}Sr_{1.5}Fe_{0.5}Rh_{0.5}O_4$ against NPD data collected at 298 K.

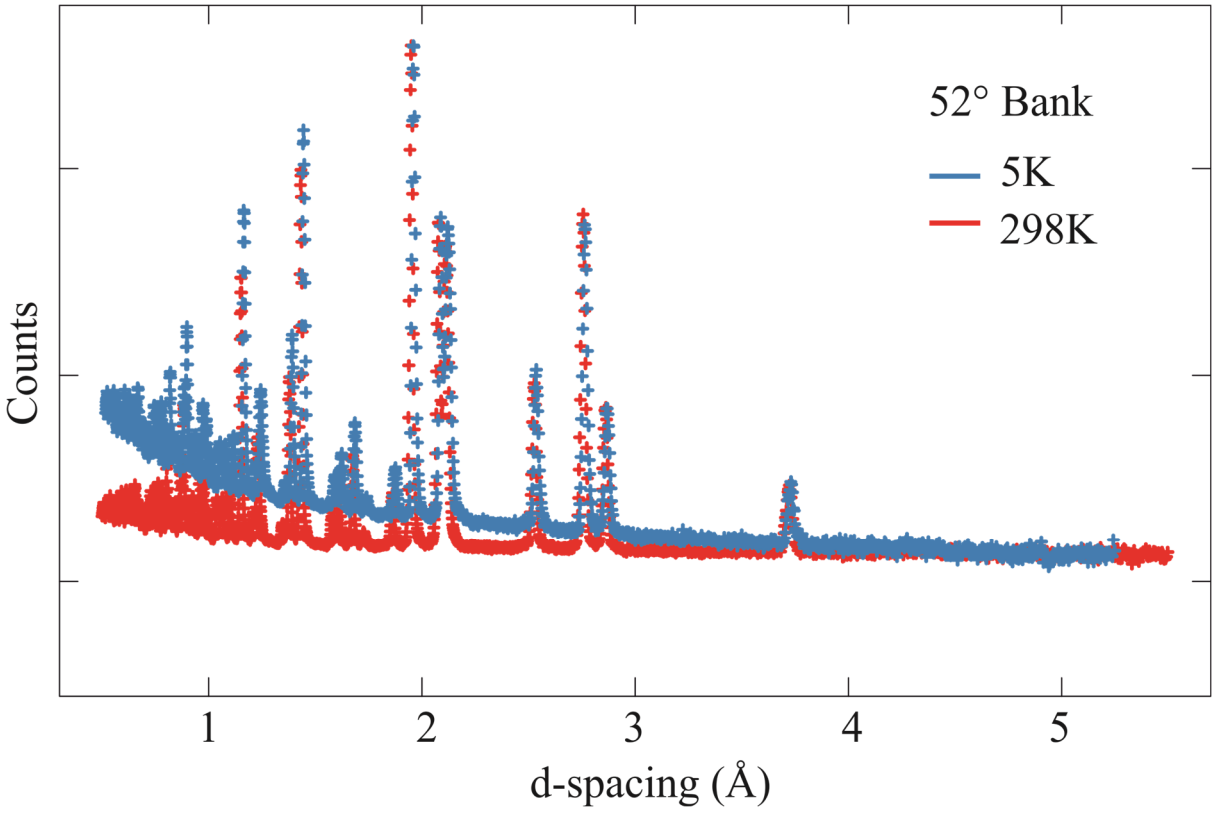


Figure 3-10 Comparison of low-angle NPD data collected from $La_{0.5}Sr_{1.5}Fe_{0.5}Rh_{0.5}O_4$ at 298 K and 5 K.

Table 3-7 Structural parameters from the refinement of $La_{0.5}Sr_{1.5}Fe_{0.5}Rh_{0.5}O_4$ against NPD data collected at 298 K.

Atom	Wyckoff Position	*x*	*y*	*z*	Fraction	U_{iso} (Å^2)
La/Sr	4*e*	0	0	0.35698(4)	0.25/0.75	0.0065(1)
Fe/Rh	2*a*	0	0	0	0.5/0.5	0.0002(1)
O(1)	4*e*	0	0	0.16447(5)	1	0.0145(2)
O(2)	4*c*	½	0	0	1	0.0024(1)

$La_{0.5}Sr_{1.5}Fe_{0.5}Rh_{0.5}O_4$ - space group *I*4/*mmm* (#139)
Formula mass: 344.25 g mol^{-1}, Z = 2
a = 3.8913(1) Å, *c* = 12.6190(4) Å, Volume = 191.08(2) Å^3
Radiation source: Time-of-flight Neutron Psowder Diffraction °
Temperature: 298 K
χ^2 = 4.094; *wRp* = 3.37 %; *Rp* = 3.92 %.

Table 3-8 Structural parameters from the refinement of $La_{0.5}Sr_{1.5}Fe_{0.5}Rh_{0.5}O_4$ against NPD data collected at 5K.

Atom	Wyckoff Position	*x*	*y*	*z*	Fraction	U_{iso} (Å^2)
La/Sr	4*e*	0	0	0.35694(3)	0.25/0.75	0.0019(2)
Fe/Rh	2*a*	0	0	0	0.5/0.5	0.0004(2)
O(1)	4*e*	0	0	0.16475(4)	1	0.0095(1)
O(2)	4*c*	½	0	0	1	0.0028(1)

$La_{0.5}Sr_{1.5}Fe_{0.5}Rh_{0.5}O_4$ - space group *I*4/*mmm* (#139)
Formula mass: 344.25 g mol^{-1}, Z = 2
a = 3.8804(1) Å, *c* = 12.5806(3) Å, Volume = 189.43(1) Å^3
Radiation source: Time-of-flight Neutron Powder Diffraction
Temperature: 5K
χ^2 = 1.725; *wRp* = 1.41 %; *Rp* = 1.77 %.

Table 3-9 Anisotropic displacement factors from refinements of $La_{0.5}Sr_{1.5}Fe_{0.5}Rh_{0.5}O_4$ against NPD data collected at 298K (top) and 5K (bottom).

Temperature: 298K			
Atom	U_{11}	U_{22}	U_{33}
La/Sr	0.00645(12)	0.00645(12)	0.00310(16)
Fe/Rh	0.00020(11)	0.00020(11)	0.00664(23)
O (1)	0.01447(16)	0.01447(16)	0.00703(23)
O (2)	0.00243(19)	0.00946(23)	0.01063(27)
Temperature: 5K			
Atom	U_{11}	U_{22}	U_{33}
La/Sr	0.00186(9)	0.00186(9)	0.00099(12)
Fe/Rh	0.00039(11)	0.00039(11)	0.00348(20)
O (1)	0.00950(14)	0.00950(14)	0.00617(25)
O (2)	0.00280(18)	0.00544(20)	0.00558(22)

Table 3-10 Selected bond lengths from the refined structure of $La_{0.5}Sr_{1.5}Fe_{0.5}Rh_{0.5}O_4$ at 298K (left) and 5K (right).

Temperature: 298K			**Temperature: 5K**		
Cation	**Anion**	**Length (Å)**	**Cation**	**Anion**	**Length (Å)**
La/Sr	O (1)	2.429(1)	**La/Sr**	O (1)	2.418(2)
	O (1)	2.765(2)		O (1)	2.757(2)
	O (2)	2.654(2)		O (2)	2.646(2)
Fe/Rh	O (1)	2.075(1)	**Fe/Rh**	O (1)	2.073(2)
	O (2)	1.946(2)		O (2)	1.940(1)

3.3.4. Magnetic Characterisation of $LaSrCo_{0.5}Rh_{0.5}O_4$

As shown in Figure 3-11 (left), zero-field-cooled (ZFC) and field-cooled (FC) magnetization data collected from $LaSrCo_{0.5}Rh_{0.5}O_4$ as a function of temperature in an applied field of 100 Oe using a SQUID magnetometer (Section 2.5). Isothermal magnetisation data were collected as a function of applied field ($-5 < H/T < +5$) at both $T = 300$ K and 5 K (Figure 3-11 (right)). Magnetization data collected at 300 K as a function of applied field is linear and passes through the origin, while the 5 K data is sigmoidal and exhibits weak hysteresis. The ZFC and FC data diverge below $T = 210$ K, hence the fitting by the Curie-Weiss law cannot be applied in the majority of temperature range (5 K - 210 K), which indicates strong magnetic interactions in the system.

The data in the range $210 < T / K < 300$ can be fitted to the Curie-Weiss law ($\chi = C / (T - \theta)$) to yield values of $C = 0.52(1)$ cm^3 K mol^{-1}, $\theta = -24.49(2)$ K (shown in the inset of Figure 3-11), hence a value of $\mu^2 = 4.16$ μ_B^2 can be calculated. The θ value indicates weak antiferromagnetic interactions in the system, which is contradictory to the conclusion obtained from early divergence of ZFC and FC curve. The contradiction indicates the possibility of impurity existance, although only one single phase is observed in the SXRD pattern.

The divergence of ZFC and FC data below 210 K, combined with the hysteresis behaviour at 5 K, suggests a canted-antiferromagnetically ordered state of $LaSrCo_{0.5}Rh_{0.5}O_4$.

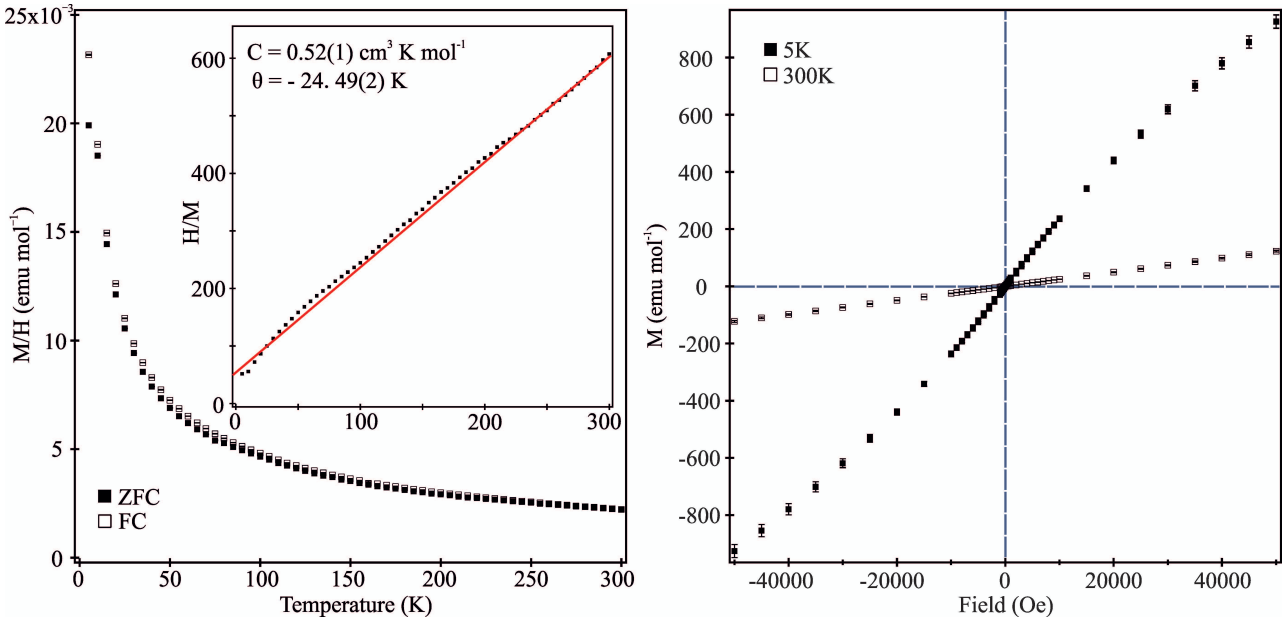


Figure 3-11 (left) Zero-field-cooled and field-cooled magnetisation data collected from $LaSrCo_{0.5}Rh_{0.5}RhO_4$ in an applied field of 100 Oe. Inset shows the fit to the Curie-Weiss law; (right) magnetisation data collected as a function of the applied field from $LaSrCo_{0.5}Rh_{0.5}RhO_4$.

3.3.5. Magnetic Characterisation of $LaSrNi_{0.5}Rh_{0.5}O_4$

ZFC and FC magnetization data collected from $LaSrNi_{0.5}Rh_{0.5}O_4$ as a function of temperature in an applied field of 100 Oe using a SQUID magnetometer (Section 2.5) are shown in Figure 3-12 (left). Isothermal magnetisation data were collected as a function of applied field ($-5 < H/T < +5$) at 5 K (Figure 3-12 (right)). Magnetization data collected at 5 K after cooling in an applied field of 5 T shows hysteresis. The ZFC and FC data diverge below around 15K, which is much lower than the $LaSrCo_{0.5}Rh_{0.5}O_4$ case.

The data in the range $145 < T / K < 300$ can be fitted to the Curie-Weiss law ($\chi = C / (T - \theta)$) to yield values of C = 0.40(4) cm^3 K mol^{-1}, θ = - 27.92(2) K with fitting statistics R = 0.99982 (shown in the inset of Figure 3-12), hence a value of $\mu^2 = 3.23\ \mu_B^2$ can be calculated.

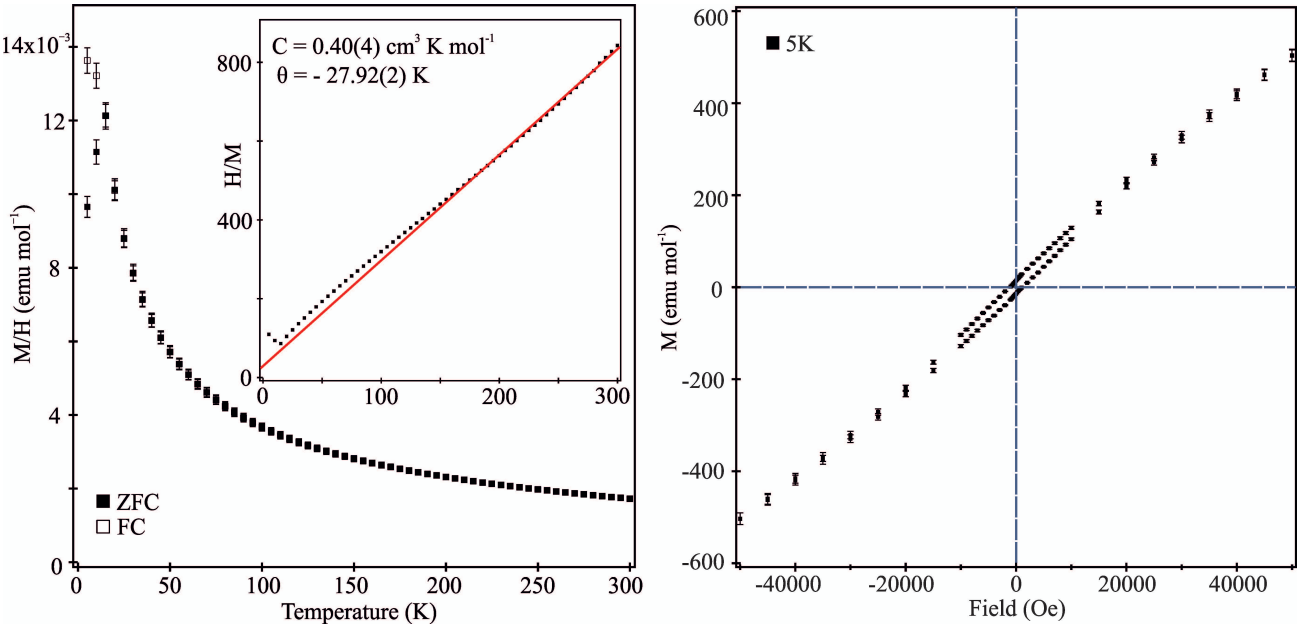


Figure 3-12 (left) Zero-field-cooled and field-cooled magnetisation data collected field from $LaSrNi_{0.5}Rh_{0.5}O_4$ in an applied field of 100 Oe. Inset shows the fit to the Curie-Weiss law; (right) Magnetisation data collected as a function of applied field from $LaSrNi_{0.5}Rh_{0.5}RhO_4$.

3.3.6. Magnetic Characterisation of $La_{0.5}Sr_{1.5}Fe_{0.5}Rh_{0.5}O_4$

ZFC and FC magnetization data collected from $La_{0.5}Sr_{1.5}Fe_{0.5}Rh_{0.5}O_4$ as a function of temperature in an applied field of 100 Oe using a SQUID magnetometer (Section 2.5) are shown in Figure 3-13 (left). The ZFC and FC data diverge below T = 50 K. The data in the range $50 < T / K < 300$ can be fitted to the Curie-Weiss law ($\chi = C / (T - \theta)$) to yield values of C = 0.44(1) cm^3 K mol^{-1}, θ = - 39.54(1) K with fitting statistics R = 0.9998 (shown in the inset of Figure 3-13), hence a value of $\mu^2 = 3.52\ \mu_B^2$ can be calculated.

Isothermal magnetisation data were collected as a function of applied field ($-5 < H / T < +5$) at 5 K (Figure 3-13 (right)). Magnetization data collected at 5 K after cooling in an applied field of 5 T indicates the presence of hysteresis.

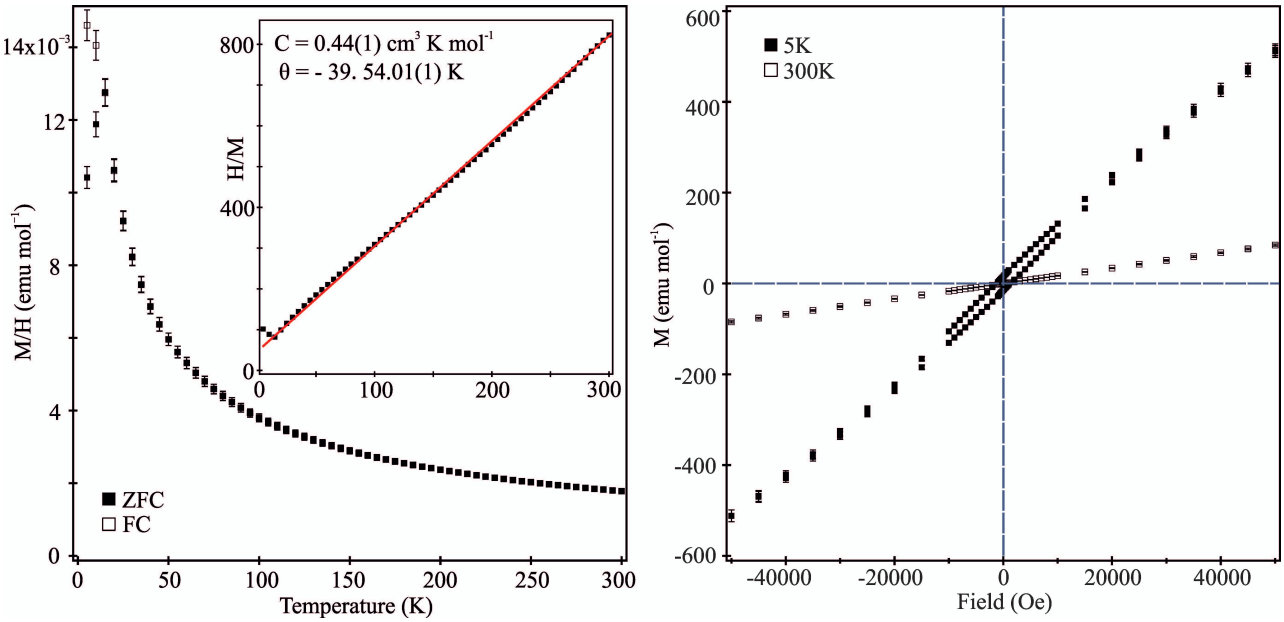


Figure 3-13 (left) Zero-field-cooled and field-cooled magnetisation data collected from $La_{0.5}Sr_{1.5}Fe_{0.5}Rh_{0.5}O_4$ in an applied field of 100 Oe. Inset shows the fit to the Curie-Weiss law; (right) Magnetisation data collected as a function of applied field from $La_{0.5}Sr_{1.5}Fe_{0.5}Rh_{0.5}O_4$.

3.4. Discussion

3.4.1. Cation Disorder in Rh-containing *n* = 1 Ruddlesden-Popper Phases

By analogy to $A_2BB'O_6$ double perovskites, $A_2B_{0.5}B'_{0.5}O_4$ n = 1 Ruddlesden-Popper phases can adopt schemes in which the B and B' cations are either ordered or disordered. The SXRD and NPD data collected from $(La/Sr)_2M_{0.5}Rh_{0.5}O_4$ (M = Co, Ni, Fe) could all be indexed using simple, body-centred unit cells, which is consistent with disordered structures. Furthermore, these data can be fit well by disordered structural models, as described in Section 3.3.4, 3.3.5 and 3.3.6.

As discussed in Section 1.2.2, $A_2BB'O_6$ perovskite phases empirically only adopt ordered structures if B and B' cations differ significantly in size and/or charge, with a 3 unit charge difference typically being required to stabilize ordered structures[22,23]. In the case of the $(La/Sr)_2M_{0.5}Rh_{0.5}O_4$ (M = Co, Ni, Fe) phases, the exact oxidation states of M and Rh are

unclear. However, the most likely combinations, M^{III}/Rh^{III} or M^{II}/Rh^{IV}, do not satisfy the '3 unit charge difference rule', so it is unsurprising that these phases do not adopt ordered configurations. In addition, there are also a series of reported $A_2BB'O_6$ double perovskites and $A_{n+1}B_nO_{3n+1}$ Ruddlesden-Popper phases where rhodium and a 3d transition metal (Cr, Mn, Fe, Co, Ni, Cu) are in a disordered arrangement on the *B*-sites.[38,74–77]

3.4.2. Spin States and Oxidation States of Transition Metals in Rh-containing *n* = 1 Ruddlesden-Popper Phases

3.4.2.1. $LaSrCo_{0.5}Rh_{0.5}O_4$

In the cation disordered $LaSrCo_{0.5}Rh_{0.5}O_4$ phase, the *B*-site cations have a summed charge of 6. This is consistent with the chemically plausible possibilities: Co^{III}/Rh^{III} and Co^{II}/Rh^{IV}.

The possibility of Co^{II}/Rh^{IV} is discussed as follows. As shown in Figure 3-14, in an octahedral coordination, we would expect Co^{II} to adopt a $t_{2g}^5 e_g^2$, $S = \frac{3}{2}$ electronic configuration, with Rh^{IV} adopting a t_{2g}^5, $S = \frac{1}{2}$ electronic configuration. This combination would be predicted to have a value of $\mu^2 = 9\ \mu_B^2$ for its magnetisation and thus C = 1.125 $cm^3\ K\ mol^{-1}$, by the spin-only formula. Both Co^{II} and Rh^{IV} can exhibit unquenched spin-orbit coupling, so the observed moment of a Co^{II}/Rh^{IV} combination would be expected to be greater than this. As shown in , the observed μ^2 of $LaSrCo_{0.5}Rh_{0.5}O_4$ is 4.16 μ_B^2 extracted from a value of C = 0.52(1) $cm^3\ K\ mol^{-1}$, which is much smaller than that predicted for the Co^{II}/Rh^{IV} combination, so the Co^{II}/Rh^{IV} combination can be discounted.

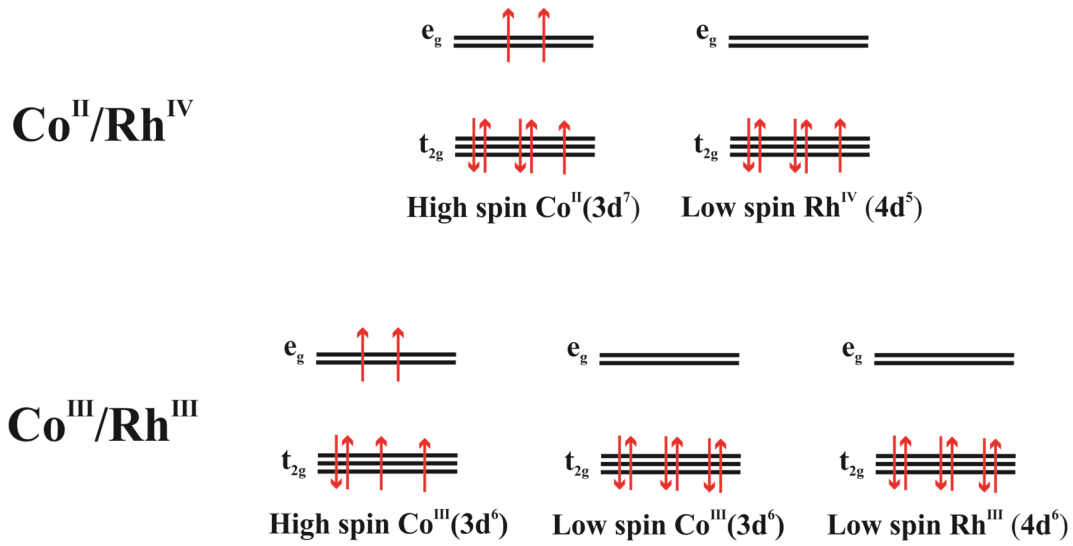


Figure 3-14 Proposed electronic configurations of $LaSrCo_{0.5}Rh_{0.5}O_4$.

The possibility of Co^{III}/Rh^{III} is discussed as follows. The large ligand field of Rh (being a 4d metal) means that a low-spin t_{2g}^6, $S = 0$ electronic configuration of Rh^{III} is highly preferred. In contrast, $Co^{III}O_6$ units have a ligand field close to the 'critical value' between high-spin (HS) and low-spin (LS) states, as discussed in Section 1.3.1. Considering these possibilities, we can calculate that an $S = 0$ Rh^{III}, $S = 0$ Co^{III} system would be diamagnetic ($\mu^2 = 0$ μ_B^2, C = 0 cm^3 K mol^{-1}) while an $S = 0$ Rh^{III}, $S = 2$ Co^{III} would give $\mu^2 = 12$ μ_B^2, C = 1.5 cm^3 K mol^{-1}. Again, neither of these values match the observed magnetization data in . In principle, a 2:1 mixture of LS Co^{III}/HS Co^{III} could explain the magnetic behaviour of $LaSrCo_{0.5}Rh_{0.5}O_4$. As in the $LaCo_{1-x}Rh_xO_3$ solid solution[37,78], the disordered distribution of large Rh atoms could result in a disordered array of HS and LS Co^{III} sites.

There is a third possible spin-state for Co^{III}, the $S = 1$ intermediate spin (IS) configuration, as described in Section 1.3.1. In isolated molecules, this spin-state is not accessible because it can never be more stable than both HS and LS states. However, there is some evidence for the IS state in $LaCoO_3$[30], which is stabilized by the filling of a σ^* bond from the e_g cobalt

orbitals. Such a $S = 0$ Rh^{III}, $S = 1$ Co^{III} system would yield a $\mu^2 = 4\ \mu_B^2$, C = 0.5 $cm^3\ K\ mol^{-1}$ in relatively good agreement with observation.

While the $S = 1$ configuration of cobalt gives a value in good agreement with experimental results, it seems likely that the presence of Rh^{III} in $LaSrCo_{0.5}Rh_{0.5}O_4$ would disrupt the formation of the extended σ^* bond required to stabilize $S = 1$ Co^{III}, so the 2:1 combination of $S = 0$ and $S = 2$ Co^{III} is preferred, but in the absence of a more direct measurement, it is hard to be unambiguously certain of the cobalt spin-state in $LaSrCo_{0.5}Rh_{0.5}O_4$.

3.4.2.2. $LaSrNi_{0.5}Rh_{0.5}O_4$

In common with $LaSrCo_{0.5}Rh_{0.5}O_4$, the *B*-site cations in $LaSrNi_{0.5}Rh_{0.5}O_4$ also have a summed charge of 6, which indicates the possibilities of oxidation state combinations: Ni^{III}/Rh^{III} and Ni^{II}/Rh^{IV}.

The possibility of Ni^{II}/Rh^{IV} is discussed as follows. As shown in Figure 3-15, in an octahedral coordination, we would expect Ni^{II} to adopt a $t_{2g}^6 e_g^2$, $S = 1$ electronic configuration. As for the Rh^{IV}, the large ligand field of Rh means that a low-spin t_{2g}^5, $S = \frac{1}{2}$ electronic configuration of Rh^{IV} is highly preferred. This combination would give a value of $\mu^2 = 5.5\ \mu_B^2$ and thus C = 0.6875 $cm^3\ K\ mol^{-1}$, by the spin-only formula. Again, both Ni^{II} and Rh^{IV} will exhibit unquenched spin-orbit cupling, so the observed moment of a Ni^{II}/Rh^{IV} combination is expected to be greater than this. As shown in , the observed μ^2 value of $LaSrNi_{0.5}Rh_{0.5}O_4$ is 3.23 μ_B^2 extracted from a value of C = 0.40(4) $cm^3\ K\ mol^{-1}$, which is much smaller than that predicted for the Ni^{II}/Rh^{IV} combination. Therefore, although $3d^8$ Ni^{II} is more stable and easier to achieve compared to $3d^7$ Ni^{III}, the possibility of Ni^{II}/Rh^{IV} is still discounted.

The possibility of Ni^{III}/Rh^{III} is discussed as follows. As for $LaSrCo_{0.5}Rh_{0.5}O_4$, the low-spin t_{2g}^6, $S = 0$ state for Rh^{III} is highly preferred due to its large ligand field, while $Ni^{III}O_6$ units have ligand field which enables Ni^{III} to adopt HS or LS states depending on the local chemical environment. As described in Section 1.3.1, if $\Delta > 2J_{ex}$ (Δ being the ligand-field splitting parameter and J_{ex} being the exchange energy) then an LS Ni^{III} is adopted; if $2J_{ex} > \Delta$ then an HS Ni^{III} is more stable.

Considering these possibilities, we can calculate that a combination of HS Ni^{III}/LS Rh^{III} yields values of $\mu^2 = 7.5\ \mu_B^2$ and $C = 0.9375\ cm^3\ K\ mol^{-1}$; a combination of LS Ni^{III}/LS Rh^{III} yields values of $\mu^2 = 1.5\ \mu_B^2$ and $C = 0.1875\ cm^3\ K\ mol^{-1}$. Both of these values do not match the observed magnetization data ($\mu^2 = 3.23\ \mu_B^2$; $C = 0.40(4)\ cm^3\ K\ mol^{-1}$) in . The observed data sit between the spin-only magnetic moment calculated from HS Ni^{III}/LS Rh^{III} and LS Ni^{III}/LS Rh^{III}. Thus, similar to $LaSrCo_{0.5}Rh_{0.5}O_4$, a 70:30 mixture of LS Ni^{III}/HS Ni^{III} could explain the magnetic behaviour of $LaSrNi_{0.5}Rh_{0.5}O_4$.

This suggests a higher possibility of Ni^{III}/Rh^{III} than Ni^{II}/Rh^{IV} for the *B*-sites in $LaSrNi_{0.5}Rh_{0.5}O_4$. In complex oxides, Ni^{III} is rarely seen but a few perovskite phases containing Ni^{III} have been reported, such as $n = \infty$, 1, and 2 members of the Ruddlesden-Popper phase $(La_{x/2}Sr_{1-(x/2)})_nSr(Ni_{0.5}Ru_{0.5})_nO_{3n+1}$ compositional series[48] and the perovskite phase La_2NiRhO_6[79]. Therefore, we can tentatively conclude that a Ni^{III}/Rh^{III} oxidation state combination is preferred in $LaSrNi_{0.5}Rh_{0.5}O_4$.

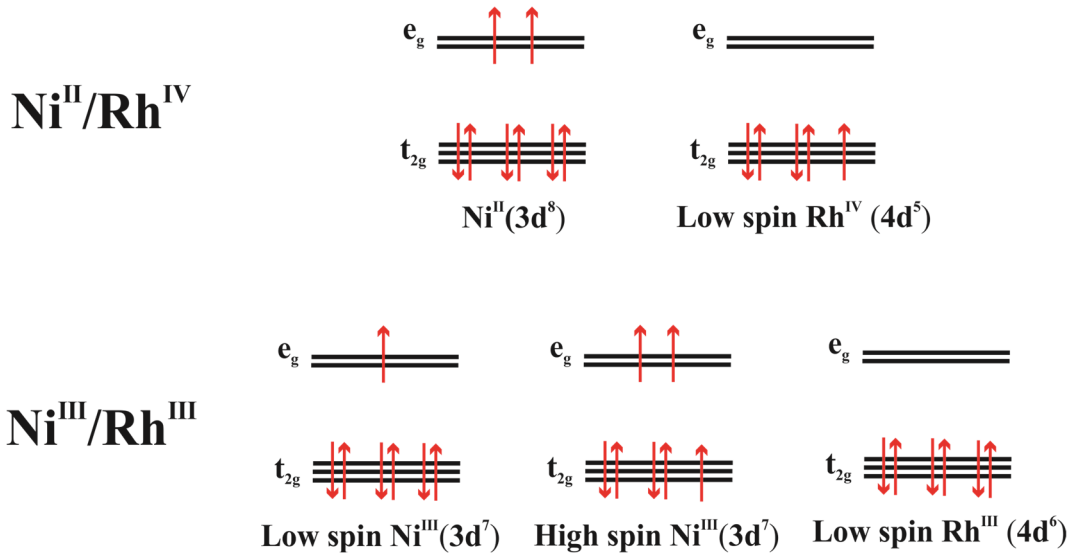


Figure 3-15 Proposed electronic configurations of $LaSrNi_{0.5}Rh_{0.5}O_4$.

3.4.2.3. $La_{0.5}Sr_{1.5}Fe_{0.5}Rh_{0.5}O_4$

The *B*-site cations in $La_{0.5}Sr_{1.5}Fe_{0.5}Rh_{0.5}O_4$ have a summed charge of 7, which indicates oxidation state combinations: Fe^{III}/Rh^{IV} and Fe^{IV}/Rh^{III}.

The possibility of Fe^{IV}/Rh^{III} is discussed as follows. As shown in Figure 3-16, in an octahedral coordination, we would expect Fe^{IV} to adopt a $t_{2g}^3 e_g^1$, $S = 2$ electronic configuration and Rh^{III} to adopt a low-spin t_{2g}^6, $S = 0$ electronic configuration. The LS $4d^6$ Rh^{III}/HS $3d^4$ Fe^{IV} combination yields values of $\mu^2 = 12\ \mu_B^2$ and C = 1.5 $cm^3\ K\ mol^{-1}$, by the spin-only formula. As shown in , the observed μ^2 value of $La_{0.5}Sr_{1.5}Fe_{0.5}Rh_{0.5}O_4$ is 3.52 μ_B^2 extracted from a value of C = 0.44(1) $cm^3\ K\ mol^{-1}$, which is much smaller than that predicted for the Fe^{IV}/Rh^{III} combination.

The combination of Fe^{III}/Rh^{IV} in octahedral sites has been discovered in the perovskite oxide phase $La_{0.5}Sr_{0.5}Fe_{0.5}Rh_{0.5}O_3$[73]. Hence, similar to $La_{0.5}Sr_{0.5}Fe_{0.5}Rh_{0.5}O_3$, the possibility of Fe^{III}/Rh^{IV} in $La_{0.5}Sr_{1.5}Fe_{0.5}Rh_{0.5}O_4$ is discussed as follows. As shown in Figure 3-16, in an octahedral coordination, we would expect Rh^{IV} to adopt a low-spin t_{2g}^5, $S = \frac{1}{2}$ electronic

configuration due to the large ligand field of Rh. If Fe^{III} adopts a LS t_{2g}^5, $S = \frac{1}{2}$ electonic configuration, combined with LS t_{2g}^5, $S = \frac{1}{2}$ Rh^{IV}, the values of $\mu^2 = 3\ \mu_B^2$ and C = 0.375 cm^3 K mol^{-1} are calculated by spin-only formula, which are in almost perfect agreement with the observed data (μ^2 = 3.52 μ_B^2, C = 0.44(1) cm^3 K mol^{-1}). However, the metastable configurations with LS Fe^{III} in an octahedral site only occur at high pressures and high temperatures[80]. Thus, although it almost perfectly matches the observed data, the possibility of LS $4d^5$ Rh^{IV}/LS $3d^5$ Fe^{III} is still discounted.

If Fe^{III} adopts an HS $t_{2g}^3 e_g^2$, $S = \frac{5}{2}$ electronic configuration, then this proposed LS $4d^5$ Rh^{IV}/HS $3d^5$ Fe^{III} yields values of μ^2 = 19 μ_B^2 and C = 2.375 cm^3 K mol^{-1}, which is much larger than the observed data μ^2 = 3.52 μ_B^2, C = 0.44(1) cm^3 K mol^{-1}.

The theoretical magnetic moments from both Fe^{III}/Rh^{IV} and Fe^{IV}/Rh^{III} combinations are much higher than the Curie constant extracted from the magnetization data collected from $La_{0.5}Sr_{1.5}Fe_{0.5}Rh_{0.5}O_4$. The reason for the mismatch between the theoretical and the observed paramagnetic behaviour in the temperature range of 50 < *T*/K < 300 remains unclear.

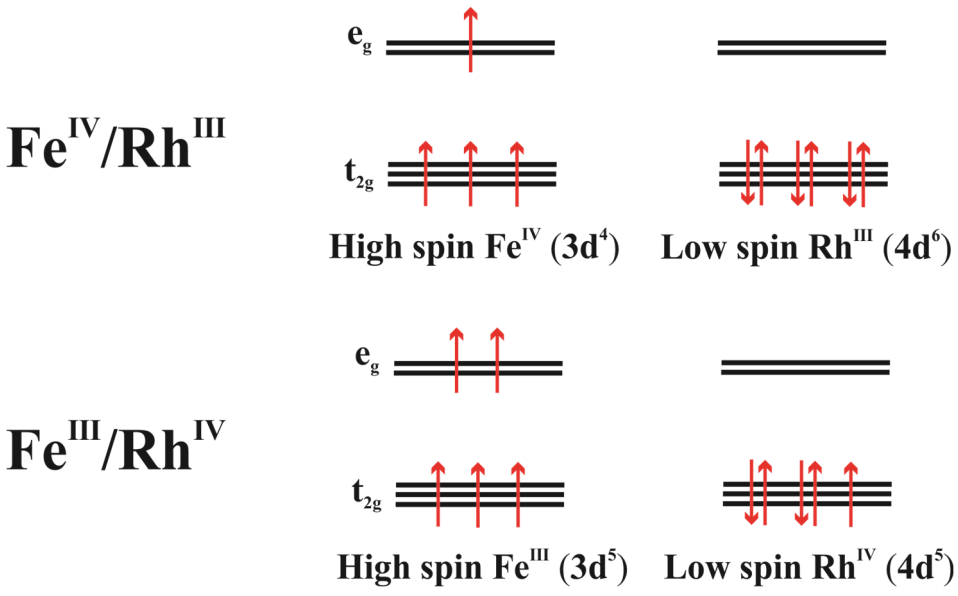


Figure 3-16 Proposed electronic configurations of $La_{0.5}Sr_{1.5}Fe_{0.5}Rh_{0.5}O_4$.

3.5. Conclusion

Three n = 1 Ruddlesden-Popper phases $LaSrCo_{0.5}Rh_{0.5}O_4$, $LaSrNi_{0.5}Rh_{0.5}O_4$ and $La_{0.5}Sr_{1.5}Fe_{0.5}Rh_{0.5}O_4$ have been prepared via a traditional high-temperature ceramic method from binary metal oxides and metal carbonates.

Both SXRD data and NPD data collected at 300 K can be indexed by a simple body-centred tetragonal unit cells (space group *I*4/*mmm*) with lattice parameters of a = 3.87941(1) Å, c = 12.51885(5) Å ($LaSrCo_{0.5}Rh_{0.5}O_4$); a = 3.8840(1) Å, c = 12.5660(4) Å ($LaSrNi_{0.5}Rh_{0.5}O_4$); a = 3.8913(1) Å, c = 12.6190(4) Å ($La_{0.5}Sr_{1.5}Fe_{0.5}Rh_{0.5}O_4$), respectively. No phase transitions or cation-ordering within the temperature range $5 < T/K < 298$ are found, with the SXRD and NPD patterns at both 298 K and 5 K being indexed using simple unit cells with high symmetry.

Magnetisation data collected using a SQUID magnetometer for all the phases show strong evidence of a canted antiferromagnetic ground state. All three phases show little hysteresis at 5 K. The Curie constants extracted from the fitting of the magnetic data of these phases cannot be easily accounted for using simple oxidation state combinations and the spin-only formula.

The topochemical reduction reactions of these n = 1 Ruddlesden-Popper phases $LaSrM_{0.5}Rh_{0.5}O_4$ (M = Co, Ni) have been investigated and details are presented in the following Chapter 4.

Chapter 4

Synthesis and Characterisation of $LaSrM_{0.5}Rh_{0.5}O_{3.25}$ (M = Co, Ni)

4.1. Introduction

As discussed in Section 3.5, in order to further explore the possibility of the formation of complex transition-metal oxides that would adopt novel metal oxidation states and coordination geometries, topochemical reduction has been carried out for the preparation of a wide range of novel metastable materials.

Building on the work describing the preparation of three new n = 1 Ruddlesden-Popper phases: $LaSrCo_{0.5}Rh_{0.5}O_4$, $LaSrNi_{0.5}Rh_{0.5}O_4$ and $La_{0.5}Sr_{1.5}Fe_{0.5}Rh_{0.5}O_4$, which has been discussed in Chapter 3, the topochemical reduction of n = 1 Ruddlesden-Popper phases $LaSrM_{0.5}Rh_{0.5}O_4$ (M = Co, Ni) was attempted using zirconium powder in sealed ampoules. This yields anion-deficient phases of composition $LaSrM_{0.5}Rh_{0.5}O_{3.25}$ (M = Co, Ni) at 510 °C, according to the reaction:

$$LaSrM_{0.5}Rh_{0.5}O_4 + \frac{3}{8}Zr \xrightarrow{510°C} LaSrM_{0.5}Rh_{0.5}O_{3.25} + \frac{3}{8}ZrO_2$$

Detailed characterisation of these reduced oxide phases are described in this chapter.

4.2. Experimental

Samples of $LaSrM_{0.5}Rh_{0.5}O_4$ (M = Co, Ni) were reduced using a zirconium getter[81], as described in Section 2.2.1. Samples to be reduced were placed in a glass 'thimble' and sealed in evacuated silica ampoules along with 2 mole equivalents of powdered zirconium placed at the bottom of the silica ampoules. Thus, the two powders shared an atmosphere but were not in physical contact. Small-scale test reactions were performed in which ~200 mg of

$LaSrM_{0.5}Rh_{0.5}O_4$ (*M*= Co, Ni) were heated at a rate of 1 °C min^{-1} to temperatures ranging from 450 °C to 520°C. It was discovered that the optimum temperature for the topochemical reduction of $LaSrCo_{0.5}Rh_{0.5}O_4$ was $T \approx 510$ °C, with no observable reaction occurring below $T = 450$ °C and non-topochemical decomposition reactions occurring above $T = 520$°C. Similarly, the optimum temperature discovered for topochemical reduction of $LaSrNi_{0.5}Rh_{0.5}O_4$ was $T \approx 500$ °C. Samples of $LaSrCo_{0.5}Rh_{0.5}O_{4-\delta}$ and $LaSrNi_{0.5}Rh_{0.5}O_{4-\delta}$ characterized by neutron powder diffraction (NPD) were prepared by heating ~2 g of $LaSrCo_{0.5}Rh_{0.5}O_4$ and $LaSrNi_{0.5}Rh_{0.5}O_4$ respectively with Zr for 3 periods of 5 days at 510 °C and 500 °C, with samples being reground and the Zr being replaced between heating periods.

4.3. Results

4.3.1. Initial Investigation of Reactivity of $LaSrM_{0.5}Rh_{0.5}O_4$ (*M*= Co, Ni) with Zr

Small scale trial reactions were performed by heating ~200 mg of $LaSrM_{0.5}Rh_{0.5}O_4$ (*M*= Co, Ni) samples along with 2 mole equivalents of Zr in evacuated silica ampoules. These sample combinations were heated in the temperature range $425 \leq T/^{o}C \leq 520$. X-ray powder diffraction (XRD) was used to monitor the reaction progress. Setting the reduction of $LaSrCo_{0.5}Rh_{0.5}O_4$ as an example, in order to describe the whole reduction profile, temperature intervals of 10 °C were chosen and the changes observed in XRD patterns at different reaction temperatures are summarized in Table 4-1. The topochemical reduction profile of $LaSrCo_{0.5}Rh_{0.5}O_4$ to form $LaSrCo_{0.5}Rh_{0.5}O_{4-\delta}$ under different temperatures are shown in Figure 4-1. As we can notice in the comparison of XRD patterns collected at different reaction temperatures, the symmetry of the main phase was lowered from tetragonal to orthorhombic once the deintercalation of axial oxide ions had started.

Table 4-1 Results from initial investigation of topochemical reduction of $LaSrCo_{0.5}Rh_{0.5}O_4$ with Zr in sealed silica ampoules.

Reaction Condition	Structure of the Main Lattice	Lattice Parameters/ Å	Description	Chemical Composition
Starting Material	Tetragonal	a =3.8794(1) c = 12.5188(1)	Nice, sharp [103] and [110] peaks, very crystalline	$LaSrCo_{0.5}Rh_{0.5}O_4$
450°C	Orthorhombic	a =3.6587(6) b = 3.8975(6) c = 12.880(2)	Visible splitting of [103] peak, not as crystalline as starting material	$LaSrCo_{0.5}Rh_{0.5}O_{3.34}$
500°C	Orthorhombic	a =3.6222(1) b = 3.9030(1) c = 12.9145(4)	Further splitting of [103] peak	$LaSrCo_{0.5}Rh_{0.5}O_{3.27}$
510°C	Orthorhombic	a =3.5894(1) b = 3.9027(1) c = 12.9527(1)	No visible changes	$LaSrCo_{0.5}Rh_{0.5}O_{3.26}$
520°C	N/A	N/A	Decomposition	La_2O_3 etc.

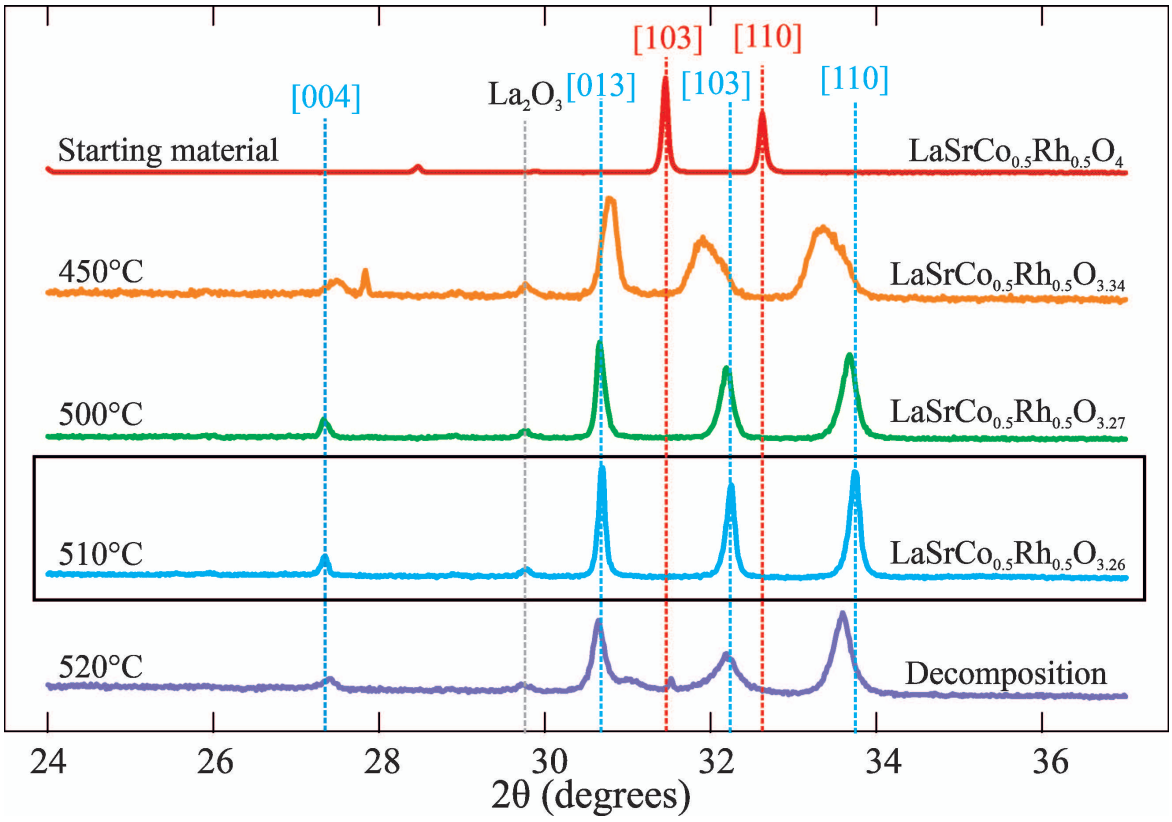


Figure 4-1 Topochemical reduction profile of $LaSrCo_{0.5}Rh_{0.5}O_4$ with Zr to form a compositional range of $LaSrCo_{0.5}Rh_{0.5}O_{4-\delta}$.

The first distinct reduced phase observed is $LaSrCo_{0.5}Rh_{0.5}O_{3.34}$ at 450 °C which could be roughly indexed by an orthorhombic cell with slight elongation of the *b* and *c* lattice parameters and shrinkage of the *a* lattice parameter compared to its tetragonal parent oxide $LaSrCo_{0.5}Rh_{0.5}O_4$. The original [103] peak in the starting material has already clearly become two peaks [103] and [013]. The phase composition was determined by the reductive thermogravimetric analysis (TGA), as described in Section 2.7, which showed a mass loss on reduction to La_2O_3, SrO, Rh and Co.

After raising the reaction temperature to 500 °C and 510 °C, further reductive deintercalation occurs with slight elongation of the *b* and *c* lattice parameters and contraction of the *a* lattice parameter. The sample reduced at 510 °C could be readily indexed using a body-centred orthorhombic cell (a = 3.59 Å, b = 3.90 Å, c = 12.95 Å) and reductive TGA indicates a composition of $LaSrCo_{0.5}Rh_{0.5}O_{3.26}$. On raising the reduction temperature to 520 °C, the sample was observed to decompose to via non-topochemical reactions.

4.3.2. Structural and Chemical Characterisation of $LaSrM_{0.5}Rh_{0.5}O_{3.25}$ (*M* = Co, Ni)

4.3.2.1. Thermogravimetric Analysis of $LaSrM_{0.5}Rh_{0.5}O_{3.25}$ (*M* = Co, Ni)

To determine the chemical composition of the reduced phases, the reductive TGA was conducted. A small quantity of the reduced samples was heated under a steady flow of 10%/90% H_2/N_2 at a rate of 5 °C min^{-1} and held at 800 °C for 1 hour to complete the reaction before cooling. The oxygen content of the reduced sample was calculated by the mass difference between $LaSrM_{0.5}Rh_{0.5}O_{4-\delta}$ and totally reduced products (La_2O_3, SrO, *M* and Rh). TGA data from $LaSrCo_{0.5}Rh_{0.5}O_{4-\delta}$ and $LaSrNi_{0.5}Rh_{0.5}O_{4-\delta}$ are shown respectively in Figure 4-2 and Figure 4-3. During the reaction, $LaSrCo_{0.5}Rh_{0.5}O_{4-\delta}$ showed a mass loss of 3.37%, which is consistent with the composition $LaSrCo0.5Rh_{0.5}O_{3.26(1)}$; $LaSrNi_{0.5}Rh_{0.5}O_{4-\delta}$ showed a

mass loss of 3.30%, which is consistent with the composition $LaSrNi_{0.5}Rh_{0.5}O_{3.24(1)}$. Henceforth, these two reduced phases will be referred to as $LaSrCo_{0.5}Rh_{0.5}O_{3.25}$ and $LaSrNi_{0.5}Rh_{0.5}O_{3.25}$.

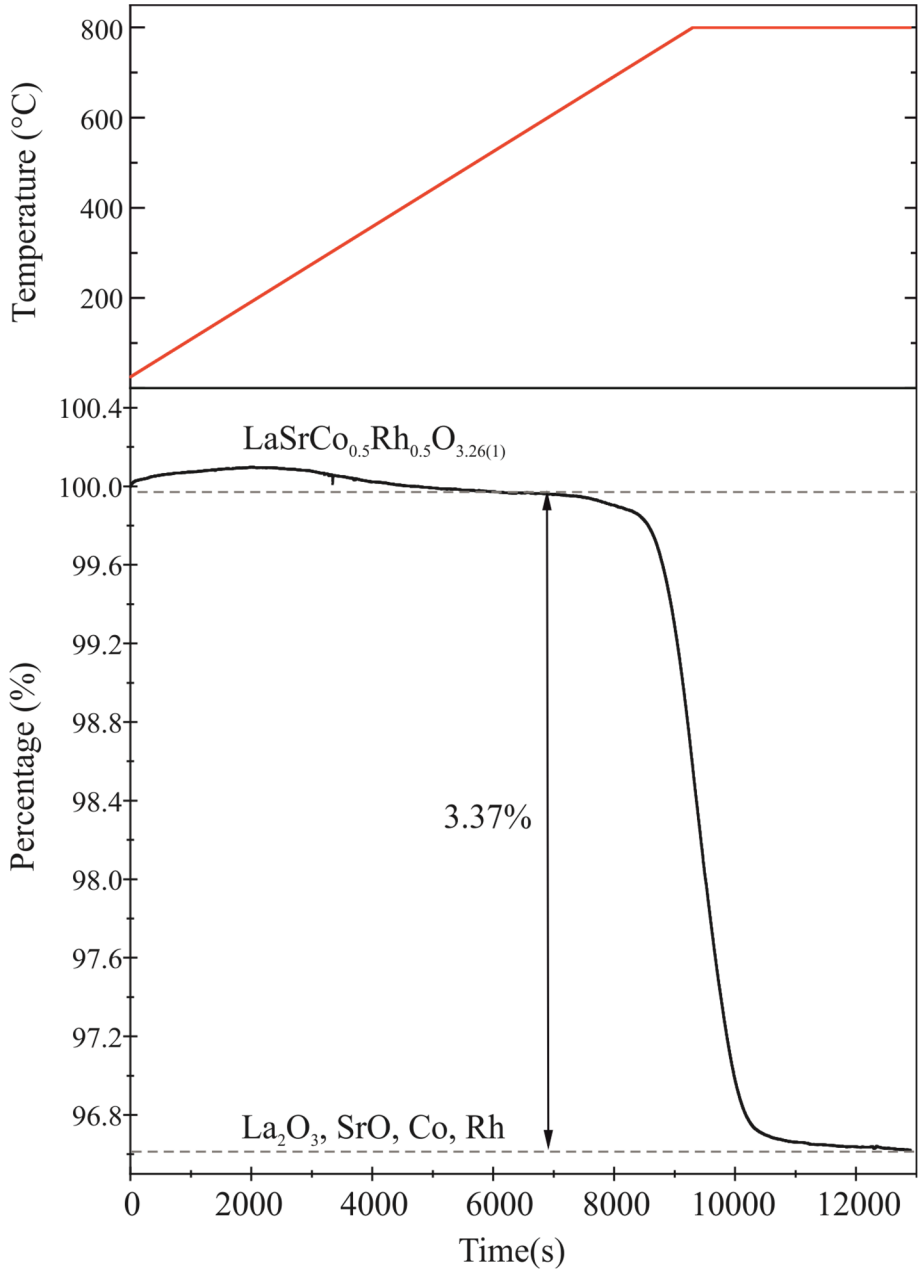


Figure 4-2 Reductive thermogravimetric data collected from $LaSrCo_{0.5}Sr_{0.5}O_{4-\delta}$. Top panel indicates the heating profile, bottom panel the relative mass of the sample.

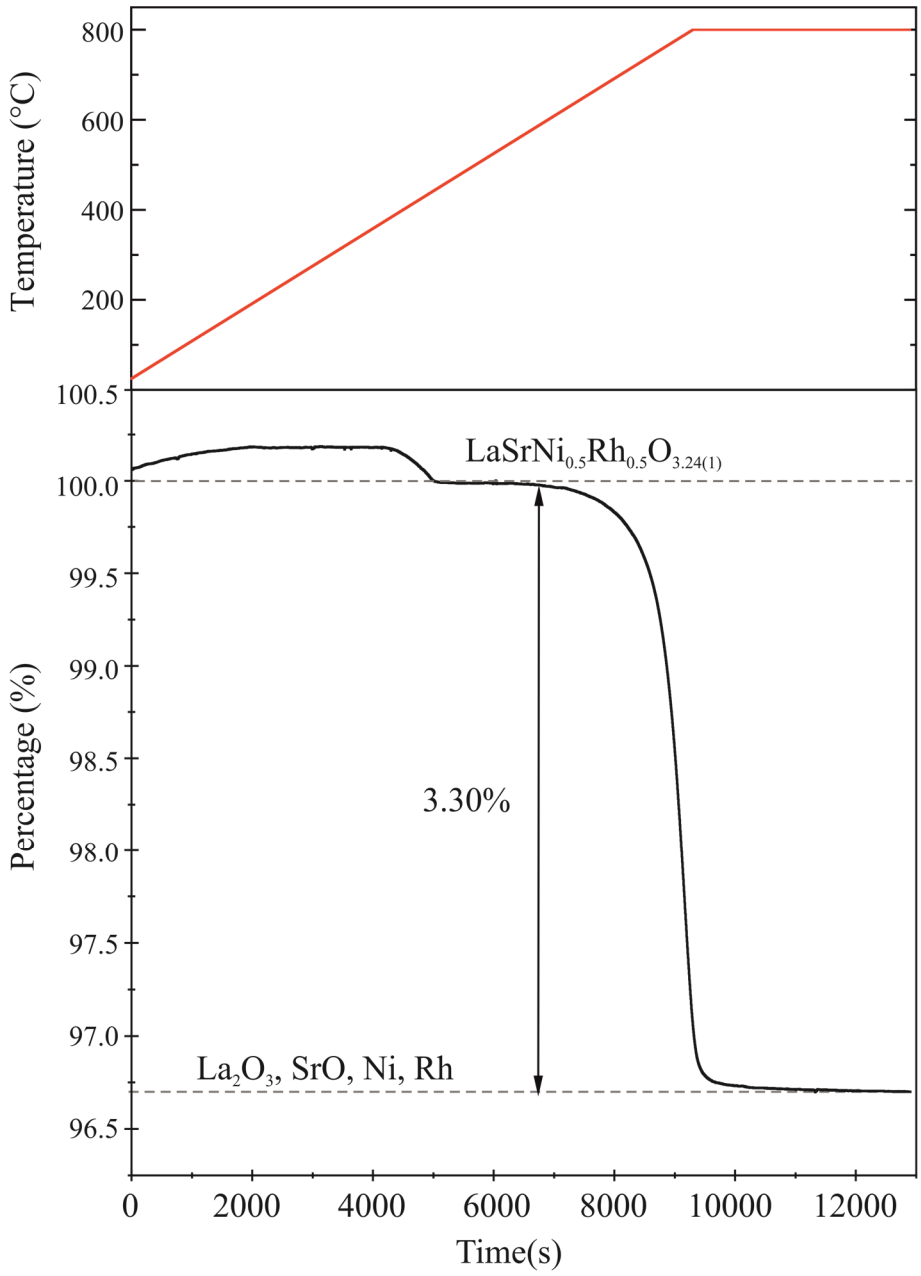


Figure 4-3 Reductive thermogravimetric data collected from $LaSrNi_{0.5}Rh_{0.5}O_{4-\delta}$. Top panel indicates the heating profile, bottom panel the relative mass of the sample.

4.3.2.2. Synchrotron X-ray Powder Diffraction of $LaSrM_{0.5}Rh_{0.5}O_{3.25}$ (M = Co, Ni)

Synchrotron X-ray powder diffraction (SXRD) (Section 2.3.1.3) data collected from $LaSrCo_{0.5}Rh_{0.5}O_{3.25}$ and $LaSrNi_{0.5}Rh_{0.5}O_{3.25}$ could be indexed using body-centered orthorhombic unit cells ($LaSrCo_{0.5}Rh_{0.5}O_{3.25}$: a = 3.602Å, b = 3.911 Å, c = 12.936 Å; $LaSrNi_{0.5}Rh_{0.5}O_{3.25}$: a = 3.580 Å, b = 3.927 Å, c = 12.810 Å). Considering the stoichiometry of these two phases, models based on the reported structure of $Sr_2Fe_{0.5}Ru_{0.5}O_{3.2517}$[82] were constructed (with the Fe/Ru solid solution replaced by M/Rh) and refined against the SXRD data of $LaSrM_{0.5}Rh_{0.5}O_{3.25}$ (M = Co, Ni). As shown in Figure 4-4, the refinement of $LaSrCo_{0.5}Rh_{0.5}O_{3.25}$ achieved a good fit, confirming sample purity and quality. The fitting of the peak shapes is good, even for the peaks at high angles as shown in the embedded plot for zoom-in area $40° \leq 2\theta \leq 60°$ in Figure 4-4. There are no extra peaks which cannot be indexed using the current model. This indicates that the selective deintercalation of oxygen atoms only occurs from 'equatorial' oxygen sites and no expansion of the unit cell due to anion vacancies ordering was observed.

$LaSrNi_{0.5}Rh_{0.5}O_{3.25}$ also follows the same arrangement of oxygen vacancies. The observed, calculated and difference plots from the Rietveld refinement of $LaSrNi_{0.5}Rh_{0.5}O_{3.25}$ against SXRD data are shown in Figure 4-5. Although some peak displacements at high angles are shown in the embedded plot for zoom-in area $40° \leq 2\theta \leq 60°$ in Figure 4-5, the same model gave a relatively good statistical fit for NPD data.

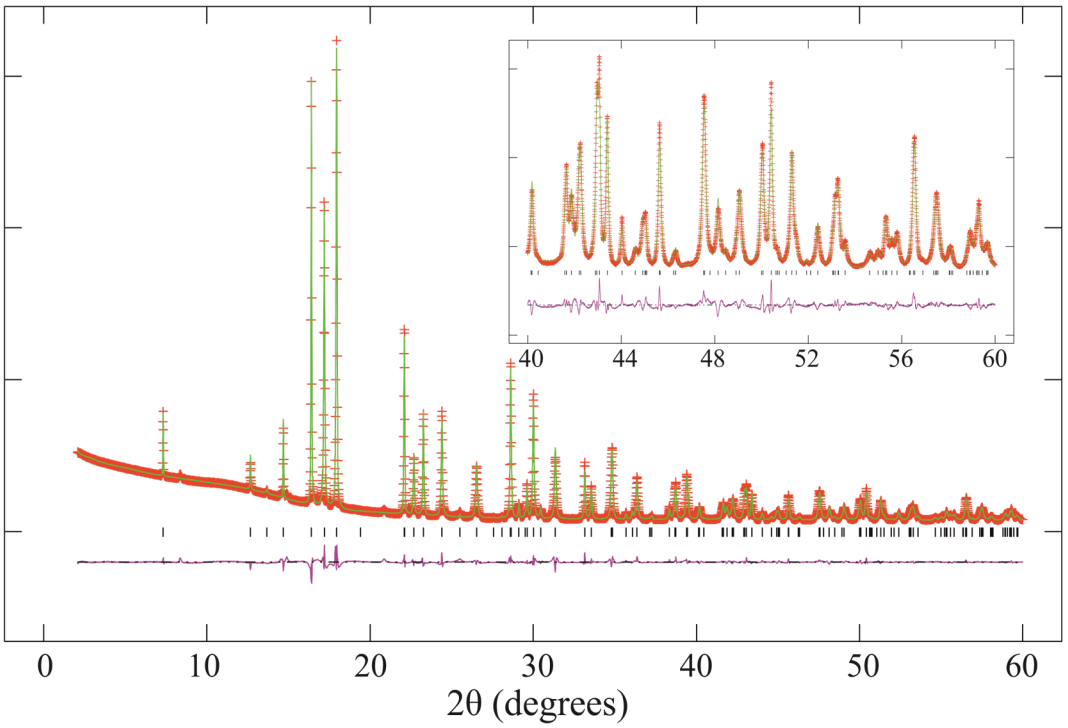


Figure 4-4 Observed(red), calculated(green) and difference plots(pink) from the Rietveld structural refinement of $LaSrCo_{0.5}Rh_{0.5}O_{3.25}$ using an *Immm* model against SXRD data collected at room temperature.

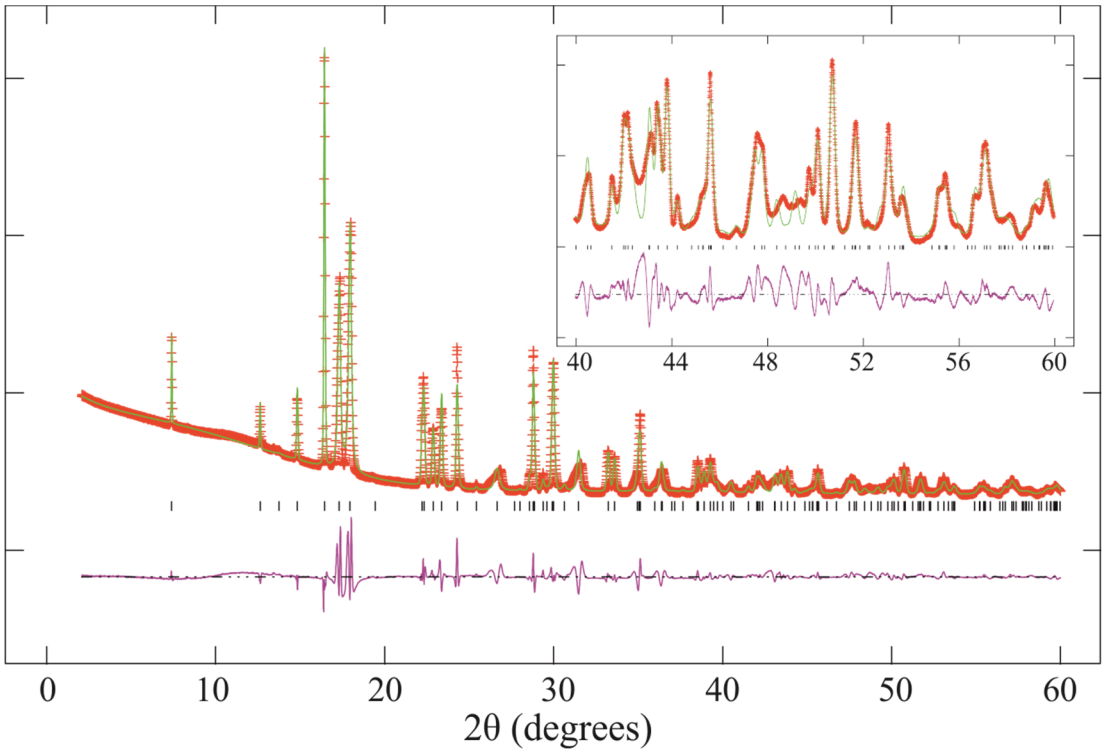


Figure 4-5 Observed(red), calculated(green) and difference plots(pink) from the Rietveld structural refinement of $LaSrNi_{0.5}Rh_{0.5}O_{3.25}$ using an *Immm* model against SXRD data collected at room temperature.

4.3.2.3. Neutron Powder Diffraction of $LaSrM_{0.5}Rh_{0.5}O_{3.25}$ (M = Co, Ni)

Time-of-flight NPD measurements at ambient temperature were carried out using the POLARIS diffractometer at ISIS (Section 2.3.2.1).

In common with SXRD data, NPD data collected from $LaSrCo_{0.5}Rh_{0.5}O_{3.25}$ could be indexed using a body-centred orthorhombic unit cell (shown in Figure 4-6), with extinction conditions consistent with *Immm* space group (No. 71). During the refinement, all atomic positional and displacement parameters were refined freely along with the occupancy of the O(3) oxide ion residing at (½, 0, 0). Close inspection of the displacement parameter of the O(2) anion site revealed that it was more than twice the size of displacement parameters of the O(1) and O(3) sites. This suggested that the O(2) site was disordered on either side of the x = 0 mirror plane, so the O(2) position was moved to a (x, ½, 0) position with half occupancy. This led to an improvement in the fit to the data (χ^2 = 1.98) and physically sensible displacement parameters (Table 4-2). In the final refinement cycles, the occupancy of the O(3) anion site was refined to a value of 0.251(5) without constraint, which is consistent with the composition $LaSrCo_{0.5}Rh_{0.5}O_{3.26(1)}$ obtained from TGA data. There was no evidence for partial occupancy on any of the other anion sites. The refinement managed to achieve good statistical fits for both 298 K data and 5 K data, with the only difference between two models refined at 298 K and 5 K being the displacement parameters. The observed, calculated and difference plots of neutron diffraction at 52° bank, 92° bank and 146° bank are shown in Figure 4-8 for 5 K and Figure 4-9 for 298 K.

Full details of the structural parameters are given in Table 4-2 for 5 K and Table 4-3 for 298 K, anisotropic displacement factors are given in Table 4-5. Selected bond lengths are given in Table 4-4. Figure 4-7 indicates that there are no additional magnetic diffraction features observed at 5 K and hence no long-range magnetic order in $LaSrCo_{0.5}Rh_{0.5}O_{3.25}$.

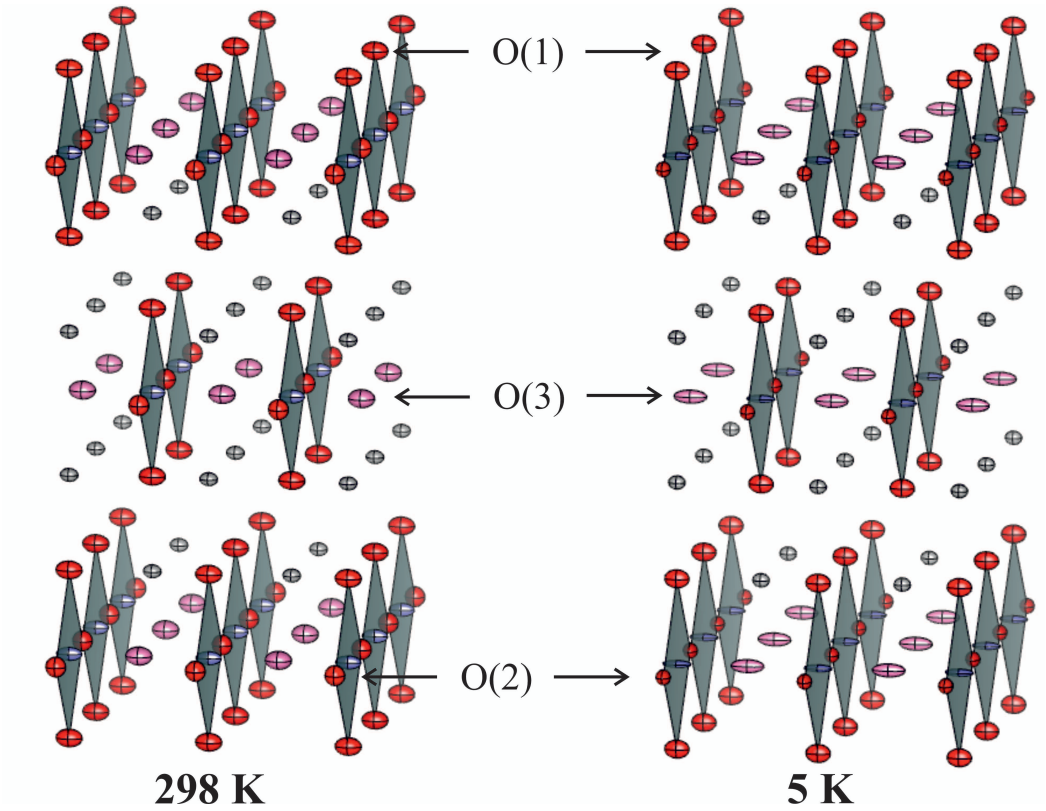


Figure 4-6 The crystal structure of $LaSrCo_{0.5}Rh_{0.5}O_{3.25}$ with displacement ellipsoids at 298 K (left) and 5 K (right); Grey, purple, red, and pink spheres represent La/Sr, Co/Rh, O and partially occupied O positions, respectively.

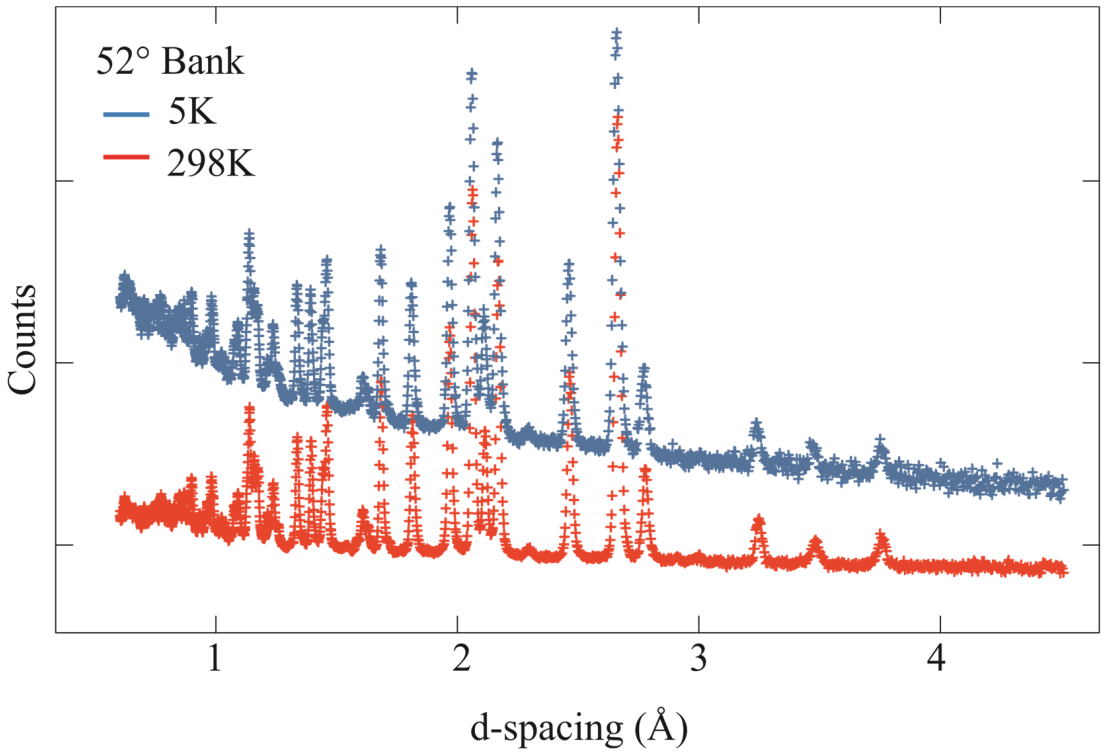


Figure 4-7 Comparison of low-angle NPD data collected from $LaSrCo_{0.5}Rh_{0.5}O_{3.25}$ at 298 K and 5 K.

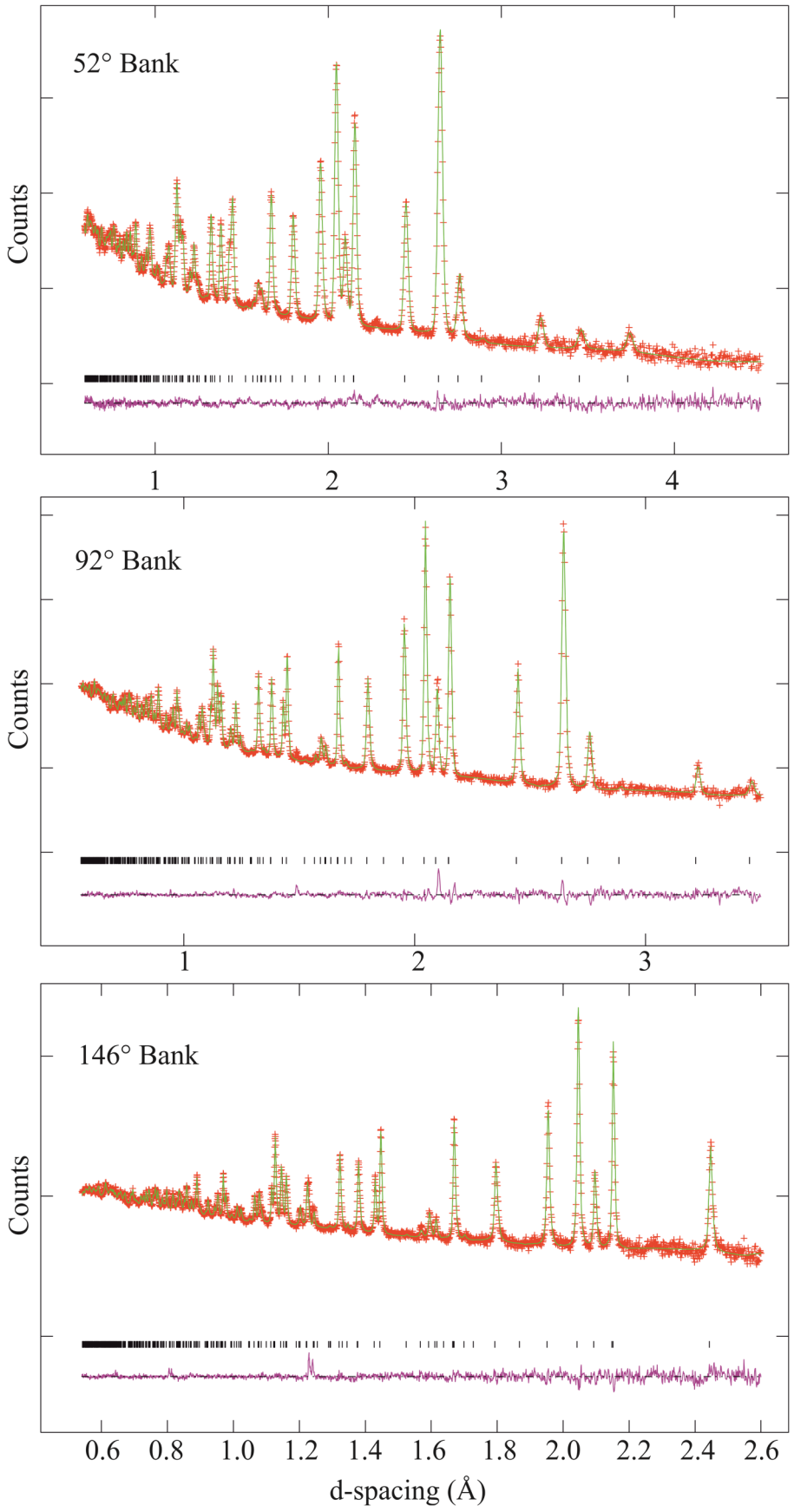


Figure 4-8 Observed, calculated and difference plots from the refinement of $LaSrCo_{0.5}Rh_{0.5}O_{3.25}$ against NPD data collected at 5 K. (The peak at 2.2 Å indicates the peak position of vanadium from the sample container.)

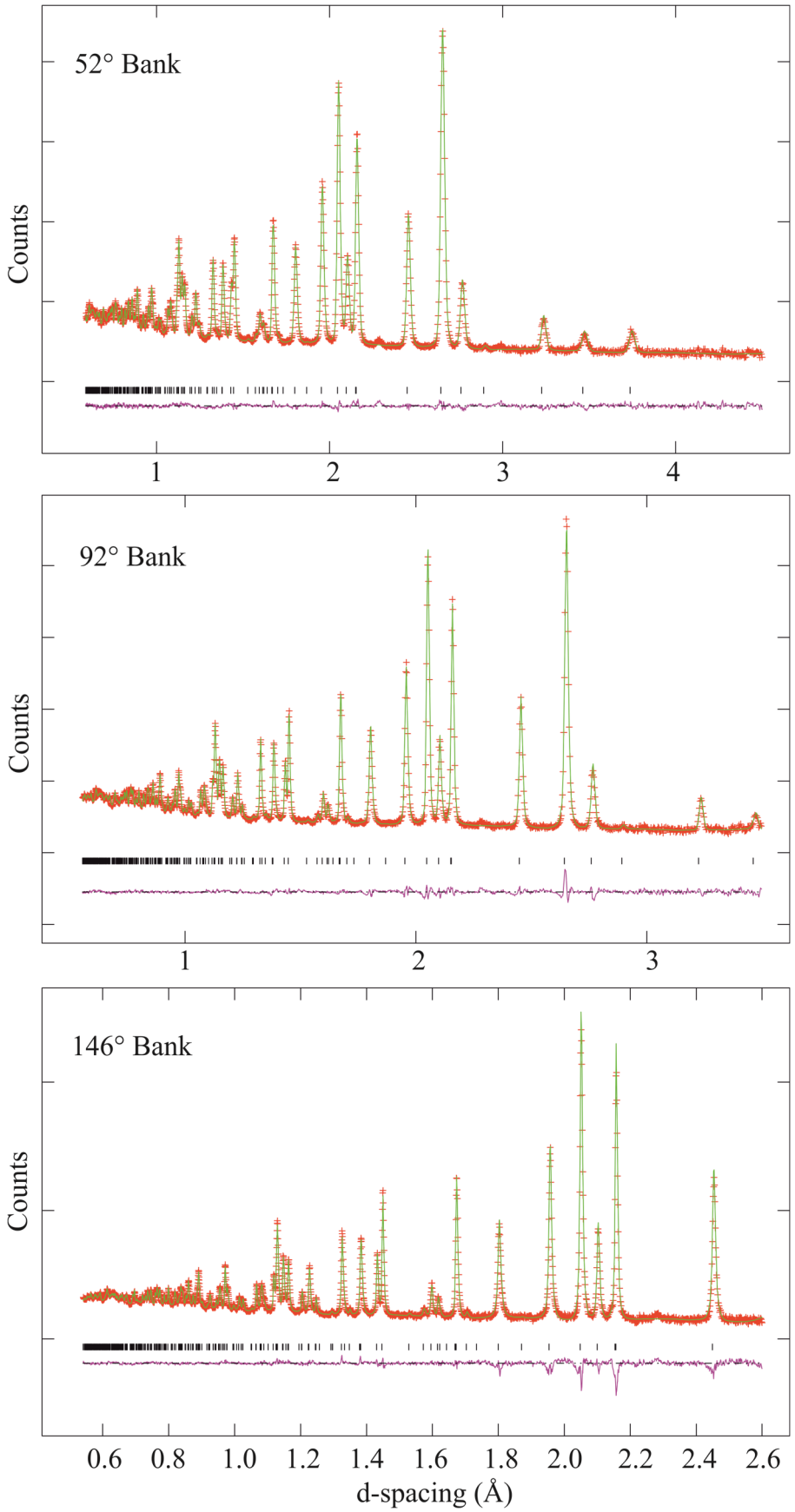


Figure 4-9 Observed, calculated and difference plots from the refinement of $LaSrCo_{0.5}Rh_{0.5}O_{3.25}$ against NPD data collected at 298 K. (The peak at 2.2 Å indicates the peak position of vanadium from the sample container.)

Table 4-2 Structural parameters from the refinement of $LaSrCo0_{.5}Rh_{0.5}O_{3.25}$ against NPD data collected at 5 K.

Atom	Wyckoff Position	*x*	*y*	*z*	Fraction	U_{11} (Å)
La/Sr	4*i*	0	0	0.35727(6)	0.5/0.5	0.0093(5)
Ni/Rh	2*a*	0	0	0	0.5/0.5	0.027(1)
O(1)	4*i*	0	0	0.16768(10)	1	0.0204(8)
O(2)	2*d*	0.045(2)	½	0	0.5	0.007(4)
O(3)	2*b*	½	0	0	0.2612	0.037(4)

$LaSrCo_{0.5}Rh_{0.5}O_{3.25}$ - space group *Immm* (#71)
Formula mass: 359.622 g mol^{-1}, Z = 2
a = 3.5905(1) Å, *b* = 3.9062(2)Å, *c* = 12.9031 (5) Å, Volume = 180.97(2) $Å^3$
Radiation source: Time-of-flight Neutron Powder Diffraction
Temperature: 5 K
χ^2 = 1.384; *wRp* = 1.38 %; *Rp* = 2.23 %.

Table 4-3 Structural parameters from the refinement of $LaSrCo_{0.5}Rh_{0.5}O_{3.25}$ against NPD data collected at 298 K.

Atom	Wyckoff Position	*x*	*y*	*z*	Fraction	U_{11} (Å)
La/Sr	4*i*	0	0	0.35715(4)	0.5/0.5	0.0110(3)
Co/Rh	2*a*	0	0	0	0.5/0.5	0.0264(7)
O(1)	4*i*	0	0	0.16760(7)	1	0.0224(5)
O(2)	2*d*	0.039(4)	½	0	0.5	0.021(5)
O(3)	2*b*	½	0	0	0.2624	0.024(3)

$LaSrCo_{0.5}Rh_{0.5}O_{3.25}$ - space group *Immm* (#71)
Formula mass: 359.642 g mol^{-1}, Z = 2
a = 3.6034(1) Å, *b* = 3.9118(1)Å, *c* = 12.9364(4) Å, Volume = 182.35(1) $Å^3$
Radiation source: Time-of-flight Neutron Powder Diffraction
Temperature: 298 K
χ^2 = 1.976; *wRp* = 2.27 %; *Rp* = 3.26 %.

Table 4-4 Selected bond lengths from the refined structure of $LaSrCo_{0.5}Rh_{0.5}O_{3.25}$ at 298 K (left) and 5 K (right).

Temperature: 298 K			Temperature: 5 K		
Cation	**Anion**	**Length (Å)**	**Cation**	**Anion**	**Length (Å)**
La/Sr	O (1)	2.4521(1) × 1	**La/Sr**	O (1)	2.4463(1) × 1
	O (1)	2.6785(1) × 4		O (1)	2.6723(1) × 4
	O (2)	2.5809(1) × 2		O (2)	2.5719(1) × 2
	O (3)	2.6908(1) × 2		O (3)	2.6845(1) × 2
Co/Rh	O (1)	2.1681(1) × 2	**Co/Rh**	O (1)	2.1636(1) × 2
	O (2)	1.9559(1) × 2		O (2)	1.9531(1) × 2
	O (3)	1.8017(1) × 2		O (3)	1.7953(1) × 2

Table 4-5 Anisotropic displacement factors from refinements of $LaSrCo0_{.5}Rh_{0.5}O_{3.25}$ against NPD data collected at 298 K (top) and 5 K (bottom).

Temperature: 298 K			
Atom	**U_{11}**	**U_{22}**	**U_{33}**
La/Sr	0.01101(32)	0.00936(30)	0.00607(25)
Co/Rh	0.02264(74)	0.00380(59)	0.00598(60)
O (1)	0.02456(51)	0.01031(36)	0.01118(43)
O (2)	0.02097(461)	0.01198(59)	0.01413(57)
O (3)	0.02451(252)	0.01733(203)	0.01184(181)
Temperature: 5 K			
Atom	**U_{11}**	**U_{22}**	**U_{33}**
La/Sr	0.00925(50)	0.00623(47)	0.00605(42)
Co/Rh	0.02733(124)	0.00656(95)	0.00168(86)
O (1)	0.02044(79)	0.00563(56)	0.01109(66)
O (2)	0.00689(405)	0.01173(95)	0.00761(83)
O (3)	0.03701(446)	0.00450(254)	0.00580(245)

NPD data collected from $LaSrNi_{0.5}Rh_{0.5}O_{3.25}$ could also be indexed using a body-centred orthorhombic unit cell, with extinction conditions consistent with the *Immm* space group (No. 71) (shown in Figure 4-10). Therefore, a structural model analogous to that used for $LaSrCo_{0.5}Rh_{0.5}O_{3.25}$ was refined against the data, following the same refinement strategy employed for $LaSrCo_{0.5}Rh_{0.5}O_{3.25}$. Close inspection of the NPD data revealed a series of weak diffraction peaks consistent with a small amount of SrO (1.2 wt %) in the sample, so SrO was added as a second phase to the model. The refinement proceeded smoothly to achieve a good fit (χ^2 = 2.62 for 5 K and χ^2 = 6.38 for 298 K), as shown in Figure 4-12 and Figure 4-13. In the final refinement cycles, the occupancy of the O(3) anion site was refined to a value of 0.231(7) without constraint, consistent with the composition $LaSrNi_{0.5}Rh_{0.5}O_{3.24(1)}$ obtained from TGA data. Full details of the refined structure of $LaSrNi_{0.5}Rh_{0.5}O_{3.25}$ are given in Table 4-6 for 5 K and Table 4-7 for 298 K, with anisotropic displacement factors given in Table 4-9. Selected bond lengths are given in Table 4-8. Figure 4-11 indicates that there are no additional magnetic diffraction features observed at 5 K and hence no long-range magnetic order in $LaSrNi_{0.5}Rh_{0.5}O_{3.25}$.

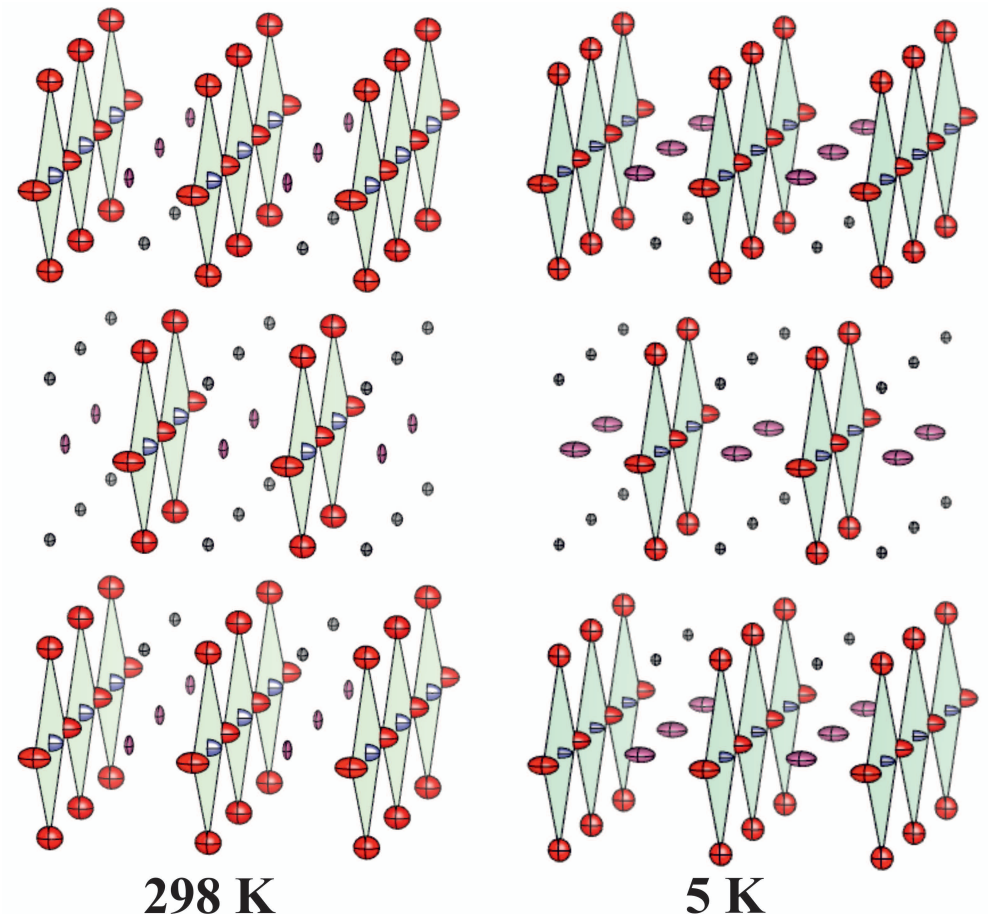


Figure 4-10 The crystal structure of $LaSrNi0_{.5}Rh_{0.5}O_{3.25}$ with displacement ellipsoids at 298 K (left) and 5 K (right).

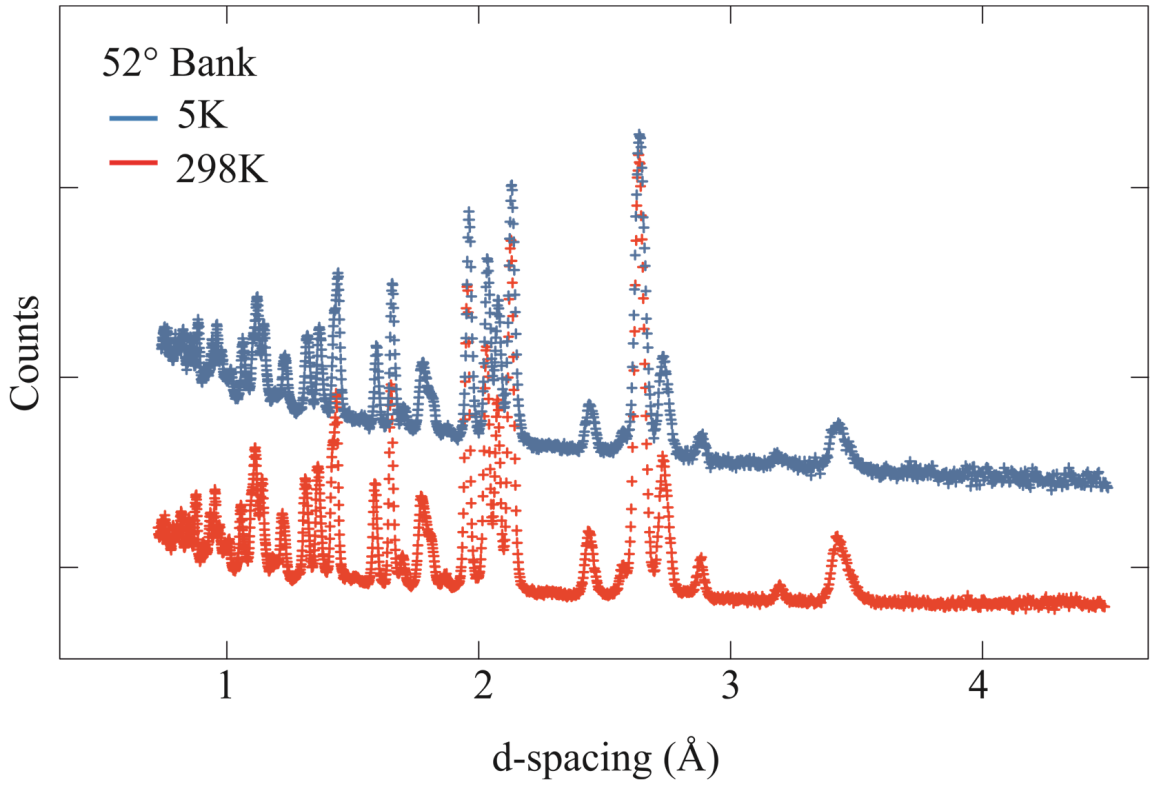


Figure 4-11 Comparison of low-angle NPD data collected from $LaSrNi_{0.5}Rh_{0.5}O_{3.25}$ at 298 K and 5 K.

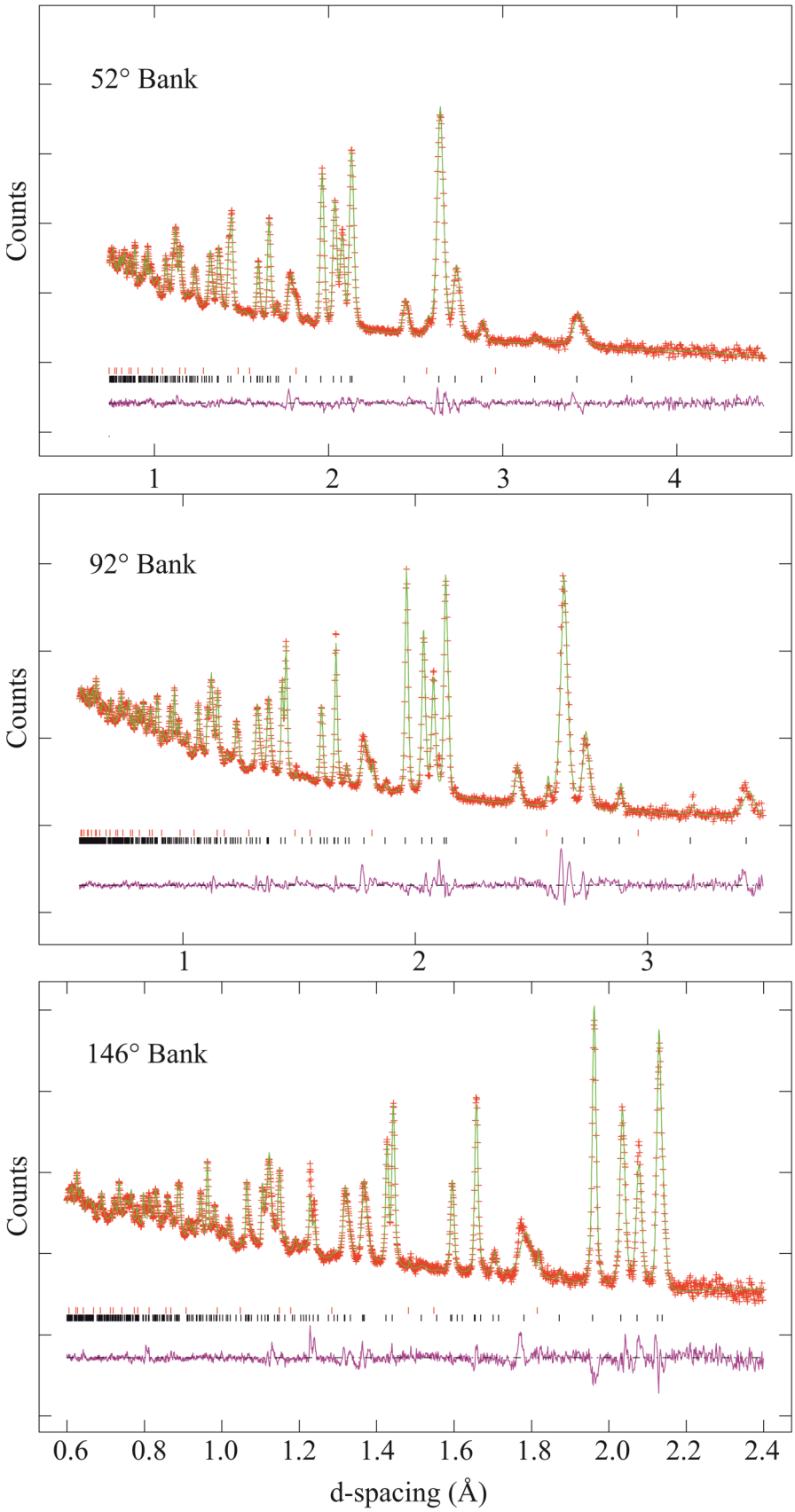


Figure 4-12 Observed, calculated and difference plots from the refinement of $LaSrNi_{0.5}Rh_{0.5}O_{3.25}$ against NPD data collected at 5 K. Black tick marks indicate peak positions of the majority phase ($LaSrNi_{0.5}Rh_{0.5}O_{3.25}$, red tick marks the minority phase (SrO).

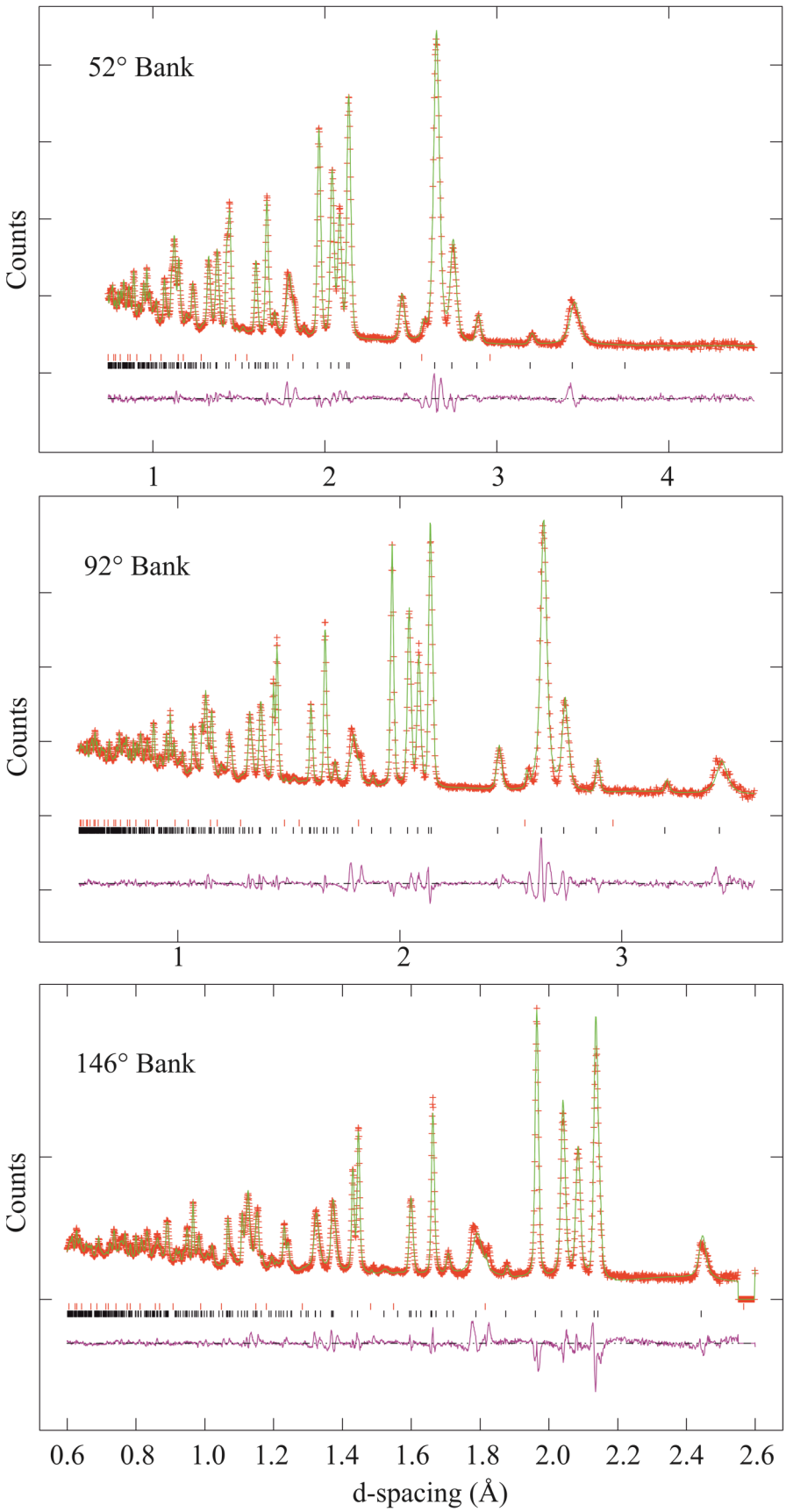


Figure 4-13 Observed, calculated and difference plots from the refinement of $LaSrNi_{0.5}Rh_{0.5}O_{3.25}$ against NPD data collected at 298 K. Black tick marks indicate peak positions of the majority phase ($LaSrNi_{0.5}Rh_{0.5}O_{3.25}$), red tick marks the minority phase (SrO).

Table 4-6 Structural parameters from the refinement of $LaSrNi_{0.5}Rh_{0.5}O_4$ against NPD data collected at 5 K.

Atom	Wyckoff Position	*x*	*y*	*z*	Fraction	U_{11} (Å)
La/Sr	4*i*	0	0	0.3582(1)	0.5/0.5	0.0022(7)
Ni/Rh	2*a*	0	0	0	0.5/0.5	0.0182(9)
O(1)	4*i*	0	0	0.1673(1)	1	0.012(1)
O(2)	2*d*	0	½	0	1	0.024(2)
O(3)	2*b*	½	0	0	0.2503	0.023(6)

$LaSrNi_{0.5}Rh_{0.5}O_{3.25}$ - space group *Immm* (#71)
Formula mass: 359.33 g mol^{-1}, Z = 2
a = 3.5653(3) Å, *b* = 3.9207(3)Å, *c* = 12.7655 (8) Å, Volume = 178.44(3) $Å^3$
Radiation source: Time-of-flight Neutron Powder Diffraction
Temperature: 5 K
χ^2 = 2.617; *wRp* = 1.73 %; *Rp* = 2.66 %.

Table 4-7 Structural parameters from the refinement of $LaSrNi_{0.5}Rh_{0.5}O_{3.25}$ against NPD data collected at 298 K.

Atom	Wyckoff Position	*x*	*y*	*z*	Fraction	U_{11} (Å)
La/Sr	4*i*	0	0	0.3580(1)	0.5/0.5	0.0029(6)
Ni/Rh	2*a*	0	0	0	0.5/0.5	0.0198(8)
O(1)	4*i*	0	0	0.1674(1)	1	0.0181(9)
O(2)	2*d*	0	½	0	1	0.028(1)
O(3)	2*b*	½	0	0	0.2317	0.002 (4)

$LaSrNi_{0.5}Rh_{0.5}O_{3.25}$ - space group *Immm* (#71)
Formula mass: 359.032 g mol^{-1}, Z = 2
a = 3.5801 (2) Å, *b* = 3.9265(2)Å, *c* = 12.8071(6) Å, Volume = 180.04(3) $Å^3$
Radiation source: Time-of-flight Neutron Powder Diffraction
Temperature: 298 K
χ^2 = 6.376; *wRp* = 3.87%; *Rp* = 5.65 %.

Table 4-8 Selected bond lengths from the refined structure of $LaSrNi_{0.5}Rh_{0.5}O_{3.25}$ at 298 K (left) and 5 K (right).

Temperature: 298 K			Temperature: 5 K		
Cation	**Anion**	**Length (Å)**	**Cation**	**Anion**	**Length (Å)**
La/Sr	O (1)	2.4411(1) × 1	**La/Sr**	O (1)	2.4366(2) × 1
	O (1)	2.6767(1) × 4		O (1)	2.6696(1) × 4
	O (2)	2.5516(1) × 2		O (2)	2.5407(1) × 2
	O (3)	2.6760(1) × 2		O (3)	2.6684(1) × 2
Ni/Rh	O (1)	2.1441(1) × 2	**Ni/Rh**	O (1)	2.1358(1) × 2
	O (2)	1.9633(1) × 2		O (2)	1.9604(1) × 2
	O (3)	1.7901(1) × 2		O (3)	1.7827(1) × 2

Table 4-9 Anisotropic displacement factors from refinements of $LaSrNi_{0.5}Rh_{0.5}O_{3.25}$ NPD data collected at 298 K (top) and 5 K (bottom).

Temperature: 298 K			
Atom	**U_{11}**	**U_{22}**	**U_{33}**
La/Sr	0.00289(56)	0.00850(46)	0.00429(37)
Ni/Rh	0.01983(78)	0.00253(57)	0.00752(61)
O (1)	0.01806(87)	0.00824(49)	0.01441(71)
O (2)	0.02834(134)	0.00967(72)	0.01138(77)
O (3)	0.00192(405)	0.01076(281)	0.00947(275)
Temperature: 5 K			
Atom	**U_{11}**	**U_{22}**	**U_{33}**
La/Sr	0.00224(67)	0.00558(51)	0.00314(44)
Ni/Rh	0.01816(87)	0.00219(64)	0.00262(63)
O (1)	0.01238(96)	0.00395(53)	0.01303(79)
O (2)	0.02402(157)	0.01066(81)	0.00829(82)
O (3)	0.02312(630)	0.02245(396)	0.00549(296)

4.3.3. X-ray Photoelectron Spectroscopy of LaSr$M_{0.5}Rh_{0.5}O_{3.25}$ (M = Co, Ni)

X-ray photoelectron spectroscopy (XPS) data collected from $LaSrCo_{0.5}Rh_{0.5}O_{3.25}$ and $LaSrNi_{0.5}Rh_{0.5}O_{3.25}$ are shown in Figure 4-14. It is clear that the Rh $3d_{5/2}$ and Rh $3d_{3/2}$ emission peaks for both reduced compounds are split, corresponding to the presence of two Rh oxidation states. The Rh 3d spectra were fitted with one doublet representing each Rh oxidation state. For each doublet, 70% Gaussian 30% Lorentzian components were utilized, and Rh $3d_{5/2}$ and Rh $3d_{3/2}$ emissions were constrained in area in a 3:2 ratio. The doublet separation was fixed at 4.71 eV. The two components of each doublet were initially constrained to have equal fwhm, and after a reasonable fitting was achieved, the $3d_{3/2}$ fwhm was allowed to increase slightly to account for the Coster−Kronig broadening expected in this core line[83]. For $LaSrCo_{0.5}Rh_{0.5}O_{3.25}$, we find Rh $3d_{5/2}$ components with binding energies of 307.0 and 308.3 eV. Analogous to $LaSrCo_{0.5}Rh_{0.5}O_{3.25}$, for $LaSrNi_{0.5}Rh_{0.5}O_{3.25}$, we find Rh $3d_{5/2}$ components at binding energies of 307.0 and 308.4 eV. In both cases, the lower binding-energy component has a lower fwhm. This has been seen previously with rhodium-containing compounds.[84] In each case, the higher-energy component (308.3 eV and 308.4 eV) matches well with Rh_2O_3, so we can assign this peak as Rh^{III}[84]. The peak close to 307 eV is in the region reported for rhodium metal, although our model does not require asymmetric components that are present in elemental rhodium. Rh^{I} molecular compounds have been reported with Rh $3d_{5/2}$ binding energy of 307.3 eV[85], but we are not aware of XPS studies of any rhodium oxides containing Rh^{I}. It is certainly possible that the Rh^{I} oxide peak will be at similar binding energy to the Rh metal peak, as is seen in other late transition metals such as Ag and Cu[86]. For both samples, the areas of the Rh^{I} and Rh^{III} doublets were constrained to be equal. These constraints led to a good fit to the data, and there are similar values of binding energy and fwhm across the two samples, showing that the presence of an equal amount of Rh^{I} and Rh^{III} is consistent with the XPS measurements.

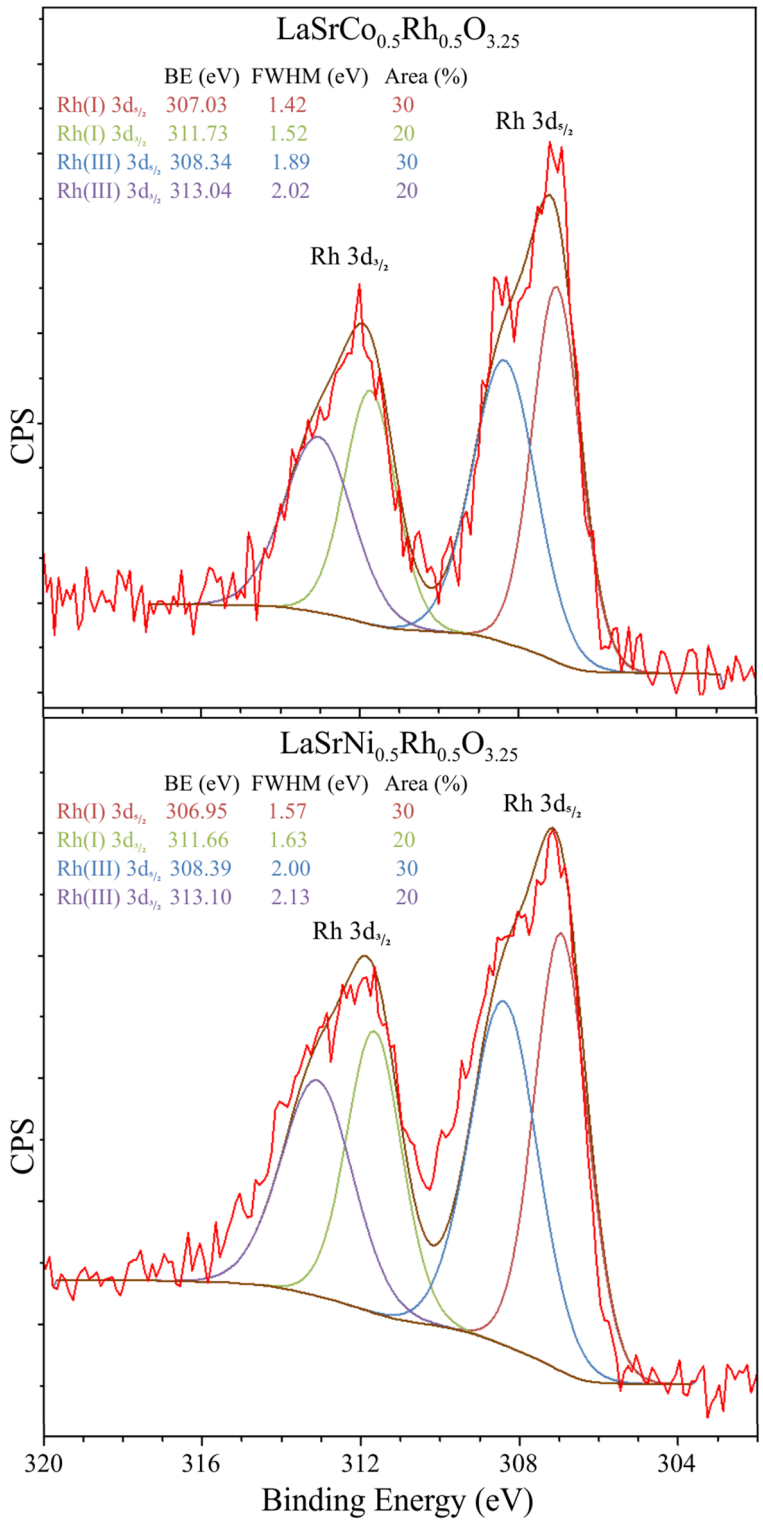


Figure 4-14 XPS collected from $LaSrCo_{0.5}Rh_{0.5}O_{3.25}$ (top) and $LaSrNi_{0.5}Rh_{0.5}O_{3.25}$ (bottom). Peaks from the Rh $3d_{5/2}$ and Rh $3d_{3/2}$ emissions are fit by two components each, corresponding to Rh^{I} and Rh^{III}.

4.3.4. Magnetic Characterisation of LaSrM0.5Rh0.5O3.25 (M = Co, Ni)

Magnetization data collected from $LaSrCo_{0.5}Rh_{0.5}O_{3.25}$ and $LaSrNi_{0.5}Rh_{0.5}O_{3.25}$ at room temperature indicate that samples contain small amounts (< 0.1 wt%) of ferromagnetic Co and Ni, respectively. Therefore, magnetization data were collected using a 'ferromagnetic subtraction' technique described in Section 2.5.3, which utilizes the fact that the magnetization of Co and Ni can saturate in the applied field which is greater than 2 T.

Figure 4-15 shows that the paramagnetic susceptibility of $LaSrCo_{0.5}Rh_{0.5}O_{3.25}$ follows the modified Curie-Weiss law ($\chi = C/(T - \theta) + K$) in the temperature range $75 < T/K < 300$. The fit of susceptibility data to the Curie-Weiss law yields values of C = 0.083(2) cm^3 K mol^{-1}, $\theta = -5.62(2)$ K and $K = 1.20(3) \times 10^{-3}$ cm^3 mol^{-1}. Below 75 K, the saturated ferromagnetic moment of $LaSrCo_{0.5}Rh_{0.5}O_{3.25}$ increases sharply, and the susceptibility exhibits a maximum at T = 10 K. These features of the data are consistent with a change to a magnetically ordered state below $T \sim 75$ K.

Magnetization data collected from $LaSrNi_{0.5}Rh_{0.5}O_{3.25}$ shown in Figure 4-16 are qualitatively similar to the data from $LaSrCo_{0.5}Rh_{0.5}O_{3.25}$. The fit of susceptibility data to the Curie-Weiss law in the temperature range $25 < T/K < 300$ yields values of C = 0.091(2) cm^3 K mol^{-1}, $\theta = -20.10(7)$ K and $K = 2.04(9) \times 10^{-4}$ cm^3 mol^{-1}. Below 25 K, there is also a sharp increase in the saturated ferromagnetic moment of $LaSrNi_{0.5}Rh_{0.5}O_{3.25}$. Again, these features of the data are consistent with a change to a magnetically ordered state below $T \sim 25$ K.

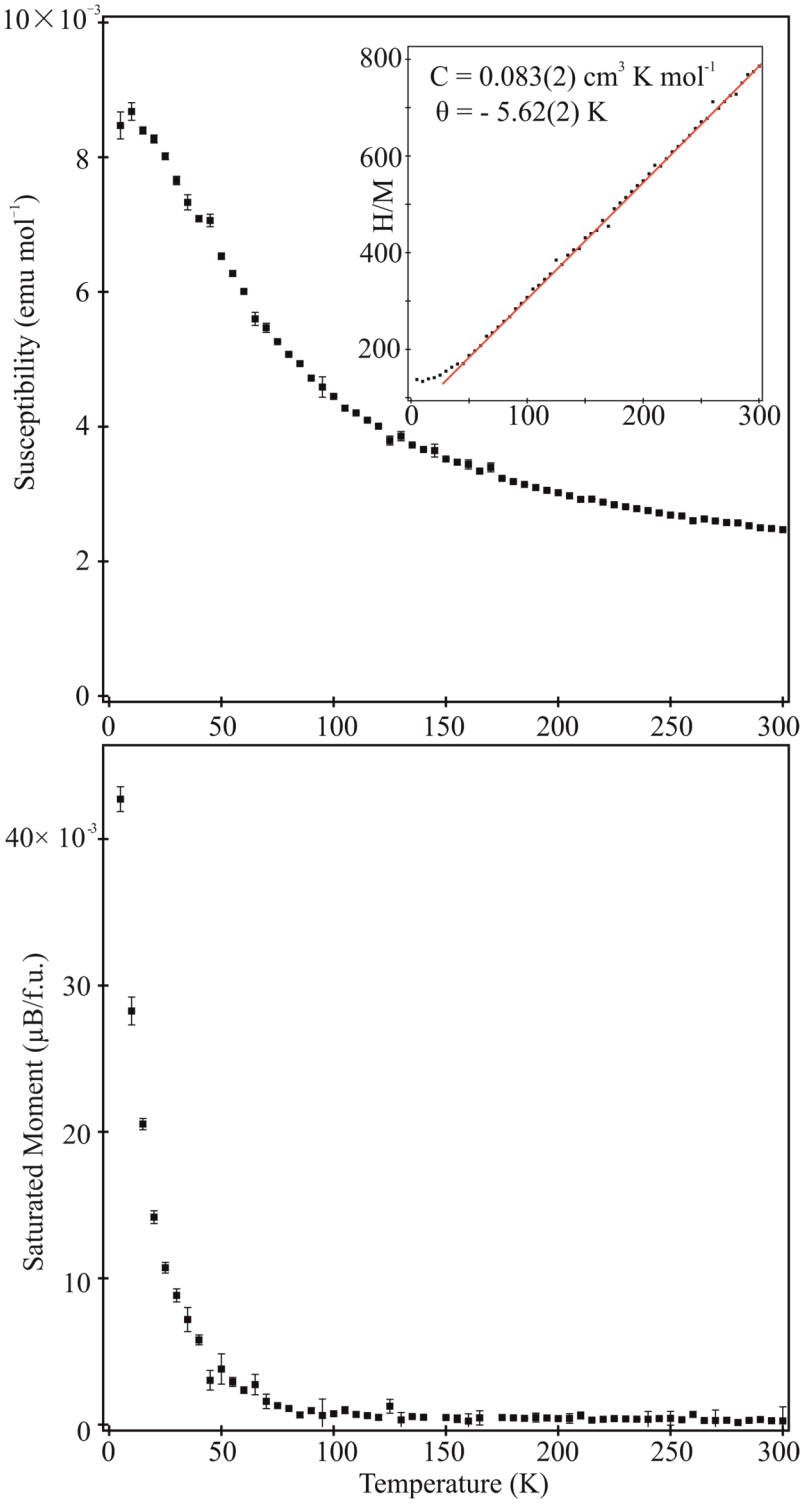


Figure 4-15 The paramagnetic susceptibility (top) and saturated ferromagnetic moment (bottom) of $LaSrCo_{0.5}Rh_{0.5}O_{3.25}$ collected as a function of temperature. Inset: the fit to the Curie-Weiss law in the temperature range 50 < *T*/K < 300.

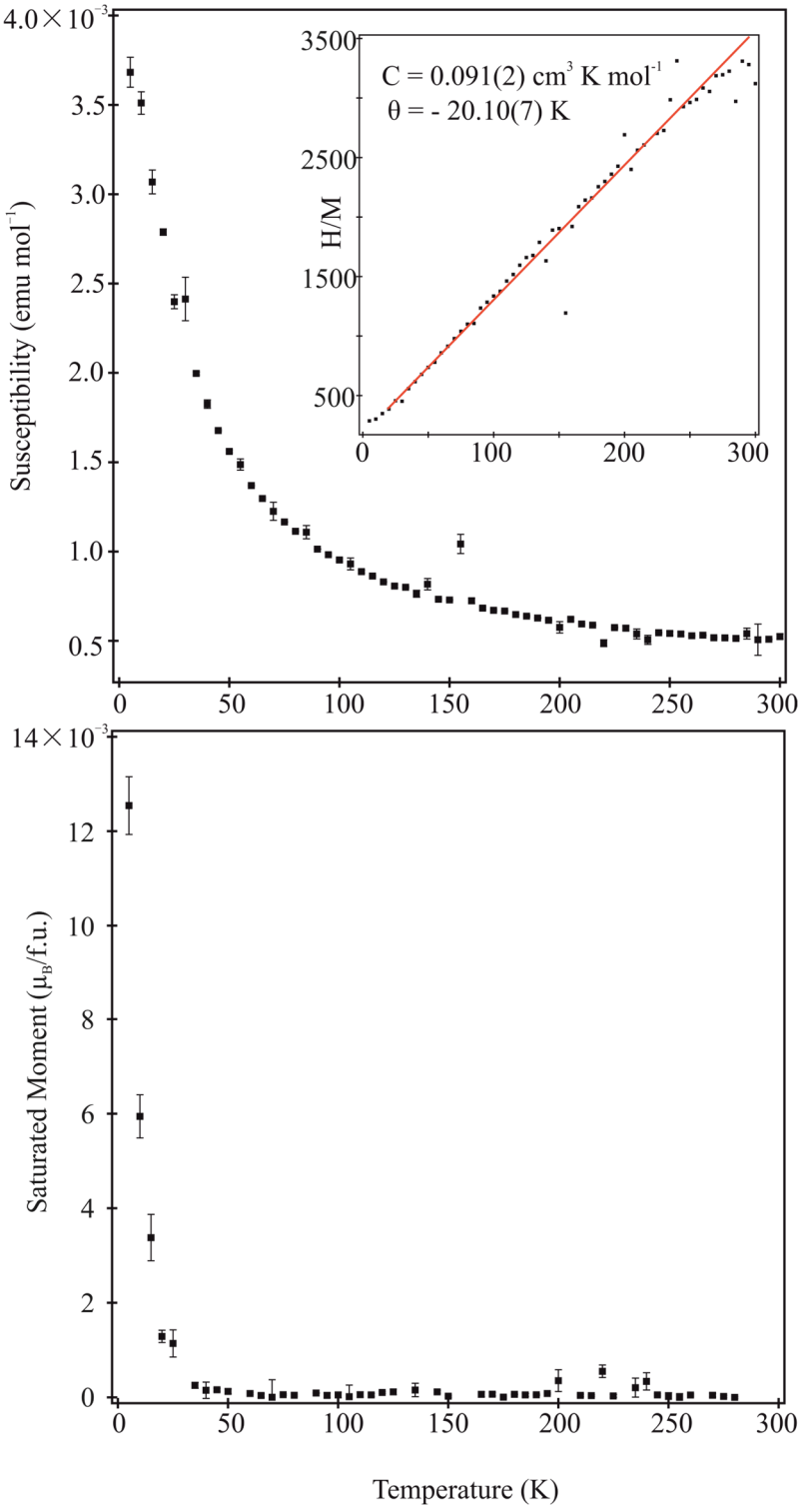


Figure 4-16 The paramagnetic susceptibility (top) and saturated ferromagnetic moment (bottom) of $LaSrNi_{0.5}Rh_{0.5}O_{3.25}$ collected as a function of temperature. Inset: the fit to the Curie-Weiss law in the temperature range 15 < *T*/K < 300.

The addition of a weak ferromagnetic component to the magnetization of $LaSrCo_{0.5}Rh_{0.5}O_{3.25}$ and $LaSrNi_{0.5}Rh_{0.5}O_{3.25}$, at 75 and 25 K, respectively, suggests that these materials adopt either a canted antiferromagnetic state or a spin-glass state at low temperature. NPD data collected from $LaSrCo_{0.5}Rh_{0.5}O_{3.25}$ and $LaSrNi_{0.5}Rh_{0.5}O_{3.25}$ at 5 K show no evidence for long-range magnetic order (Figure 4-7 and Figure 4-11). This made the possibility of a canted antiferromagnetic state less likely. In addition, the magnetisation-field data collected from $LaSrCo_{0.5}Rh_{0.5}O_{3.25}$ at 5 K in Figure 4-17 (left) shows an obvious shift from the origin point. We therefore believe that it is likely that the changes in magnetic behaviour observed at 75 K for $LaSrCo_{0.5}Rh_{0.5}O_{3.25}$ is the transition to a spin-glass state. The magnetisation-field data collected from $LaSrNi_{0.5}Rh_{0.5}O_{3.25}$ in Figure 4-17 (right) indicates paramagnetic behaviour at 298 K and weak ferromagnetic behaviour at 5 K. It is likely that the changes in magnetic behaviour observed at 25 K for $LaSrNi_{0.5}Rh_{0.5}O_{3.25}$ is also the transition to a spin-glass state. However, the presence of the ferromagnetic impurities prevents this from being established definitively via magnetization measurements.

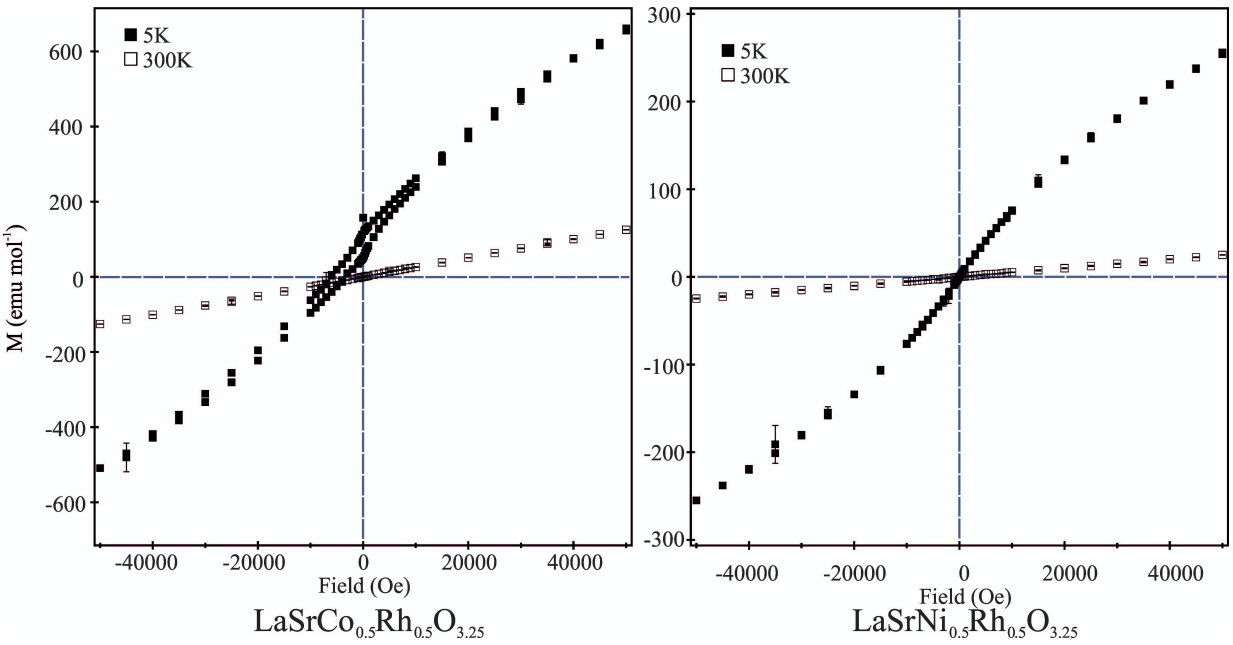


Figure 4-17 Magnetisation data collected as a function of applied field from $LaSrCo_{0.5}Rh_{0.5}O_{3.25}$ (left) and $LaSrNi_{0.5}Rh_{0.5}O_{3.25}$ (right).

4.4. Discussion

4.4.1. Structure Analysis of LaSr$M_{0.5}$Rh$_{0.5}$O$_{3.25}$ (M = Co, Ni)

Topochemical reduction of LaSr$M_{0.5}$Rh$_{0.5}$O$_4$ (M = Co, Ni) with a Zr oxygen getter yields LaSr$M_{0.5}$Rh$_{0.5}$O$_{3.25}$ (M = Co, Ni) phases as shown schematically in Figure 4-18. The principal difference between LaSr$M_{0.5}$Rh$_{0.5}$O$_4$ and LaSr$M_{0.5}$Rh$_{0.5}$O$_{3.25}$ is the partial occupancy of the O(3) anion site marked in pink in Figure 4-18. The reduction converts the (M/Rh)O$_6$ octahedra present in LaSr$M_{0.5}$Rh$_{0.5}$O$_4$ into a 1:1 disordered array of 5-coordinate, square-based pyramidal (M/Rh)O$_5$ units and 4-coordinate, square-planar (M/Rh)O$_4$ units in LaSr$M_{0.5}$Rh$_{0.5}$O$_{3.25}$. In the B-site network of LaSr$M_{0.5}$Rh$_{0.5}$O$_{3.25}$, M and Rh cations randomly occupy a 1:1 ratio of square-based pyramidal sites (C$_{4v}$) and square-planar sites (D$_{4h}$).

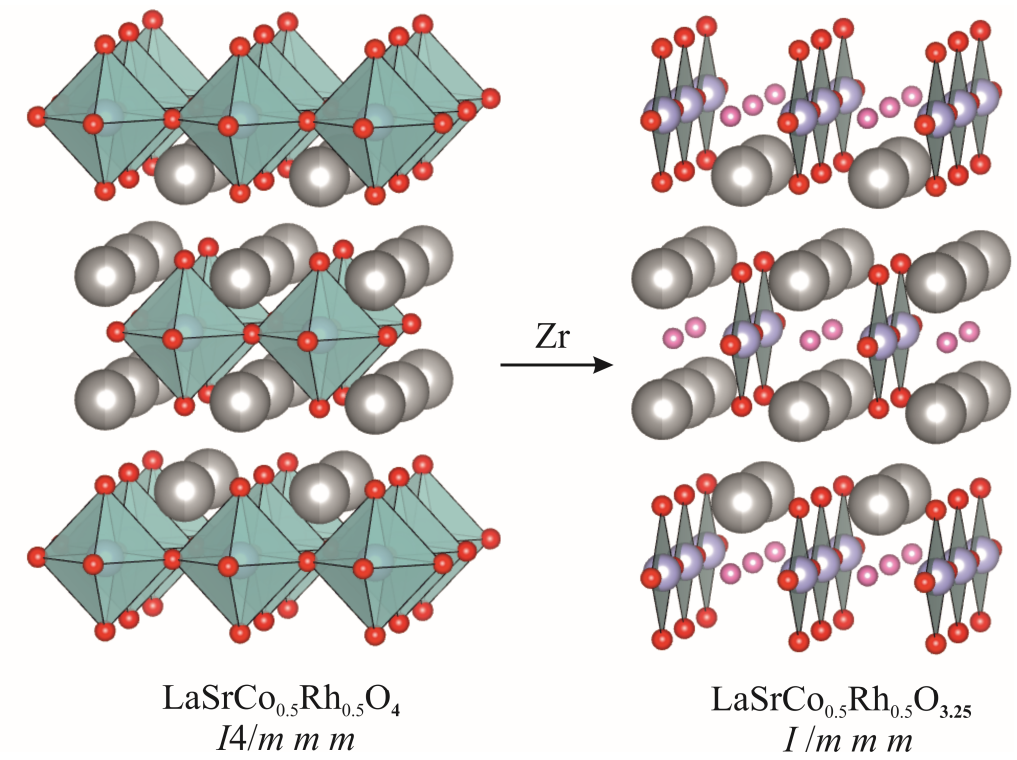


Figure 4-18 A schematic presentation of the conversion from LaSr$M_{0.5}$Rh$_{0.5}$O$_4$ to LaSr$M_{0.5}$Rh$_{0.5}$O$_{3.25}$ (M = Co, Ni). Grey, blue, red, and pink spheres represent La/Sr, M/Rh, O, and partially occupied O positions, respectively.

4.4.2. Disproportionation of Rh^{II} in $LaSrM_{0.5}Rh_{0.5}O_{3.25}$ (M = Co, Ni)

The $LaSrM_{0.5}Rh_{0.5}O_{3.25}$ stoichiometry of the reduced phases means that the *B*-site cations (*M* and Rh) have a summed charge of +3, suggesting two possible oxidation-state combinations: $(Co/Ni)^{I}/Rh^{II}$ and $(Co/Ni)^{II}/Rh^{I}$.

The possibility of $(Co/Ni)^{I}/Rh^{II}$ combination is discussed as follows. As discussed in Section 4.4.1, *B*-site cations randomly occupy D_{4h} and C_{4v} sites. The spin-only calculation of the expected magnetic moments of $LaSrM_{0.5}Rh_{0.5}O_{3.25}$ (M = Co, Ni) for different spin-state combinations in the scenario of $(Co/Ni)^{I}/Rh^{II}$ are shown in Figure 4-19.

For $LaSrCo_{0.5}Rh_{0.5}O_{3.25}$, if Co^{I} in D_{4h} sites exhibit a low-spin (LS) state then the combination Co^{I} (LS in D_{4h})/Rh^{II} is expected to provide a value of C = 0.4375 cm^3 K mol^{-1}; if Co^{I} in D_{4h} sites exhibit a high-spin (HS) state, the combination Co^{I} (HS in D_{4h})/Rh^{II} is expected to provide a value of C = 0.6875 cm^3 K mol^{-1}. However, both of the values are much larger than the experimental data 0.083 cm^3 K mol^{-1} extracted from magnetization data of $LaSrCo_{0.5}Rh_{0.5}O_{3.25}$.

For $LaSrNi_{0.5}Rh_{0.5}O_{3.25}$, the predicted Curie constant for a Ni^{I}/Rh^{II} combination is 0.375 cm^3 K mol^{-1}, which is also higher than the observed value of 0.091 cm^3 K mol^{-1} extracted from magnetization data of $LaSrNi_{0.5}Rh_{0.5}O_{3.25}$.

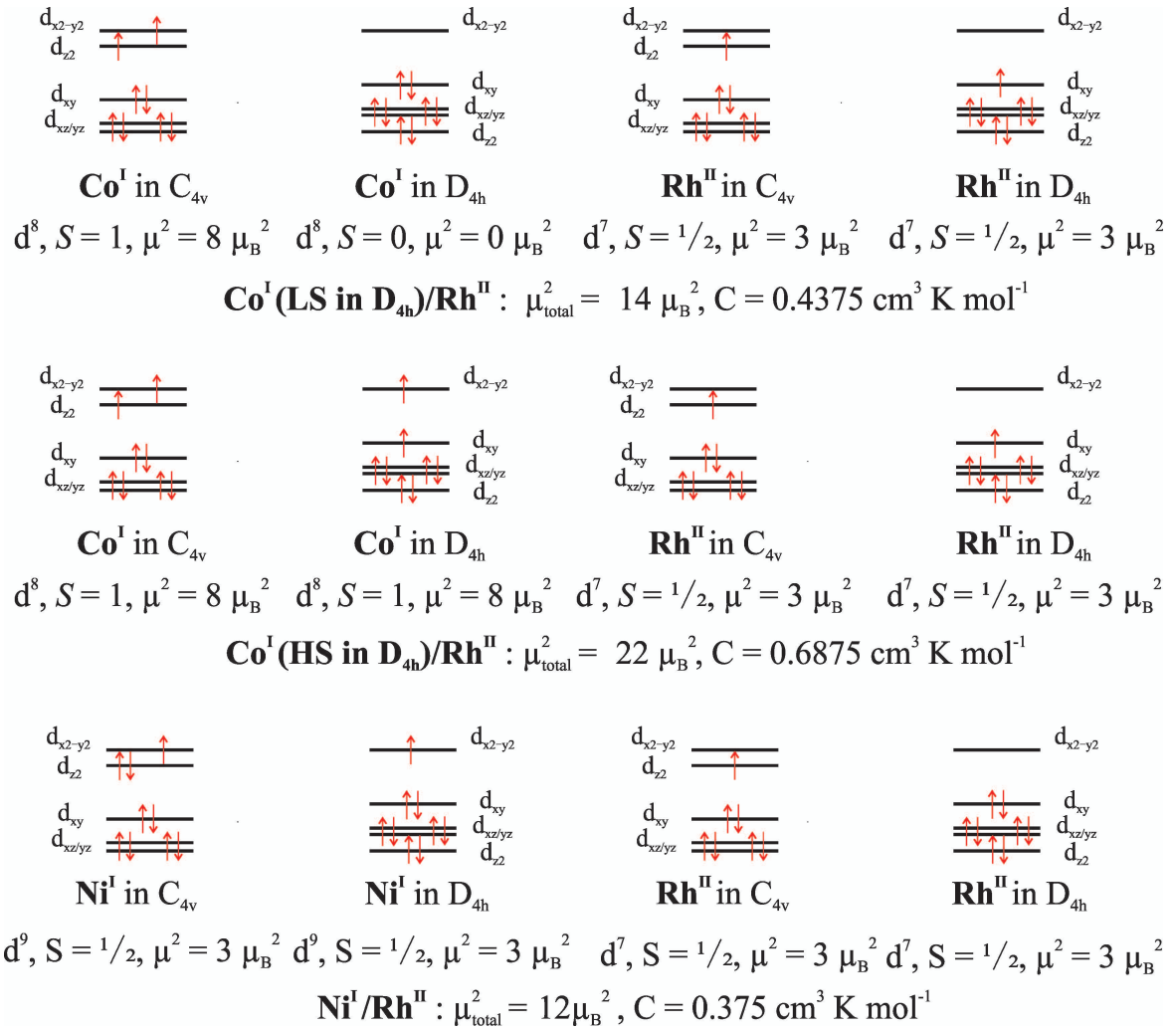


Figure 4-19 Predicted Curie constants of LaSr$M_{0.5}$Rh$_{0.5}$O$_{3.25}$ (M = Co, Ni) for M^{I}/Rh^{II} oxidation-state combination.

The possibility of (Co/Ni)^{II}/Rh^{I} combination is discussed as follows. The spin-only calculation of the expected magnetic moments of LaSr$M_{0.5}$Rh$_{0.5}$O$_{3.25}$ (M = Co, Ni) for different spin-state combinations in the scenario of (Co/Ni)^{II}/Rh^{I} are shown in Figure 4-20.

For LaSrCo$^{II}_{0.5}$Rh$^{I}_{0.5}$O$_{3.25}$, the combination is expected to yield a value of C = 0.4375 cm^3 K mol^{-1} which is also much larger than the experimental data 0.083 cm^3 K mol^{-1}.

For LaSrNi$^{II}_{0.5}$Rh$^{I}_{0.5}$O$_{3.25}$, the combination Ni^{II} (LS in D$_{4h}$)/Rh^{I} is expected to provide a value of C = 0.5 cm^3 K mol^{-1}, and the combination Ni^{II} (HS in D$_{4h}$)/Rh^{I} is expected to provide a value of C = 0.75 cm^3 K mol^{-1}. Again, both of the values are more than 5 times of the observed magnetisation data from LaSrNi$_{0.5}$Rh$_{0.5}$O$_{3.25}$. Thus, the (Co/Ni)^{II}/Rh^{I} combination can be discounted.

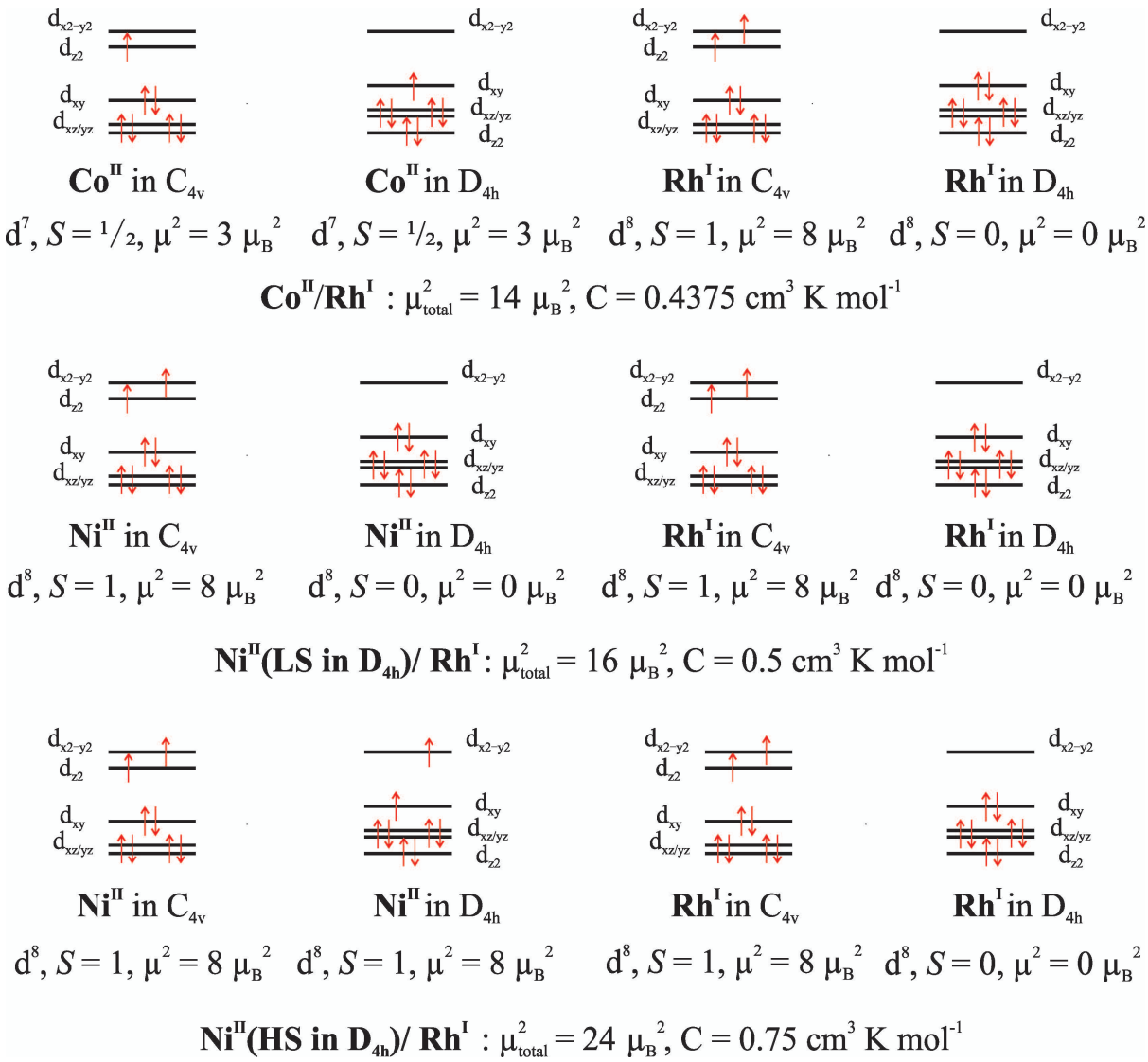


Figure 4-20 Predicted Curie constants of $LaSrM_{0.5}Rh_{0.5}O_{3.25}$ (M = Co, Ni) for M^{II}/Rh^{I} oxidation-state combination.

Resistivity measurements performed on cold-pressed powder samples indicate that both $LaSrCo_{0.5}Rh_{0.5}O_{3.25}$ and $LaSrNi_{0.5}Rh_{0.5}O_{3.25}$ are highly insulating, eliminating itinerant electronic behaviour as an explanation for the low moments. The very small magnetic moment observed for both reduced phases suggests that there is only a modest contribution from rhodium centres. In addition, the clear splitting of the Rh 3d XPS peaks observed in both $LaSrCo_{0.5}Rh_{0.5}O_{3.25}$ and $LaSrNi_{0.5}Rh_{0.5}O_{3.25}$ indicates two split components assigned to Rh^{III} and Rh^{I} separately.

Thus, we can propose a scenario in which the Co/Ni cations are in a monovalent oxidation state and the nominal Rh^{II} cations have disproportionated into a 1:1 ratio of Rh^{I} and Rh^{III} which are located within C_{4v} and D_{4h} sites, respectively, both with $S = 0$ electronic configurations as shown in Figure 4-21. The primary drive for this disproportionation is attributed to the crystal-field stabilization energy gained by d^8, $S = 0$ Rh^{I} in D_{4h} sites and d^6, $S = 0$ Rh^{III} in C_{4v} sites, which is advantageous compared to locating d^7 Rh^{II} in these two sites.

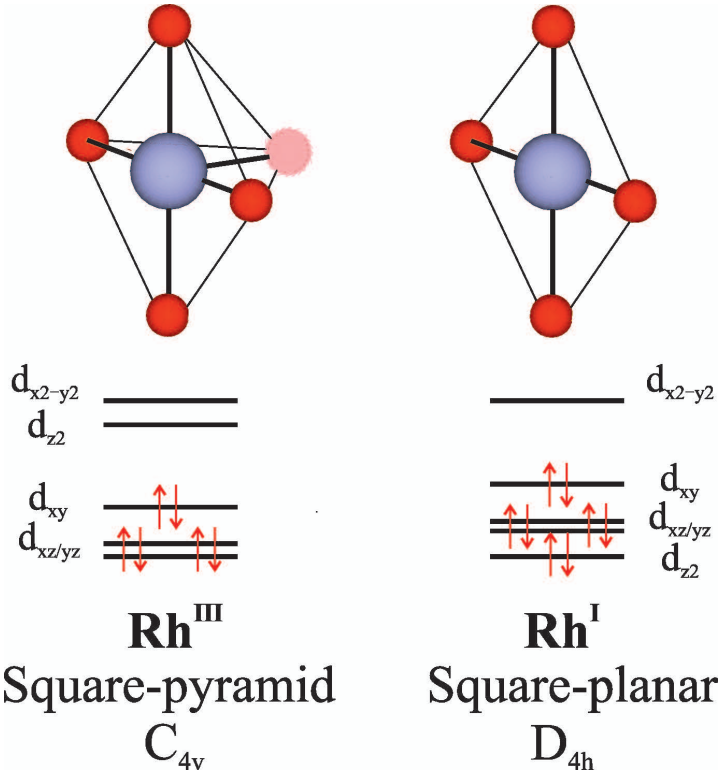


Figure 4-21 Square-based pyramidal and square-planar transition-metal coordination sites in $LaSrM_{0.5}Rh_{0.5}O_{3.25}$ (M = Co, Ni) with local electronic configurations of d^6 Rh^{III} and d^8 Rh^{I} in C_{4v} and D_{4h} sites, respectively.

As shown in Figure 4-22, these combinations containing disproportionated Rh^{II} are expected to yield values of C = 0.1875 cm^3 K mol^{-1} when M = Ni, and either 0.25 or 0.5 cm^3 K mol^{-1} when M = Co (depending on the spin state adopted by Co^{I} in D_{4h} sites). These values are in broad agreement with the observed values 0.091(2) cm^3 K mol^{-1} ($LaSrNi_{0.5}Rh_{0.5}O_{3.25}$) and 0.083(2) cm^3 K mol^{-1} ($LaSrCo_{0.5}Rh_{0.5}O_{3.25}$), respectively.

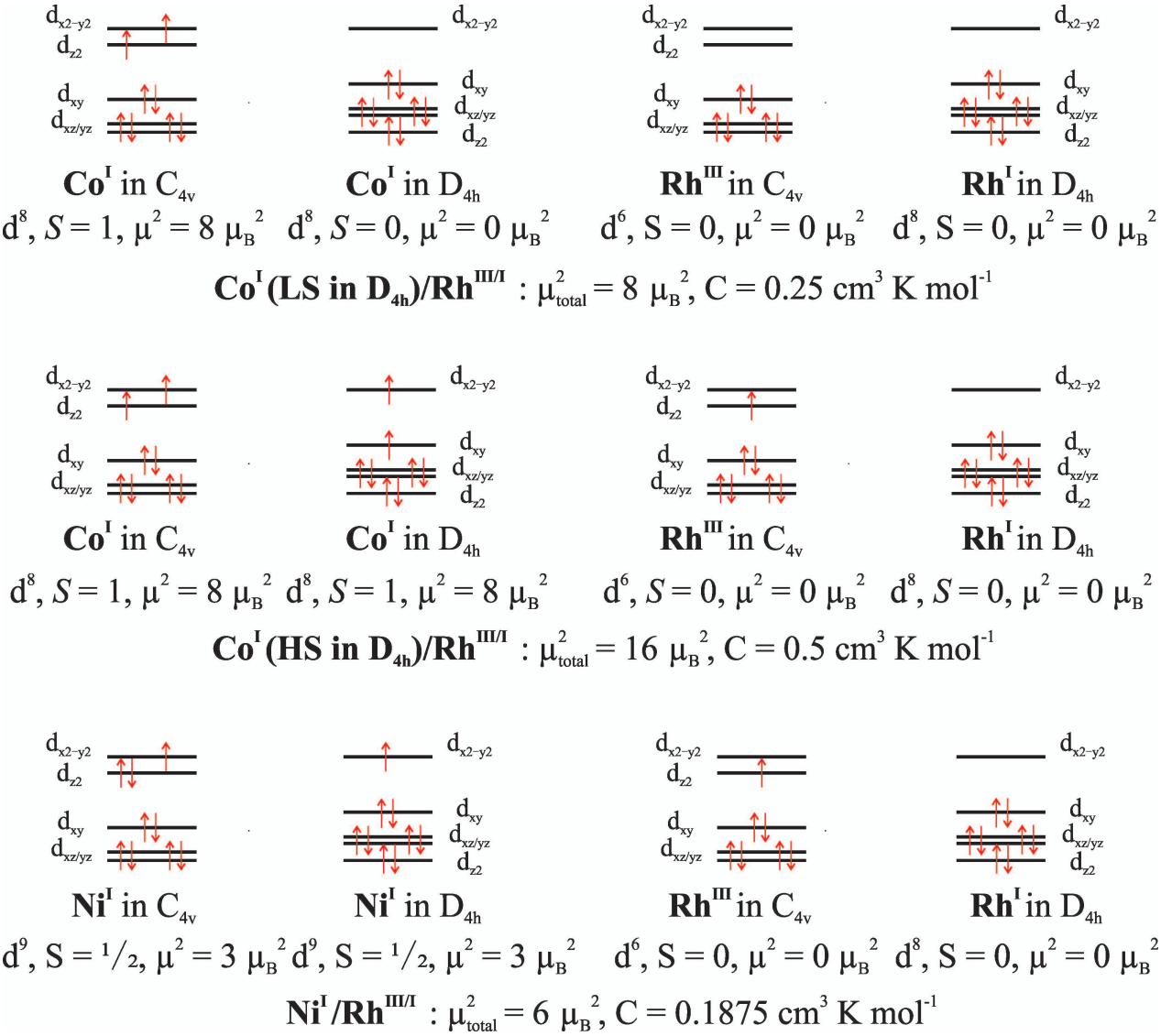


Figure 4-22 Predicted Curie constants of LaSr$M_{0.5}$Rh$_{0.5}$O$_{3.25}$ (M = Co, Ni) for M^{I}, Rh$^{I/III}$ oxidation-state combination.

Analogous disproportionation to "avoid" oxidation states with d^7 electron counts are observed for other 4d and 5d transition metals as well. For example, KPd_2O_3 has an average Pd oxidation state of $Pd^{2.5+}$, suggesting a mixture of Pd^{II} and Pd^{III}[87]. However, close inspection of the crystal structure of this compound reveals that it is better formulated as $K_2Pd^{II}_3\ Pd^{IV}O_6$, with d^8 Pd^{II} located in square-planar $Pd^{II}O_4$ units and d^6 Pd^{IV} located in octahedral $Pd^{IV}O_6$ units. Likewise, $BiPd_2O_4$[88] and $Ba_2Hg_3Pd_7O_{14}$[89] are better formulated as

$Bi_2Pd^{II}_3Pd^{IV}O_8$ and $Ba_2Hg_3Pd^{II}_5Pd^{IV}_2O_{14}$ based on their crystal structures, which also contain distinct $Pt^{II}O_4$ and $Pd^{IV}O_6$ units. Similar behaviour is also observed for 5d transition metals such as platinum, with octahedral $Pt^{IV}O_6$ and square-planar $Pt^{II}O_4$ units observed in a wide range of $M^{II}Pt^{II}Pt^{IV}_2O_6$ (M = Cd, Mn, Co, Zn, Ni, Mg) oxides[90],[91].

Unlike Pd or Pt, to date analogous charge-separated $Ir^{I/III}$ oxides have not been prepared. Reported topochemically reduced iridium oxides such as Sr_2FeIrO_4 and $Sr_2Co_{0.5}Ir_{0.5}O_3$ are observed to contain d^7 Ir^{II} cations in square-planar coordination sites[92],[93], indicating that Ir^{II} is easier to prepare compared to Rh^{II}. However, it is hard to say anything comprehensive about the different behaviour of reduced compounds containing Rh or Ir given that, to the best of our knowledge, $LaSrNi_{0.5}Rh_{0.5}O_{3.25}$ and $LaSrCo_{0.5}Rh_{0.5}O_{3.25}$ are the first reports of extended oxides containing Rh in an oxidation state below Rh^{III}. It is also worth noting that if $LaSrCo_{0.5}Rh_{0.5}O_4$ is treated under the same conditions required to convert $Sr_2Fe^{III}Ir^{V}O_6$ to $Sr_2Fe^{II}Ir^{II}O_4$ (CaH_2, 400 °C)[93], the oxyhydride phase $LaSrCo^{I}_{0.5}Rh^{III}_{0.5}O_3H$ is observed[94], suggesting the difference of reduction chemistry between Rh and Ir.

4.5. Conclusion

Topochemical reduction of n = 1 Ruddlesden−Popper phases $LaSrNi_{0.5}Rh_{0.5}O_4$ and $LaSrCo_{0.5}Rh_{0.5}O_4$ with Zr yields $LaSrNi_{0.5}Rh_{0.5}O_{3.25}$ and $LaSrCo_{0.5}Rh_{0.5}O_{3.25}$, respectively. Both of the reduced oxides can be indexed using body-centred orthorhombic unit cells ($LaSrCo_{0.5}Rh_{0.5}O_{3.25}$: a = 3.602Å, b = 3.911 Å, c = 12.936 Å; $LaSrNi_{0.5}Rh_{0.5}O_{3.25}$: a = 3.580 Å, b = 3.927 Å, c = 12.810 Å) with the selective deintercalation of oxygen on 'equatorial' oxygen atoms in transition-metal octahedra. Analysis reveals that while the rhodium centres in $LaSrM_{0.5}Rh_{0.5}O_{3.25}$ (M = Co, Ni) have an average oxidation state of Rh^{II}, these are actually disproportionated into 1:1 ratio of Rh^{I} and Rh^{III}, making $LaSrM_{0.5}Rh_{0.5}O_{3.25}$ (M = Co, Ni) the first observation of Rh^{I} in an extended oxides.

The 'disproportionation' of Rh^{II} raises a number of questions about the factors controlling the extent of anion-deintercalation process. What is the factor aiding $LaSrM_{0.5}Rh_{0.5}O_{3.25}$ formation and providing a large kinetic barrier to further reduction to the corresponding $LaSrM^{I}_{0.5}Rh^{I}_{0.5}O_3$ phases? Is the oxygen stoichiometry which results in 1:1 C_{4v}:D_{4h} structural arrangement and the 1:1 Rh^{I}:Rh^{III} oxidation state arrangement linked to each other? Further investigations on the primary drive for this disproportionation and 1:1 C_{4v}:D_{4h} structural arrangement will be carried out in the following Chapter 5, but the results presented here hint at a rich oxide chemistry for low-valent, late transition metal oxides.

Chapter 5

A-site Doping of $La_xSr_{2-x}Co_{0.5}Rh_{0.5}O_4$ Series

5.1. Introduction

In Chapter 4 the phases resulting from the reduction of the $n = 1$ Ruddlesden-Popper phases $LaSrM_{0.5}Rh_{0.5}O_4$ (M = Co, Ni) and the oxygen stoichiometry, crystal structure and transition metal oxidation states of $LaSrM_{0.5}Rh_{0.5}O_{3.25}$ (M = Co, Ni) were discussed. Here the *A*-site doping of $La_xSr_{2-x}Co_{0.5}Rh_{0.5}O_4$ series is investigated and discussed.

5.2. Experimental

Samples of $La_xSr_{2-x}Co_{0.5}Rh_{0.5}O_4$ ($0.85 \leq x \leq 1.15$) were synthesized by a high-temperature ceramic method as described in Section 2.1. Suitable stoichiometric ratios of La_2O_3 (99.999%, dried at 900 °C), $SrCO_3$ (99.994%), Co_3O_4 (99.99%) and Rh_2O_3 (99.998%, dried at 850 °C for two hours), for each composition respectively, were ground together using an agate mortar and pestle, transferred into an alumina crucible, and then heated at a rate of 5 ºC min^{-1} to 1000°C in air to decompose the carbonate. The pellet was heated in an alumina boat for 3 periods of 50 hours at 1300°C in a steady pure O_2 flow with re-grinding and re-pelleting between heating cycles. The high partial pressure of O_2 plays a significant role in isolating $La_xSr_{2-x}Co_{0.5}Rh_{0.5}O_4$, as mentioned in Section 3.2.1. The reaction progress was monitored by laboratory X-ray powder diffraction and once the reaction was deemed complete, synchrotron X-ray powder diffraction data were collected from the resulting phase. All the doped $La_xSr_{2-x}Co_{0.5}Rh_{0.5}O_4$ ($0.85 \leq x \leq 1.15$) parent oxide phases are formed at the same reaction temperature (1300 °C) as the $x = 1$ analogue $LaSrCo_{0.5}Rh_{0.5}O_4$.

5.3. Results

5.3.1. Structural Characterisation of $La_xSr_{2-x}Co_{0.5}Rh_{0.5}O_4$ ($0.85 \leq x \leq 1.15$)

Synchrotron X-ray powder diffraction (SXRD) data (Section 2.3.1.3) were collected from $La_xSr_{2-x}Co_{0.5}Rh_{0.5}O_4$ ($0.85 \leq x \leq 1.15$). These data could be readily indexed using the same body-centred tetragonal unit cell (space group *I4/mmm*), as the $x = 1$ phase, $LaSrCo_{0.5}Rh_{0.5}O_4$, mentioned in Section 3.3.1, with slight variations in lattice parameters. Although neutron powder diffraction data were not collected for these doped phases, atomic positions of oxide ions, *A*- and *B*- site cations are still relatively reliable. Data collected from all compositions were refined against a model based on an $n = 1$, A_2BO_4 Ruddlesden-Popper phase with an x:2-x ratio of La:Sr solid-solution on the *A*-site and a 1:1 ratio of Co:Rh solid-solution on the *B*-site to achieve good statistical fits. Plots of the observed and calculated data for the refinement of $La_{0.85}Sr_{1.15}Co_{0.5}Rh_{0.5}O_4$ are shown in Figure 5-1, as a representative sample, with other plots found in Appendix 2.1.

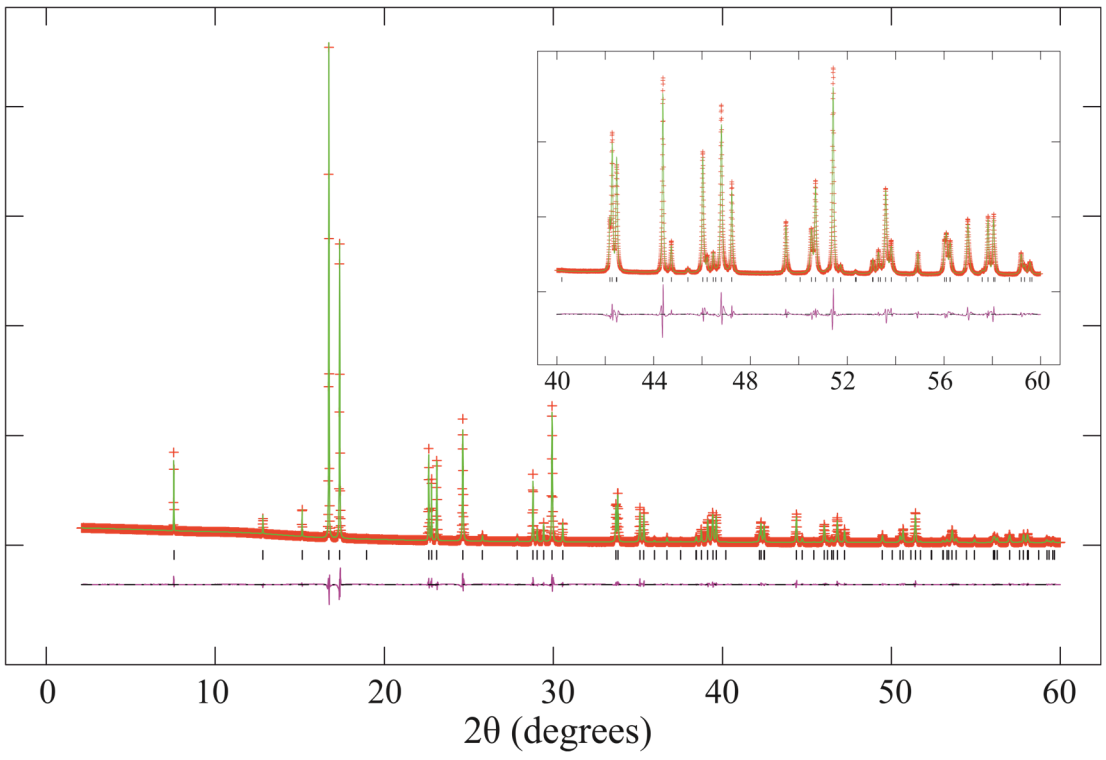


Figure 5-1 Observed(red), calculated(green) and difference plots(pink) from the Rietveld structural refinement of $La_{0.85}Sr_{1.15}Co_{0.5}Rh_{0.5}O_4$ using an *I4/mmm* model against SXRD data collected at room temperature.

Lattice parameters extracted from refinements against SXRD data collected from $La_xSr_{2-x}Co_{0.5}Rh_{0.5}O_4$ ($0.85 \leq x \leq 1.15$) are summarized below in Figure 5-2. The blue dash lines in Figure 5-2 represent the $x = 1$ phase, $LaSrCo_{0.5}Rh_{0.5}O_4$, here the right-hand-side (RHS) represents La-rich compounds and left-hand-side (LHS) represents La-deficient compounds.

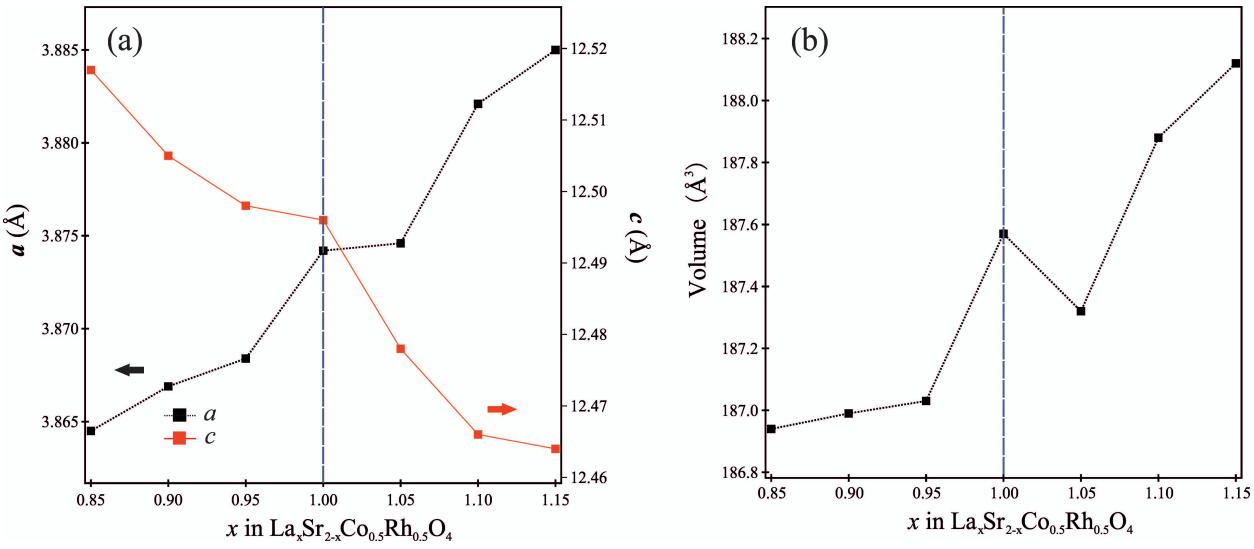


Figure 5-2 Plot (a) *a*, *c*; (b) volume against *x* in $La_xSr_{2-x}Co_{0.5}Rh_{0.5}O_4$ ($0.85 \leq x \leq 1.15$) series of compounds. (Error bars for the parameters are smaller than the points plotted.)

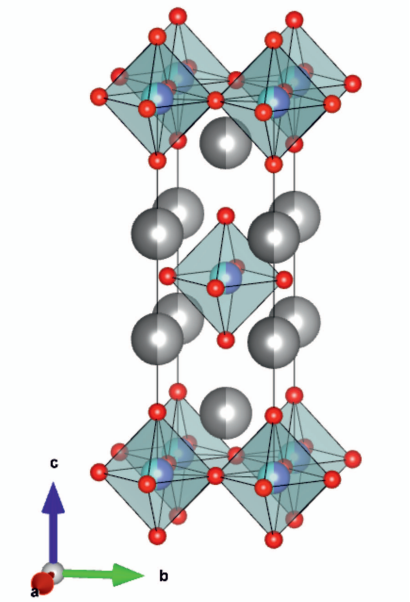


Figure 5–3 Unit cell of $LaSrCo_{0.5}Rh_{0.5}O_4$ (space group *I4/mmm*)

As shown in Figure 5-3, the differences in ionic radii of Co/Rh ions contribute to changes in the *a* lattice parameter and both the La^{III}/ Sr^{II} size difference and Co/Rh size difference contribute to the changes in the *c* lattice parameter.

As shown in Figure 5-2, the monotonic changes in the *a* and *c* lattice parameters of the $La_xSr_{2-x}Co_{0.5}Rh_{0.5}O_4$ series are consistent with the formation of single phases of the stated composition. We can conclude that the contraction in the *c* lattice parameter upon increasing *x* arises from substitution of Sr^{II} by La^{III}; the expansion in the *a* lattice parameter upon increasing *x* arises from the

reduction of the transition metals. The ionic radii of these *A*-site and *B*-site cations have been summarized below in Table 5-1 as a reference.

Table 5-1 Ionic Radii of *A*-site and *B*-site cations in $La_xSr_{2-x}Co_{0.5}Rh_{0.5}O_4$ ($0.85 \leq x \leq 1.15$) series of compounds.[20]

Cations	Coordination Number	Ionic Radius(Å)
La^{III}	9	1.216
Sr^{II}	9	1.310
Co^{II} (high spin d^7)	6	0.745
Co^{II} (low spin d^7)	6	0.650
Co^{III} (high spin d^6)	6	0.610
Co^{III} (low spin d^6)	6	0.545
Rh^{III} (low spin d^6)	6	0.665
Rh^{IV} (low spin d^5)	6	0.600

5.3.2. Magnetic Characterisation of $La_xSr_{2-x}Co_{0.5}Rh_{0.5}O_4$ ($0.85 \leq x \leq 1.15$)

Zero-field-cooled (ZFC) and field-cooled (FC) magnetization data were collected from samples of $La_xSr_{2-x}Co_{0.5}Rh_{0.5}O_4$ ($0.85 \leq x \leq 1.15$) as a function of temperature in an applied field of 100 Oe using a SQUID magnetometer (Section 2.5). Magnetisation data collected from $La_{0.95}Sr_{1.05}Co_{0.5}Rh_{0.5}RhO_4$ are shown in Figure 5-4 as a representative data set, and the others can be found in Appendix 2.2. Data in limited temperature ranges were fitted by the Curie-Weiss law ($\chi = C/(T - \theta)$) to yield values of the Curie constant, C, and the Weiss temperature, θ, for each composition respectively, which are plotted below in Figure 5-5. The blue dashed lines in Figure 5-5 represent the $x = 1$ phase $LaSrCo_{0.5}Rh_{0.5}O_4$, hence the RHS area represents La-rich compounds and the LHS area represents La-deficient compounds. In general, all the doped phases appear to exhibit canted antiferromagnetic behaviour, like the $x = 1$ phase $LaSrCo_{0.5}Rh_{0.5}O_4$, with a divergence between ZFC and FC data occurring below $T = 25$ K, and the temperature range which can be fitted by the Curie-Weiss law ($25 < T / K < 300$) being similar for all compositions measured.

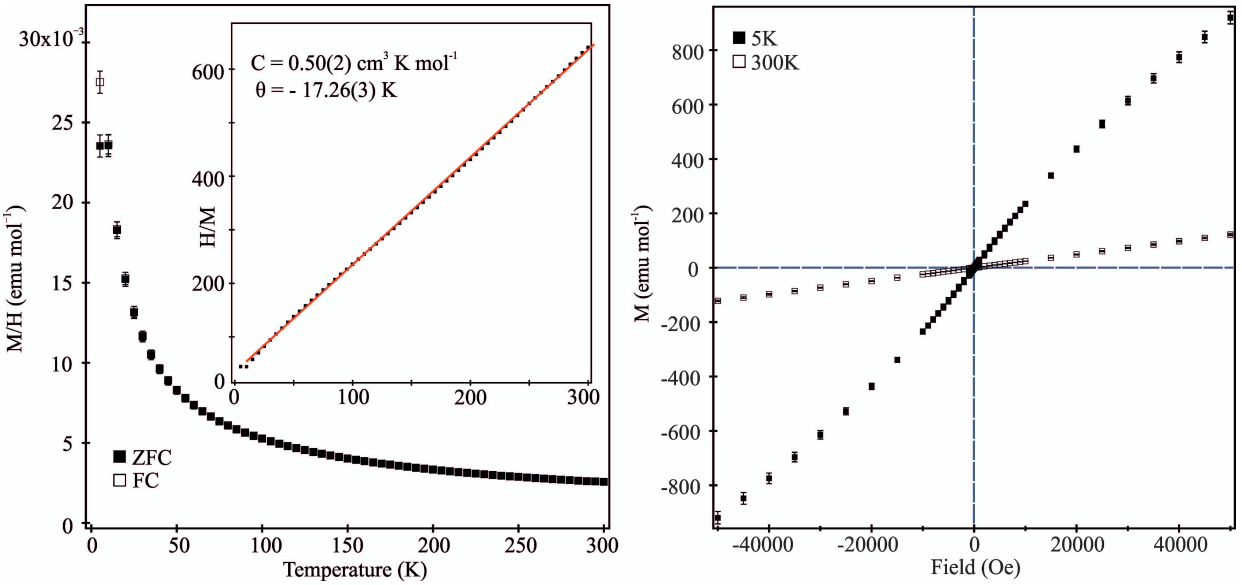


Figure 5-4 (left) Zero-field-cooled and field-cooled magnetisation data collected in an applied field of 100 Oe. Inset shows the fit to the Curie-Weiss law; (right) Magnetisation data collected as a function of applied field from $La_{0.95}Sr_{1.05}Co_{0.5}Rh_{0.5}RhO_4$.

Magnetization data collected from $La_xSr_{2-x}Co_{0.5}Rh_{0.5}O_4$ ($0.85 \leq x \leq 1.15$) at 300 K and 5 K as a function of applied field (Section 2.5.2), are shown in Appendix 2.2. For all compositions of $La_xSr_{2-x}Co_{0.5}Rh_{0.5}O_4$ ($0.85 \leq x \leq 1.15$), magnetisation-field data collected at 300 K are linear and pass through the origin, and analogous data collected at 5 K exhibit weak hysteresis, which is consistent with weak canted antiferromagnetic behaviour.

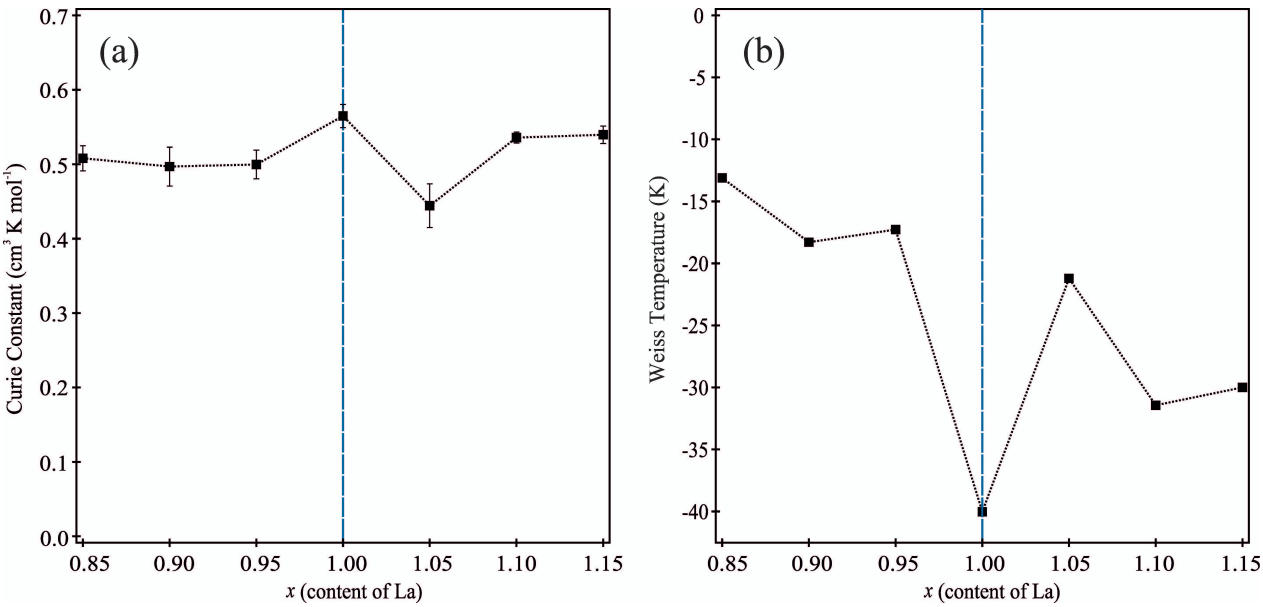


Figure 5-5 Plot of (a) Curie constant, C; and (b) Weiss temperature , θ, against x in $La_xSr_{2-x}Co_{0.5}Rh_{0.5}O_4$ ($0.85 \leq x \leq 1.15$) series of compounds. (Error bars for the parameters are smaller than the points plotted.)

5.4. Discussion

As shown in Figure 5-5, the whole $La_xSr_{2-x}Co_{0.5}Rh_{0.5}O_4$ ($0.85 \leq x \leq 1.15$) series of compounds yields unexpectedly low Curie constants (< 0.6 cm^3 K mol^{-1}). Based on the Curie constants and Weiss temperatures extracted from the magnetisation data of this series of compounds, it can be concluded that the magnetic behaviour doesn't change much with *A*-site doping, which cannot be easily explained simply using single-ion combinations.

In the series of compounds, the large ligand field of Rh^{III} means that a low-spin t_{2g}^6, $S = 0$ electronic configuration of Rh^{III} is highly preferred. Thus, understanding how the electronic configuration of Co^{III} varies with *A*-site doping is the key to understanding the magnetic behaviour.

As discussed in Section 1.3.1, $Co^{III}O_6$ units have a ligand field close to the 'critical value' between high-spin (HS), low-spin (LS) and intermediate-spin (IS) states. Thus, to gain a deeper understanding of the *A*-site doping of the $La_xSr_{2-x}Co_{0.5}Rh_{0.5}O_4$ ($0.85 \leq x \leq 1.15$) series, reported phases containing high spin and low spin Co^{III} mixtures, $LaCoO_3$[95] and $La_xSr_{2-x}CoO_4$[96,97], have been chosen as references. The equatorial Co-O bond length in the CoO_6 octahedra of these phases has been plotted as a function of temperature and composition respectively as a comparison to the doped $La_xSr_{2-x}Co_{0.5}Rh_{0.5}O_4$ ($0.85 \leq x \leq 1.15$) phases in Figure 5-6.

$LaCoO_3$ adopts an LS spin state in the temperature interval $0 < T/K < 35$. On heating above 35 K, a mixed LS/IS spin state is adopted, which then becomes a mixture of IS/HS at higher temperature. This LS-to-IS-to-HS change is accompanied by an increase in the average Co-O bond length as shown in Figure 5-6. The analogous $n = 1$ Ruddlesden-Popper phase, $LaSrCoO_4$, adopts an IS spin state at room temperature. Hole-doped $La_xSr_{2-x}CoO_4$ ($x < 1.0$) phases don't lead to a large change in average Co-O bond length, as shown in Figure 5-6,

consistent with similar ionic radii of IS Co^{III} and Co^{IV}. In contrast, electron doping of $La_xSr_{2-x}CoO_4$ ($x > 1.0$) is observed to increase the average Co-O bond length. This increase can be attributed to a larger ion radii of Co^{II} which are introduced on reduction. However, this increase in average Co-O bond length leads to a decline in the ligand field strength of the remaining Co^{III} and a change from IS Co^{III} to HS Co^{III} for some of these ions.

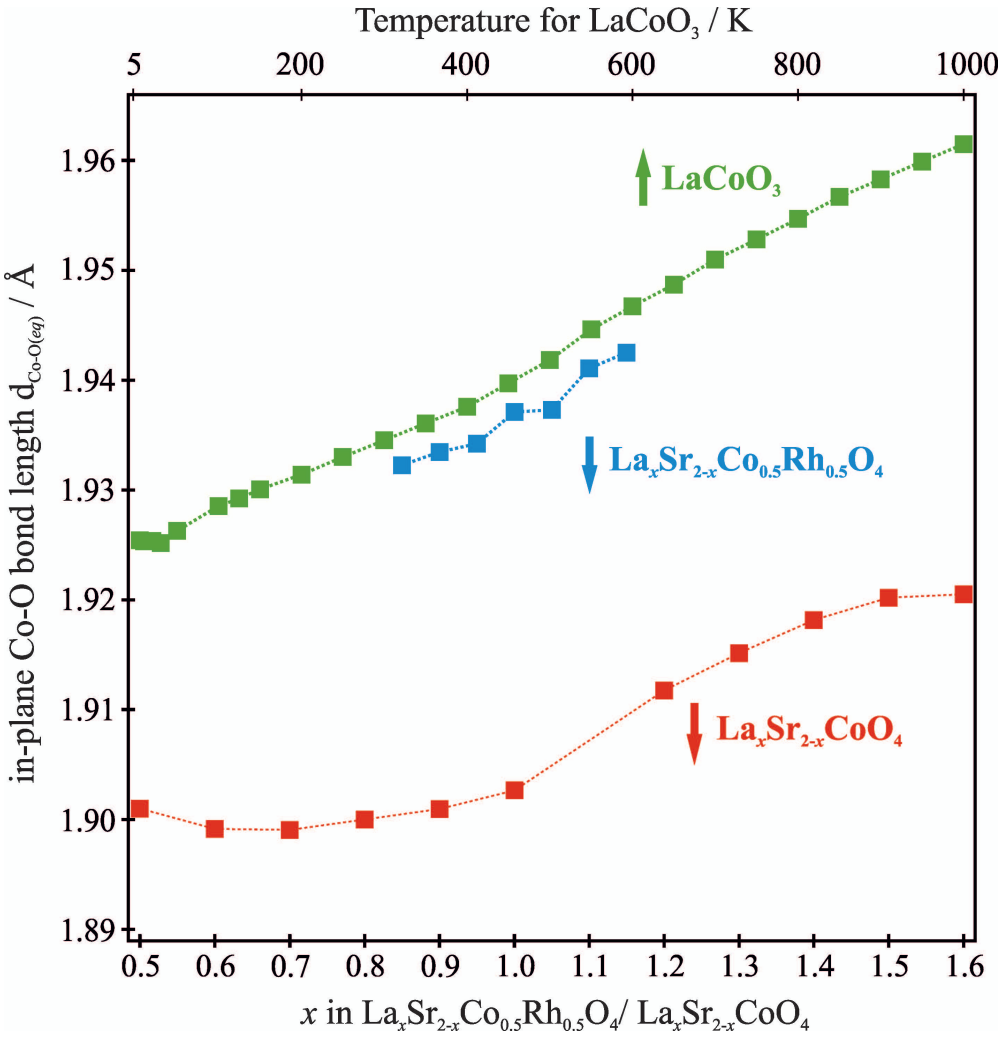


Figure 5-6 The comparison of in-plane Co-O bond length in a series of doped compounds $La_xSr_{2-x}Co_{0.5}Rh_{0.5}O_4$ ($0.85 \leq x \leq 1.15$) shown in blue markers, a series of doped compound $La_xSr_{2-x}CoO_4$ ($0.5 \leq x \leq 1.6$)[96,97] shown in red markers and $LaCoO_3$ with respect to temperature changing shown in green markers[95].

The average Co-O bond length in $LaSrCo_{0.5}Rh_{0.5}O_4$ is larger than the corresponding value for $LaSrCoO_4$ due to the introduction of Rh^{III} (radius: 0.665 Å). As a result, the ligand field experienced by the Co^{III} centres in $LaSrCo_{0.5}Rh_{0.5}O_4$ is less than that of the equivalent centres in $LaSrCoO_4$. This is consistent with the proposed 1:2 ratio of HS:LS Co^{III} in $LaSrCo_{0.5}Rh_{0.5}O_4$ compared to the intermediate spin state of Co^{III} in $LaSrCoO_4$.

Electron doped $La_xSr_{2-x}Co_{0.5}Rh_{0.5}O_4$ ($x > 1.0$) exhibits an expansion in the average Co-O bond length with increasing La concentration. If $S = \frac{3}{2}$ Co^{II} (radius:0.745 Å) replaces HS Co^{III} (radius: 0.61 Å), there would be a large expansion in the average Co-O bond length and a decline in the effective magnetic moment of the system (HS Co^{III}: $\mu_{eff}^2 = 24\ \mu_B^2$; HS Co^{II}: $\mu_{eff}^2 \approx 15\ \mu_B^2$). However, the expansion of the average Co-O bond length lowers the average ligand field experienced by the remaining Co^{III}, leading to an increase of HS Co^{III}. Therefore, an increase in the effective moment coming from HS Co^{III} centres, which counterbalances the drop due to reduction of Co^{III} to Co^{II}, resulting in an almost constant effective moment on electron doping as shown in Figure 5-5.

In contrast, hole-doped $La_xSr_{2-x}Co_{0.5}Rh_{0.5}O_4$ ($x < 1.0$) exhibits a decline in average Co-O bond length, attributable to a small decrease in the ionic radius of Rh^{IV} (0.665 Å) compared to Rh^{III} (0.6 Å). This leads to a modest increase in the cobalt ligand field, so a small proportion of the HS Co^{III} becomes LS Co^{III} upon hole doping, leading to a decline in the magnetic moment. This decline from cobalt centres counterbalances the increasing moment due to oxidation of $S = 0$ Rh^{III} to $S = \frac{1}{2}$ Rh^{IV}, resulting in the almost constant effective moment of hole doping.

5.5. Conclusion

The n = 1 Ruddlesden-Popper phase $LaSrCo_{0.5}Rh_{0.5}O_4$ can accommodate chemical 'doping' to form single phases in the composition range $La_xSr_{2-x}Co_{0.5}Rh_{0.5}O_4$ ($0.85 \leq x \leq 1.15$) under the same reaction conditions. The interplay between the HS/LS ratio of Co^{III} and the reduction of Co^{III} to Co^{II} on electron doping, or the oxidation of Rh^{III} to Rh^{IV} on hole doping result in an almost constant effective magnetic moment across the compositional range. The reduction chemistry of $La_xSr_{2-x}Co_{0.5}Rh_{0.5}O_4$ ($0.85 \leq x \leq 1.15$) with Zr getter will be discussed in Chapter 6.

Chapter 6

A-site Doping of $La_xSr_{2-x}Co_{0.5}Rh_{0.5}O_{3.25}$ Series

6.1. Introduction

In Chapter 5, the doping story of $La_xSr_{2-x}Co_{0.5}Rh_{0.5}O_4$ ($0.85 \leq x \leq 1.15$) is discussed. The further reduction chemistry of this series of compounds is investigated and analysed in this chapter.

6.2. Experimental

6.2.1. Synthesis of $La_xSr_{2-x}Co_{0.5}Rh_{0.5}O_{3.25}$ ($0.85 \leq x \leq 1.15$)

Samples of $La_xSr_{2-x}Co_{0.5}Rh_{0.5}O_{3.25}$ ($0.85 \leq x \leq 1.15$) were prepared by sealing the respective parent $La_xSr_{2-x}Co_{0.5}Rh_{0.5}O_4$ ($0.85 \leq x \leq 1.15$) oxide phase in a glass 'thimble' inside an evacuated silica ampoule along with 2 mole equivalents of powdered zirconium placed at the bottom of the silica ampoule to avoid physical contact between two chemicals, as described in Section 4.2. Small-scale test reactions were performed in which ~200 mg of a $La_xSr_{2-x}Co_{0.5}Rh_{0.5}O_4$ ($0.85 \leq x \leq 1.15$) sample was heated along with zirconium powder at a rate of 1 °C min^{-1} to temperatures ranging from 450 °C to 520 °C with the best conditions found, shown in Table 6-1. Samples were heated for 3 periods of 7 days, being reground with fresh zirconium powder replaced between heating periods. The reaction progress was monitored by laboratory X-ray powder diffraction and once the reaction was deemed complete, synchrotron X-ray powder diffraction data were collected from the resulting phases.

Although all the doped $La_xSr_{2-x}Co_{0.5}Rh_{0.5}O_4$ ($0.85 \leq x \leq 1.15$) parent oxide phases were formed at the same reaction temperature (1300 °C) as the undoped analogue $LaSrCo_{0.5}Rh_{0.5}O_4$, their corresponding reduced phases were formed at slightly different

temperatures. In general, compared to the $x = 1$ material, all the La-rich ($x > 1.0$) parent oxide phases were less reactive and required higher reaction temperatures (510 °C) to be fully converted into corresponding reduced phases, while the La-deficient ($x = 0.85$) parent oxide phase was more fragile and formed the corresponding reduced phase at a slightly lower reaction temperature (500 °C).

Table 6-1 Topochemical reaction temperatures of $La_xSr_{2-x}Co_{0.5}Rh_{0.5}O_{3.25}$ ($0.85 \leq x \leq 1.15$) with Zr in sealed silica ampoules, yielding respective reduced oxide phases.

***x* (content of La)**	**Topochemical Reaction Temperature (°C)**
0.85	500
0.90	510
0.95	510
1.00	510
1.05	510
1.10	510
1.15	510

6.2.2. Preparation for Sintered Pellet Phase of $La_xSr_{2-x}Co_{0.5}Rh_{0.5}O_{3.25}$ ($0.85 \leq x \leq 1.15$) for Resistance Measurements

The reduced $La_xSr_{2-x}Co_{0.5}Rh_{0.5}O_{3.25}$ ($0.85 \leq x \leq 1.15$) phases exhibit air sensitivity and can only be stored in an argon filled glovebox. Between 3 periods of reactions, samples were reground in an argon filled glovebox using an agate mortar and pestle. The resulting phases obtained from the method mentioned above are in powder form, which are not suitable for resistance measurements. Cold-pressed powder samples are not suitable for accurate measurements of their intrinsic electrical conductivity because they lack close contact between grains.

Thus, a pellet sintering method was applied to prepare pellets of reduced phases for resistance measurements. Samples of around 100 mg of the parent $La_xSr_{2-x}Co_{0.5}Rh_{0.5}O_4$ ($0.85 \leq x \leq 1.15$) oxide phases were pressed into pellets (diameter 5mm) under 0.5 tonnes of force and sintered

at 1300°C under air for 48 hours. The sintered pellets were then buried into 2 mole equivalents of powdered zirconium in an argon filled glove box. The mixture was then sealed in evacuated silica ampoules. Samples were heated at a rate of 1 °C min^{-1} to the temperatures detailed in Table 6-1. Since the oxygen diffusion was more difficult for pelletized phases than powder phases, the reaction was performed for 2 periods of 14 days. Between the reaction periods, the zirconium powder at the pellet surface was cleared away by a toothbrush in an argon filled glove box and small pieces cut from the pellet were ground for X-ray powder diffraction analysis. The reaction progress was monitored by laboratory X-ray powder diffraction and once the reaction was deemed complete, the resistance measurement was performed on the remaining pellet piece.

6.3. Results

6.3.1. Structural Characterisation of $La_xSr_{2-x}Co_{0.5}Rh_{0.5}O_{3.25}$ ($0.85 \leq x \leq 1.15$)

6.3.1.1. Thermogravimetric Analysis of $La_xSr_{2-x}Co_{0.5}Rh_{0.5}O_{3.25}$ ($0.85 \leq x \leq 1.15$)

To determine the chemical composition of the reduced series of compounds, reductive thermogravimetric analysis (TGA) were conducted for all samples in the series. A small quantity of the reduced samples was heated under a steady flow of 10%/90% H_2/N_2 and held at 800 °C for 1 hour to complete the reaction before cooling down. The oxygen content of the reduced sample was calculated from the mass difference between $La_xSr_{2-x}Co_{0.5}Rh_{0.5}O_{4-\delta}$ and totally reduced products (La_2O_3, SrO, Co and Rh). The reductive thermogravimetric measurement was chosen rather than the oxidative thermogravimetric measurement for higher accuracy, as discussed in Section 4.3.2.1.

The oxygen contents of the series of $La_xSr_{2-x}Co_{0.5}Rh_{0.5}O_{4-\delta}$ ($0.90 \leq x \leq 1.15$) samples are listed in Table 6-2, with TGA data collected from $La_{1.05}Sr_{0.95}Co_{0.5}Rh_{0.5}O_{3.243(1)}$ and

$La_{0.90}Sr_{1.10}Co_{0.5}Rh_{0.5}O_{3.252(1)}$ shown below, in Figure 6-1. TGA data collected from other phases can be found in Appendix 2.3. Apart from the most electron-doped sample ($La_{1.15}Sr_{0.85}Co_{0.5}Rh_{0.5}O_{3.636}$), TGA data from the remaining samples indicated an average mass loss of around 3.7%, consistent with compositions of $La_xSr_{2-x}Co_{0.5}Rh_{0.5}O_{3.25}$.

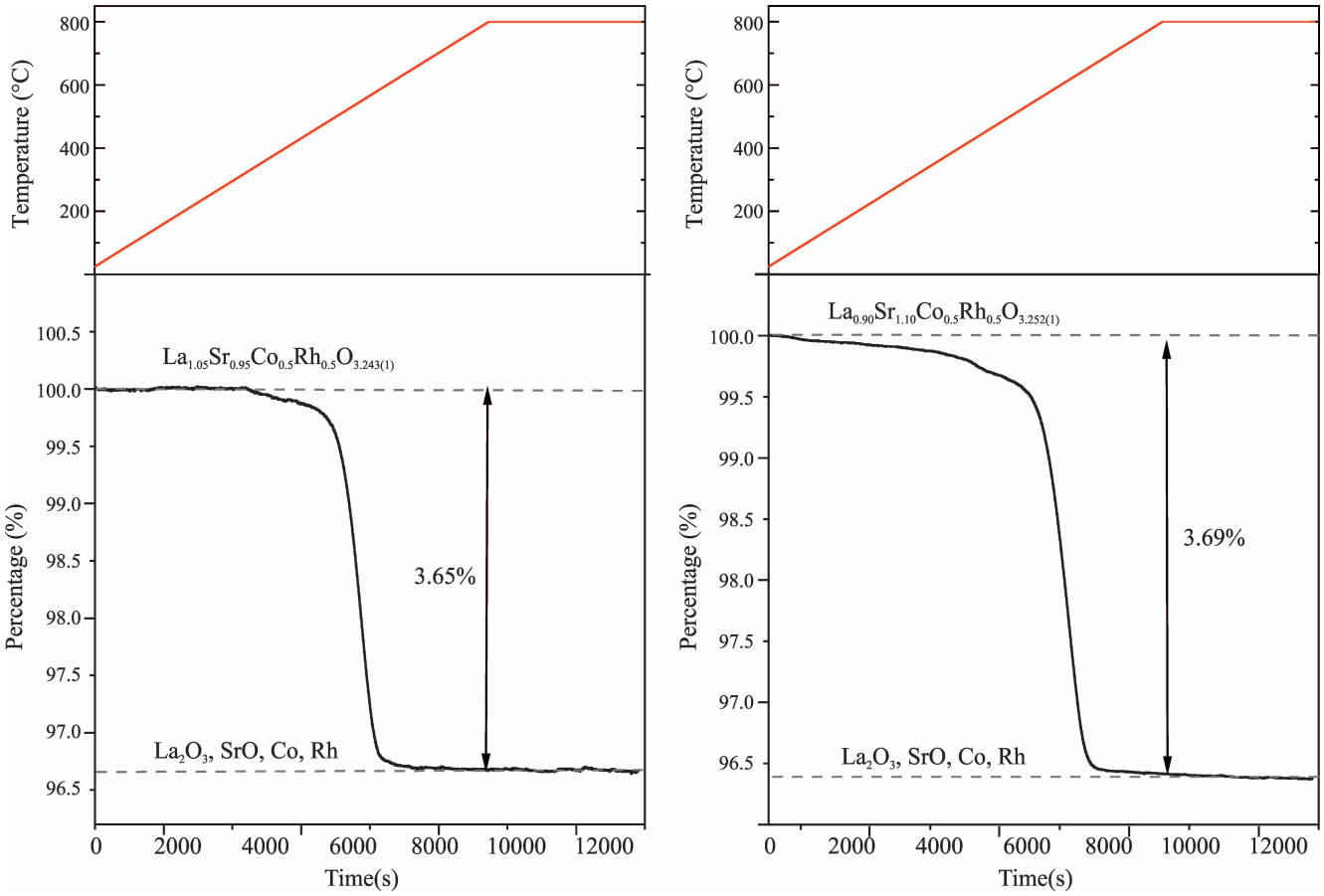


Figure 6-1 Reductive thermogravimetric data collected from $La_{1.05}Sr_{0.95}Co_{0.5}Rh_{0.5}O_{3.25}$ (left) and $La_{0.90}Sr_{1.10}Co_{0.5}Rh_{0.5}O_{3.25}$ (right). Top panel indicates the heating profile, bottom panel the relative mass of the sample.

Table 6-2 Oxygen content of the series of samples $La_xSr_{2-x}Co_{0.5}Rh_{0.5}O_{4-\delta}$ ($0.90 \leq x \leq 1.15$).

La Content	Oxygen Content	Reduced Sample Composition
0.90	3.252	$La_{0.90}Sr_{1.10}Co_{0.5}Rh_{0.5}O_{3.252}$
0.95	3.272	$La_{0.95}Sr_{1.05}Co_{0.5}Rh_{0.5}O_{3.272}$
1.0	3.251	$LaSrCo_{0.5}Rh_{0.5}O_{3.251}$
1.05	3.243	$La_{1.05}Sr_{0.95}Co_{0.5}Rh_{0.5}O_{3.243}$
1.10	3.277	$La_{1.10}Sr_{0.90}Co_{0.5}Rh_{0.5}O_{3.277}$

6.3.1.2. Synchrotron X-ray Powder Diffraction of $La_xSr_{2-x}Co_{0.5}Rh_{0.5}O_{3.25}$ ($0.85 \leq x \leq 1.15$)

Synchrotron X-ray powder diffraction (SXRD) (Section 2.3.1.3) collected from samples of $La_xSr_{2-x}Co_{0.5}Rh_{0.5}O_{3.25}$ ($0.90 \leq x \leq 1.15$), prepared by the Zr getter reduction from $La_xSr_{2-x}Co_{0.5}Rh_{0.5}O_4$ ($0.90 \leq x \leq 1.15$), could be readily indexed using body-centred orthorhombic unit cells (space group *Immm*) based on the undoped analogue $LaSrCo_{0.5}Rh_{0.5}O_{3.25}$ mentioned in Section 4.3.2, with slight variations in lattice parameters. Data collected from all compositions were refined against a model based on the refined structure of $LaSrCo_{0.5}Rh_{0.5}O_{3.25}$. The observed, calculated and difference plots from the Rietveld refinement of $La_{0.95}Sr_{1.05}Co_{0.5}Rh_{0.5}O_{3.25}$ were shown in Figure 6-2 as a representative and others can be found in Appendix 2.4.

Lattice parameters extracted from refinements against SXRD data collected from samples of $La_xSr_{2-x}Co_{0.5}Rh_{0.5}O_{3.25}$ ($0.90 \leq x \leq 1.15$) are summarized below in Figure 6-3. The dark blue dash lines in Figure 6-3 represent the undoped compound, $LaSrCo_{0.5}Rh_{0.5}O_{3.25}$, the right-hand-side (RHS) represents La-rich compounds and the left-hand-side (LHS) represents La-deficient compounds.

Data of the $x = 1.15$ phase are not shown in the figure because its lattice parameters are less reliable, as this end member really approaches to the doping limit of the structure and the oxygen content has deviated from 3.25 according to TGA data.

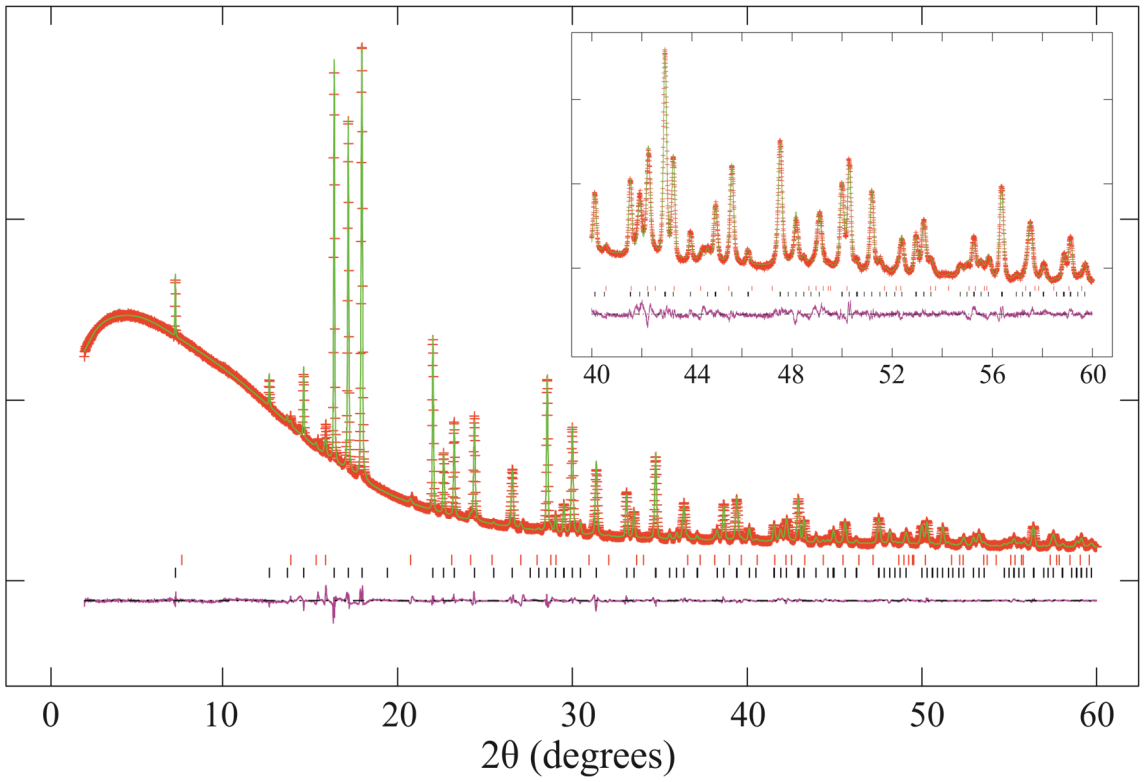


Figure 6-2 Observed(red), calculated(green) and difference plots(pink) from the Rietveld structural refinement of $La_{0.95}Sr_{1.05}Co_{0.5}Rh_{0.5}O_{3.25}$ using an *Immm* model against SXRD data collected at room temperature. Black tick marks indicate peak positions of the majority phase, red tick marks peak positions of the La_2O_3 phase.

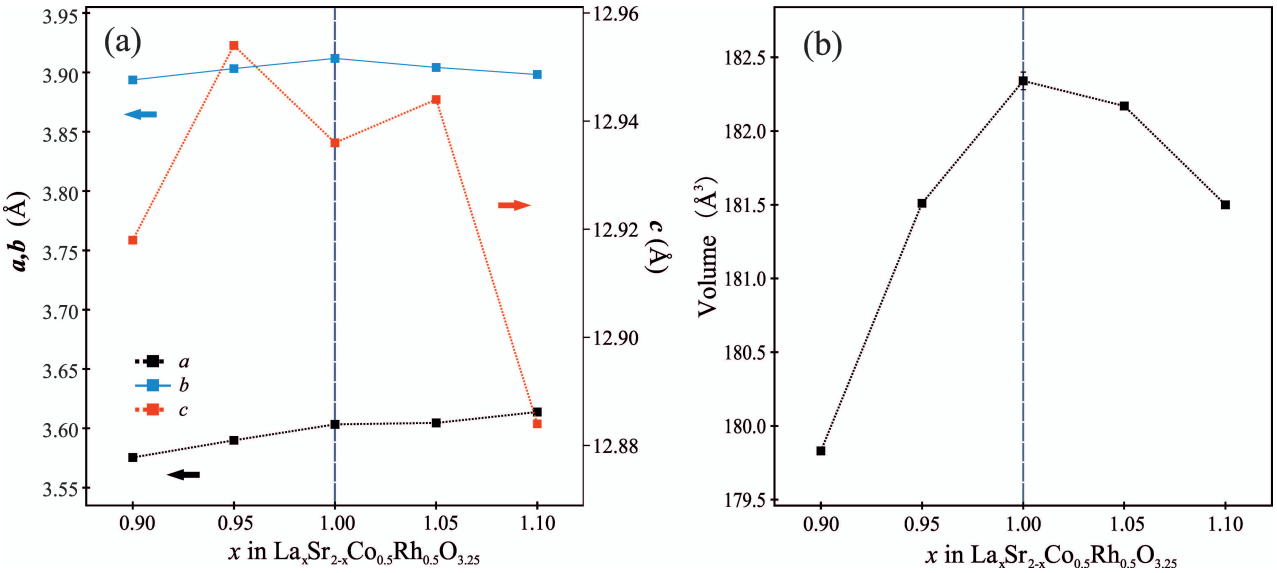


Figure 6-3 Plot (a) *a*, *b*, *c*; (b) volume against *x* in $La_xSr_{2-x}Co_{0.5}Rh_{0.5}O_{3.25}$ ($0.90 \leq x \leq 1.10$) series of compounds.

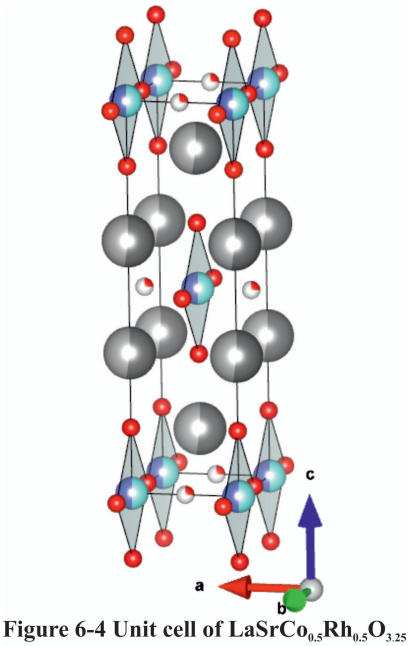


Figure 6-4 Unit cell of $LaSrCo_{0.5}Rh_{0.5}O_{3.25}$ (space group *Immm*)

As shown in Figure 6-3 (a), the changes in the *a*, *b* lattice parameters in this series of compounds are subtle (< 0.02 Å). The unit cell shown in Figure 6-4 indicates that the differences in ionic radii of Co/Rh atoms contribute to changes in the *a* and *b* lattice parameters and both the La^{III}/ Sr^{II} size difference and Co/Rh size difference contribute to the changes in the *c* lattice parameter. Compared to the unit cell of the parent oxide $LaSrCo_{0.5}Rh_{0.5}O_4$, the selective deintercalation of oxygen atoms on 'equatorial' oxygen atoms along *a* axis makes the *a* lattice parameter shorter, while *b* and *c* remains roughly the same.

With combination of TGA data and SXRD data from $La_xSr_{2-x}Co_{0.5}Rh_{0.5}O_{3.25}$ ($0.90 \leq x \leq 1.10$), it can be confirmed that an isostructural series of compounds was made where the oxygen contents are uniform.

As discussed in Section 4.4, XPS and XRD analysis reveal that the rhodium centres in $LaSrCo_{0.5}Rh_{0.5}O_{3.25}$ exhibit a mixed-valence of 1:1 ratio of Rh^I/Rh^{III} combination with Rh^I located in square-planar coordination sites (D_{4h}) and Rh^{III} located in square-based pyramidal coordination sites (C_{4v}), suggesting that the oxidation states of the transition metals and the oxygen vacancy concentration are linked. However, the uniform oxygen content in the $La_xSr_{2-x}Co_{0.5}Rh_{0.5}O_{3.25}$ ($0.90 \leq x \leq 1.10$) series of compounds implies that the metal oxidation states and oxygen deficiency are not coupled. The special ratio of 1:1 Rh^I in D_{4h} site:Rh^{III} in C_{4v} site does not hold upon doping.

6.3.2. Magnetic Characterisation of $La_xSr_{2-x}Co_{0.5}Rh_{0.5}O_{3.25}$ ($0.85 \leq x \leq 1.15$)

Magnetization data collected from $La_xSr_{2-x}Co_{0.5}Rh_{0.5}O_{3.25}$ ($0.85 \leq x \leq 1.15$) at room temperature indicate that samples contain small amounts (< 0.1 wt%) of ferromagnetic Co. Therefore, magnetization data were collected using a 'ferromagnetic subtraction' technique described in Section 2.5.3, which utilizes the fact that the magnetisation of Co saturates in the applied field which is greater than 2 T. The magnetisation data of $La_{0.95}Sr_{1.05}Co_{0.5}Rh_{0.5}O_{3.25}$ is shown in Figure 6-5 and others can be found in Appendix 2.5. The paramagnetic susceptibility of $La_{0.95}Sr_{1.05}Co_{0.5}Rh_{0.5}O_{3.25}$ follows the modified Curie-Weiss law ($\chi = C/(T - \theta) + K$) in the range $45 < T/K < 300$ to yield values of $C = 0.0998(1)$ cm^3 K mol^{-1}, $\theta = -5.48(2)$ K, and $K = 1.28(2) \times 10^{-3}$ cm^3 mol^{-1}. Below 45 K, the saturated ferromagnetic moment of $La_{0.95}Sr_{1.05}Co_{0.5}Rh_{0.5}O_{3.25}$ increases sharply, and the susceptibility exhibits a maximum at $T = 10$ K. These features of the data are consistent with a change to a magnetically ordered state or a spin-glass state below $T \sim 45$ K.

In general, the magnetisation of all the $La_xSr_{2-x}Co_{0.5}Rh_{0.5}O_{3.25}$ doped oxide phases exhibits a weak ferromagnetic component, which indicates that these materials adopt either a canted antiferromagnetic state or a spin-glass state at low temperature. As discussed in Section 4.3.2.3, neutron powder diffraction data collected from $LaSrCo_{0.5}Rh_{0.5}O_{3.25}$ at 5 K show no evidence of long-range magnetic order and thus the possibility of a canted antiferromagnetic state is quite low. Although neutron powder diffraction data were not collected from this series of doped reduced phases, it's highly likely that the absence of long-range magnetic order remains in the doped reduced oxides due to the high level of both structural and chemical disorder in the system.

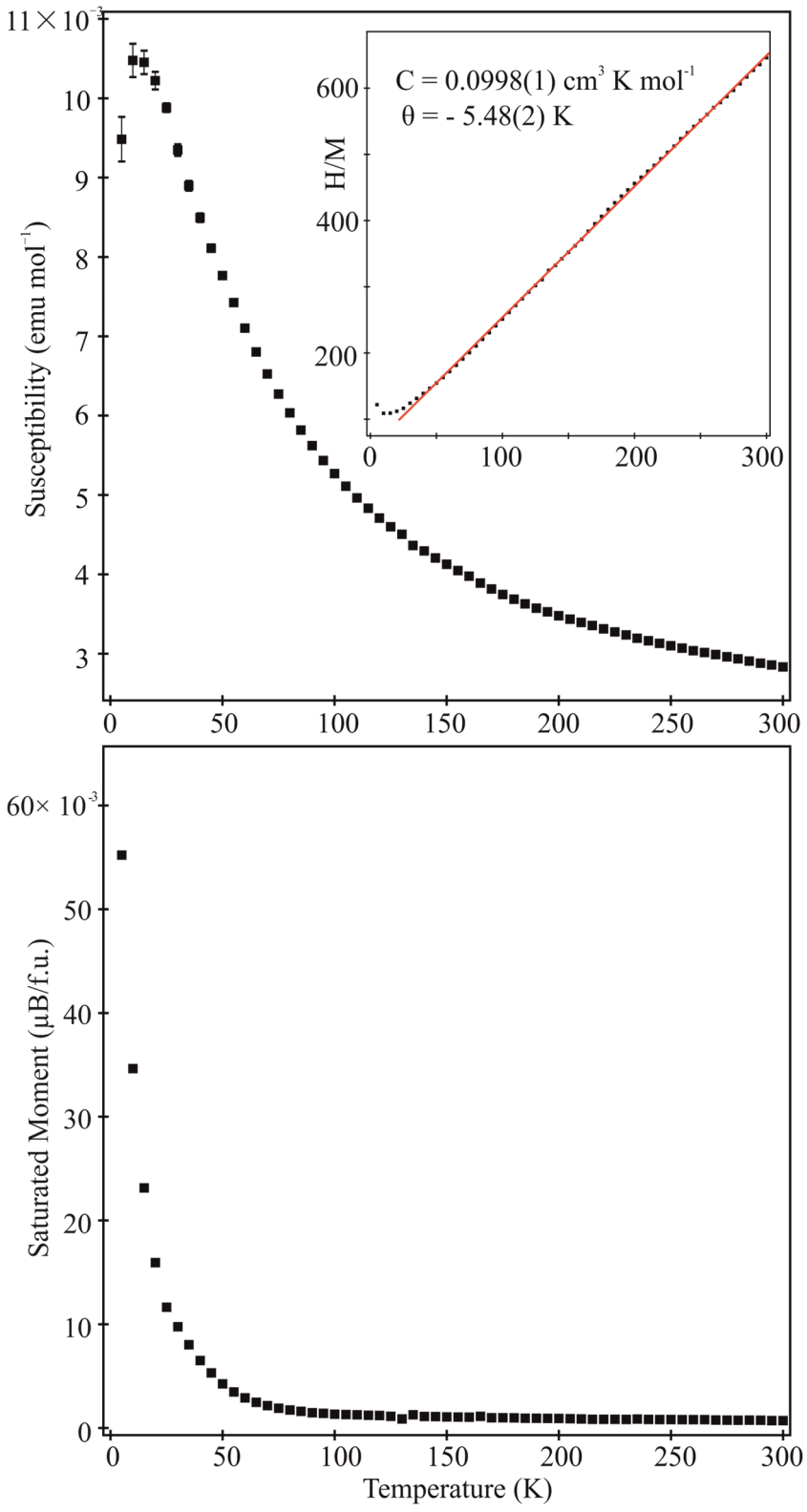


Figure 6-5 The paramagnetic susceptibility (top) and saturated ferromagnetic moment (bottom) of $La_{0.95}Sr_{1.05}Co_{0.5}Rh_{0.5}O_{3.25}$ collected as a function of temperature. Inset: the fit to the Curie-Weiss law in the temperature range 25 < *T*/K < 300.

The temperature-dependent magnetisation data of each $La_xSr_{2-x}Co_{0.5}Rh_{0.5}O_{3.25}$ composition can be fitted by the Curie-Weiss law within slightly different temperature ranges. The Curie constant and the Weiss temperature of each composition are summarized below in Figure 6-6. The blue dashed lines represent the undoped compound $LaSrCo_{0.5}Rh_{0.5}O_{3.25}$, hence the right-hand-side (RHS) represents La-rich compounds and the left-hand-side (LHS) represents La-deficient compounds. As we can see in Figure 6-6, the values of experimental Curie constant from each composition ($0.056 < C/cm^3\ K\ mol^{-1} < 0.099$) are not significantly different from undoped phase $LaSrCo_{0.5}Rh_{0.5}O_{3.25}$ and so are the Weiss temperatures ($-5.6 < T/K < -4.2$).

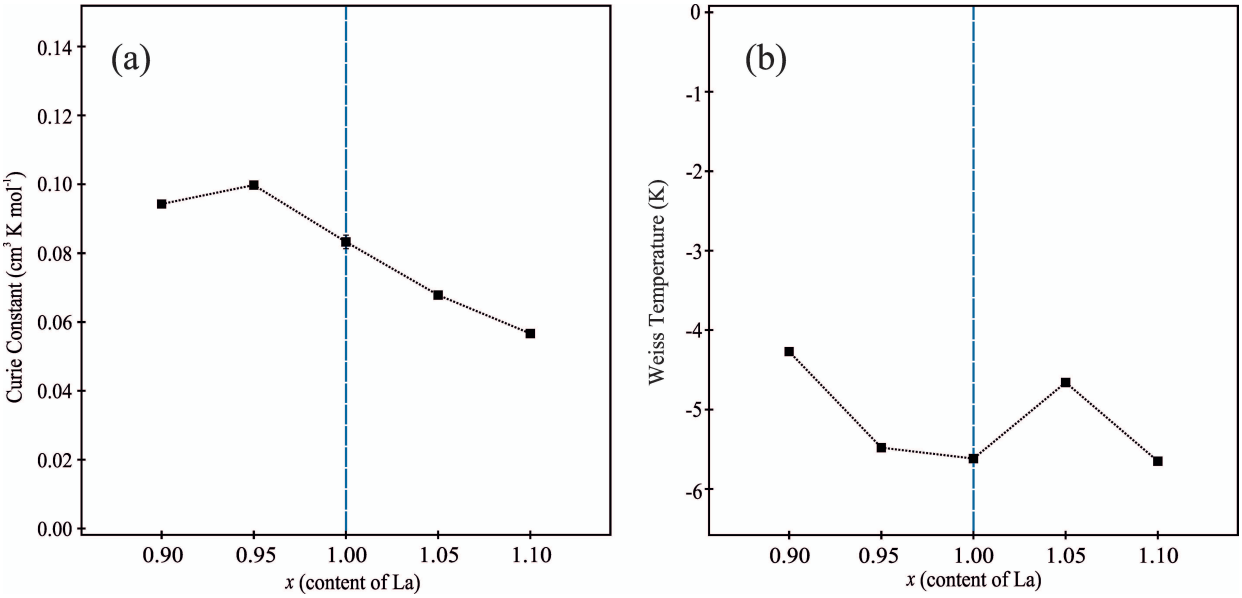


Figure 6-6 Plot of (a) Curie constant, C; and (b) Weiss temperature, θ, against *x* in $La_xSr_{2-x}Co_{0.5}Rh_{0.5}O_{3.25}$ ($0.90 \leq x \leq 1.10$) series of compounds.

Magnetisation-field data collected from $La_{0.95}Sr_{1.05}Co_{0.5}Rh_{0.5}O_{3.25}$ and its parent oxide, $La_{0.95}Sr_{1.05}Co_{0.5}Rh_{0.5}O_4$, at both 300K and 5K are shown in Figure 6-7. Compared to the parent oxide, there is an obvious shift in the mangetisation-field data collected from $La_{0.95}Sr_{1.05}Co_{0.5}Rh_{0.5}O_{3.25}$ at 5 K. This suggests that the changes in magnetic behaviour observed at 45 K for $La_{0.95}Sr_{1.05}Co_{0.5}Rh_{0.5}O_{3.25}$ is its transition to a spin-glass state. This observation is compatible with the partially disordered samples of $La_{0.95}Sr_{1.05}Co_{0.5}Rh_{0.5}O_{3.25}$ since neither the oxygen vacancies nor the Co/Rh sites exhibit long-range order. The other

doped reduced phases show the same behaviour as $La_{0.95}Sr_{1.05}Co_{0.5}Rh_{0.5}O_{3.25}$, with details listed in Appendix 2.6.

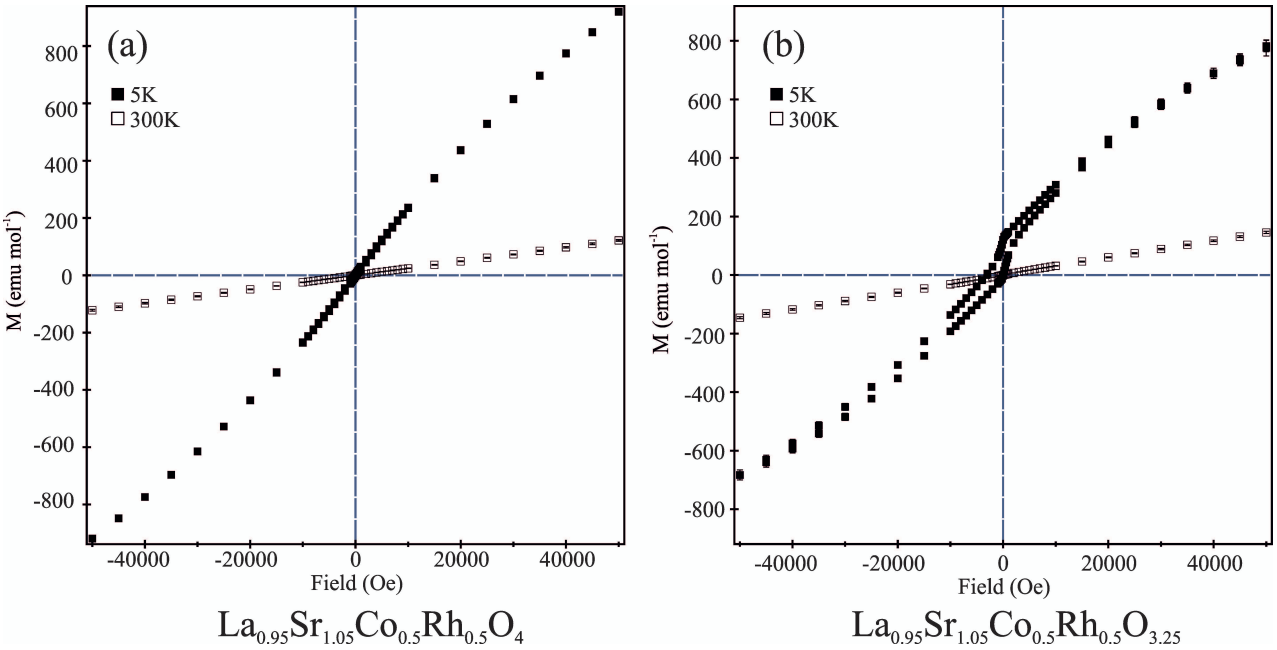


Figure 6-7 Magnetisation data collected as a function of applied field from (a) $La_{0.95}Sr_{1.05}Co_{0.5}Rh_{0.5}O_4$; and (b) $La_{0.95}Sr_{1.05}Co_{0.5}Rh_{0.5}O_{3.25}$.

6.3.3. Conductivity Measurement of $La_xSr_{2-x}Co_{0.5}Rh_{0.5}O_{3.25}$ ($0.85 \leq x \leq 1.15$)

Resistivity measurements were performed on sintered pellet phases of $La_xSr_{2-x}Co_{0.5}Rh_{0.5}O_{3.25}$ (x = 0.90, 1.0, 1.10). Results are listed in Table 6-3.

Table 6-3 The resistance of selected phases of $La_xSr_{2-x}Co_{0.5}Rh_{0.5}O_{3.25}$ (x = 0.90, 1.0, 1.10).

Reduced Sample Composition	Resistance/ MΩ
$La_{0.90}Sr_{1.10}Co_{0.5}Rh_{0.5}O_{3.25}$	0.8
$LaSrCo_{0.5}Rh_{0.5}O_{3.25}$	0.4
$La_{1.10}Sr_{0.90}Co_{0.5}Rh_{0.5}O_{3.25}$	1.8

As we can see, all the undoped and electron-/hole- doped samples are highly insulating, eliminating the possibility of itinerant electronic behaviour.

6.4. Discussion

6.4.1. Doping Limits of $La_xSr_{2-x}Co_{0.5}Rh_{0.5}O_{3.25}$ ($0.85 \leq x \leq 1.15$)

As described in Chapter 5, it has been observed that $LaSrCo_{0.5}Rh_{0.5}O_4$ can accommodate *A*-site doping chemical doping, forming single phase samples in the composition range $La_xSr_{2-x}Co_{0.5}Rh_{0.5}O_4$ ($0.85 \leq x \leq 1.15$). As discussed in this chapter, the $LaSrCo_{0.5}Rh_{0.5}O_{3.25}$ topochemically reduced phase can also accommodate *A*-site doping with slight variations of reaction temperatures (listed in Table 6-1) required to form a series of reduced compounds with the same oxygen deficiency ($La_xSr_{2-x}Co_{0.5}Rh_{0.5}O_{3.25}$ ($0.90 \leq x \leq 1.10$)). The most doped parent oxides ($La_{0.85}Sr_{1.15}Co_{0.5}Rh_{0.5}O_4$ and $La_{1.15}Sr_{0.85}Co_{0.5}Rh_{0.5}O_4$) cannot form reduced phases with the same oxygen deficiency as the other reduced phases ($La_xSr_{2-x}Co_{0.5}Rh_{0.5}O_{3.25}$ ($0.90 \leq x \leq 1.10$)), which indicates that there is a narrower doping range for $La_xSr_{2-x}Co_{0.5}Rh_{0.5}O_{3.25}$ ($0.90 \leq x \leq 1.10$) phases.

Similar scenarios can be found in $LaSrNiRuO_6$ and its reduced infinite layer $LaSrNiRuO_4$ phase. The cation-ordered double perovskite $LaSrNiRuO_6$ is able to accommodate *A*-site doping to form single phases in the composition range $La_xSr_{2-x}NiRuO_6$ ($0.75 \leq x \leq 1.375$) using a citrate gel method. However, only compositions in a narrower range ($0.85 \leq x \leq 1.25$) can be topochemically reduced to the corresponding $La_xSr_{2-x}NiRuO_4$ phase[98].

Based on the particular structural behaviour of $LaSrCo_{0.5}Rh_{0.5}O_{3.25}$, the formation of $La_xSr_{2-x}Co_{0.5}Rh_{0.5}O_{3.25}$ was not expected since the metal oxidation states and the oxygen deficiency were thought to be linked. However, the fact that the oxygen deficiency is retained in the composition range of $La_xSr_{2-x}Co_{0.5}Rh_{0.5}O_{3.25}$ ($0.90 \leq x \leq 1.10$) shows that the system is more complicated. Combined with the example of $La_xSr_{2-x}NiRuO_4$, it's suggested that the pathway that this topochemical reduction reaction takes is less dependent of the oxidation states of the metals than the structural arrangement caused by the special oxygen deficiency.

6.4.2. Magnetic Behaviour of $La_xSr_{2-x}Co_{0.5}Rh_{0.5}O_{3.25}$ ($0.85 \leq x \leq 1.15$)

As discussed in Section 4.4, $LaSrCo_{0.5}Rh_{0.5}O_{3.25}$ is believed to exhibit an structural arrangement of 1:1:1:1 ratio of D_{4h} Co^{I} : D_{4h} Rh^{I} : C_{4v} Rh^{III} : C_{4v} Co^{I}. Since both Rh^{III} and Rh^{I} cations are diamagnetic, thus only Co^{I} contributes to the magnetic behaviour of the sample, as shown in Figure 6-8.

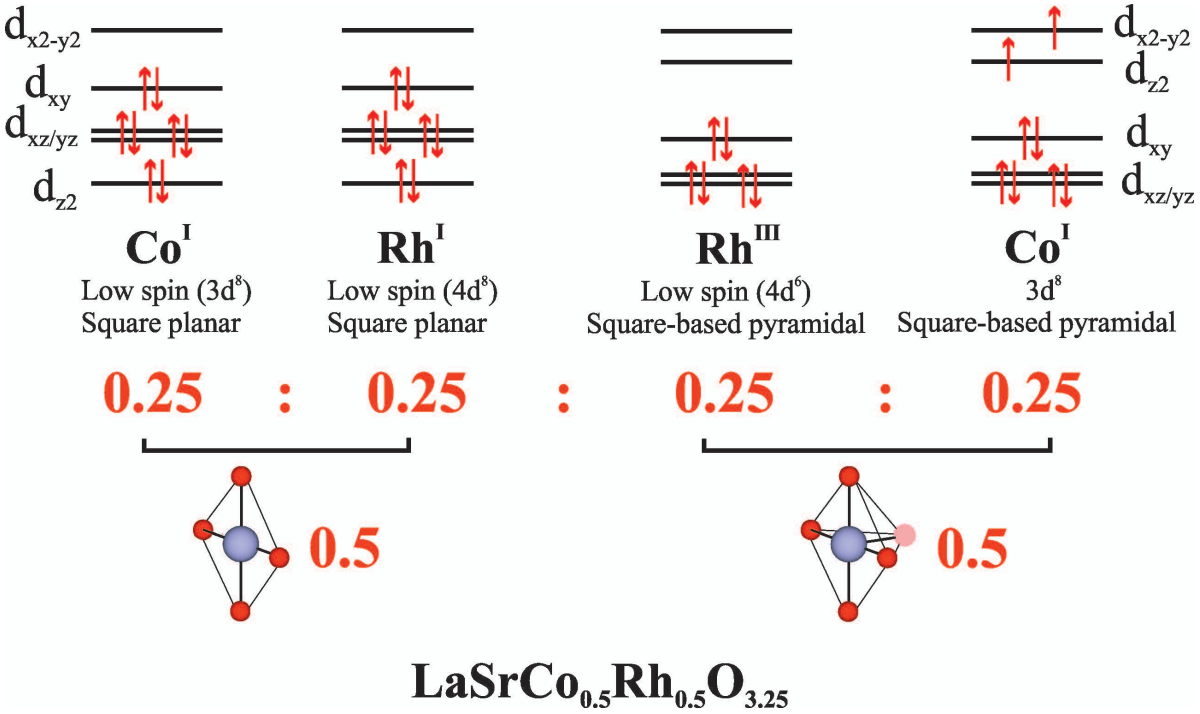


Figure 6-8 Predicted spin states of *B*-site transition metal cations in $LaSrCo_{0.5}Rh_{0.5}O_{3.25}$.

For hole-doped, La-deficient compounds (x < 1.0), upon substituting La^{III} with Sr^{II}, the oxidation of Co^{I} to Co^{II} leads to an increase in effective moments of the system, no matter whether Co^{II} replaces Co^{I} in C_{4v} site or D_{4h} site, with both possibilities shown in Figure 6-9. However, the observed magnetisation of the hole-doped compounds remains almost constant as a function of composition, which indicates that this model of localized, weakly interacting spins is not an accurate description of the hole-doped materials.

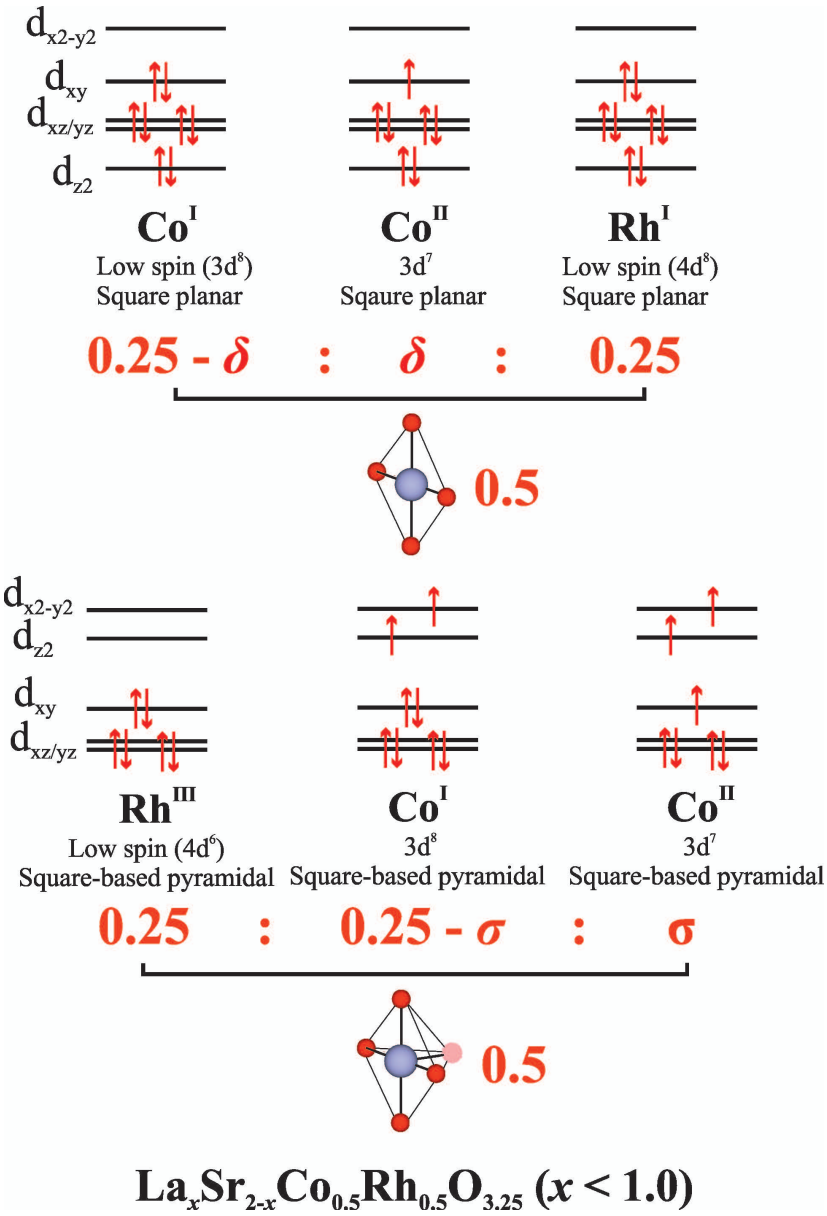


Figure 6-9 Predicted spin states of *B*-site transition metal cations in $La_xSr_{2-x}Co_{0.5}Rh_{0.5}O_{3.25}$ ($x < 1.0$).

In the electron-doped, La-rich compounds ($x > 1.0$), upon substituting Sr^{II} with La^{III}, the Rh^{III}:Rh^{I} ratio must deviate from 1:1 since some Rh^{III} are reduced to Rh^{I}. Given that the 1:1 ratio of D_{4h}:C_{4v} site arrangement is retained for hole-doped samples, the reduction of Rh^{III} must introduce Rh^{I} in C_{4v} sites with unpaired electrons located in $d_{x^2-y^2}$ and d_{xy} orbitals, shown in Figure 6-10. The introduction of Rh^{I} on the 'wrong' coordination site may generate delocalized electrons in the system. Although conductivity measurements indicate insulating behaviour for the electron-doped materials.

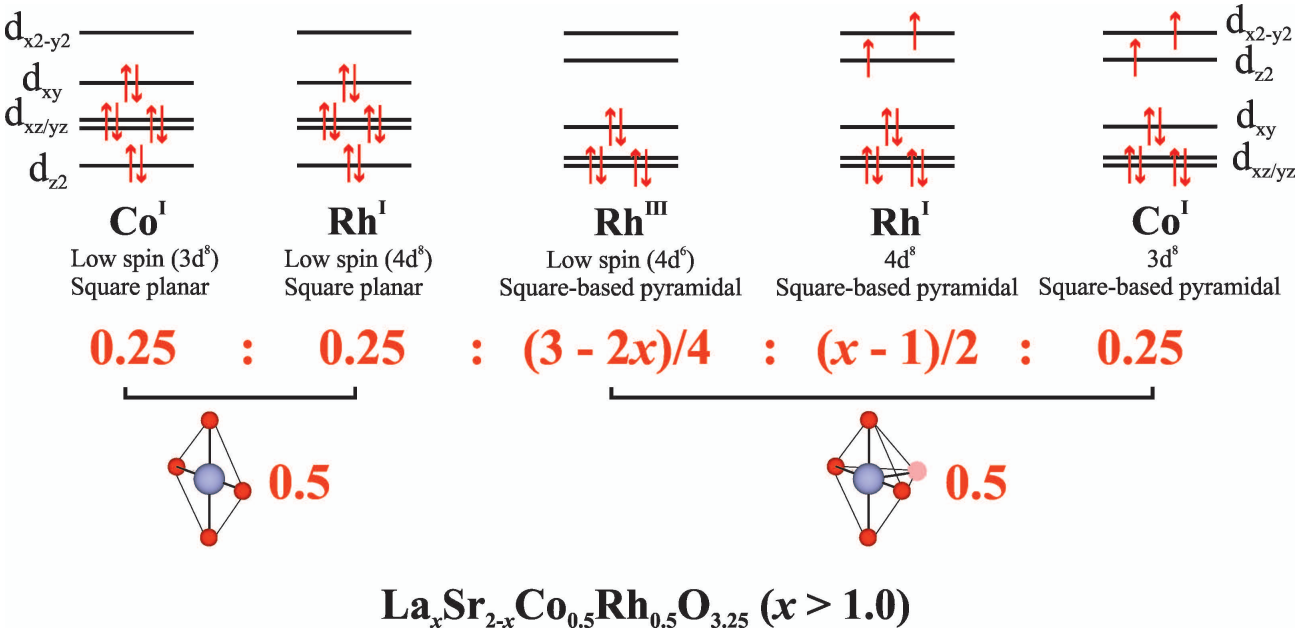


Figure 6-10 Predicted spin states of *B*-site transition metal cations in $La_xSr_{2-x}Co_{0.5}Rh_{0.5}O_{3.25}$ ($x > 1.0$).

6.5. Conclusion

The reduced $n = 1$ Ruddlesden-Popper phase $LaSrCo_{0.5}Rh_{0.5}O_{3.25}$ can accommodate chemical 'doping' to form single phases in the composition range $La_xSr_{2-x}Co_{0.5}Rh_{0.5}O_{4-\delta}$ ($0.85 \leq x \leq 1.15$). All the reduced oxides in the composition range $La_xSr_{2-x}Co_{0.5}Rh_{0.5}O_{4-\delta}$ ($0.85 \leq x \leq 1.15$) are isostructural. TGA data confirm that the reduced doped phases are referred to as $La_xSr_{2-x}Co_{0.5}Rh_{0.5}O_{3.25}$ ($0.90 \leq x \leq 1.10$), suggesting that the oxidation-states of the transition-metals and the oxygen-vacancy concentration are not coupled. The presence of a 1:1 ratio of D_{4h}:C_{4v} coordination for *B*-sites remains across the whole range of compositions, which suggests that the formation of this series of compounds is controlled by this structural feature rather than metal oxidation state.

Chapter 7

Synthesis and Characterisation of $La_2NiRhO_{4.6}$ and $LaSrMnRhO_{4.5}$

7.1. Introduction

As described in Chapter 3 and Chapter 4, the topochemical reduction of the cation-disordered n = 1 Ruddlesden-Popper phase $LaSrCo_{0.5}Rh_{0.5}O_4$ to $LaSrCo_{0.5}Rh_{0.5}O_{3.25}$ in the presence of Zr has been intensively investigated. The nominal Rh^{II} centres present in the material were observed to disproportionate to Rh^{I} and Rh^{III} in the phase $LaSrCo_{0.5}Rh_{0.5}O_{3.25}$.

The study was extended to include the cation-disordered La_2MRhO_6 (M = Mn, Co, Ni) and $LaSrMnRhO_6$ perovskite phases. Topochemical reduction of these 'parent oxides' has been conducted and three among them were considered successful ($La_2CoRhO_{6-\delta}$, $La_2NiRhO_{6-\delta}$, $LaSrMnRhO_{6-\delta}$). In this chapter, the detailed trials, characterisations and analysis of the topochemical reduction of La_2NiRhO_6 and $LaSrMnRhO_6$ are discussed.

7.2. Experimental

7.2.1. Synthesis of La_2MRhO_6 (M = Mn, Ni) and $LaSrMnRhO_6$

Samples of La_2MRhO_6 (M = Mn, Ni) and $LaSrMnRhO_6$ were synthesized via a high-temperature ceramic method as described in Section 2.1. Suitable stoichiometric ratios of La_2O_3 (99.999%, dried at 900 °C), $SrCO_3$ (99.994%), Rh_2O_3 (99.998%, dried at 850 °C for two hours) and elemental Mn (99.996%) / elemental Ni (99.996%) were ground together using an agate mortar and pestle. Mixed powders containing $SrCO_3$ were then transferred into an alumina crucible and heated in air at a rate of 5 °C min^{-1} to 1000 °C to decompose the carbonate. After the decomposition, samples were reground and pressed into pellets (diameter 13mm) under 5.5 tonnes of force in order to increase contact area. The pellets were then

transferred into alumina crucibles and heated for 3 periods of 48 hours at 1000°C, 1200 °C and 1250 °C in air for La_2NiRhO_6, 1000°C, 1100°C and 1300°C for La_2MnRhO_6 and $LaSrMnRhO_6$ with grinding and pelleting between heating cycles. Reaction progress was monitored by laboratory X-ray diffraction and once the reactions were deemed complete, synchrotron X-ray powder diffraction data were collected from the resulting phases.

7.2.2. Synthesis of $La_2MRhO_{6-\delta}$ (M = Mn, Ni) and $LaSrMnRhO_{6-\delta}$

Samples of La_2MRhO_6 (M = Mn, Ni) and $LaSrMnRhO_6$ were reduced using a zirconium getter[81] (as described in (Section 2.2.1). Samples to be reduced were placed in a glass 'thimble' and sealed in evacuated silica ampoules along with 2 mole equivalents of powdered zirconium placed at the bottom of the silica ampoules. Small-scale trial reactions were performed in which ~200 mg of La_2MRhO_6 (M = Mn, Ni) or $LaSrMnRhO_6$ were heated at a rate of 1 °C min^{-1} to temperatures in the range $350 < T/°C < 600$ for 3 periods of 5 days, with samples being reground and the Zr being replaced between heating periods. The reaction progress was monitored by laboratory X-ray diffraction (XRD) and the optimum temperatures for topochemical reductions were screened via XRD analysis. Once the reactions were deemed complete, synchrotron X-ray powder diffraction data were collected from the resulting phases. Samples of $La_2NiRhO_{6-\delta}$ and $LaSrMnRhO_{6-\delta}$ characterized by neutron powder diffraction were prepared by heating ~2 g of La_2NiRhO_6 or $LaSrMnRhO_6$ with Zr for 3 periods of 5 days at their optimum reduction temperatures, with samples being reground and the Zr being replaced between heating periods.

7.3. Results

7.3.1. Structural Characterisation of 'parent oxides'

7.3.1.1. X-ray Powder Diffraction of La_2NiRhO_6

XRD data were collected from La_2NiRhO_6 and then analysed by the Rietveld refinement method. The refinement was performed using a model based on the $GdFeO_3$ distorted perovskite model in space group *Pbnm*[99]. The refined structure shown in Figure 7-1 is consistent with the previous report of La_2NiRhO_6[76] with a unit cell in space group *Pbnm* (*a* = 5.546 Å, *b* = 5.541 Å, *c* = 7.845 Å). As shown in Figure 7-2, the refinement achieved a good fit with *wRp* = 6.50%, confirming sample purity and quality. Detailed structural parameters are listed in Table 7-1. Magnetisation data collected from La_2NiRhO_6 are detailed in Appendix 2.7, and these data agree with previous reports as well.[73]

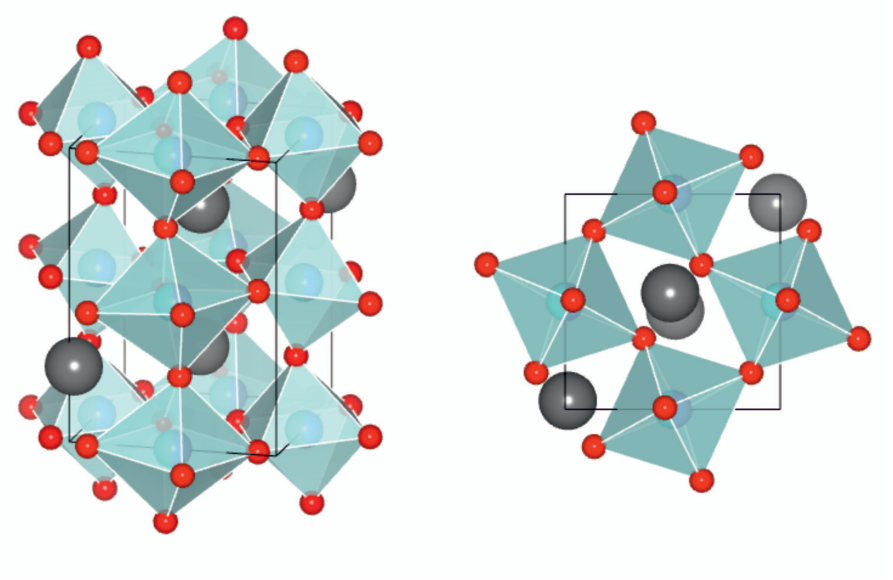


Figure 7-1 The crystal Structure of La_2NiRhO_6 (space group *Pbnm* with $a^+b^-b^-$ rotation).

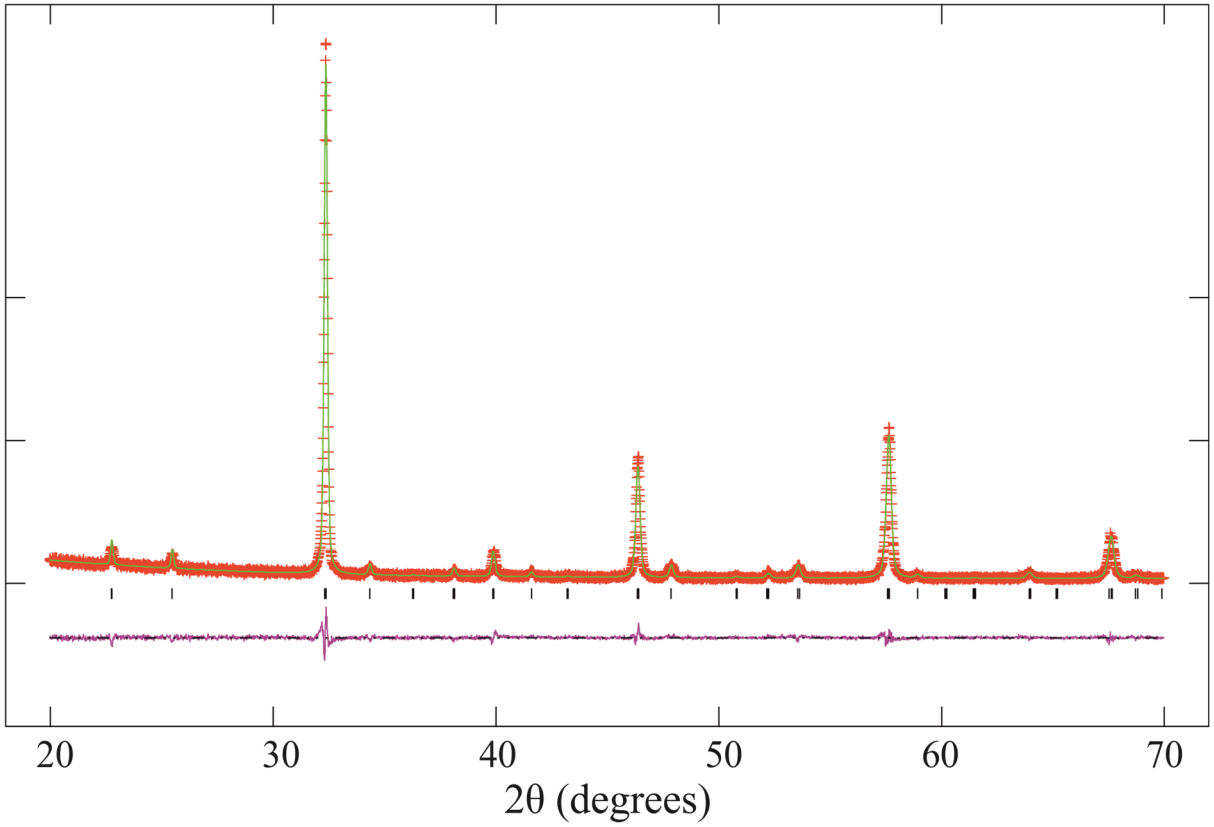


Figure 7-2 Observed(red), calculated(green) and difference plots(pink) from the Rietveld structural refinement of La_2NiRhO_6 using a *Pbnm* model against laboratory XRD data collected at room temperature. (Bruker diffractometer λ = 1.5418 Å)

Table 7-1 Structural parameters from the refinement of La_2NiRhO_6 against laboratory XRD data collected at 298 K.

Atom	Wyckoff Position	*x*	*y*	*z*	Fraction	U_{iso} (Å^2)
La	4*c*	0.142(8)	0.040(1)	¼	1	0.039(1)
Ni/Rh	4*b*	½	0	0	0.5/0.5	0.019(1)
O(1)	4*c*	0.845(5)	0.186(7)	0.977(3)	1	0.093(10)
O(2)	8*d*	0.996(7)	0.494(3)	¼	1	0.042(8)

La_2NiRhO_6 - space group *Pbnm* (#62)
Formula mass: 535.412 g mol^{-1}, Z = 2
a = 5.5478(4) Å, *b* = 5.5612(5) Å, *c* = 7.8458(5) Å, Volume = 242.07(3) Å^3
Radiation source: Bruker X-ray, λ = 1.5418 Å
Temperature: 298 K
χ^2 = 1.542; *wRp* = 6.50 %; *Rp* = 5.07 %.

7.3.1.2. Synchrotron X-ray Powder Diffraction of La_2MnRhO_6 and $LaSrMnRhO_6$

Synchrotron X-ray Diffraction (SXRD) data collected from La_2MnRhO_6 and $LaSrMnRhO_6$ can also be indexed using models based on the $GdFeO_3$ model in space group *Pbnm*. Figure 7-3 shows the crystal structures of La_2MnRhO_6 and $LaSrMnRhO_6$ used for Rietveld refinements. The results of Rietveld refinements are shown in Figure 7-4 for La_2MnRhO_6 and Figure 7-5 for $LaSrMnRhO_6$. Detailed structural parameters are listed in Table 7-2 for La_2MnRhO_6 and Table 7-3 for $LaSrMnRhO_6$. Comparisons of lattice parameters and selected bond lengths between La_2MnRhO_6 and $LaSrMnRhO_6$ are given in Table 7-4. It has been confirmed that $LaSrMnRhO_6$ has an unexpected *B*-site oxidation state combination Mn^{III}/Rh^{IV}[73], which would explain the shrinkage of the size of Mn/RhO_6 units compared to that in $La_2Mn^{III}Rh^{III}O_6$. Magnetisation data collected from $LaSrMnRhO_6$ are shown in Appendix 2.7, and these data agree with previous reports.[73]

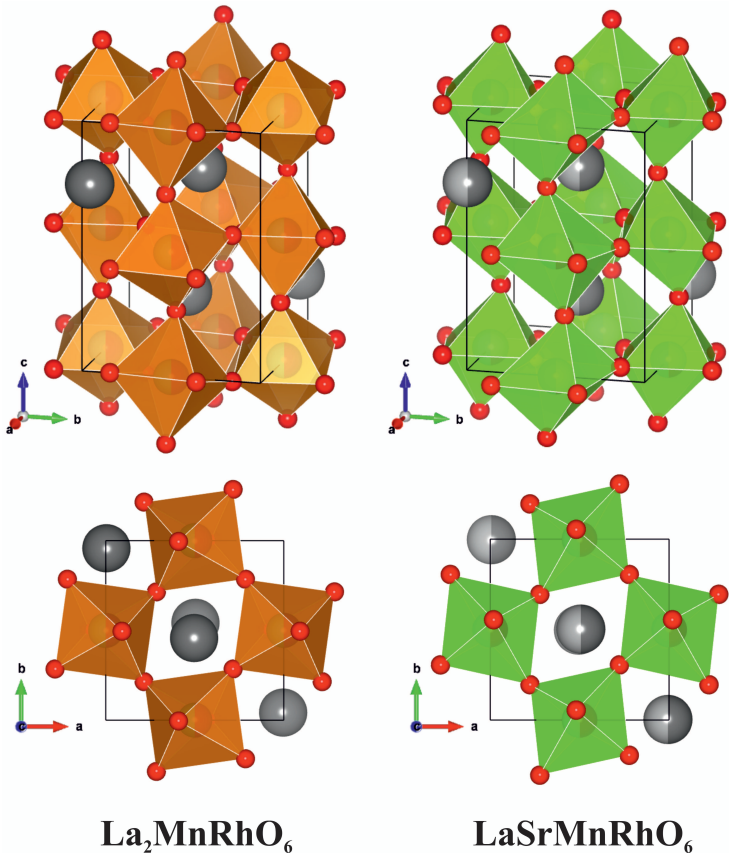


Figure 7-3 Crystal structures of La_2MnRhO_6 (left) and $LaSrMnRhO_6$ (right) in space group *Pnma*. The bottom panel shows views down the [010] directions. Brown and green octahedra denote the Mn/Rh site. Dark grey, light grey, purple, blue spheres represent La, Sr, Mn, Rh sites respectively.

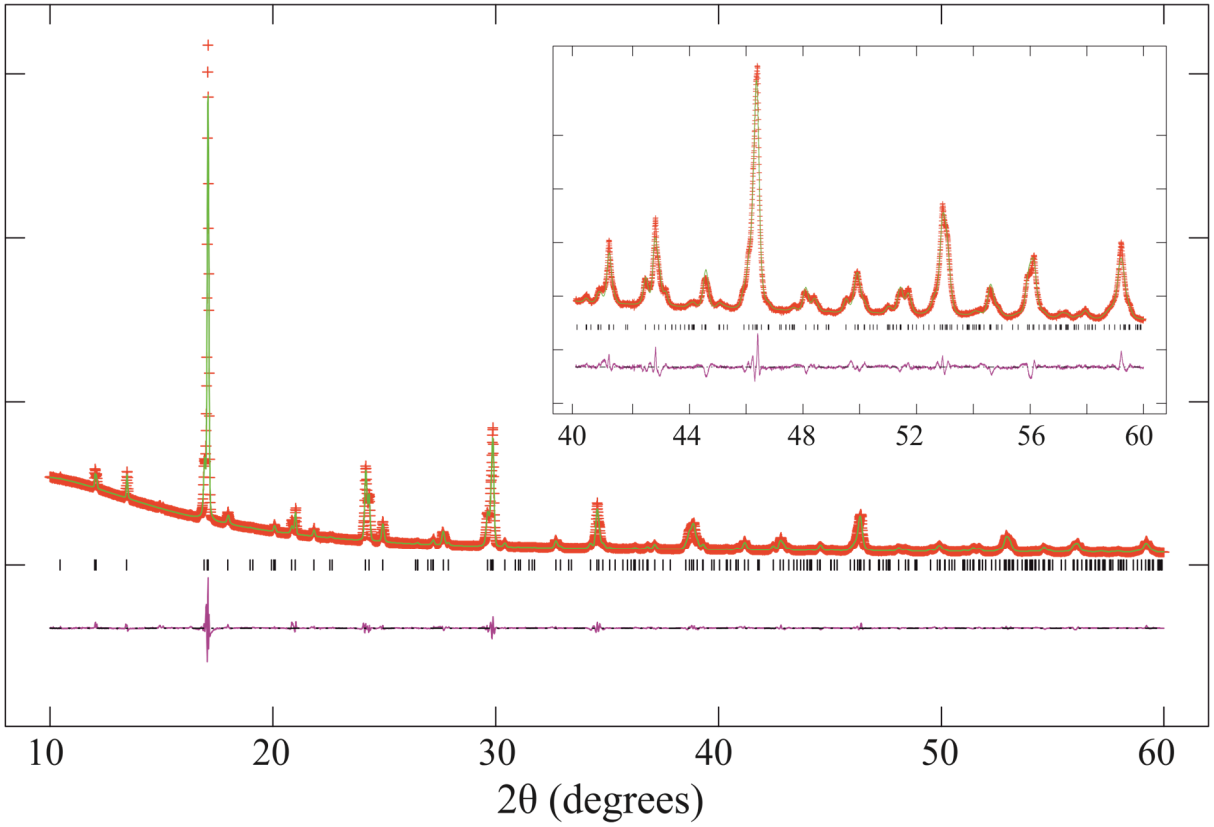


Figure 7-4 Observed(red), calculated(green) and difference plots(pink) from the Rietveld structural refinement of La_2MnRhO_6 using a *Pbnm* model against SXRD data collected at room temperature.

Table 7-2 Structural parameters from the refinement of La_2MnRhO_6 against SXRD data collected at 298 K.

Atom	Wyckoff Position	*x*	*y*	*z*	Fraction	U_{iso} (Å^2)
La	4*c*	0.9931(2)	0.0422(1)	¼	1	0.0018(1)
Mn/Rh	4*b*	½	0	0	0.5/0.5	0.0017(2)
O(1)	4*c*	0.223(1)	0.203(1)	0.962(1)	1	0.006(1)
O(2)	8*d*	0.091(1)	0.494(1)	¼	1	0.005(2)

La_2MnRhO_6 - space group *Pbnm* (#62)
Formula mass: 531.5 g mol^{-1}, Z = 2
a = 5.5498(1) Å, *b* = 5.6097(1) Å, *c* = 7.8440(1) Å, Volume = 244.21(1) Å^3
Radiation source: Synchrotron X-ray, λ = 0.8249 Å
Temperature: 298 K
χ^2 = 22.56; *wRp* = 2.62 %; *Rp* = 1.52 %.

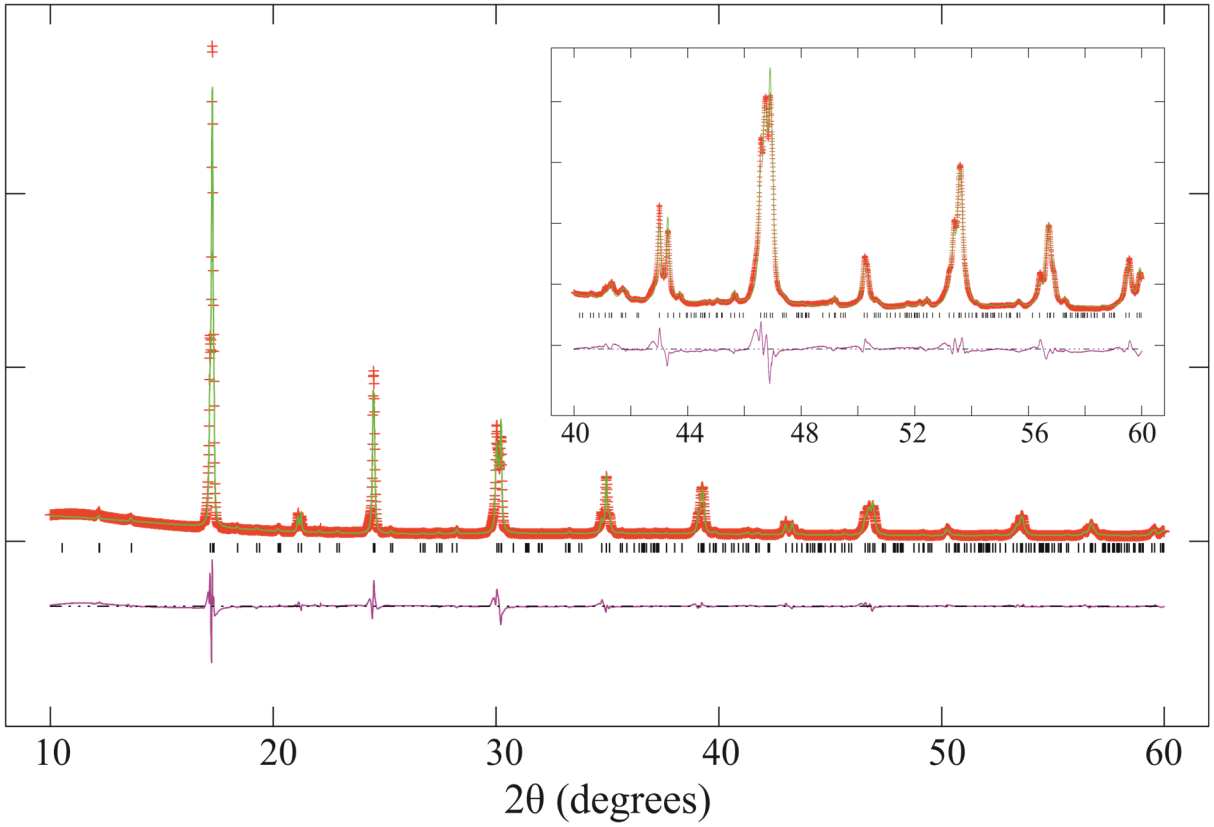


Figure 7-5 Observed(red), calculated(green) and difference plots(pink) from the Rietveld structural refinement of $LaSrMnRhO_6$ using a *Pbnm* model against SXRD data collected at room temperature.

Table 7-3 Structural parameters from the refinement of $LaSrMnRhO_6$ against SXRD data collected at 298 K.

Atom	Wyckoff Position	*x*	*y*	*z*	Fraction	U_{iso} (Å^2)
La/Sr	4*c*	0.0066(5)	0.9971(6)	¼	0.5/0.5	0.0060(2)
Mn/Rh	4*b*	½	0		0.5/0.5	0.0022(3)
O(1)	4*c*	0.223(2)	0.195(1)	0.989(3)	1	0.015(1)
O(2)	8*d*	0.019(5)	0.554(2)	¼	1	0.023(2)

$LaSrMnRhO_6$ - space group *Pbnm* (#62)
Formula mass: 480.364 g mol^{-1}, Z = 2
a = 5.4815(1) Å, *b* = 5.5351(1) Å, *c* = 7.7749(2) Å, Volume = 235.90(1)Å^3
Radiation source: Synchrotron X-ray, λ = 0.8249 Å
Temperature: 298 K
χ^2 = 379.9; *wRp* = 7.49%; *Rp* = 5.40%.

Table 7-4 Selected bond lengths from the refined structure of La_2MnRhO_6 (left) and $LaSrMnRhO_6$ (right).

La_2MnRhO_6			$LaSrMnRhO_6$		
a **/Å**	5.5544(3)		***a*** **/Å**	5.4815(1)	
b **/Å**	5.6079(4)		***b*** **/Å**	5.5351(1)	
c **/Å**	7.8503(5)		***c*** **/Å**	7.7749(2)	
Volume /Å^3	244.53(3)		**Volume /Å^3**	235.90(1)	
Cation	**Anion**	**Length (Å)**	**Cation**	**Anion**	**Length (Å)**
La/Sr	O_{eq} × 2	2.471(1)	**La/Sr**	O_{eq} × 2	2.466(1)
	O_{eq} × 2	2.634(1)		O_{eq} × 2	2.630(1)
	O_{eq} × 2	2.775(1)		O_{eq} × 2	2.826(1)
	O_{ax}	2.306(1)		O_{ax}	2.306(1)
	O_{ax}	2.595(1)		O_{ax}	2.595(1)
Mn/Rh	O_{ax} × 2	2.027(1)	**Mn/Rh**	O_{ax} × 2	1.970(1)
	O_{eq} × 2	2.016(1)		O_{eq} × 2	1.931(1)
	O_{eq} × 2	2.025(1)		O_{eq} × 2	2.031(1)

7.3.2. Initial Investigation of Reactivity of La_2MRhO_6 (*M* = Ni, Mn) and $LaSrMnRhO_6$ with Zr

7.3.2.1. Initial Investigation of Reactivity of La_2NiRhO_6 with Zr

Small-scale trial reactions of La_2NiRhO_6 with Zr were performed in the temperature range $390 \leq T/^{o}C \leq 440$. In order to describe the whole reduction profile, temperature intervals of 10 °C were chosen and the changes observed in XRD patterns at different reaction temperatures are plotted in Figure 7-6. The symmetry of the main phase changed from orthorhombic to tetragonal when the deintercalation of axial oxide ions started. The [112] and [220] peaks in the starting material (shown in red dashed lines in Figure 7-6) gradually vanished upon increasing the reaction temperature and at 420 °C. Instead, new [200], [112] and [220] peaks from the tetragonal phase became sharp and symmetric at 420 °C (shown in blue dashed lines in Figure 7-6). When raising the reduction temperature to 440 °C, the sample was observed to decompose via non-topochemical reactions. Thus, it can be concluded that 420 °C is the best temperature for isolating $La_2NiRhO_{6-\delta}$ in the reduction reaction.

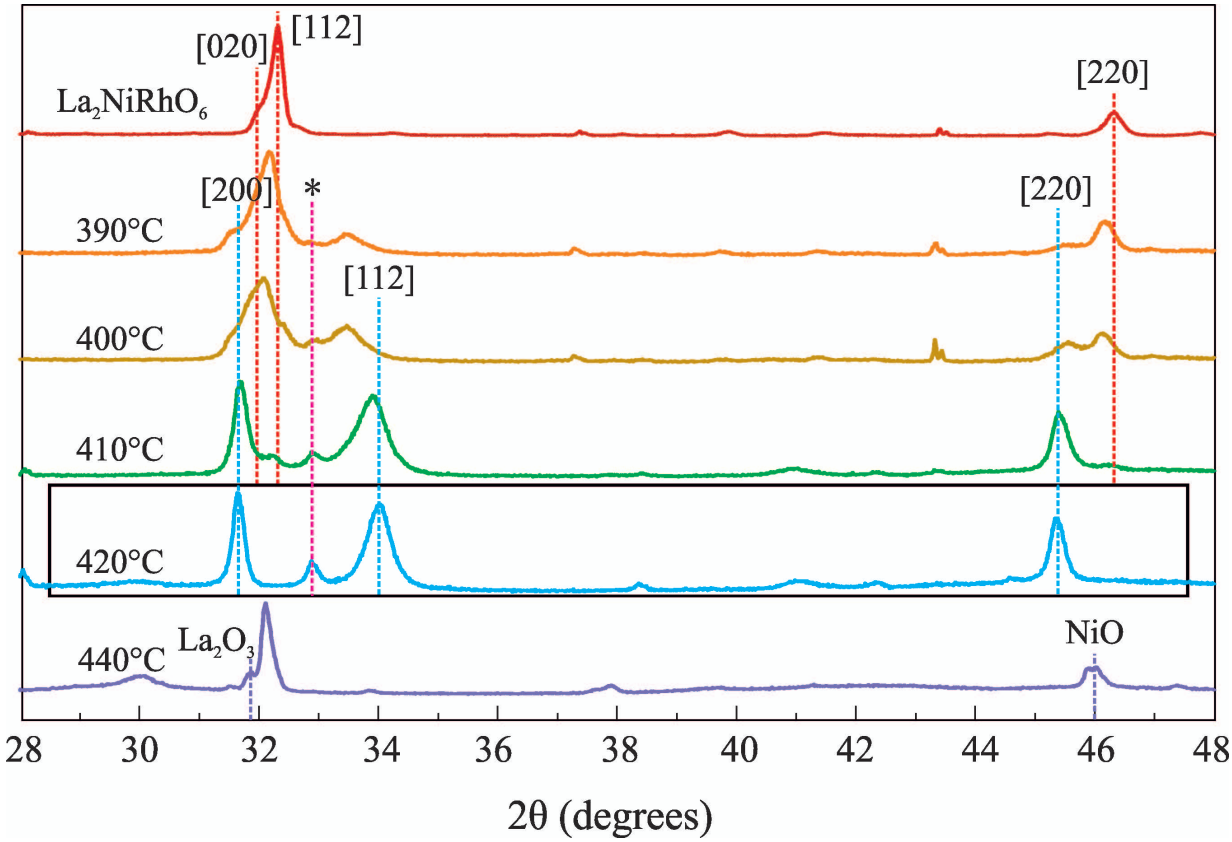


Figure 7-6 Topochemical reduction profile of La_2NiRhO_6 with Zr to form a compositional range of $La_2NiRhO_{6-\delta}$. The red dashed lines represent the orthorhombic peaks from La_2NiRhO_6; the blue dashed lines represent the tetragonal peaks from $La_2NiRhO_{6-\delta}$ at 420 °C; the pink dashed line with * indexes an impurity phase.

7.3.2.2. Initial Investigation of Reactivity of La_2MnRhO_6 and $LaSrMnRhO_6$ with Zr

Compared to La_2NiRhO_6, topochemical reduction reactions of La_2MnRhO_6 and $LaSrMnRhO_6$ encountered obstacles. Small-scale trial reactions of La_2MnRhO_6 with Zr were performed in the temperature range $300 \leq T/\ ^{o}C \leq 500$. The changes observed in XRD patterns at different reaction temperatures are plotted in Figure 7-7. The shoulder peak indexed as La_2O_3 (pink dashed line in Figure 7-7) indicates that the decomposition via non-topochemical reactions occurred in reduction reactions at 300 °C. The amorphous background observed at 500 °C indicates the total decomposition of the sample, suggesting that topochemically reducing La_2MnRhO_6 with Zr is highly unlikely.

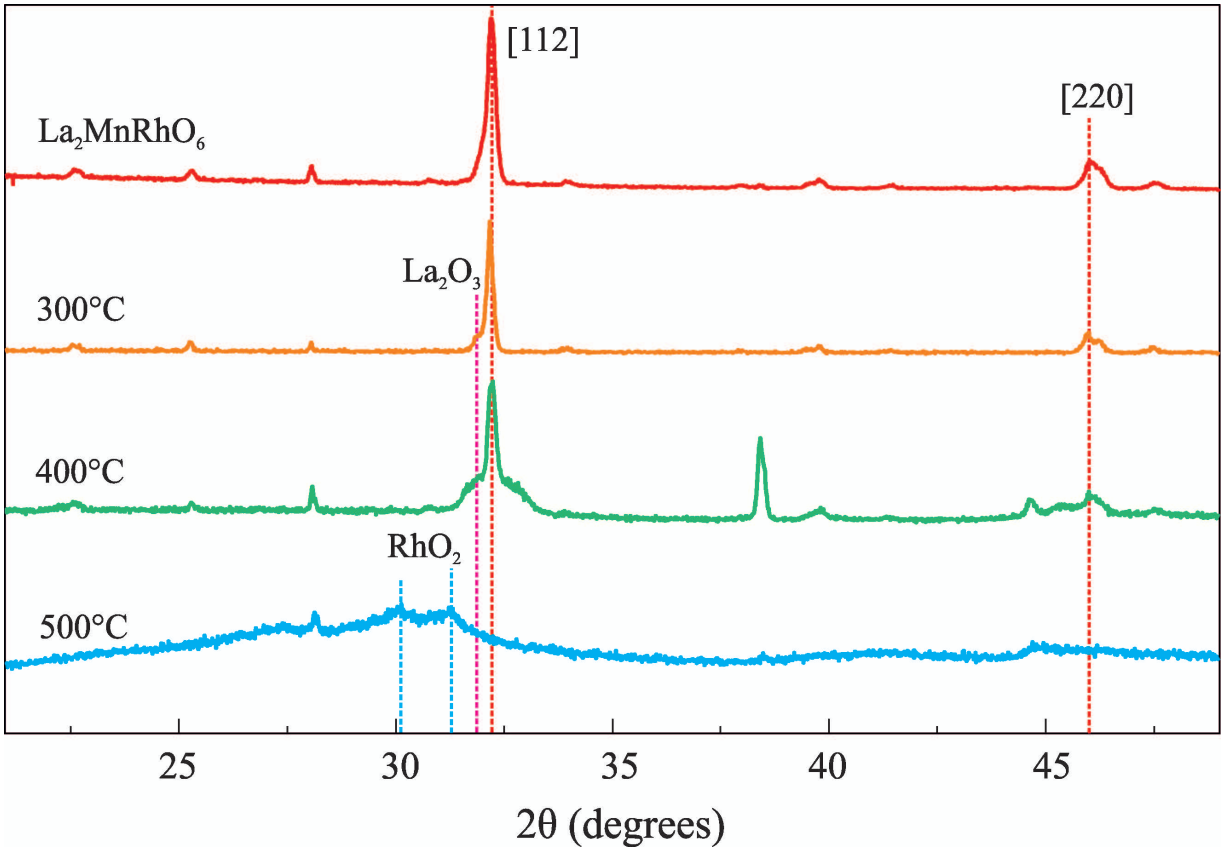


Figure 7-7 Trial reduction profile of La_2MnRhO_6 with Zr.

Small-scale trial reactions of $LaSrMnRhO_6$ with Zr were performed in the temperature range $400 \leq T/\,^{\circ}C \leq 500$. The changes observed in XRD patterns at different reaction temperatures are plotted in Figure 7-8. The symmetry of the main phase increased from orthorhombic to tetragonal once the deintercalation of apical oxide ions had started. The [112] peak in the starting material (shown in red dashed lines in Figure 7-8) vanished at 400 °C. The [200], [112] peaks from the tetragonal phase became sharp and symmetric at 450 °C (shown in blue dashed lines in Figure 7-8). When raising the reduction temperature to 500 °C, the sample was observed to decompose via non-topochemical reactions.

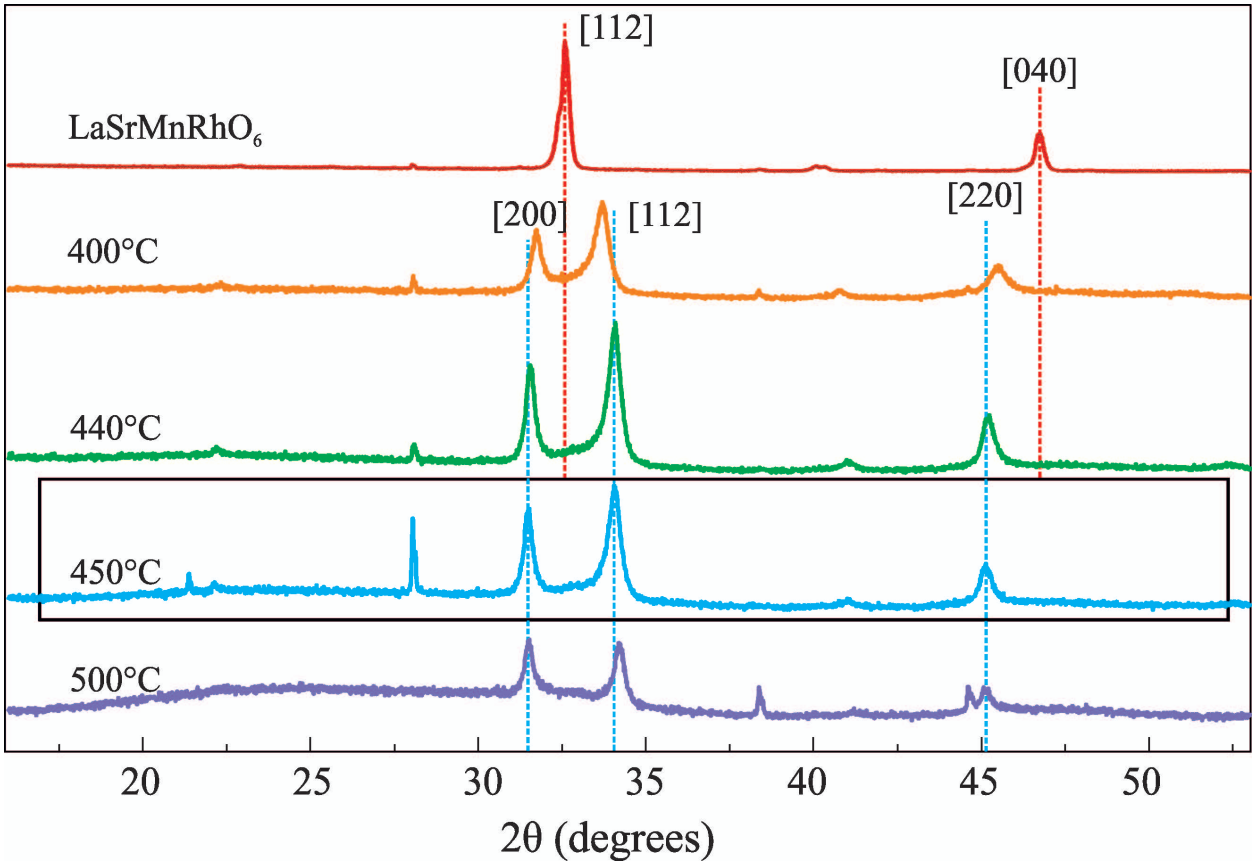


Figure 7-8 Topochemical reduction profile of $LaSrMnRhO_6$ with Zr to form a compositional range of $LaSrMnRhO_{6-\delta}$.

7.3.3. Structural and Chemical Characterisation of $La_2NiRhO_{6-\delta}$ and $LaSrMnRhO_{6-\delta}$

7.3.3.1. Thermogravimetric Analysis of $La_2NiRhO_{6-\delta}$ and $LaSrMnRhO_{6-\delta}$

Reductive thermogravimetric experiments were conducted to determine the chemical composition of the reduced $La_2NiRhO_{6-\delta}$ and $LaSrMnRhO_{6-\delta}$ phases. A small quantity of the reduced sample was heated under a steady flow of 10%/90% H_2/N_2 at a rate of 5 °C min^{-1} and held at 800 °C for 1 hour to complete the reaction before cooling. The oxygen content of the reduced sample was calculated by the mass difference between $La_2NiRhO_{6-\delta}$ or $LaSrMnRhO_{6-\delta}$ and totally reduced products (La_2O_3, Ni/MnO and Rh). TGA data from $La_2NiRhO_{6-\delta}$ and $LaSrMnRhO_{6-\delta}$ are shown in Figure 7-9 and Figure 7-10, respectively. During the reaction, $La_2NiRhO_{6-\delta}$ showed a mass loss of 1.93%, which is consistent with the composition of $La_2NiRhO_{4.462(1)}$; $LaSrMnRhO_{6-\delta}$ showed a mass loss of 3.38%, which is

consistent with the composition of $LaSrMnRhO_{4.46(2)}$. Henceforth, the reduced phases are referred to as $La_2NiRhO_{4.6}$ and $LaSrMnRhO_{4.5}$.

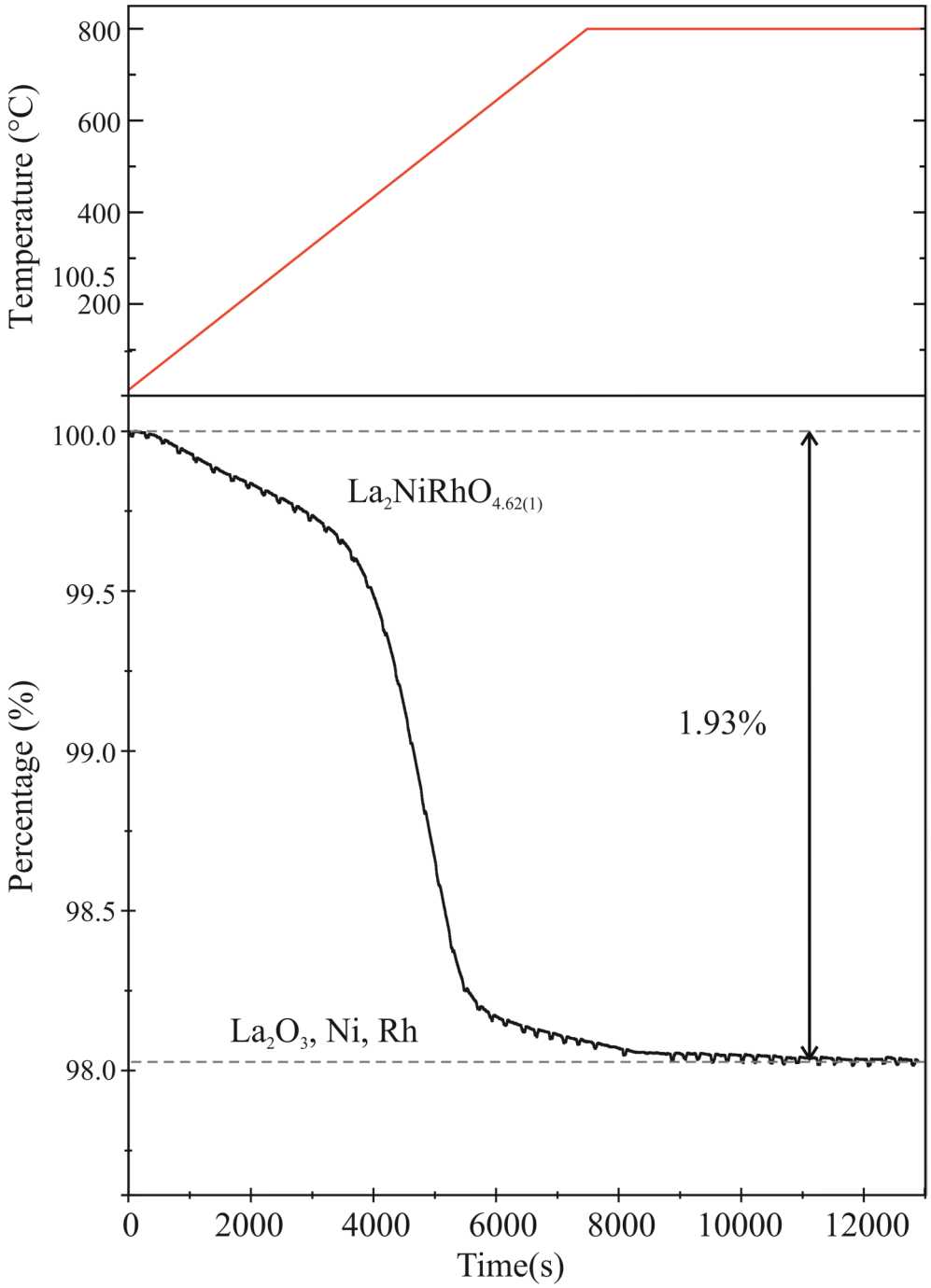


Figure 7-9 Reductive thermogravimetric data collected from $La_2NiRhO_{6-\delta}$. Top panel indicates the heating profile, bottom panel the relative mass of the sample.

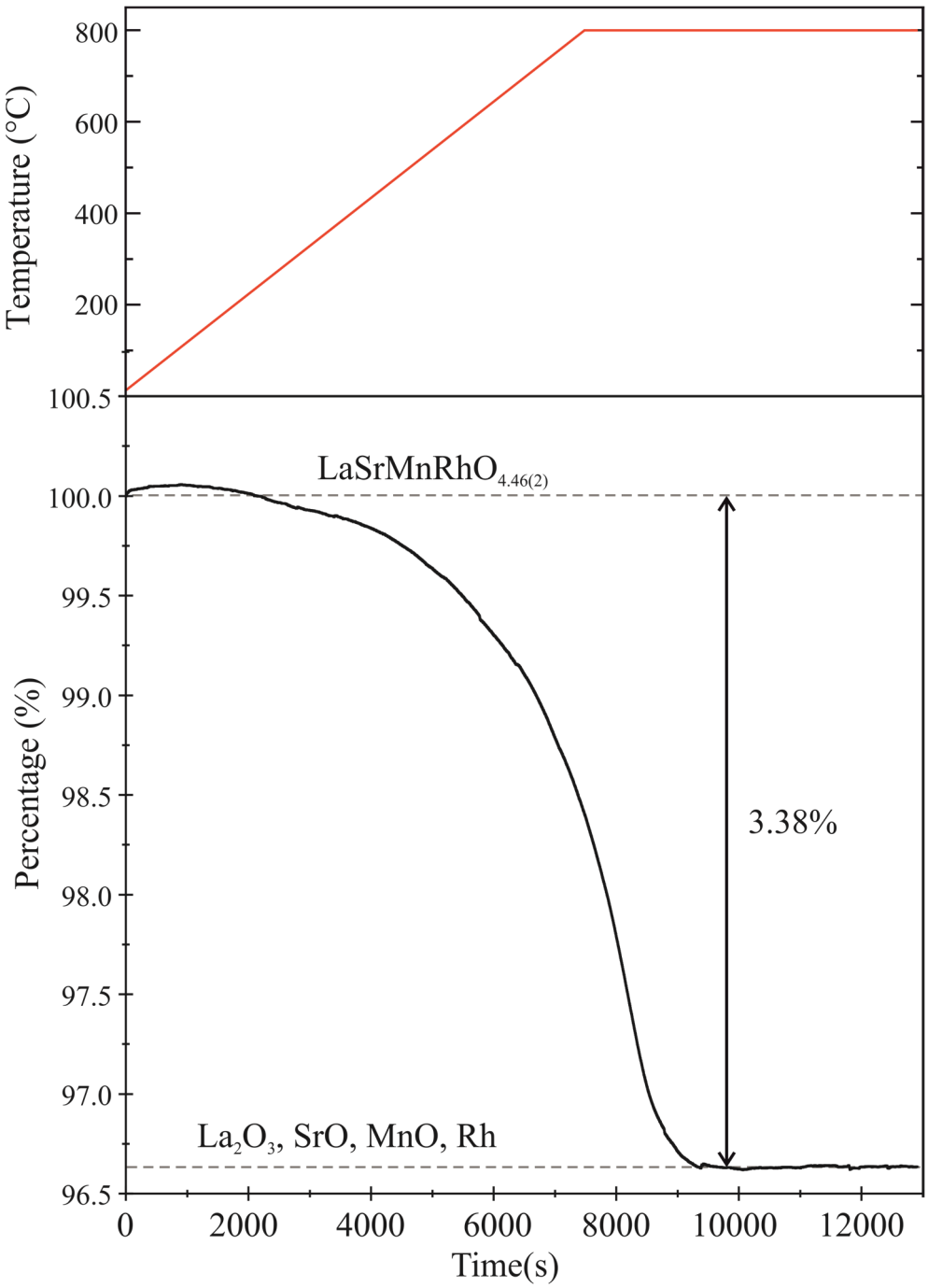


Figure 7-10 Reductive thermogravimetric data collected from $LaSrMnRhO_{6-\delta}$. Top panel indicates the heating profile, bottom panel the relative mass of the sample.

7.3.3.2. Space Group Determination of $La_2NiRhO_{4.6}$ and $LaSrMnRhO_{4.5}$

Neutron powder diffraction (NPD) data were collected from $La_2NiRhO_{4.6}$ and $LaSrMnRhO_{4.5}$ at ambient temperature using the D2B diffractometer and at 2 K using the D1B diffractometer in ILL, France (Section 2.3.2.2). These data can be indexed using tetragonal cells.

There had been an ambiguity over the accurate structure of both $La_2NiRhO_{4.6}$ and $LaSrMnRhO_{4.5}$, so the NPD data were refined against tetragonal models with different distortion modes. Among all the candidates, a *P*4*/mmm* model without a tilting distortion and an *I*4*/mcm* model with an $a^0a^0c^-$ tilting distortion (shown in Figure 7-11) are the most likely structures of $La_2NiRhO_{4.6}$ and $LaSrMnRhO_{4.5}$. Thus, comparisons of refinements using these two models were carried out.

The observed, calculated and difference plots of the Rietveld refinement against 298 K NPD data from $La_2NiRhO_{4.6}$ using an *I*4*/mcm* model and a *P*4*/mmm* model are shown in Figure 7-12. As shown in the insets of Figure 7-12 (bottom), a peak mismatch at 39° and 120° is observed in the refinement using a *P*4*/mmm* model while the refinement using an *I*4*/mcm* model shows a satisfactory fit (Figure 7-12 (top)). The observed, calculated and difference plots of Rietveld refinement against 298 K NPD data from $LaSrMnRhO_{4.5}$ using an *I*4*/mcm* model and a *P*4*/mmm* model are shown in Figure 7-13. Similarly, a peak mismatch at 39° is observed in the refinement using a *P*4*/mmm* model (Figure 7-13 (bottom)) while the refinement using an *I*4*/mcm* model shows a satisfactory fit (Figure 7-13 (top)). Table 7-5 shows the fitting statistics of the refinements of $La_2NiRhO_{4.6}$ and $LaSrMnRhO_{4.5}$ against the two models, respectively. The Rietveld refinements of both $La_2NiRhO_{4.6}$ and $LaSrMnRhO_{4.5}$ using an *I*4*/mcm* model are superior to these using a *P*4*/mmm* model. Thus, it is confirmed that both $La_2NiRhO_{4.6}$ and $LaSrMnRhO_{4.5}$ have *I*4*/mcm* symmetry, due to an $a^0a^0c^-$ tilting distortion.

Table 7-5 Fitting statistics from the structural refinements of $La_2NiRhO_{4.6}$ and $LaSrMnRhO_{4.5}$.

Sample	Space Group	χ^2	*wRp* (%)	*Rp* (%)
$La_2NiRhO_{4.6}$	***P4/mmm* (#123)**	7.452	7.10	5.14
	***I4/mcm* (#140)**	5.548	6.12	4.52
$LaSrMnRhO_{4.5}$	***P4/mmm* (#123)**	2.441	4.27	3.33
	***I4/mcm* (#140)**	2.178	3.98	3.12

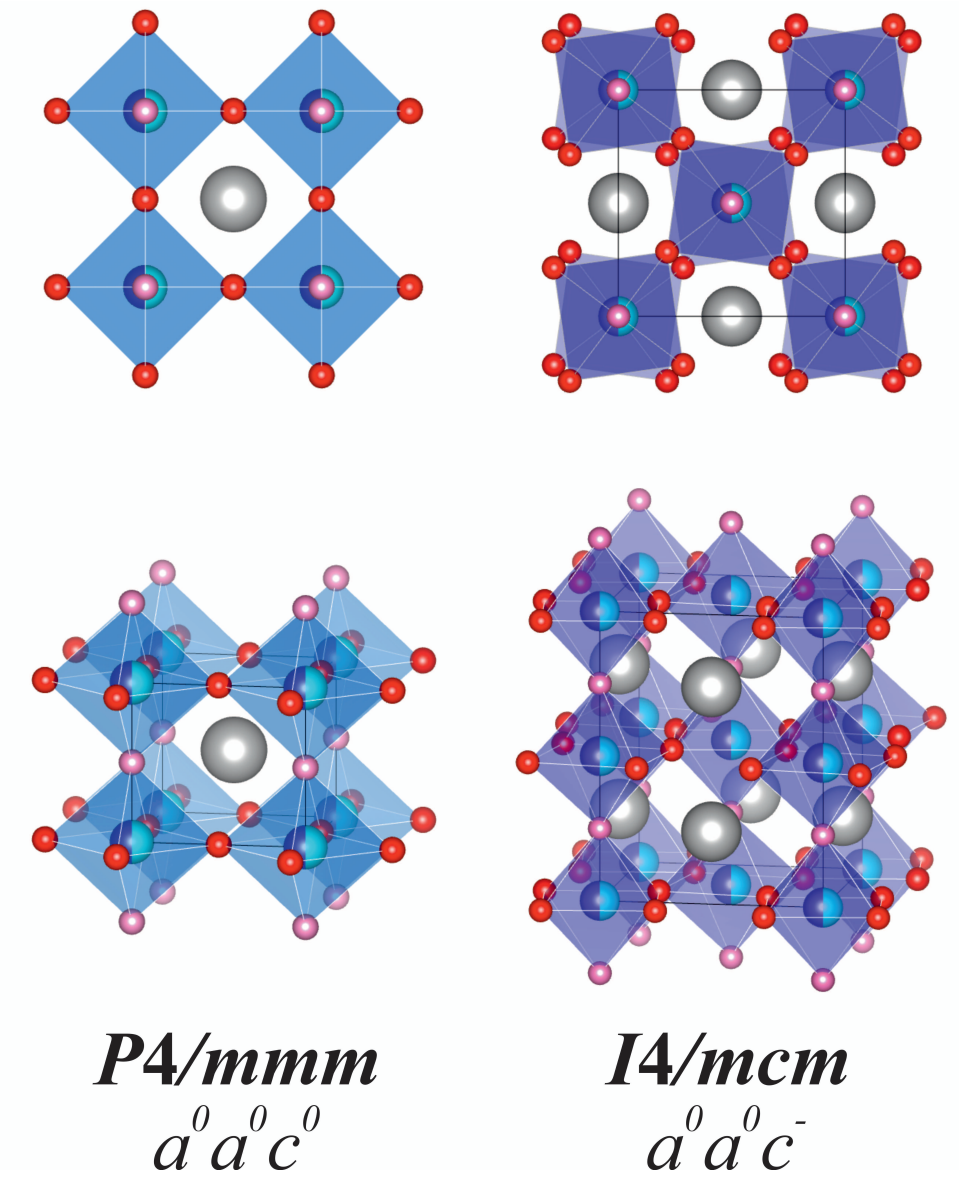


Figure 7-11 Crystal structures of $La_2NiRhO_{4.6}$ in *P4/mmm* space group (left) and *I4/mcm* space group (right). The top panel shows views down the [010] directions. Blue and purple octahedra denote the Ni/Rh site. Grey, dark purple, light blue, red, pink spheres represent La, Ni, Rh, O, partially occupied O sites, respectively.

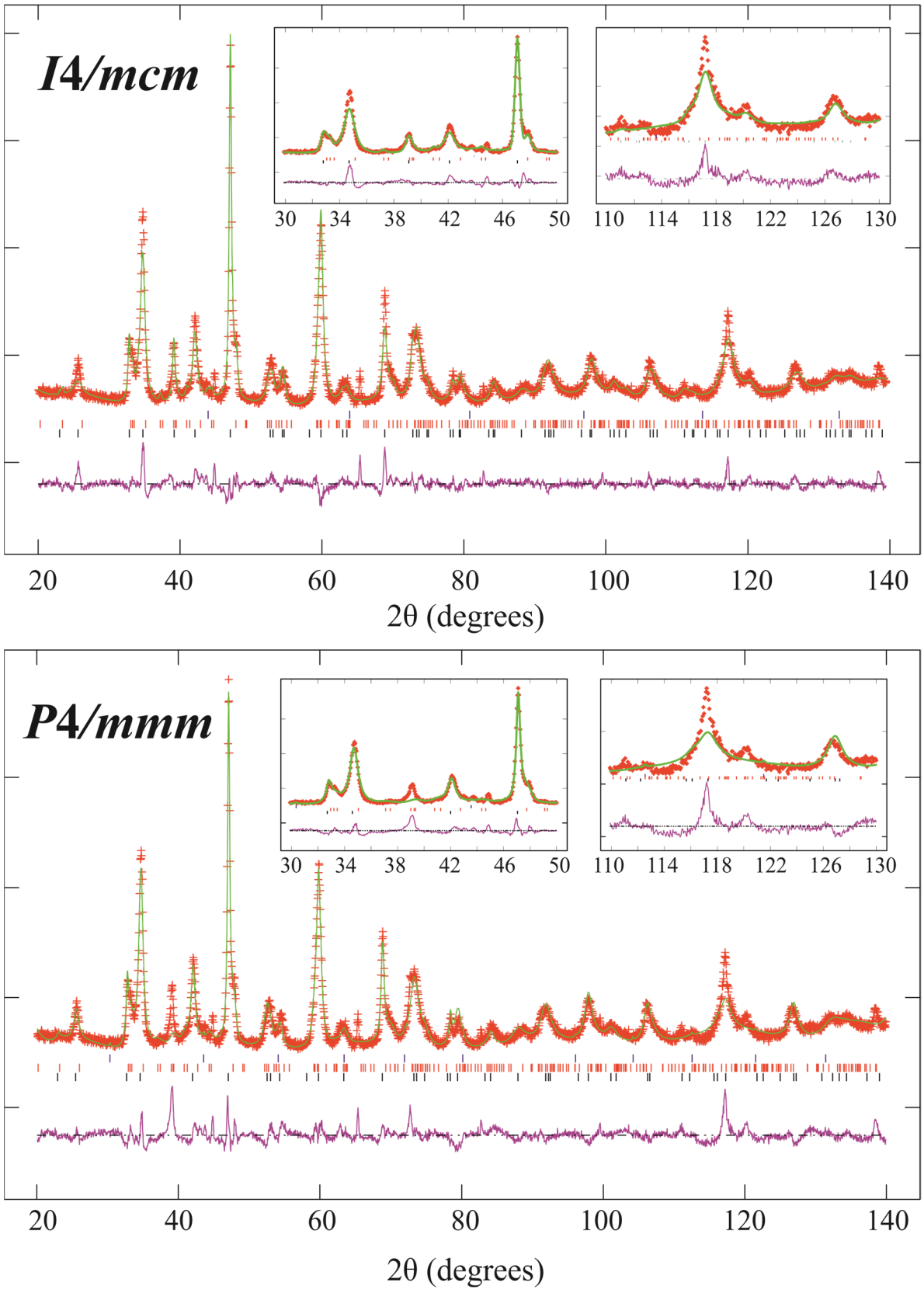


Figure 7-12 Observed, calculated and difference plots from the refinement of $La_2NiRhO_{4.6}$ against NPD data collected at 298 K using an *I4/mcm* model (top) and a *P4/mmm* model (bottom). Upper tick marks present the peak positions of vanadium from sample containers, middle ticks mark the minority phase La_2NiRhO_6 and lower tick marks the majority phase $La_2NiRhO_{4.6}$.

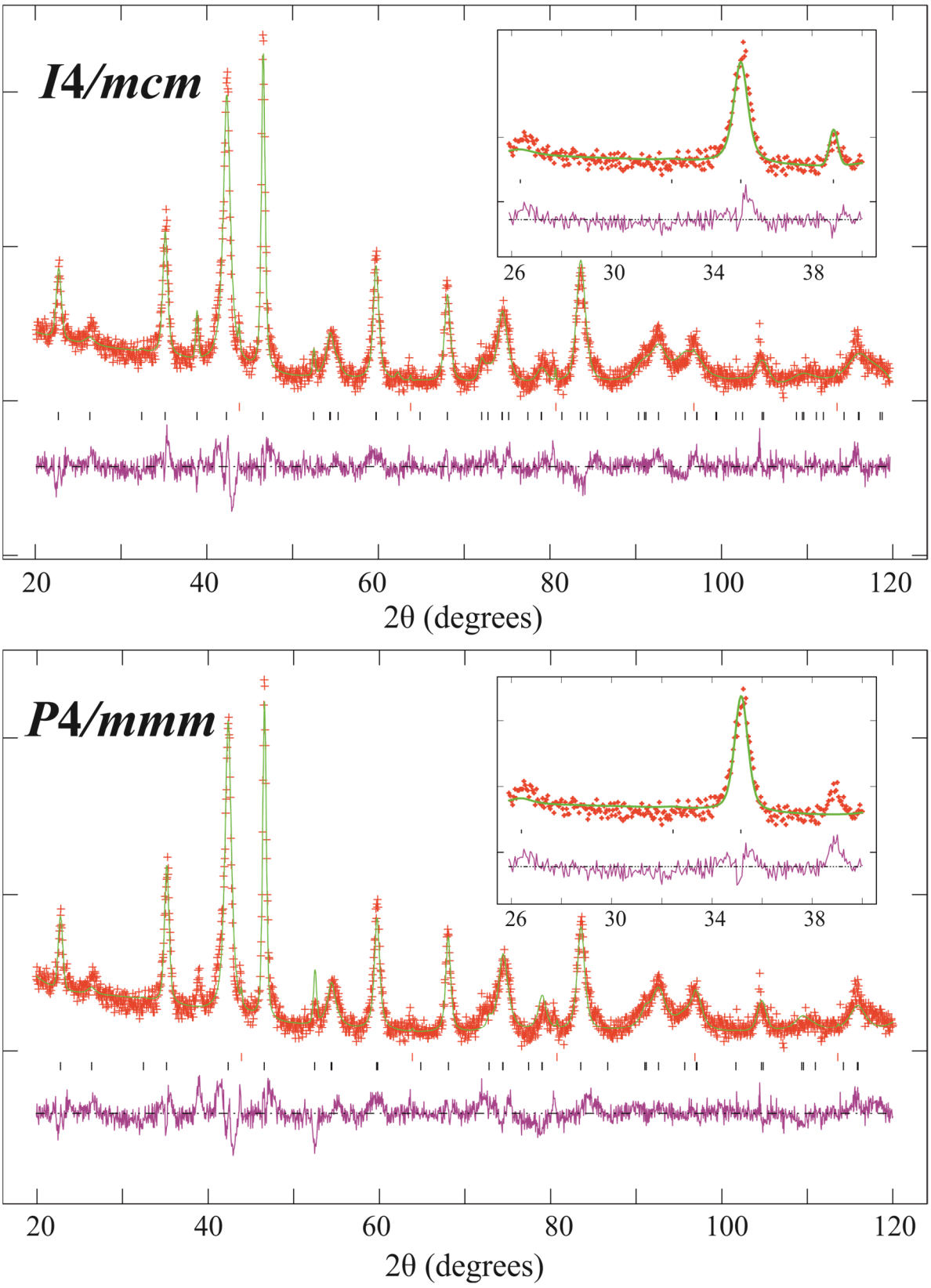


Figure 7-13 Observed, calculated and difference plots from the refinement of $LaSrMnRhO_{4.5}$ against NPD data collected at 298 K using an *I4/mcm* model (top) and a *P4/mmm* model (bottom). Upper tick marks present the peak positions of vanadium from sample containers, lower tick marks present the peak positions of $LaSrMnRhO_{4.5}$.

7.3.3.3. Neutron Powder Diffraction of $La_2NiRhO_{4.6}$ and $LaSrMnRhO_{4.5}$

In the previous section, the unit cells of $La_2NiRhO_{4.6}$ and $LaSrMnRhO_{4.5}$ have been confirmed. The observed, calculated and difference plots of NPD data from $La_2NiRhO_{4.6}$ and $LaSrMnRhO_{4.5}$ at 298 K are shown in Figure 7-14 and Figure 7-15.

In the final refinement cycles of $La_2NiRhO_{4.6}$, the occupancy of the O(2) anion site was refined to a value of 0.255(1) without constraint, consistent with the composition of $La_2NiRhO_{4.6}$ obtained from TGA data. There is no evidence for partial occupancy on any of other anion sites. Compared to the NPD pattern of $La_2NiRhO_{4.6}$ at 298 K, the NPD pattern of $La_2NiRhO_{4.6}$ at 2 K differs slightly with a weak magnetic peak at around 3.9 Å (Figure 7-16). However, as the only difference between the NPD patterns at 298 K and 2 K, it's difficult to confirm any long-range magnetic order in the system from this peak.

Similarly, in the final refinement cycles of $LaSrMnRhO_{4.5}$, the occupancy of the O(2) anion site was refined to a value of 0.211(1) without constraint, close to the composition of $LaSrMnRhO_{4.5}$ obtained from TGA data. The consistency of the NPD patterns of $LaSrMnRhO_{4.5}$ at both 298 K and 2 K (Figure 7-17), particularly the lack of extra diffraction peaks, indicates the absence of long-range magnetic order in the system.

Full details of the structural parameters and selected bond lengths are given in Table 7-6 and Table 7-7 for $La_2NiRhO_{4.6}$, Table 7-8 and Table 7-9 for $LaSrMnRhO_{4.5}$.

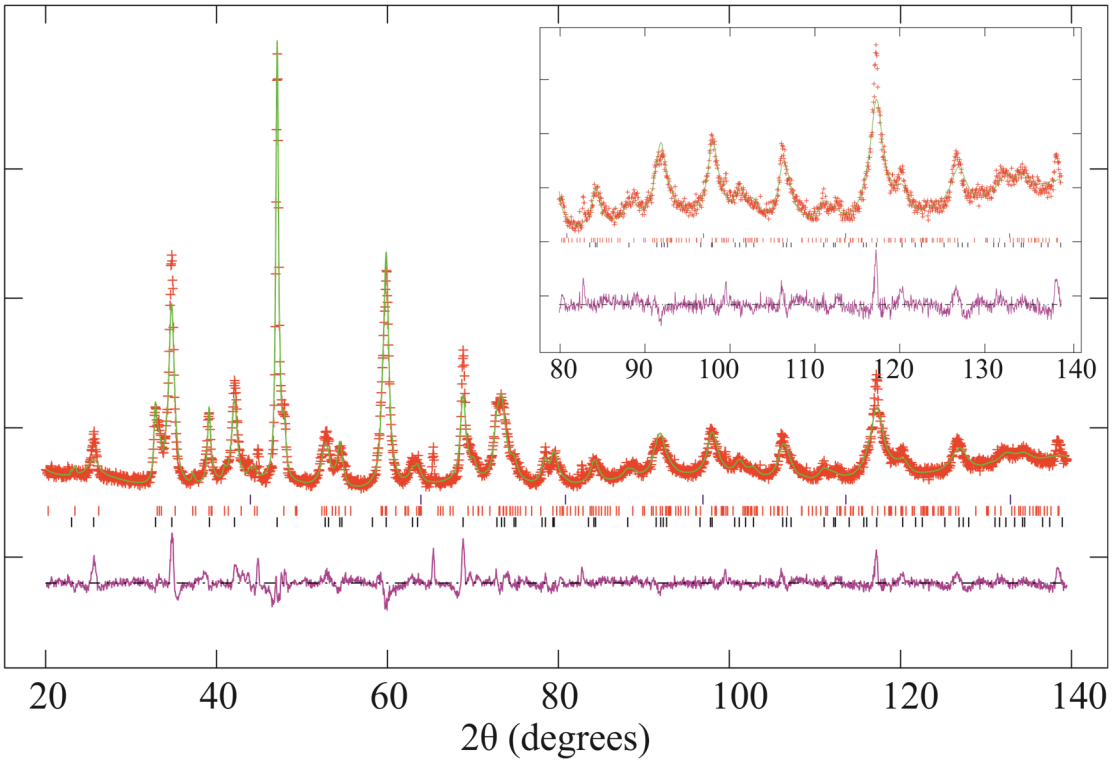


Figure 7-14 Observed, calculated and difference plots from the refinement of $La_2NiRhO_{4.6}$ against NPD data collected at 298 K using an *I4/mcm* model. Upper tick marks indicate peak positions of vanadium from sample containers, middle tick marks indicate peak positions of La_2NiRhO_6 and lower tick marks indicate peak positions of $La_2NiRhO_{4.6}$.

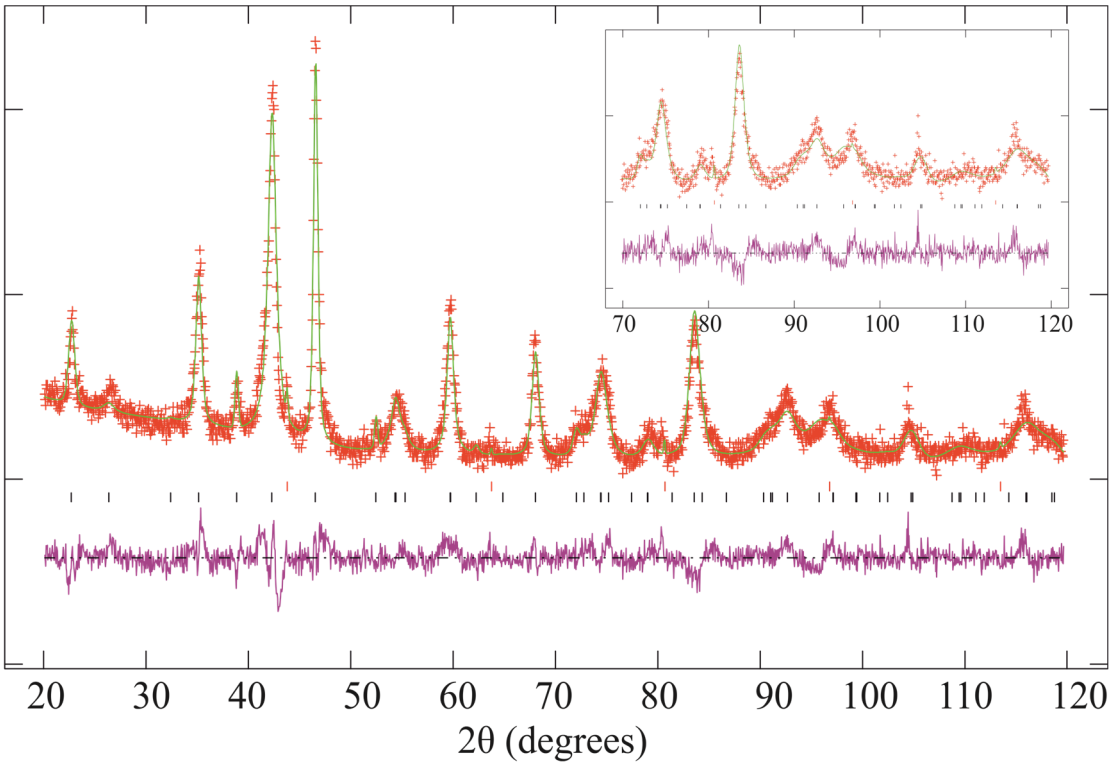


Figure 7-15 Observed, calculated and difference plots from the refinement of $LaSrMnRhO_{4.5}$ against NPD data collected at 298 K using an *I4/mcm* model. Upper tick marks indicate peak positions of vanadium from sample containers and lower tick marks indicate peak positions of $LaSrMnRhO_{4.5}$.

Table 7-6 Structural parameters from the refinement of $La_2NiRhO_{4.6}$ against NPD data collected at 298 K.

Atom	Wyckoff Position	*x*	*y*	*z*	Fraction	U_{iso} (Å^2)
La	4*i*	½	0	¼	1	0.019(1)
Ni/Rh	2*a*	0	0	0	0.5/0.5	0.018(2)
O(1)	4*i*	0.2134(5)	0.2865(5)	0	1	0.028(1)
O(2)	2*d*	0	0	¼	0.255(1)	0.111(18)

$La_2NiRhO_{4.6}$ - space group *I*4/*mcm* (#140)
Formula mass: 509.58 g mol^{-1}, Z = 2
a = 5.6387(5) Å, *c* = 7.1818(13) Å, Volume = 2228.35(6) Å^3
Radiation source: Neutron Powder Diffraction
Temperature: 298 K
χ^2 = 5.548, *wRp* = 6.12 %; *Rp* = 4.52 %.

Table 7-7 Selected bond lengths from the refined structure of $La_2NiRhO_{4.5}$ at 298 K.

Cation	Anion	Length (Å)
La	O (1)	2.4742(3) × 4
	O (1)	2.9059(3) × 4
	O (2)	2.8193(3) × 4
Ni/Rh	O (1)	2.0147(2) × 4
	O (2)	1.7955(4) × 2

Table 7-8 Structural parameters from the refinement of $LaSrMnRhO_{4.5}$ against NPD data collected at 298 K.

Atom	Wyckoff Position	*x*	*y*	*z*	Fraction	U_{iso} (Å^2)
La/Sr	4*i*	½	0	¼	0.5/0.5	0.014(2)
Mn/Rh	2*a*	0	0	0	0.5/0.5	0.045(3)
O(1)	4*i*	0.2324(6)	0.2676(6)	0	1	0.020(2)
O(2)	2*d*	0	0	¼	0.211(1)	0.127(24)

$LaSrMnRhO_{4.5}$ - space group *I*4/*mcm* (#140)
Formula mass: 455.1 g mol^{-1}, Z = 2
a = 5.6889(9) Å, *c* = 6.9588(19) Å, Volume = 225.2(1) Å^3
Radiation source: Neutron Powder Diffraction
Temperature: 298 K
χ^2 = 2.178, *wRp* = 3.98 %; *Rp* = 3.12 %.

Table 7-9 Selected bond lengths from the refined structure of $LaSrMnRhO_{4.5}$ at 298 K.

Cation	Anion	Length (Å)
La/Sr	O (1)	2.5539(5) × 4
	O (1)	2.7680(5) × 4
	O (2)	2.8445(5) × 4
Mn/Rh	O (1)	2.0163(4) × 4
	O (2)	1.7397(5) × 2

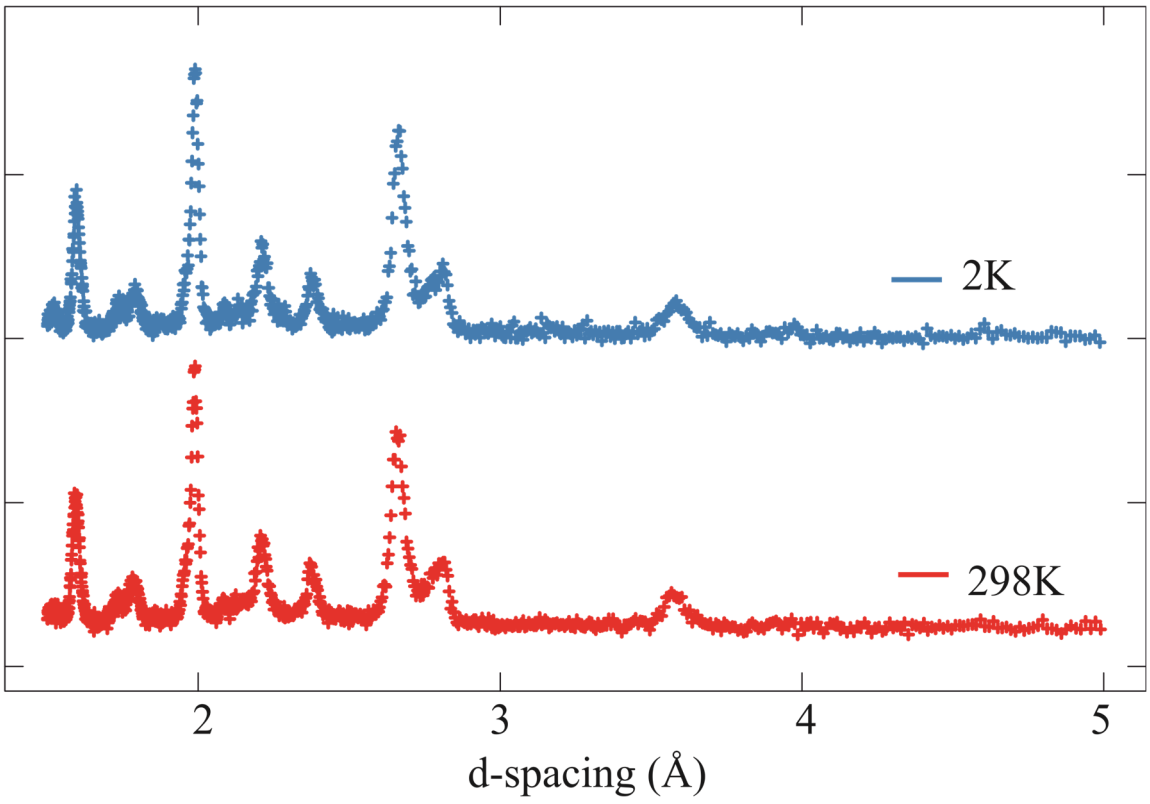


Figure 7-16 Comparison of NPD data collected from $La_2NiRhO_{4.6}$ at 298 K (using D2B diffractometer) and 2 K (using D1B diffractometer).

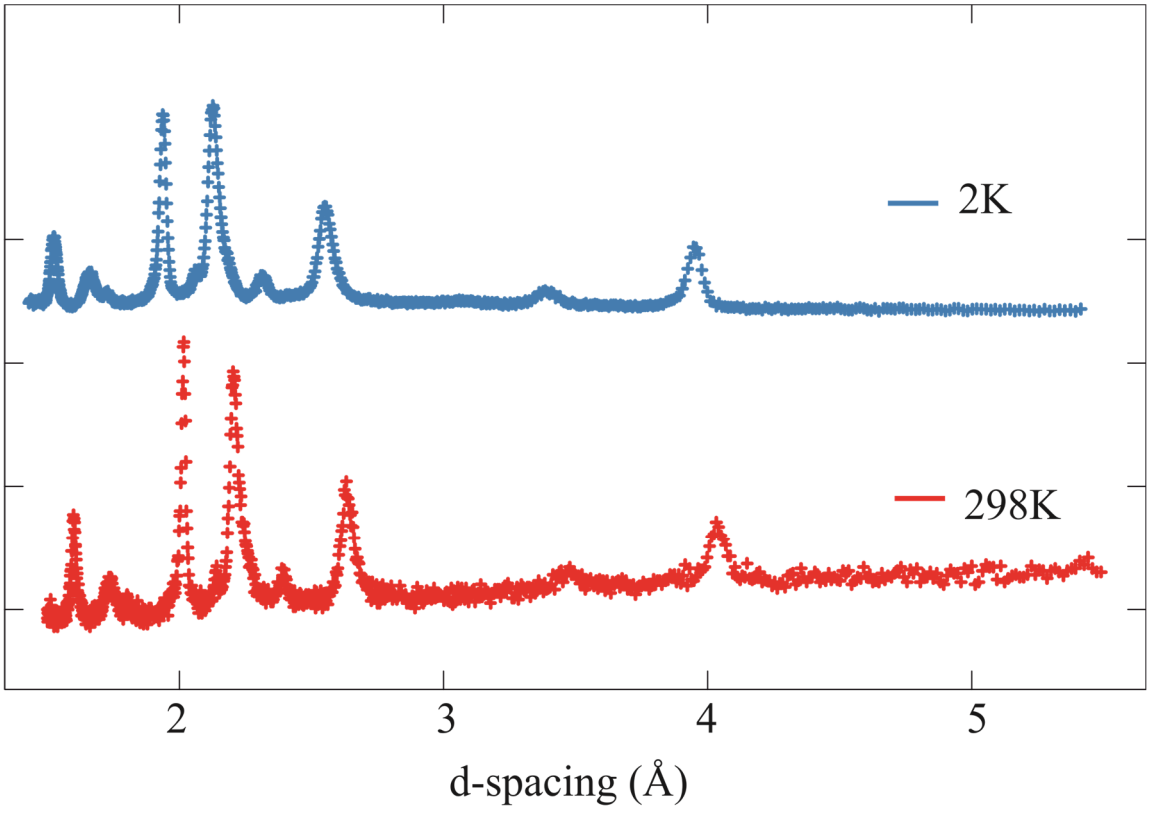


Figure 7-17 Comparison of NPD data collected from $LaSrMnRhO_{4.5}$ at 298 K (using D2B diffractometer) and 2 K (using D1B diffractometer).

7.3.4. Magnetic Characterisation of $La_2NiRhO_{4.6}$ and $LaSrMnRhO_{4.5}$

7.3.4.1. Magnetic Characterisation of $La_2NiRhO_{4.6}$

A 'ferromagnetic subtraction' technique (Section 2.5.3) was used to collect the magnetisation data from $La_2NiRhO_{4.6}$ due to the presence of small amounts (< 0.1 wt%) of ferromagnetic elemental Ni.

Figure 7-18 (top) shows that the paramagnetic susceptibility of $La_2NiRhO_{4.6}$ follows the Curie-Weiss law ($\chi = C/(T - \theta) + K$) in the range $70 < T/K < 300$ to yield values of $C = 0.223(1)$ cm^3 K mol^{-1} and $\theta = -7.24(3)$ K. Below 70 K, the saturated ferromagnetic moment of $La_2NiRhO_{4.6}$ increases sharply (Figure 7-18 (bottom)).

Based on previous studies of reduced rhodium-containing Ruddlesden-Popper phase $LaSrCo_{0.5}Rh_{0.5}O_{3.25}$, Ni and Rh cations in $La_2NiRhO_{4.6}$ are believed to be randomly and equally occupying square-based pyramidal sites (C_{4v}) and square-planar sites (D_{4h}) in a 1:1 ratio, with an oxidation state combination of Ni^{I} and Rh^{II}. The nominal Rh^{II} is believed to disproportionate to a 1:1 ratio of Rh^{III}:Rh^{I}, with Rh^{III} located in C_{4v} sites and Rh^{I} located in D_{4h} sites. Both low-spin $4d^6$ Rh^{III} and low-spin $4d^8$ Rh^{I} are diamagnetic, thus only the $3d^9$ Ni^{I} centres contribute to the magnetic behaviour. The proposed combination is expected to give a value of $\mu^2 = 3\ \mu_B^2$ and $C = 0.375$ cm^3 K mol^{-1} in spin only formula, which is close to the observed value of 0.223(1) cm^3 K mol^{-1}. Magnetisation-field data shown in Figure 7-19 indicates that $La_2NiRhO_{4.6}$ exhibits weak hysteresis at both 300 K and 5 K.

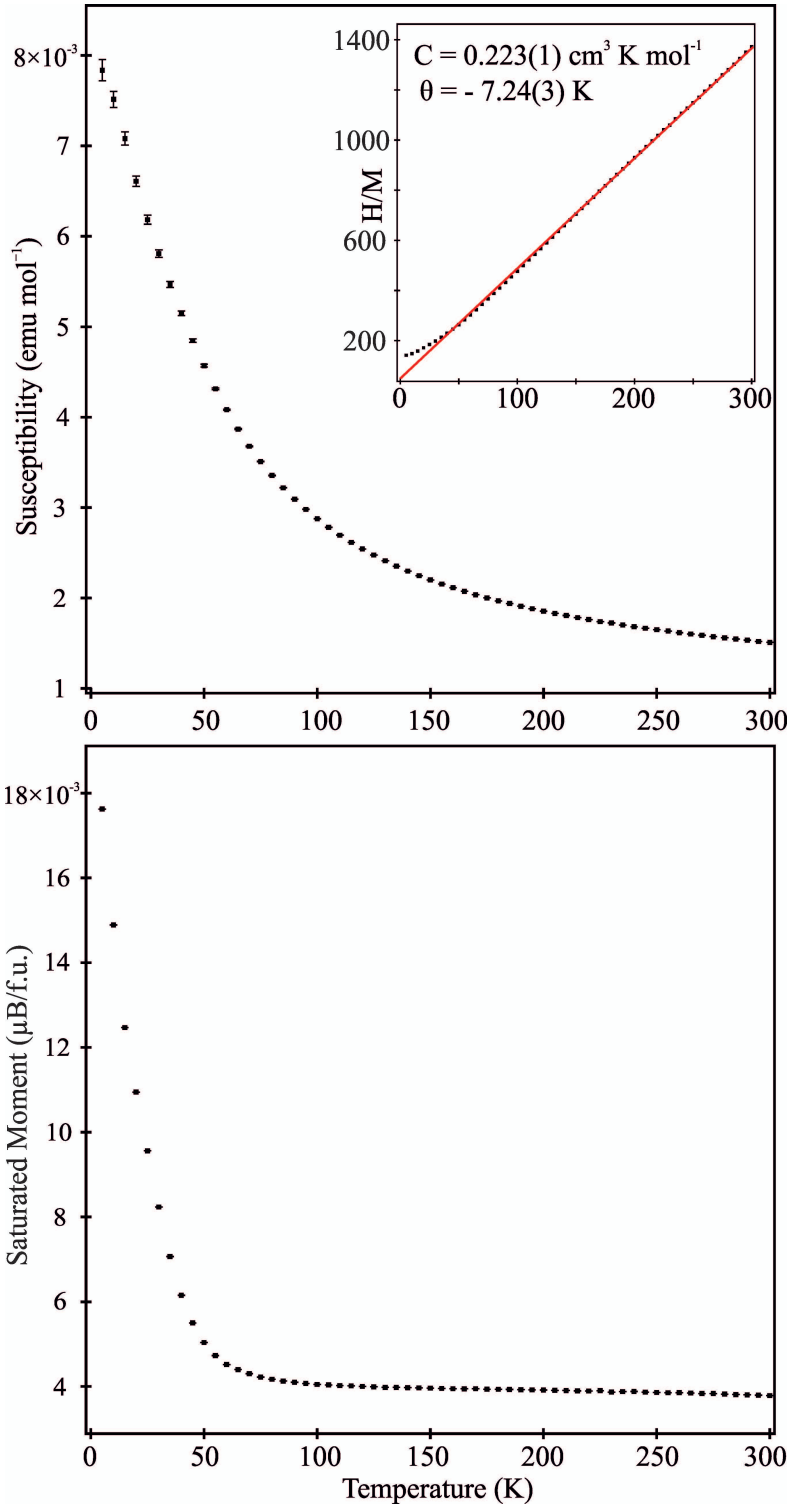


Figure 7-18 The paramagnetic susceptibility (top) and saturated ferromagnetic moment (bottom) of $La_2NiRhO_{4.6}$ collected as a function of temperature. Inset: the fit to the Curie-Weiss law in the temperature range $70 < T/K < 300$.

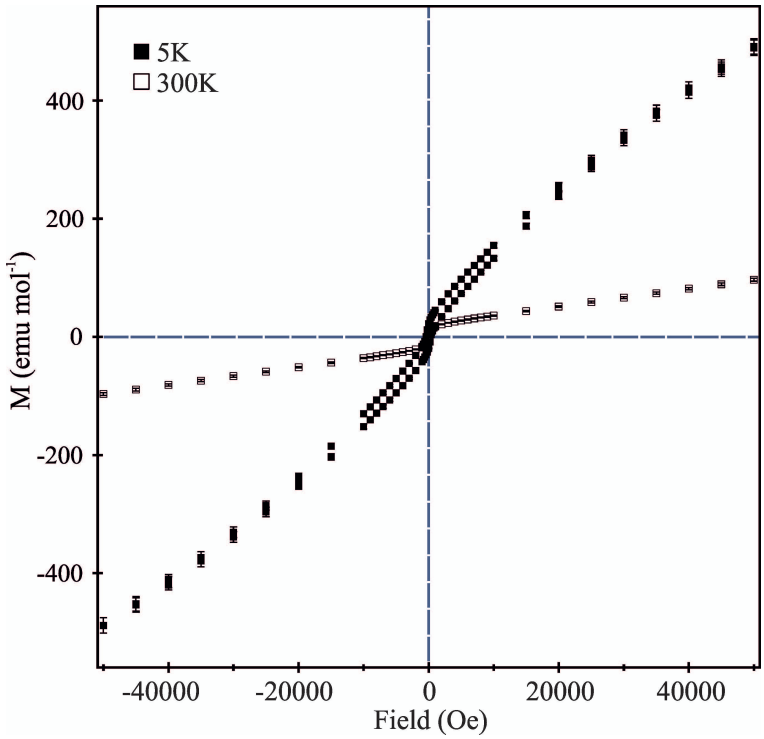


Figure 7-19 Magnetisation data collected as a function of applied field from $La_2NiRhO_{4.6}$.

7.3.4.2. Magnetic Characterisation of $LaSrMnRhO_{4.5}$

Since there are no ferromagnetic impurities in the $LaSrMnRhO_{4.5}$ phase, zero-field-cooled (ZFC) and field-cooled (FC) magnetization data were collected from $LaSrMnRhO_{4.5}$. As shown in the inset of Figure 7-20 (left), ZFC and FC data diverge at an early stage from room temperature, which means the Curie Weiss law is not applicable in the case of $LaSrMnRhO_{4.5}$. Analogous to $La_2NiRhO_{4.6}$, the most likely structural arrangement for *B*-site cations in $LaSrMnRhO_{4.5}$ is also a 1:1 ratio of C_{4v} sites:D_{4h} sites, with Rh^{III} located in C_{4v} sites, Rh^{I} located in D_{4h} sites and Mn^{II} located in both sites. The multiple unpaired electrons in $3d^5$ Mn^{II} lead to strong magnetic interactions and huge moments, as observed in ZFC/FC data. The complicated and strong magnetic interactions between Mn and Rh sites suggest a high level of structural and chemical disorder in the phase $LaSrMnRhO_{4.5}$ and can explain why the Curie-Weiss law is not applicable.

As shown in Figure 7-20 (right), the magnetisation data collected at 300 K as a function of applied field is linear and passes through the origin, while the analogous data collected at 5 K exhibit weak hysteresis. Hence, we can conclude that $LaSrMnRhO_{4.5}$ adopts a magnetically ordered state at 5 K which is contributed by $3d^5$ Mn^{II} sites.

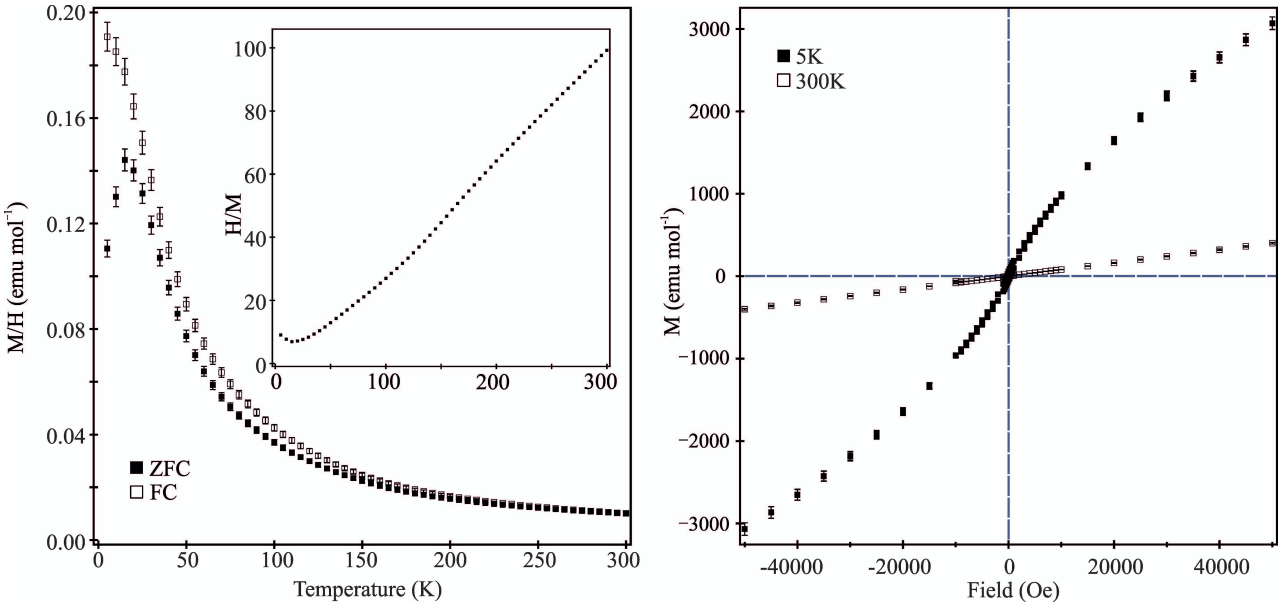


Figure 7-20 (left) Zero-field-cooled and field-cooled magnetisation data collected in an applied field of 100 Oe. Inset shows the fit to the Curie-Weiss law; (right) Magnetisation data collected as a function of applied field from $LaSrMnRhO_{4.5}$.

7.4. Discussion

The magnetisation data collected from $La_2NiRhO_{4.6}$ as a function of magnetic field show hysteresis at both 300 K and 5 K. The hysteresis observed at 300 K is attributed to the presence of elemental nickel. However, the large increase in the coercive field in the data collected at 5 K suggest $La_2NiRhO_{4.6}$ adopts a canted antiferromagnetic state, although no sign of long-range magnetic order is observed in NPD data collected at 2 K.

As discussed in Section 7.3.4.1, the electron configurations of the Ni and Rh sites in $La_2NiRhO_{4.6}$ are shown in Figure 7-21. Thus, the proposed antiferromagnetic behaviour of $La_2NiRhO_{4.6}$ can be explained on the basis of exchange coupling between $S = ½$ $3d^9$ Ni^I sites and $S = 0$ $4d^8/4d^6$ Rh^I/Rh^{III} sites.

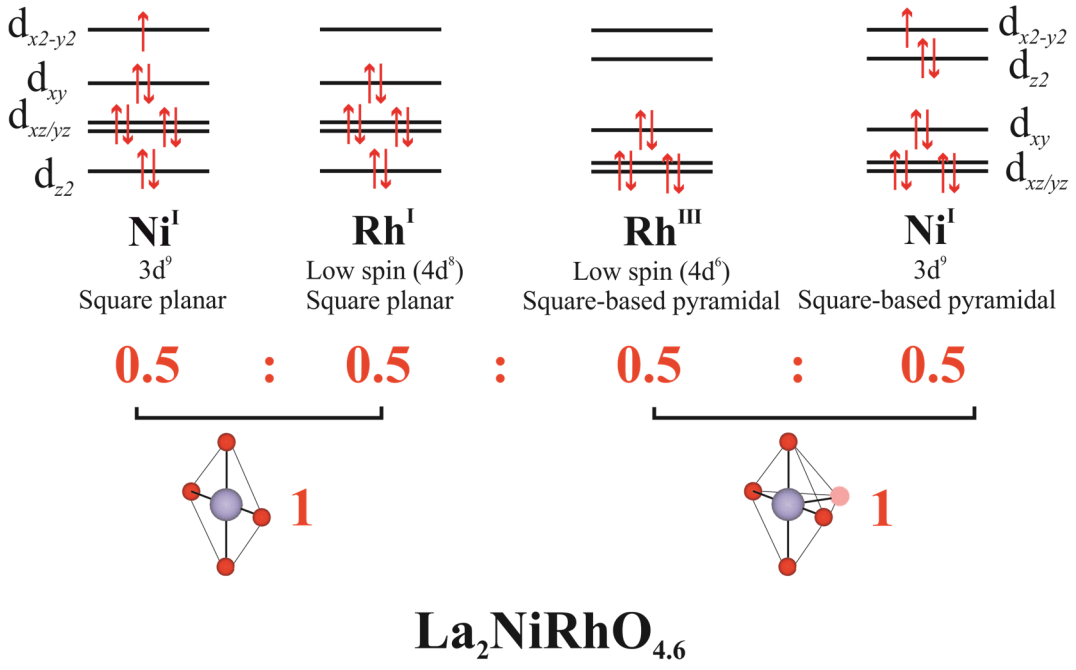


Figure 7-21 Electron configurations of Ni^I and $Rh^{I/III}$ sites in $La_2NiRhO_{4.6}$.

The in-plane magnetic interactions in $La_2NiRhO_{4.6}$ are listed in Figure 7-22. As we can see, Ni in both C_{4v} and D_{4h} sites have only one unpaired electron located in $3d_{x^2-y^2}$ orbital, thus the in-plane (Ni $3d_{x^2-y^2}$)^1 - O $2p$ - (Ni $3d_{x^2-y^2}$)^1 super-exchange couplings between Ni sites yield strong antiferromagnetic interactions.

The out-of-plane interactions between d_{z^2} orbitals are listed in Figure 7-23. Compared to the in-plane magnetic interactions, the out-of-plane interactions are weak as the Ni 3d orbitals which have a z-component (d_{z^2}, d_{xz}, d_{yz}) are all filled, indicating the absence of ordering in interlayer couplings. In addition, the random distribution of Ni and Rh in the system also works against the long-range magnetic order.

Therefore, the strong antiferromagnetic in-plane (Ni $3d_{x^2-y^2}$)^1 - O $2p$ - (Ni $3d_{x^2-y^2}$)^1 couplings can yield intralayer antiferromagnetic interactions, which is consistent with the observation of a canted antiferromagnetic state from magnetisation-field data. The weak out-of-plane interactions can explain the lack of 3d magnetic order in $La_2NiRhO_{4.6}$, which is consistent with the observation that there are no extra diffraction peaks in the comparison of NPD data collected at 298 K and 2 K.

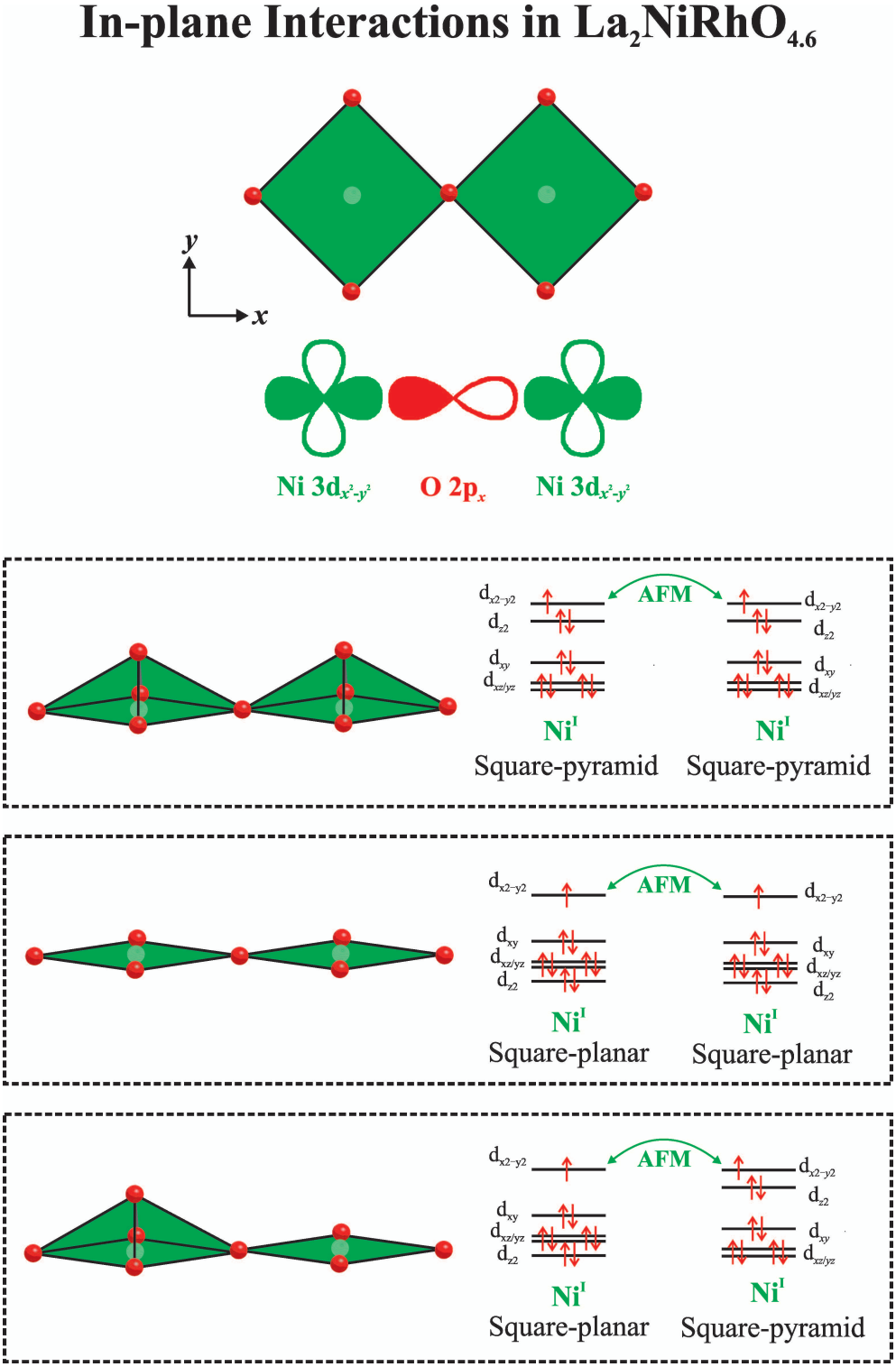


Figure 7-22 In-plane magnetic interactions between Ni and Rh centres in $La_2NiRhO_{4.6}$.

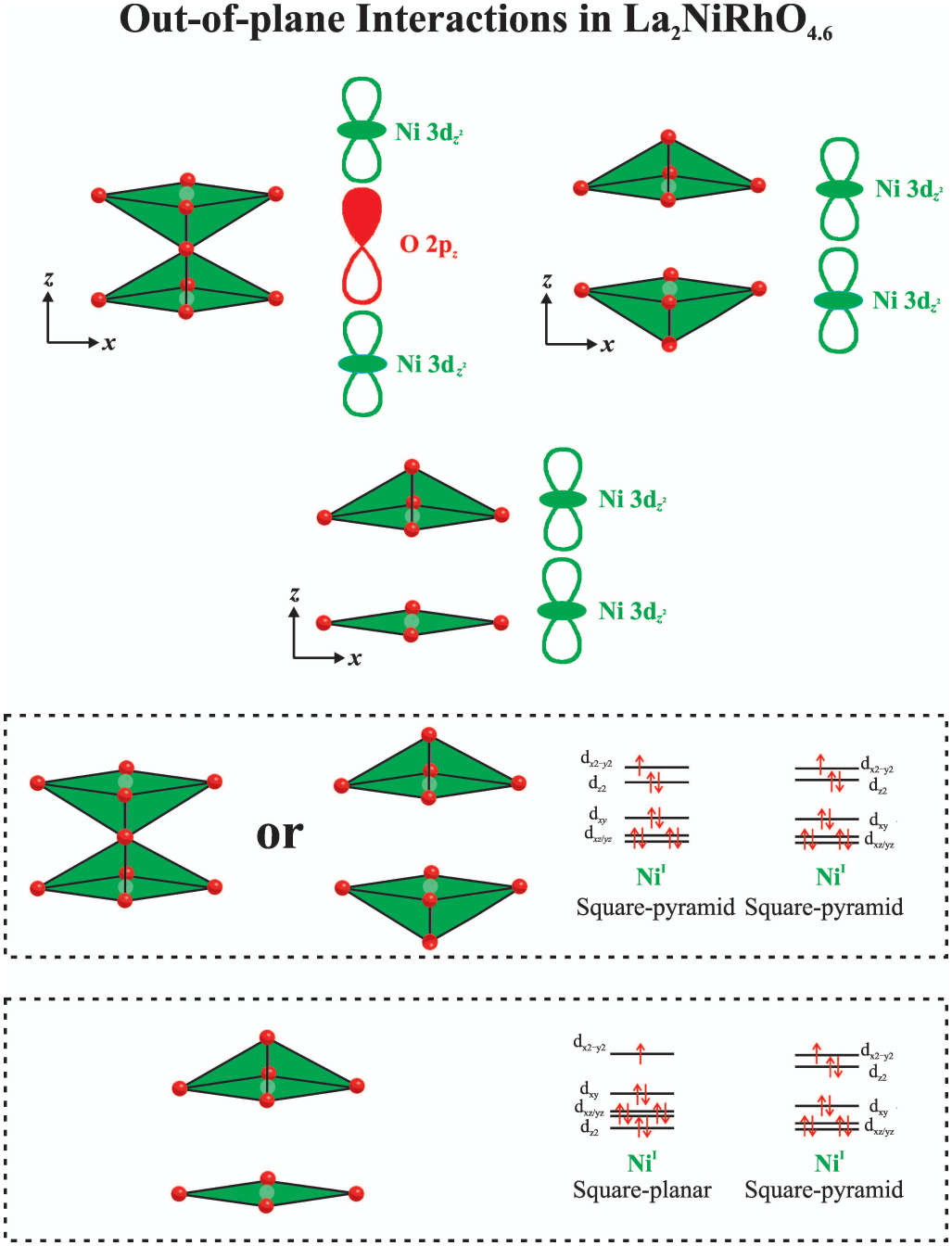


Figure 7-23 Out-of-plane magnetic interactions between Ni and Rh centres in $La_2NiRhO_{4.6}$.

7.5. Conclusion

Topochemical reduction of the solid solution phases La_2NiRhO_6 and $LaSrMnRhO_6$ with Zr yields $La_2NiRhO_{4.6}$ and $LaSrMnRhO_{4.5}$. The reduced oxides can be indexed using tetragonal unit cells ($La_2NiRhO_{4.6}$: a = 5.6387(5) Å, c = 7.1818(13) Å; $LaSrMnRhO_{4.5}$: a = 5.6889(9) Å, c = 6.9588(19) Å). Analogous to $LaSrCo_{0.5}Rh_{0.5}O_{3.25}$, both of the reduced phases are mixed valence $Rh^{I/III}$ compounds and no magnetic ordering at low temperature is observed in these two phases. For $La_2NiRhO_{4.6}$, the strong in-plane antiferromagnetic interactions result in a short range of antiferromagnetic couplings while the weak out-of-plane interactions disrupt the three-dimensional magnetic order of the system.

Chapter 8

Synthesis and Characterisation of $La_2CoRhO_{4.5}$

8.1. Introduction

The topochemical reduction study has been extended to the La_2MRhO_6 (M = Mn, Co, Ni) perovskite phases. In Chapter 7, $La_2NiRhO_{4.6}$ and $LaSrMnRhO_{4.5}$ are investigated and analysed. However, no magnetic order at low temperature is observed in these two phases. In contrast to $La_2NiRhO_{4.5}$ and $LaSrMnRhO_{4.5}$, the topochemically reduced product from La_2CoRhO_6 exhibits interesting magnetic behaviour at low temperature, as presented in this chapter.

8.2. Experimental

8.2.1. Synthesis of La_2CoRhO_6

La_2CoRhO_6 was synthesized via a high-temperature ceramic method as described in Section 2.1. Suitable stoichiometric ratios of La_2O_3 (99.999%, dried at 900 °C), Rh_2O_3 (99.998%, dried at 850 °C for two hours) and Co_3O_4 (99.99%) were ground together using an agate mortar and pestle, pressed into pellets (diameter 13mm) under 5.5 tonnes of force in order to increase contact area, then transferred into alumina crucibles, heated for 3 periods of 48 hours at 1000°C, 1200 °C and 1250 °C in air with grinding and pelleting between heating cycles. The reaction progress was monitored by laboratory X-ray diffraction and once the reaction was deemed complete, synchrotron X-ray powder diffraction data were collected from the resulting phase.

8.2.2. Synthesis of $La_2CoRhO_{6-\delta}$

Samples of La_2CoRhO_6 were reduced using a zirconium getter[81] (as described in Section 2.2.1). The sample to be reduced was placed in a glass 'thimble' and sealed in evacuated silica ampoules along with 2 mole equivalents of powdered zirconium placed at the bottom of the silica ampoules, so that the two powders shared an atmosphere but were not in physical contact. Small scale trial reactions were performed in which ~200 mg of La_2CoRhO_6 was heated at a rate of 1 °C min^{-1} to 400°C for 3 periods of 5 days, with samples being reground and the Zr replaced between heating periods. Reaction progress was monitored by laboratory X-ray diffraction (XRD) and the optimum temperature for topochemical reduction was screened via XRD analysis. Once the reaction was deemed complete, synchrotron X-ray powder diffraction data were collected from the resulting phase. The sample of $La_2CoRhO_{6-\delta}$ characterized by neutron powder diffraction was prepared by heating ~2 g of La_2CoRhO_6 with Zr for 3 periods of 5 days at 400°C, with samples being reground and the Zr replaced between heating periods.

8.3. Results

8.3.1. Structural Characterisation of La_2CoRhO_6

Synchrotron X-ray powder diffraction (SXRD) (Section 2.3.1.3) data were collected from La_2CoRhO_6 and then analysed by the Rietveld refinement method. The refinement was performed using a model based on the $GdFeO_3$ distorted perovskite model in space group *Pbnm*[99]. The refined structure shown in Figure 8-1 is consistent with the previous report of La_2CoRhO_6[76] with a unit cell in *Pbnm* space group (a = 5.505 Å, b = 7.787 Å, c = 5.519 Å). As shown in Figure 8-2, the refinement achieved a good fit with wRp = 2.73%, confirming

sample purity and quality. Detailed structural parameters are listed in Table 8-1. The magnetisation data of La_2CoRhO_6 are listed in Appendix 2.7.

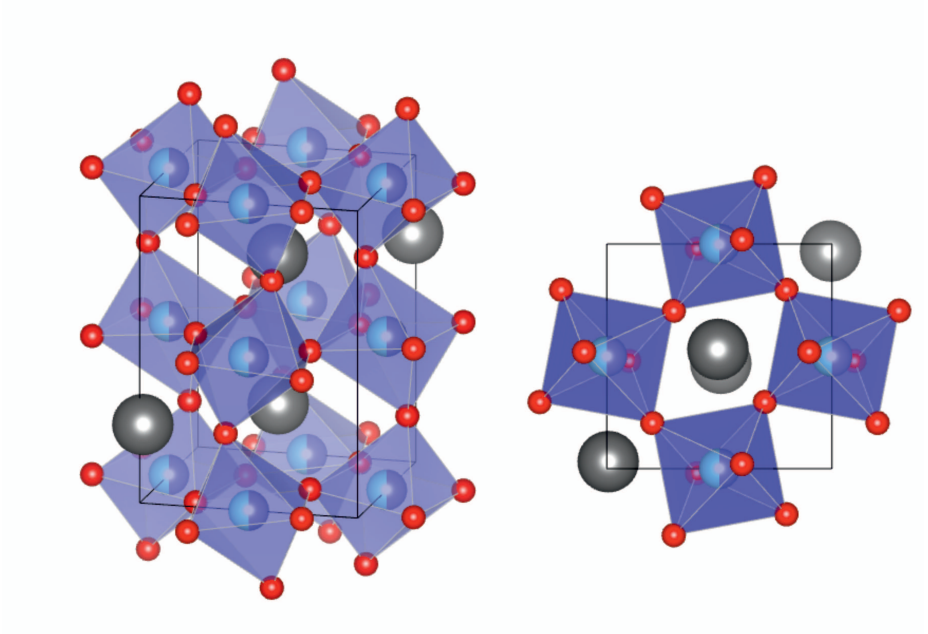


Figure 8-1 The crystal Structure of La_2CoRhO_6 (space group *Pbnm* with $a^+b^-b^-$ rotation).

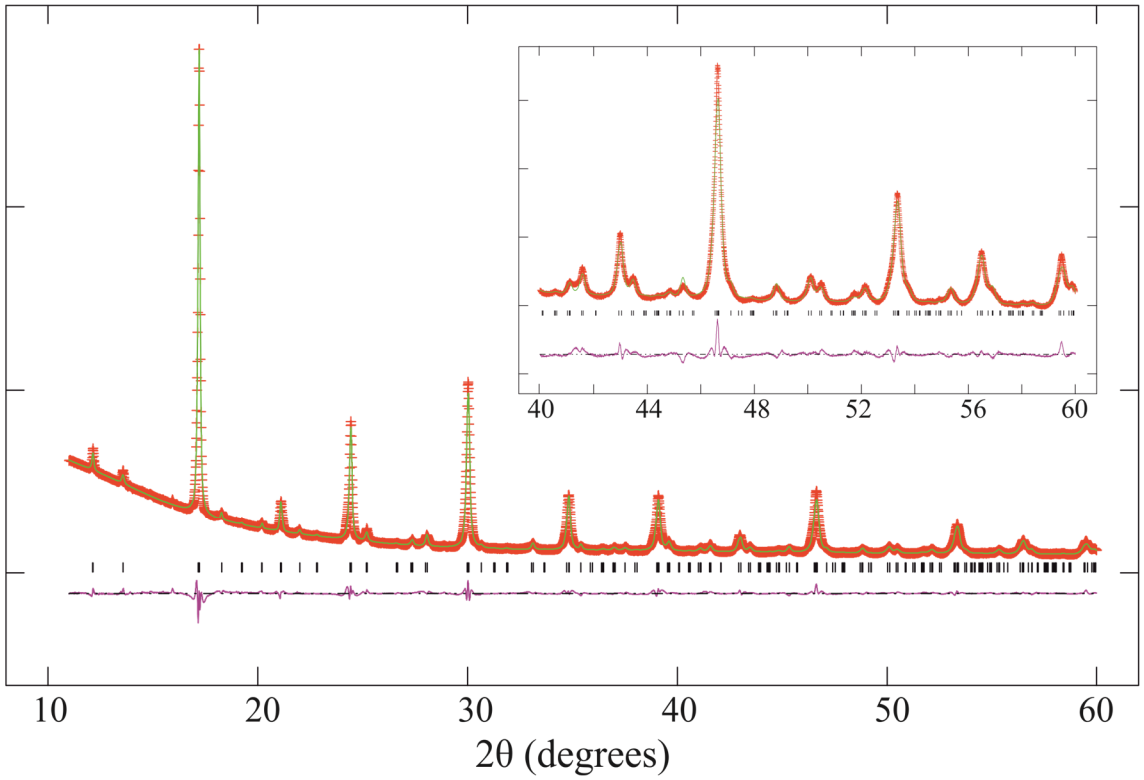


Figure 8-2 Observed(red), calculated(green) and difference plots(pink) from the Rietveld structural refinement of La_2CoRhO_6 using a *Pbnm* model against SXRD data collected at room temperature.

Table 8-1 Structural parameters from the refinement of La_2CoRhO_6 against SXRD data collected at 298 K.

Atom	Wyckoff Position	*x*	*y*	*z*	Fraction	U_{iso} (Å^2)
La	4*c*	0.0051(1)	0.0276(2)	¼	1	0.0037(1)
Co/Rh	4*b*	½	0		0.5/0.5	0.0036(1)
O(1)	4*c*	0.3067(2)	0.3124(1)	0.0320(1)	1	0.013(2)
O(2)	8*d*	0.070(1)	0.471(1)	¼	1	0.0029(1)

La_2CoRhO_6 - space group *Pbnm* (#62)
Formula mass: 535.64 g mol^{-1}, Z = 2
a = 5.5215(2) Å, *b* = 5.5070(2) Å, *c* = 7.7849(2) Å, Volume = 236.71(1) Å^3
Radiation source: Synchrotron X-ray, λ = 0.8249 Å
Temperature: 298 K
χ^2 = 25.08; *wRp* = 2.73 %; *Rp* = 1.92 %.

8.3.2. Initial Investigation of Reactivity of La_2CoRhO_6 with Zr

Small-scale trial reactions were performed by heating ~200 mg of La_2CoRhO_6 along with 2 mole equivalents of zirconium in evacuated silica ampoules. The best temperature (400 °C) for topochemical reduction of La_2CoRhO_6 with zirconium is easy to find due to the large structural change which accompanies the reaction. The symmetry of the main phase observed in XRD patterns increased from orthorhombic to tetragonal once the deintercalation of apical oxide ions had started with the reduced phase exhibiting a large change in lattice parameters compared to the oxygen stoichiometric starting material. The topochemical reduction profile of La_2CoRhO_6 to form $La_2CoRhO_{6-\delta}$ during each cycle is shown in Figure 8-3. The first distinct reduced phase observed after the first heating cycle at 400 °C could be indexed using a mixture of phases including a tetragonal perovskite phase. In the following heating cycles, the formation of symmetric and sharp [200] and [112] peaks is observed and the reaction is deemed complete after 4 cycles of heating at 400 °C.

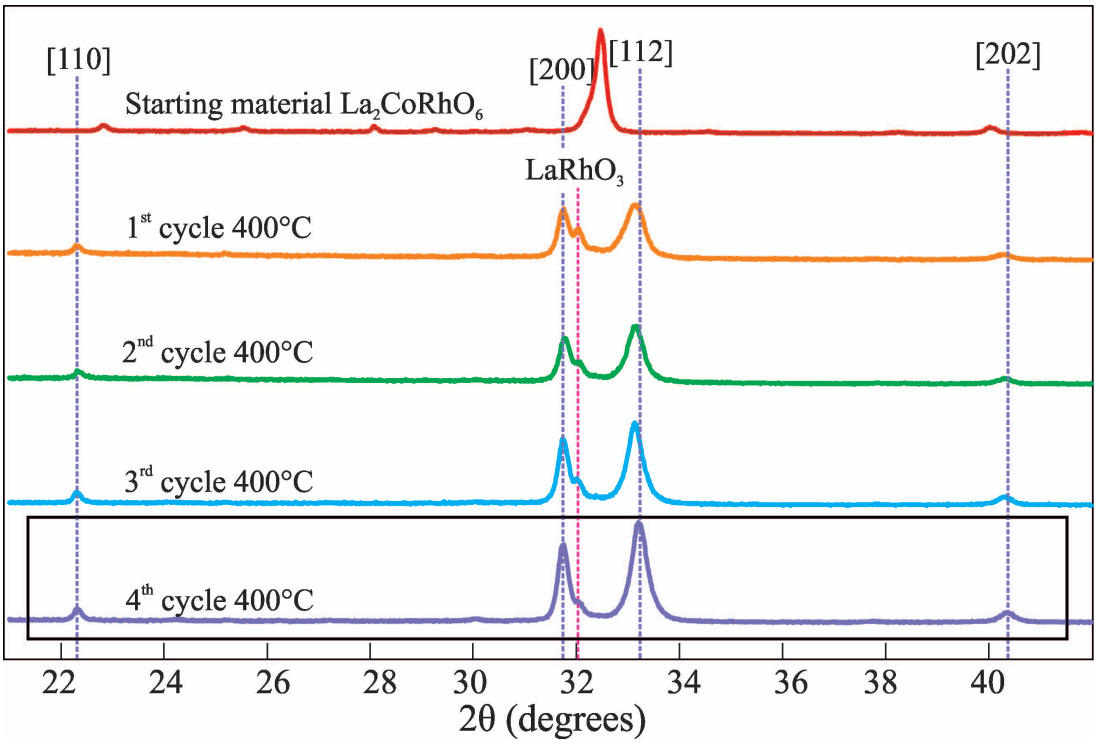


Figure 8-3 Topochemical reduction profile of La_2CoRhO_6 with Zr to form a compositional range of $La_2CoRhO_{6-\delta}$.

8.3.3. Structural and Chemical Characterisation of $La_2CoRhO_{6-\delta}$

8.3.3.1. Thermogravimetric Analysis of $La_2CoRhO_{6-\delta}$

To determine the chemical composition of the reduced phase, a reductive thermogravimetric experiment was conducted. A small quantity of the reduced sample was heated under a steady flow of 10%/90% H_2/N_2 at a rate of 5 °C min^{-1} and held at 800 °C for 1 hour to complete the reaction before cooling. The oxygen content of the reduced sample was calculated by the mass difference between $La_2CoRhO_{6-\delta}$ and totally reduced products (La_2O_3, Co and Rh). The TGA data from $La_2CoRhO_{6-\delta}$ is shown in Figure 8-4. During the reaction, $La_2CoRhO_{6-\delta}$ showed a 4.67% mass loss, which is consistent with a composition of $La_2CoRhO_{4.492(1)}$. Henceforth, the reduced phase will be referred to as $La_2CoRhO_{4.5}$.

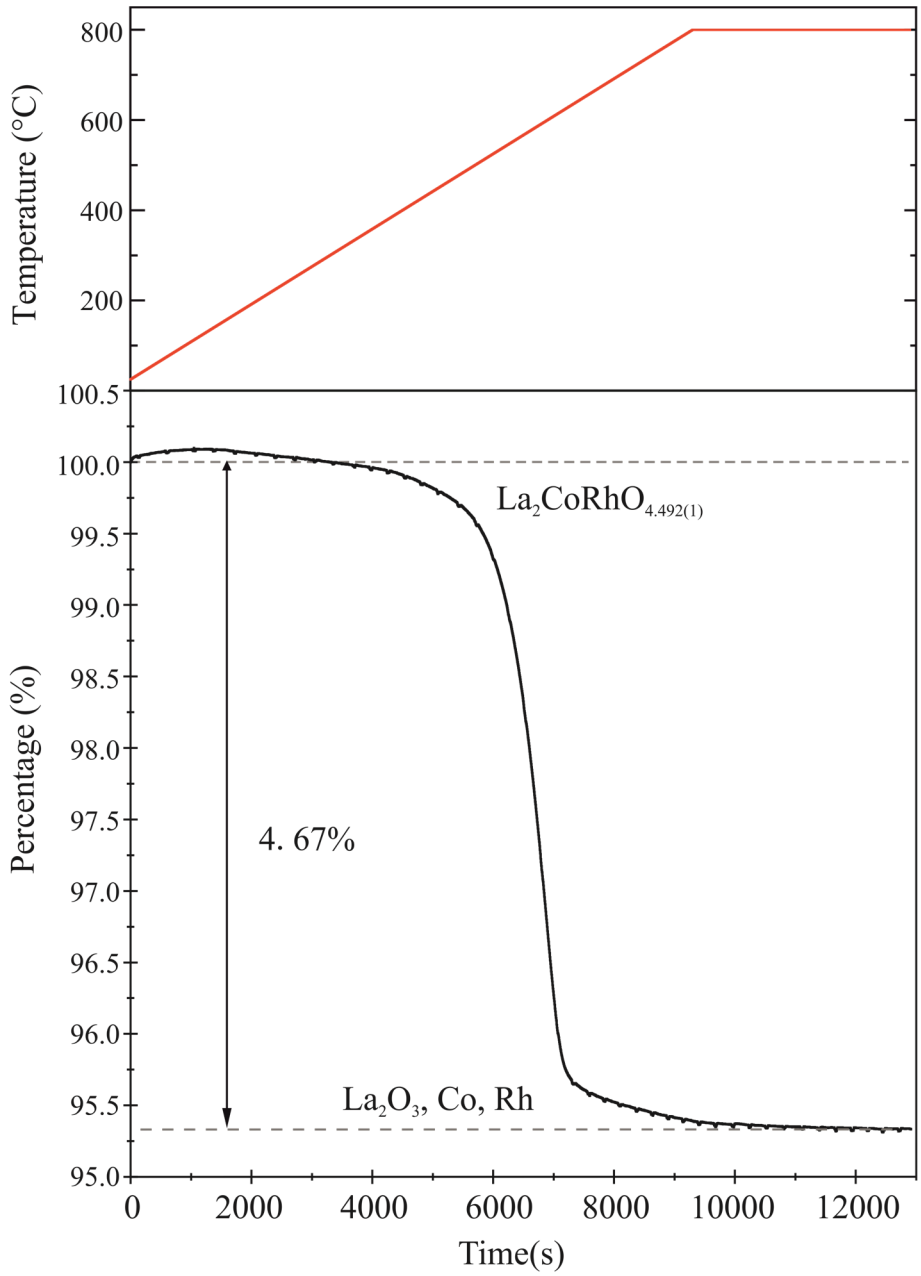


Figure 8-4 Reductive thermogravimetric data collected from $La_2CoRhO_{6-\delta}$. Top panel indicates the heating profile, bottom panel the relative mass of the sample.

8.3.3.2. Neutron Powder Diffraction of $La_2CoRhO_{4.5}$

8.3.3.2.1. Space Group Determination of $La_2CoRhO_{4.5}$

Neutron powder diffraction (NPD) data were collected at ambient temperature using the D2B diffractometer in ILL (Section 2.3.2.2). As with $La_2NiRhO_{4.6}$ and $LaSrMnRhO_{4.5}$ discussed in Chapter 7, NPD data collected from $La_2CoRhO_{4.5}$ at 298 K were also refined using an *I*4/*mcm* model and a *P*4/*mmm* model. The observed, calculated and difference plots of 298 K NPD data using an *I*4/*mcm* model and a *P*4/*mmm* model are shown in Figure 8-5. As shown in the insets of Figure 8-5 (bottom), a peak mismatch at 39° and 120° is observed in the refinement using a *P*4/*mmm* model while the refinement using an *I*4/*mcm* model shows a satisfactory fit. Table 8-2 shows the fitting statistics of the refinements of $La_2CoRhO_{4.5}$ against two models, respectively. The Rietveld refinement using an *I*4/*mcm* model is superior to that using a *P*4/*mmm* model. Thus, it is confirmed that $La_2CoRhO_{4.5}$ also has a structure with *I*4/*mcm* symmetry, as $La_2NiRhO_{4.6}$ and $LaSrMnRhO_{4.5}$. Full details of the structural parameters are given in Table 8-3, anisotropic displacement factors are given in Table 8-4 and the selected bond lengths are given in Table 8-5.

Table 8-2 Fitting statistics from the structural refinement of $La_2CoRhO_{4.5}$.

Space Group	χ^2	*wRp* (%)	*Rp* (%)
***P4/mmm* (#123)**	5.987	5.41	3.69
***I4/mcm* (#140)**	2.339	3.38	2.66

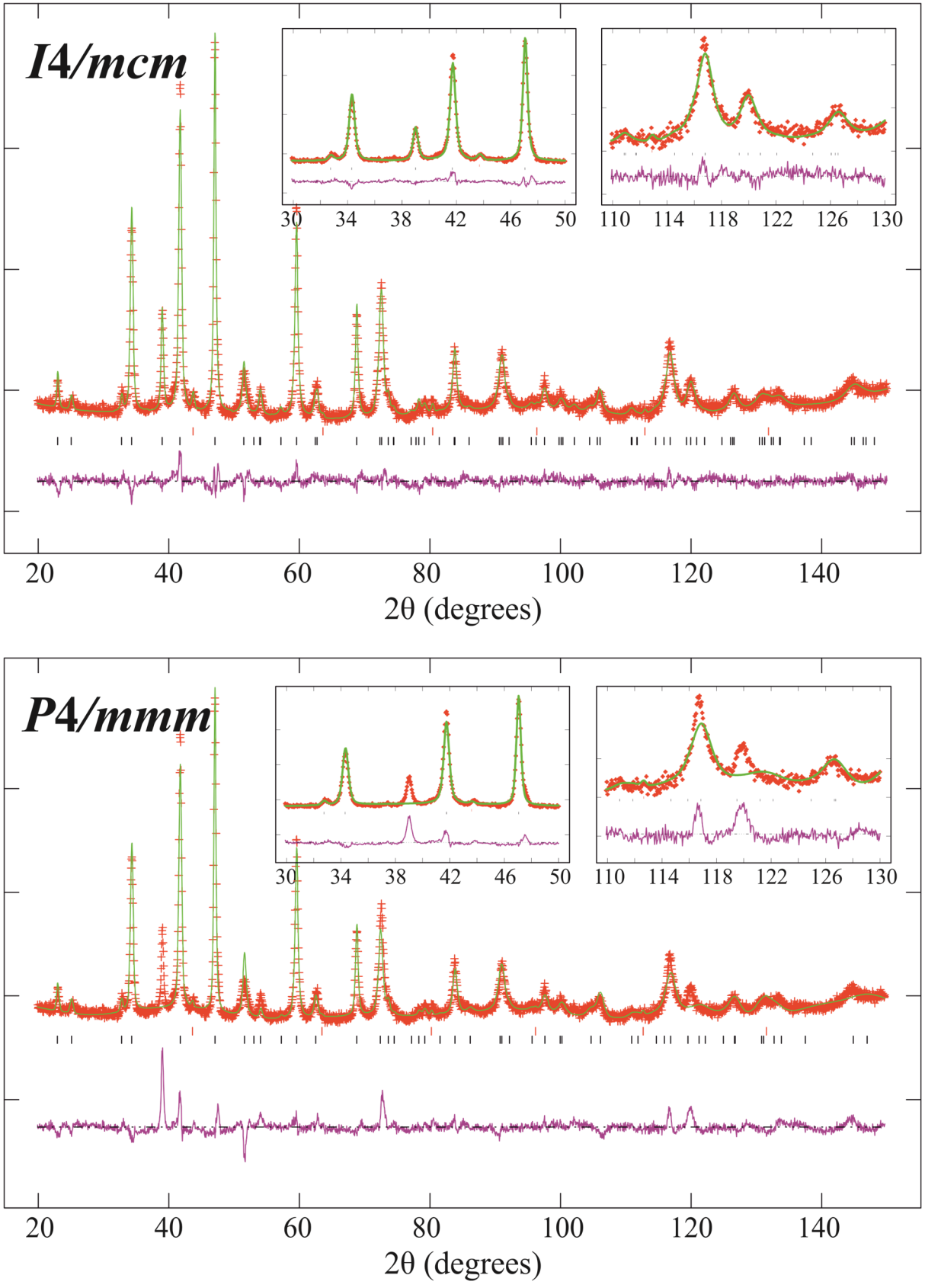


Figure 8-5 Observed, calculated and difference plots from the refinement of $La_2CoRhO_{4.5}$ against NPD data collected at 298 K using an *I4/mcm* model (top) and a *P4/mmm* model (bottom). Red tick marks indicate peak positions of vanadium from sample containers, black tick marks indicate peak positions of $La_2CoRhO_{4.5}$.

Table 8-3 Structural parameters from the refinement of $La_2CoRhO_{4.5}$ against NPD data collected at 298 K.

Atom	Wyckoff Position	*x*	*y*	*z*	Fraction	U_{iso} (Å^2)
La	4*i*	½	0	¼	1	0.022(1)
Co/Rh	2*a*	0	0	0	0.5/0.5	0.003(1)
O(1)	4*i*	0.2116(3)	0.2883(3)	0	1	0.006(1)
O(2)	2*d*	0	0	¼	0.25	0.104(9)

$La_2CoRhO_{4.5}$ - space group *I*4/*mcm* (#140)
Formula mass: 511.65 g mol^{-1}, Z = 2
a = 5.6431(3) Å, *c* = 7.3305(9) Å, Volume = 233.44(5) Å^3
Radiation source: Neutron Powder Diffraction
Temperature: 298 K
χ^2 = 2.339, *wRp* = 3.38 %; *Rp* = 2.66 %.

Table 8-4 Anisotropic displacement factors from refinements of $La_2CoRhO_{4.5}$ against NPD data collected at 298 K.

Atom	U_{11}	U_{22}	U_{33}
La	0.02190(97)	0.02190(97)	0.04062(251)
Co/Rh	0.00320(142)	0.00320(142)	0.13886(653)
O (1)	0.00572(71)	0.00572(71)	0.14334(327)
O (2)	0.10468(992)	0.10468(992)	0.03321(788)

Table 8-5 Selected bond lengths from the refined structure of $La_2CoRhO_{4.5}$ at 298 K.

Cation	Anion	Length (Å)
La	O (1)	2.4921(2) × 4
	O (1)	2.9420(2) × 4
	O (2)	2.8216(2) × 4
Co/Rh	O (1)	2.0185(1) × 4
	O (2)	1.8326(3) × 2

8.3.3.2.2. Magnetic Ordering Determination of $La_2CoRhO_{4.5}$

A comparison of NPD data collected at 298 K using the D2B diffractometer and that collected at 2 K using the D1B diffractometer is plotted as Figure 8-6. The comparison shows that the 2 K data has additional peaks at d-spacings of 4.47 Å and 5.64 Å, which are not observed in the 298 K data. These two peaks can be indexed using the nuclear unit cell (*I*4/*mcm*, a = 5.6431(3) Å, c = 7.3305(9) Å) and are identified as [101] peak at 4.47 Å and [100] peak at 5.64 Å, respectively.

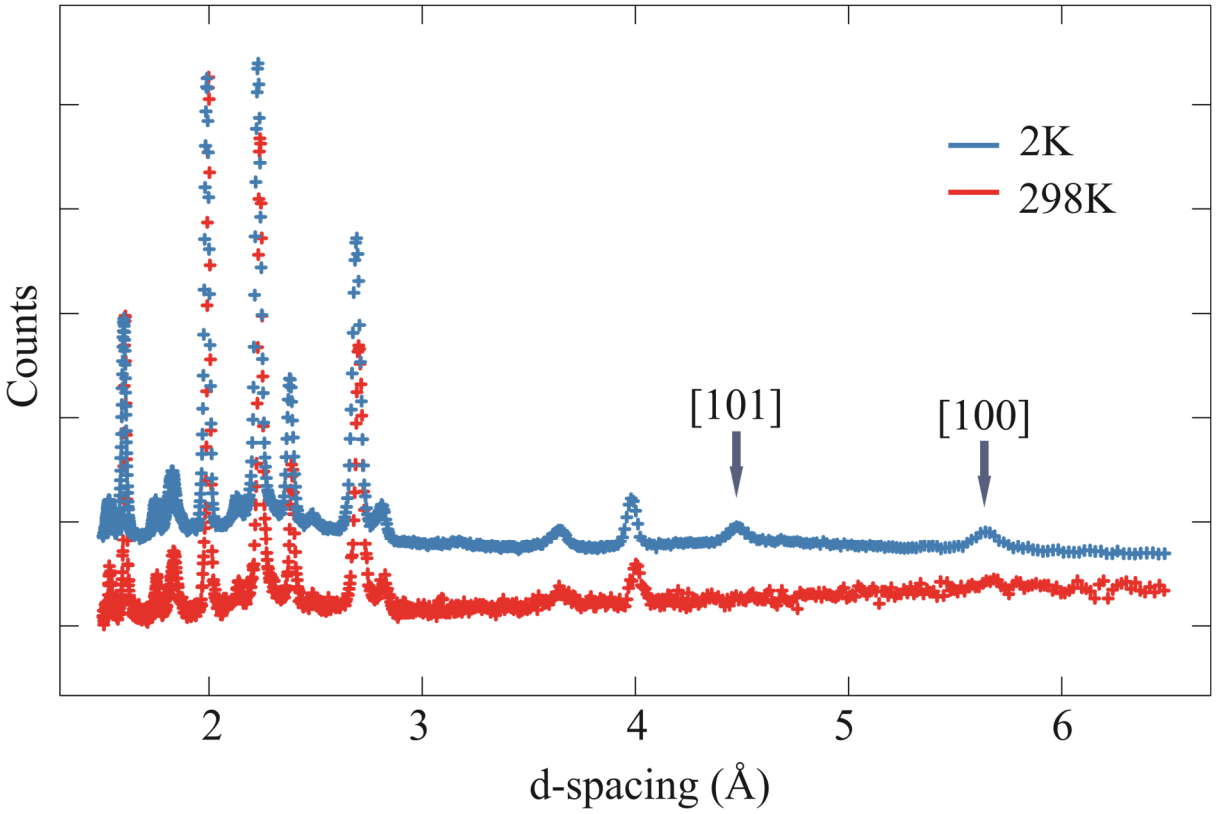


Figure 8-6 Comparison of NPD data collected from $La_2CoRhO_{4.5}$ at 2 K and 298 K. Dark blue arrows index 2 additional peaks shown in 2 K data: [101] peak at 4.47Å and [100] peak at 5.64 Å.

Given that the [101] and [100] diffraction peaks are attributed to magnetic scattering, a series of symmetry compatible magnetic models was constructed using the ISODISTORT software[100,101]. This procedure yielded 6 magnetic models consistent with the *I*4/*mcm* symmetry of the phase, described by the irreducible representations $m\Gamma_1^+$, $m\Gamma_3^+$, $m\Gamma_5^+$, $m\mathrm{M}_1^+$,

$m\mathrm{M}_3^+$ and $m\mathrm{M}_5^+$. Diffraction patterns corresponding to these magnetic models were simulated and compared to the experimental data. Among all the candidates, the [101] magnetic peak at 4.47 Å could only be indexed using the $m\Gamma_1^+$ model. In contrast, the [100] magnetic peak at 5.64 Å could be indexed using either $m\mathrm{M}_3^+$ or $m\mathrm{M}_5^+$ models. Simulations of these three candidates ($m\Gamma_1^+$, $m\mathrm{M}_3^+$ and $m\mathrm{M}_5^+$) are plotted in Figure 8-7, with the diffraction peaks that cannot be indexed using the *I*4*/mcm* nuclear unit cell listed in Table 8-6. The [101] magnetic peak can only be indexed using the $m\Gamma_1^+$ model while all the other magnetic reflections can be indexed using the $m\mathrm{M}_5^+$ model, so the best match to NPD data at 2 K was achieved by using the model which is the combination of $m\Gamma_1^+$ and $m\mathrm{M}_5^+$ models.

Table 8-6 The checklist of magnetic peaks that can be indexed using magnetic models $m\Gamma_1^+$, $m\mathrm{M}_3^+$ and $m\mathrm{M}_5^+$.

Peak d-spacing/Å	*hkl*	$m\Gamma_1^+$	$m\mathrm{M}_3^+$	$m\mathrm{M}_5^+$
1.88	**[300]**		✓	✓
1.92	**[221]**			✓
2.52	**[210]**		✓	✓
4.47	**[101]**	✓		
5.64	**[100]**		✓	✓

In the $m\Gamma_1^+/m\mathrm{M}_5^+$ combined model which is shown in Figure 8-8, the Co cations are G-type antiferromagnetically ordered with the spins aligned parallel to the *z*-axis and C-type antiferromagnetically ordered with spins aligned in the *xy*-plane. It is not possible to determine the specific orientation of the spins in the *xy*-plane from powder diffraction data, given that the crystal structure is tetragonal. Thus, this magnetic model was refined against 2 K NPD data with moments defined to be parallel to the *x*-axis, to achieve an excellent fit.

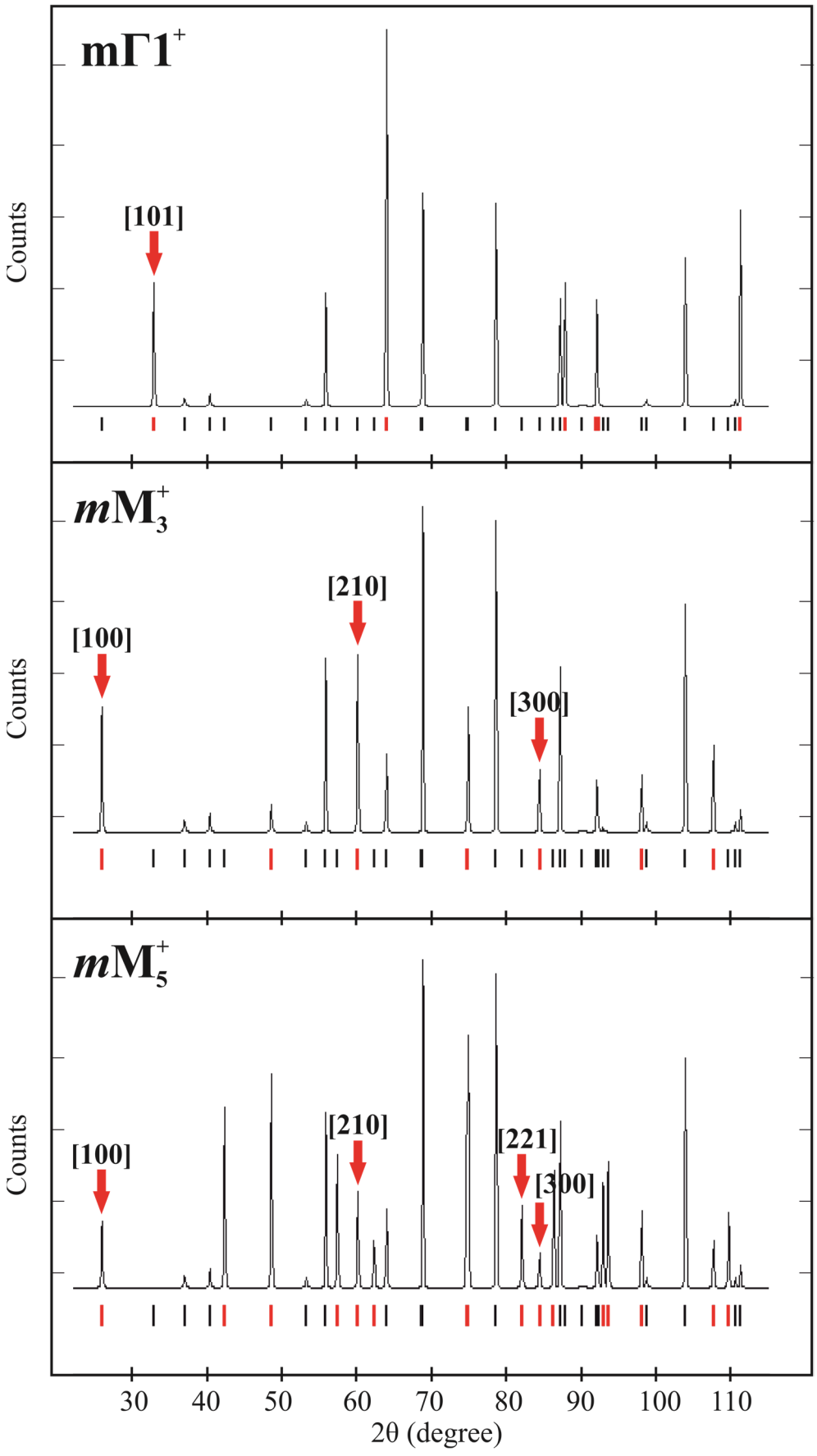


Figure 8-7 Simulations of NPD patterns of $La_2CoRhO_{4.5}$ using magnetic structure models $m\Gamma_1^+$, mM_3^+ and mM_5^+.

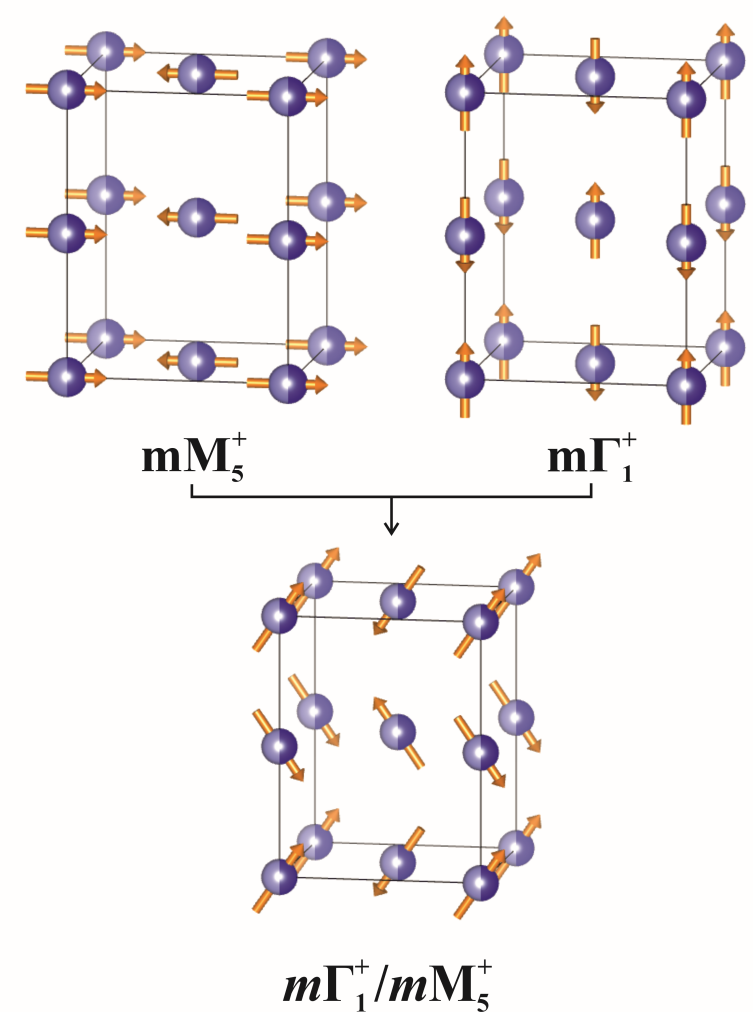


Figure 8-8 The refined magnetic unit cell ($m\Gamma_1^+/mM_5^+$) of $La_2CoRhO_{4.5}$. The light purple and dark purple spheres are cobalt and rhodium, respectively. Lanthanum and oxygen in the unit cell are hidden for a better view.

Figure 8-9 shows the observed, calculated and difference plots for the combination of magnetic and structural refinement against NPD data. The refined magnetic and structural parameters are detailed in Table 8-7. The ordered magnetic moments were refined to be 1.31(8) μ_B per cobalt centre along *x* axis and 1.47(6) μ_B per cobalt centre along *z* axis, which gives a combined moment of 1.97 μ_B per cobalt centre.

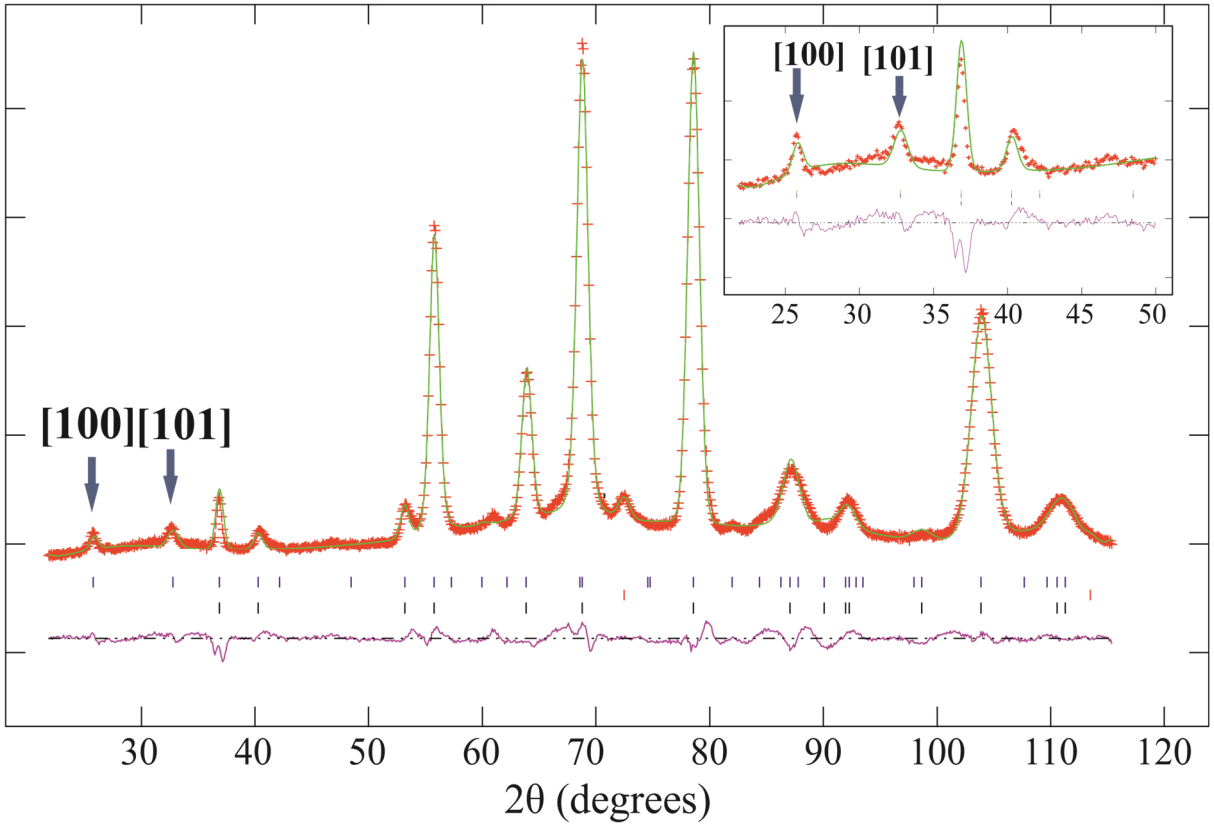


Figure 8-9 Observed, calculated and difference plots from the refinement of $La_2CoRhO_{4.5}$ against NPD data collected at 2 K using an *I4/mcm* nuclear structure model and magnetic models $m\Gamma_1^+$ and mM_5^+. The blue arrows indicate the two additional magnetic peaks: [100] peak at 25.8° and [101] peak at 32.7°. Upper tick marks indicate the peak positions for magnetic reflections; middle tick marks indicate the peak positions of vanadium from sample containers; lower tick marks indicate the peak positions from the nuclear structure of $La_2CoRhO_{4.5}$.

Table 8-7 The magnetic model refined for $La_2CoRhO_{4.5}$ against NPD data collected at 2 K.

Atom	Fraction of Occupancy	*x*	*y*	*z*	M_x/μ_B	M_y/μ_B	M_z/μ_B
Co(1)	½	0	0	0	1.31(8)	0	1.47(6)
Co(2)	½	½	½	0	-1.31(8)	0	-1.47(6)
Co(3)	½	0	0	½	1.31(8)	0	-1.47(6)
Co(4)	½	½	½	½	-1.31(8)	0	1.47(6)

8.3.3.3. Variable-temperature Measurement of $La_2CoRhO_{4.5}$

8.3.3.3.1. Variable-temperature Neutron Powder Diffraction Data

NPD data were collected from $La_2CoRhO_{4.5}$ at temperatures between 2 K and 174 K (Figure 8-10). The patterns collected at 174 K and below are all similar, differing only in the intensity of the Bragg peaks associated with the magnetic order. As shown in Figure 8-10, on warming from 2 K, the intensity of the [101] magnetic diffraction peak declines, while the intensity of the [100] magnetic diffraction peak stays approximately constant. The rather poor signal to noise ratio of the data and the broad feature observed to sit under the [101] diffraction peak make the fitting of the data at intermediate temperatures challenging. To quantify the relative intensities of the magnetic diffraction peaks, the adjacent nuclear [110] peak at 36.5° was chosen as a standard to study the intensity change of [100] and [101] peaks over temperature. The fitting of the pattern was carried out to determine the intensity ratio of [100] peak/[110] peak and [101] peak/[110] peak, and these are listed in Table 8-8. It's observed that [100] peak/[110] peak ratio remains at ~ 50% within the temperature range $2 \leq T/\mathrm{K} \leq 175$ while [101] peak /[110] peak starts decreasing at 50 K (50.30%) and stops decreasing at ~ 125K (6.33%). Thus, the variable-temperature NPD data show that we therefore have three different regimes where there are both C- and G-type antiferromagnetic (AFM) states, only an C-type AFM state and a paramagnetic state. Unfortunately, we don't have NPD data to show where the paramagnetic state starts and there is no dramatic change in Figure 8-10 showing the transition of G-type AFM order vanishing. So other indications were investigated from magnetisation data and SXRD data.

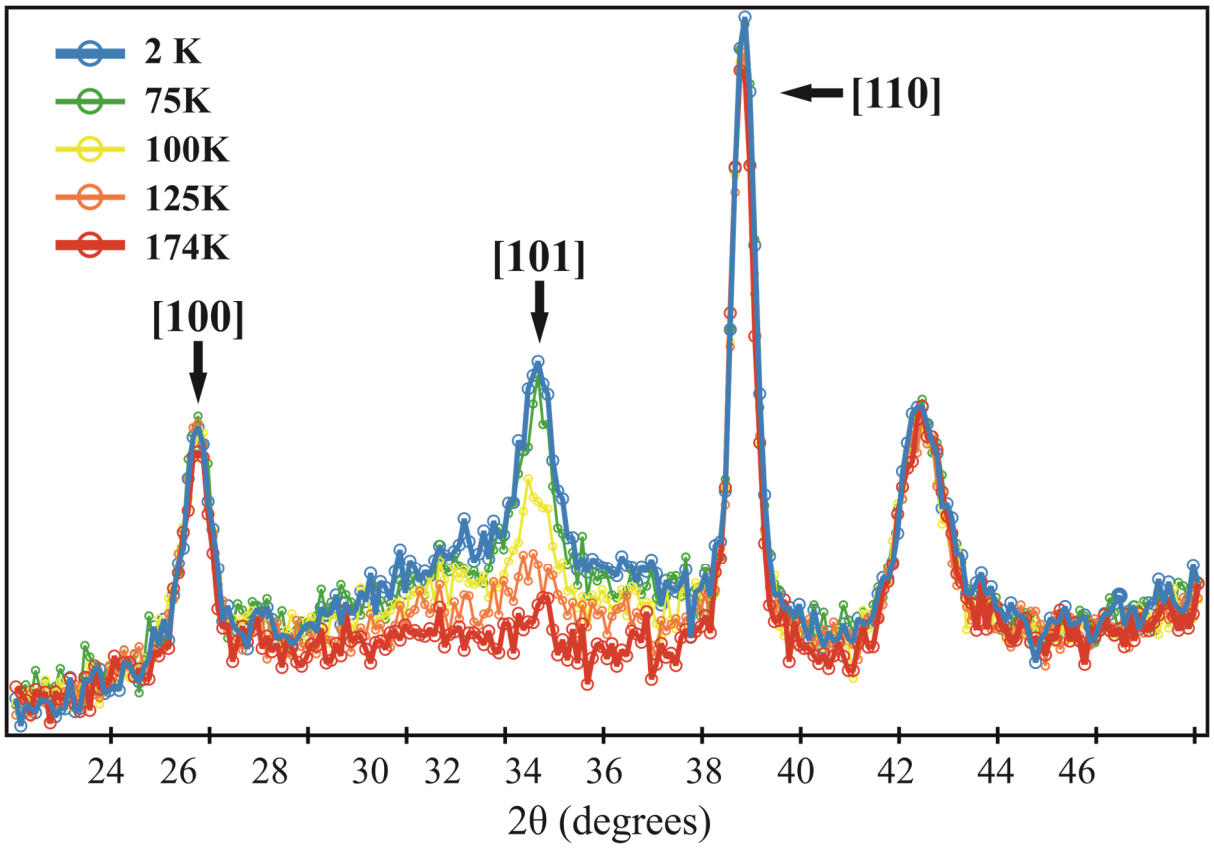


Figure 8-10 Observed plots of variable temperature NPD data collected from $La_2CoRhO_{4.5}$ at 2 K, 10 K, 75 K, 100 K, 125 K and 174 K. The black arrows indicate the [100] magnetic peak ($m\mathrm{M}_5^+$), the [101] magnetic peak ($m\Gamma_1^+$) and [110] nuclear peak.

Table 8-8 The list of the intensity ratio of [100], [101] and [110] peaks in NPD data of $La_2CoRhO_{4.5}$ collected from 2 K to 174 K.

Temperature (K)	Intensity ratio [100] peak/[110] peak	Intensity ratio [101] peak/[110] peak
2	47.42%	48.22%
10	44.12%	52.98%
50	48.11%	50.30%
75	44.82%	44.51%
100	49.54%	25.69%
125	52.68%	15.65%
150	48.31%	6.33%
174	42.26%	6.13%

8.3.3.3.2. Magnetic Characterisation of $La_2CoRhO_{4.5}$

A 'ferromagnetic subtraction' technique (Section 2.5.3) was used to collect the magnetization data from $La_2CoRhO_{4.5}$ due to the existence of small amounts (< 0.1 wt%) of ferromagnetic Co in $La_2CoRhO_{4.5}$.

Figure 8-11 (top) shows that the paramagnetic susceptibility of $La_2CoRhO_{4.5}$ follows the modified Curie-Weiss law ($\chi = C/(T - \theta) + K$) in the range $210 < T/K < 300$ to yield values of $C = 0.87(1)$ cm^3 K mol^{-1} , $\theta = -14.5(2)$ K and $K = 3.24(4) \times 10^{-3}$ cm^3 mol^{-1}. The feature of fitting range being $210 \leq T/K \leq 300$ agrees with the C-type in-plane ordering temperature above 175 K. However, it's hard to observe any obvious change which can indicate magnetic transition from magnetisation data of $La_2CoRhO_{4.5}$.

Below 120 K, the saturated ferromagnetic moment of $La_2CoRhO_{4.5}$ increases sharply (Figure 8-11 (bottom)) and the susceptibility exhibits a maximum value at T = 15 K. The Curie constant yields a value of $\mu^2 = 6.96\ \mu_B^2$, which differs from the value of 3.88 μ_B^2 from the NPD data refinement, indicating tha Curie-Weiss paramagnetism and the magnetic Bragg peaks in NPD data rely on contradictory models of magnetic moment. However, the value of 6.96 μ_B^2, obtained from magnetization data, roughly matches with the $S = 1$ Co^I giving a μ^2 value of 8 μ_B^2. The magnetisation-field data of $La_2CoRhO_{4.5}$ at 5 K in Figure 8-12 shows an obvious shift from the origin point, which indicates a spin glass behaviour.

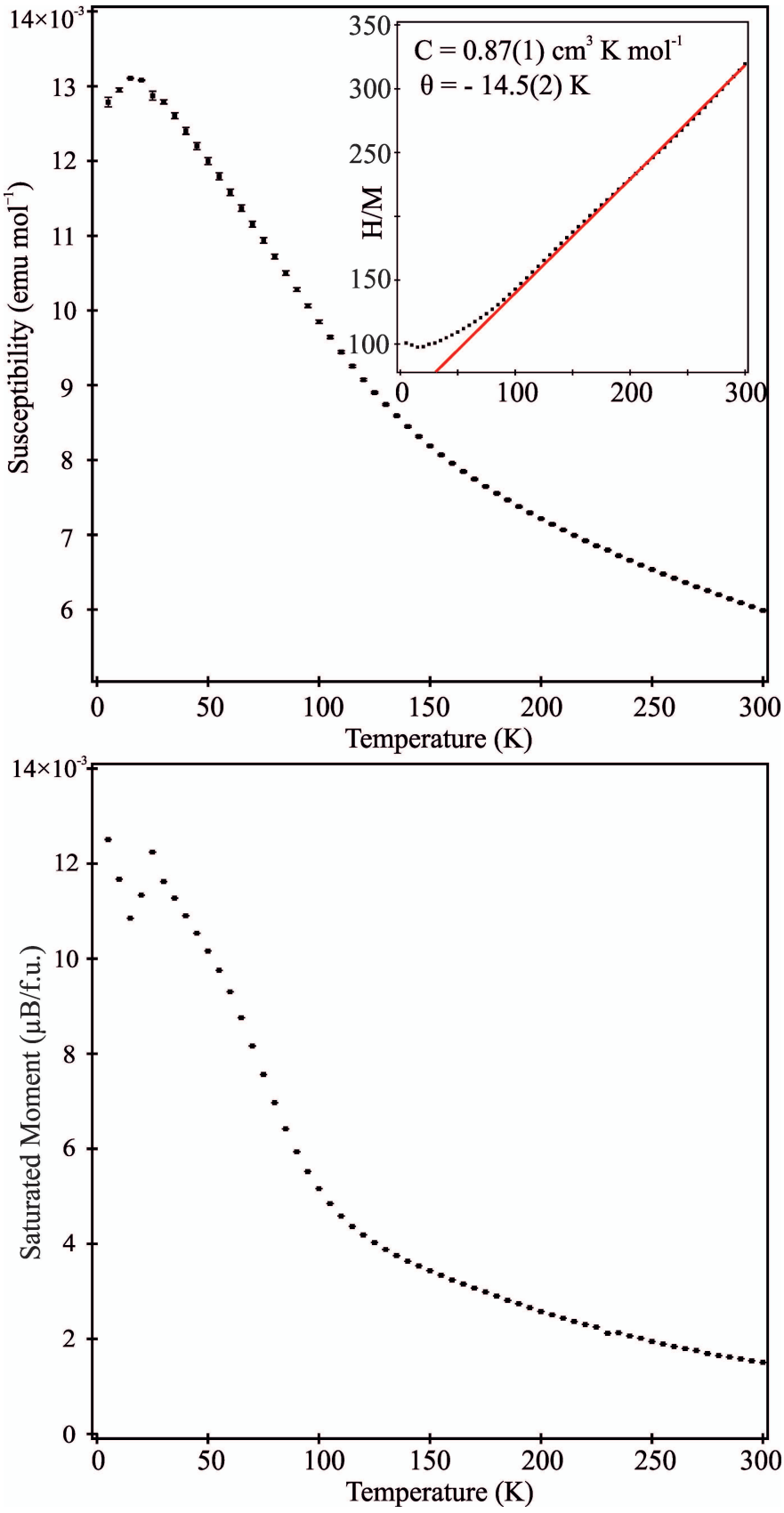


Figure 8-11 The paramagnetic susceptibility (top) and saturated ferromagnetic moment (bottom) of $La_2CoRhO_{4.5}$ collected as a function of temperature. Inset: the fit to the Curie-Weiss law in the temperature range 115 < *T*/K < 300.

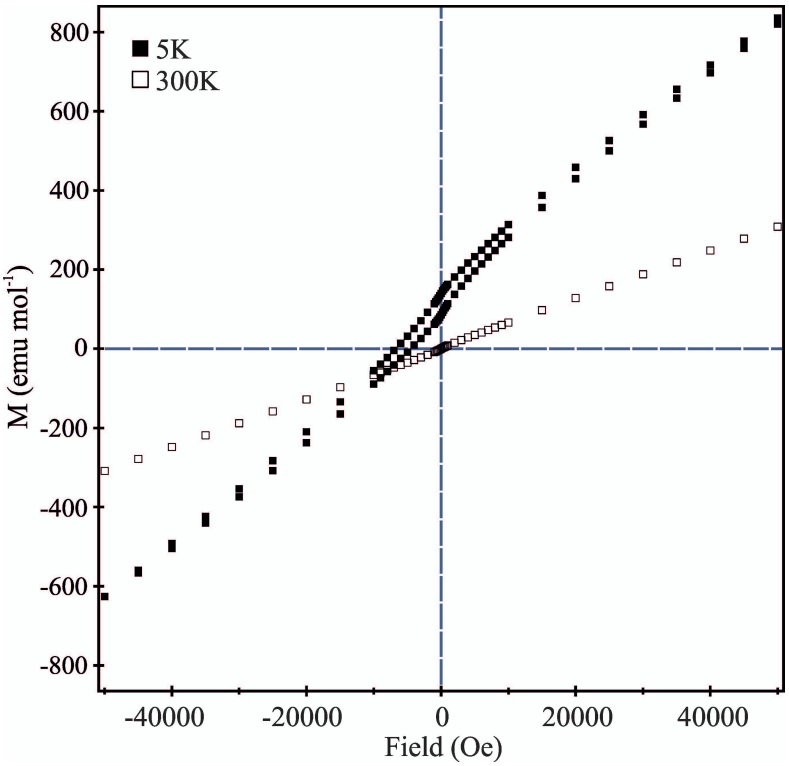


Figure 8-12 Magnetisation data collected as a function of applied field from $La_2CoRhO_{4.5}$.

8.3.3.3.3. Variable-temperature Synchrotron X-ray Powder Diffraction of $La_2CoRhO_{4.5}$

To further understand the magnetic behaviour of $La_2CoRhO_{4.5}$, SXRD data were collected from $La_2CoRhO_{4.5}$ as a function of temperature from 94 K to 299 K with the step size being 1 K. The structural model refined against the 94 K data was used for the refinements against the variable-temperature SXRD data to extract the lattice parameters at these temperatures. To avoid the interference from other parameters, only the lattice parameters and the background parameters were refined. Figure 8-13 shows the evolution of the refined lattice parameters as a function of temperature in the temperature range $94 \leqslant T/\mathrm{K} \leqslant 299$. Both the *a* and *c* lattice parameters increase upon heating due to the thermal expansion of the unit cell. However, a small change in the gradient at around 150 K as highlighted as the linear fits, displayed in Figure 8-13 (a) and (b). This change in the gradient is so subtle that no change in SXRD patterns is found. However, this slight deviation of gradients from the linear fit upon

lowering the temperature might correspond to the onset of G-type AFM order. It does not appear to be any feature associated with the transition from a paramagnetic state to a magnetic ordered state above 175 K since the line of the lattice parameter changing over temperature is linear in the temperature range 160 < *T*/K < 300.

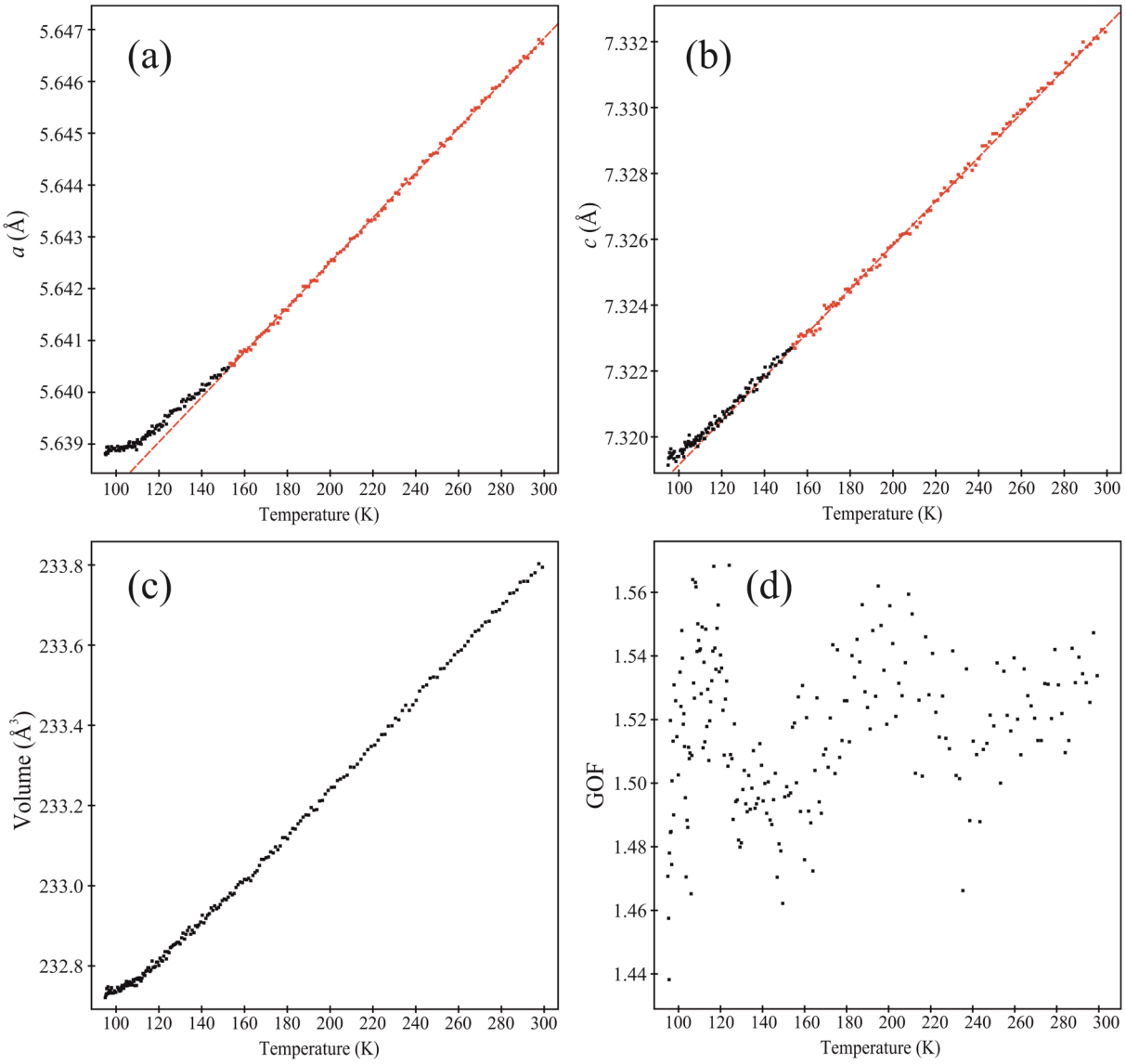


Figure 8-13 Temperature evolution of (a) *a* lattice parameter; (b) *c* lattice parameter; (c) volume of the unit cell; (d) goodness of fit for $La_2CoRhO_{4.5}$ determined from the analysis of variable temperature SXRD data at 94 ≤ *T*/K ≤ 299. The red dashed lines in (a) and (b) show the linear fit of the *a* and *c* lattice parameters at 153 ≤ *T*/K ≤ 299.

8.3.3.3.4. Serial Magnetic Refinement of $La_2CoRhO_{4.5}$ over Temperature

Figure 8-14 shows the evolution of the refined magnetic moment (M_x and M_z) and the *a* and *c* lattice parameters determined by NPD data as a function of temperature. The ordered moment M_x remains at around 1.23 μ_B across the whole temperature range while M_z starts declining at around 50 K from 1.184 μ_B and reaches a plateau at around 150 K with the value of around 0 μ_B. The starting point (50 K) of the shrinkage of G-type AFM order extracted from the magnetic refinement is consistent with the decline of [101] peak intensity observed in pattern fitting (Table 8-8). In addition, the M_z plateau obtained from ~125K is also consistent with the pattern fitting data (Table 8-8) and can explain the small change in the gradient of the thermal expansion of lattice parameters at ~ 150 K observed in variable temperature SXRD data (Figure 8-13).

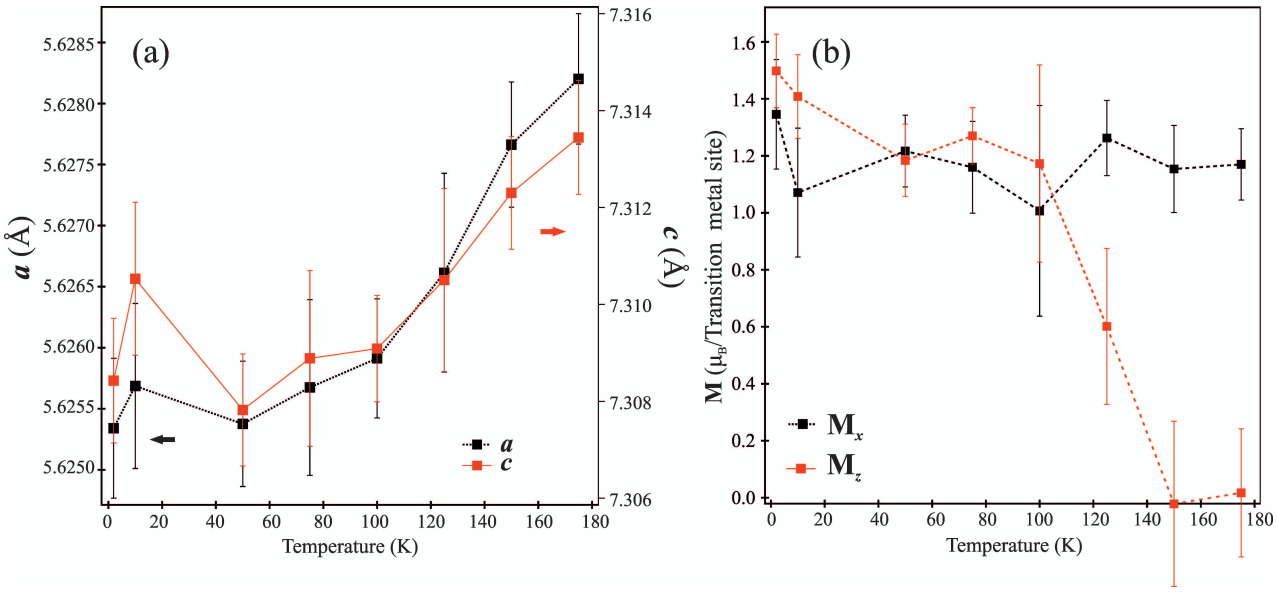


Figure 8-14 (a) The *a* and *c* lattice parameters extracted from fits to $La_2CoRhO_{4.5}$ NPD data over temperature. (b)The ordered magnetic moment M_x and M_z on Co centres extracted from fits to $La_2CoRhO_{4.5}$ NPD data over temperature.

8.3.3.3.5. Conclusion of the Magnetic Transition of $La_2CoRhO_{4.5}$ over Temperature

Based on NPD data, magnetisation data and SXRD data discussed above, it can be concluded that $La_2CoRhO_{4.5}$ exhibits three magnetic regimes at different temperature ranges as shown in the schematic diagram in Figure 8-15. $La_2CoRhO_{4.5}$ shows a paramagnetic state at room temperature. Upon cooling to some point between $174 < T/K < 300$, $La_2CoRhO_{4.5}$ adopts an C-type AFM state with spins aligned in the *xy*-plane. At around 125 K, a G-type AFM state with the spins aligned parallel to the *z*-axis joins the ordered regime and $La_2CoRhO_{4.5}$ exhibits a combination of both C- and G-type AFM order.

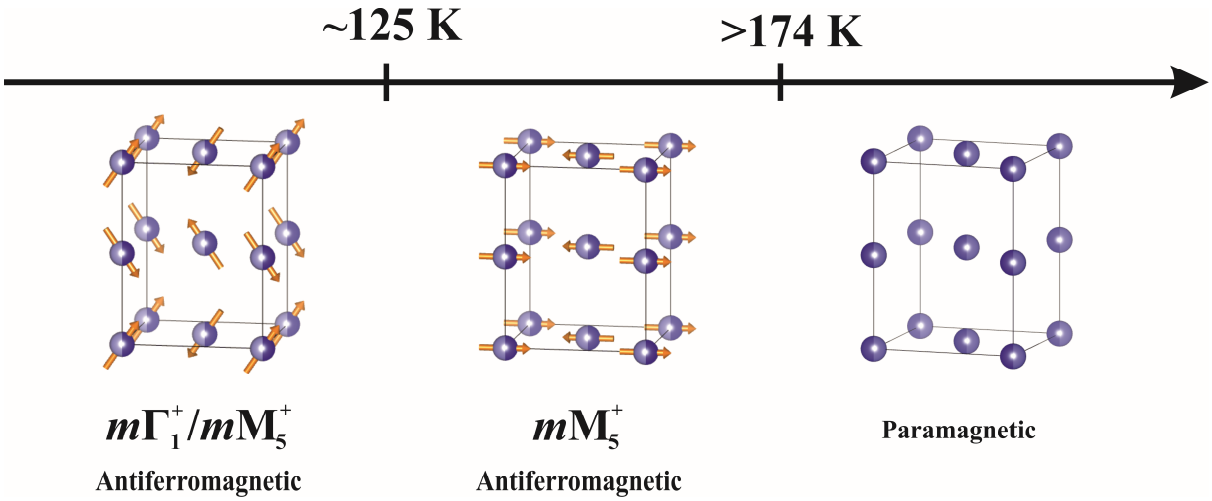


Figure 8-15 A schematic diagram of the magnetic structure of $La_2CoRhO_{4.5}$ as a function of temperature.

Close inspection of the NPD data reveals that a broad magnetic scattering feature appears in the range of $28° \leq 2\theta \leq 36°$ with the appearance of the sharp [101] magnetic peak. A comparison of NPD pattern at 2 K and 174 K is plotted in Figure 8-16, highlighting this feature. Given that the $m\Gamma_1^+$ model is the only candidate indexing the [101] peak in the irreducible search for the magnetic behaviour of $La_2CoRhO_{4.5}$, the possibility of a third pattern of magnetic ordering can be excluded. Therefore, the coexistence of the sharp [101] peak and the broad [101] feature simultaneously in the 2 K data suggests that the system has both long-range G-type AFM order and short-range G-type AFM order at the same time.

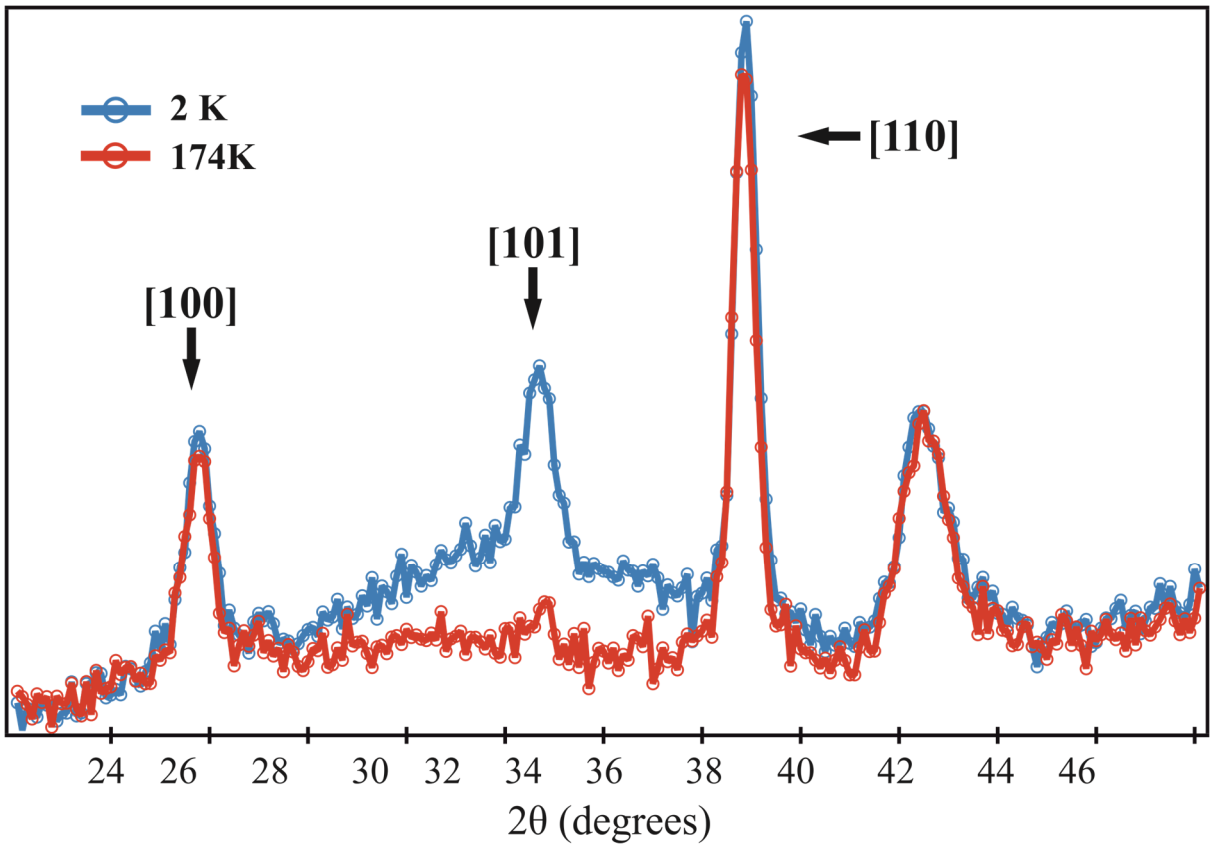


Figure 8-16 Observed plots of variable-temperature NPD data collected from $La_2CoRhO_{4.5}$ at 2 K and 174 K. The black arrows indicate the [100] magnetic peak ($m\Gamma_5^+$), the [101] magnetic peak ($m\Gamma_1^+$) and [110] nuclear peak.

8.4. Discussion

The combination of TGA data and NPD data indicates that $La_2CoRhO_{4.5}$ is isostructural to $La_2NiRhO_{4.6}$ and $LaSrMnRhO_{4.5}$. Thus, the Co and Rh cations are also randomly and equally occupying square-based pyramidal sites (C_{4v}) and square-planar sites (D_{4h}) in a 1:1 ratio. In the $La_2CoRhO_{4.5}$ phase, the *B*-site cations have a summed charge of 3, which is consistent with the combination of Co^{I} and Rh^{II}. Based on the previous studies of reduced rhodium-containing Ruddlesden-Popper phase $LaSrCo_{0.5}Rh_{0.5}O_{3.25}$, the nominal Rh^{II} in $La_2CoRhO_{4.5}$ is believed to disproportionate to a 1:1 ratio of Rh^{III}:Rh^{I}, with Rh^{III} located in C_{4v} sites and Rh^{I} located in D_{4h} sites. The resulting electron configurations of Co and Rh cations in $La_2CoRhO_{4.5}$ are shown in Figure 8-17.

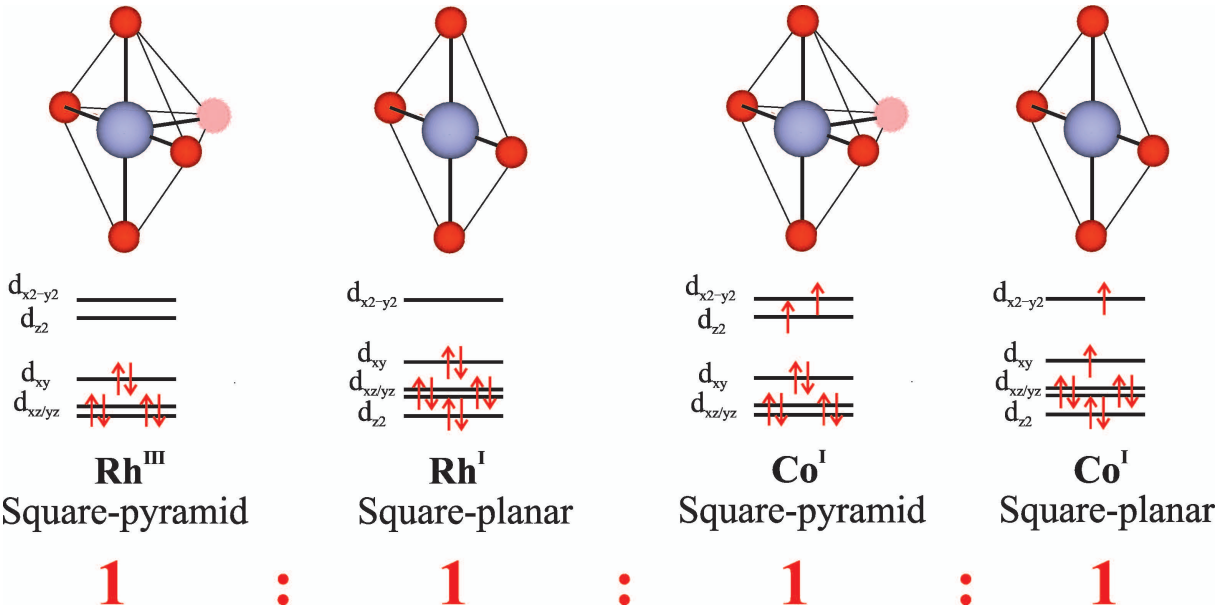


Figure 8-17 Electron configurations of Co^{I} and $Rh^{I/III}$ sites in $La_2CoRhO_{4.5}$.

As discussed in Section 8.3.3.2, the observation of three magnetic regimes suggests that the evolution of the magnetic behaviour of $La_2CoRhO_{4.5}$ with temperature is unusual. At 2 K, $La_2CoRhO_{4.5}$ adopts an antiferromagnetically ordered state with a magnetic structure combining two magnetic irreducible models $m\Gamma_1^+$ (G-type AFM) and mM_5^+ (C-type AFM).

These two magnetic irreducible models share a common feature, the AFM order within the *xy*-plane. On the other hand, G-type AFM order exhibits AFM order along the *z*-axis while C-type AFM order exhibits FM order along the *z*-axis. The mechanism of the formation of these two different AFM orders is discussed based on the electronic configuration of $3d^8$ Co^{I} cations, since both low-spin $4d^6$ Rh^{III} and low-spin $4d^8$ Rh^{I} are diamagnetic.

All of the in-plane interactions between Co centres in $La_2CoRhO_{4.5}$ are listed in Figure 8-18. All of them are (Co $3d_{x^2-y^2}$)^1 - O $2p$ - (Co $3d_{x^2-y^2}$)^1 super-exchange couplings, which are expected to be strong AFM interactions according to the Goodenough−Kanamori rules[42]. These interactions are consistent with the observed in-plane AFM order in both C-type and G-type AFM order.

As shown in Figure 8-19, three different chemical configurations can occur in the out-of-plane direction. Firstly, we can consider the coupling between C_{4v} coordinated cobalt centres. As shown in Figure 8-19 (A), either (Co $3d_{z^2}$)^1 - O $2p$ - (Co $3d_{z^2}$)^1 super-exchange coupling or (Co $3d_{z^2}$)^1 - (Co $3d_{z^2}$)^1 direct exchange coupling should yield an AFM interaction. Secondly, the coupling between a C_{4v} and a D_{4h} coordinated cobalt centres should yield an FM (Co $3d_{z^2}$)^1 - (Co $3d_{z^2}$)^2 direct exchange coupling as shown in Figure 8-19 (B). Finally, the coupling between two D_{4h} coordinated cobalt centres will be weak as the orbitals which have a z-component (d_{z^2}, d_{xz}, d_{yz}) are all filled. Among these three configurations, the AFM C_{4v} - C_{4v} interaction is consistent with the out-of-plane AFM order in G-type AFM model while the FM D_{4h} - C_{4v} interaction can be related to the out-of-plane FM order in C-type AFM model. Thus, the overall magnetic order along the *z*-axis remains unclear since the FM interactions and AFM interactions compete with each other.

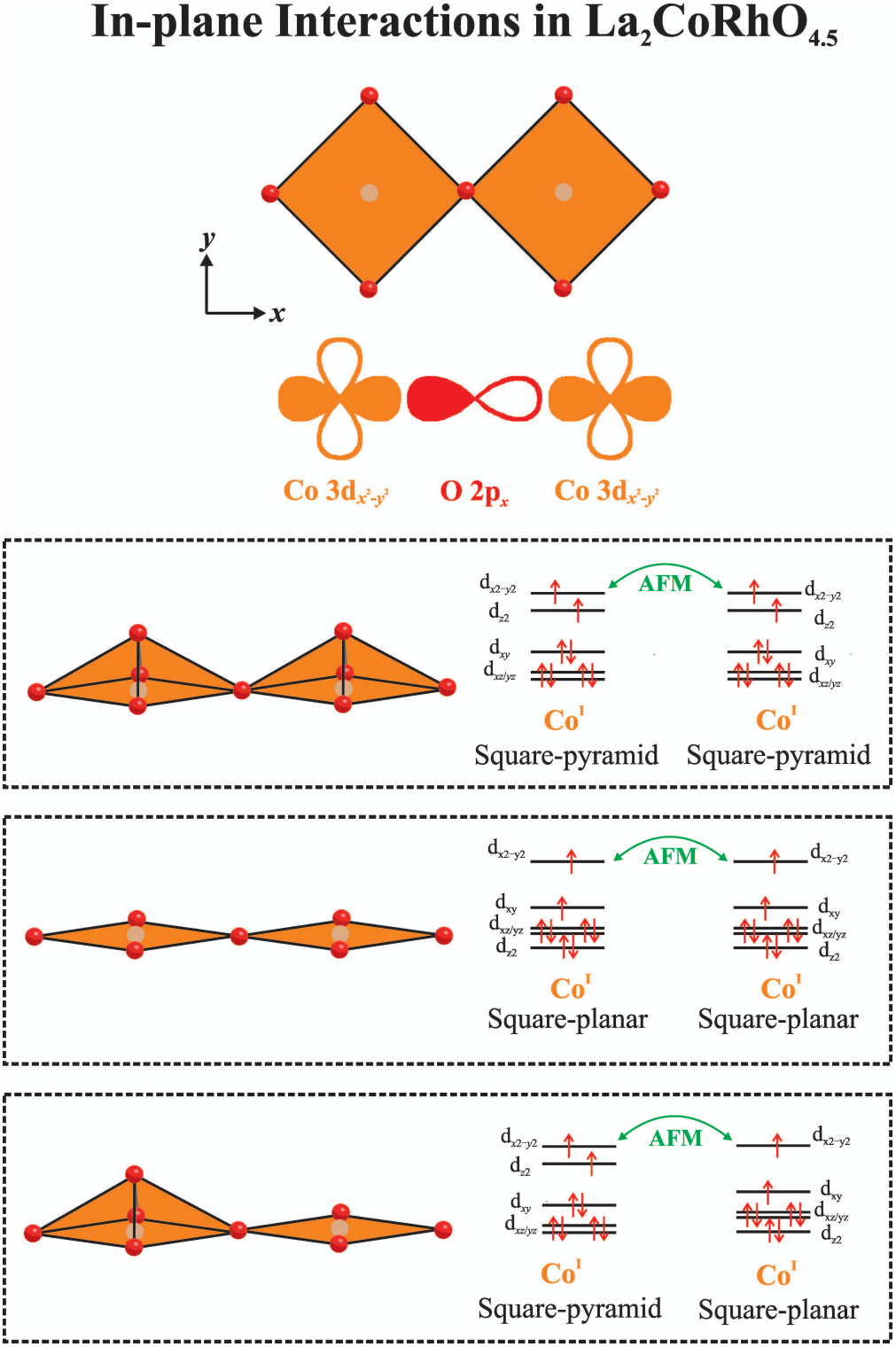


Figure 8-18 In-plane magnetic interactions between Co centres in $La_2CoRhO_{4.5}$.

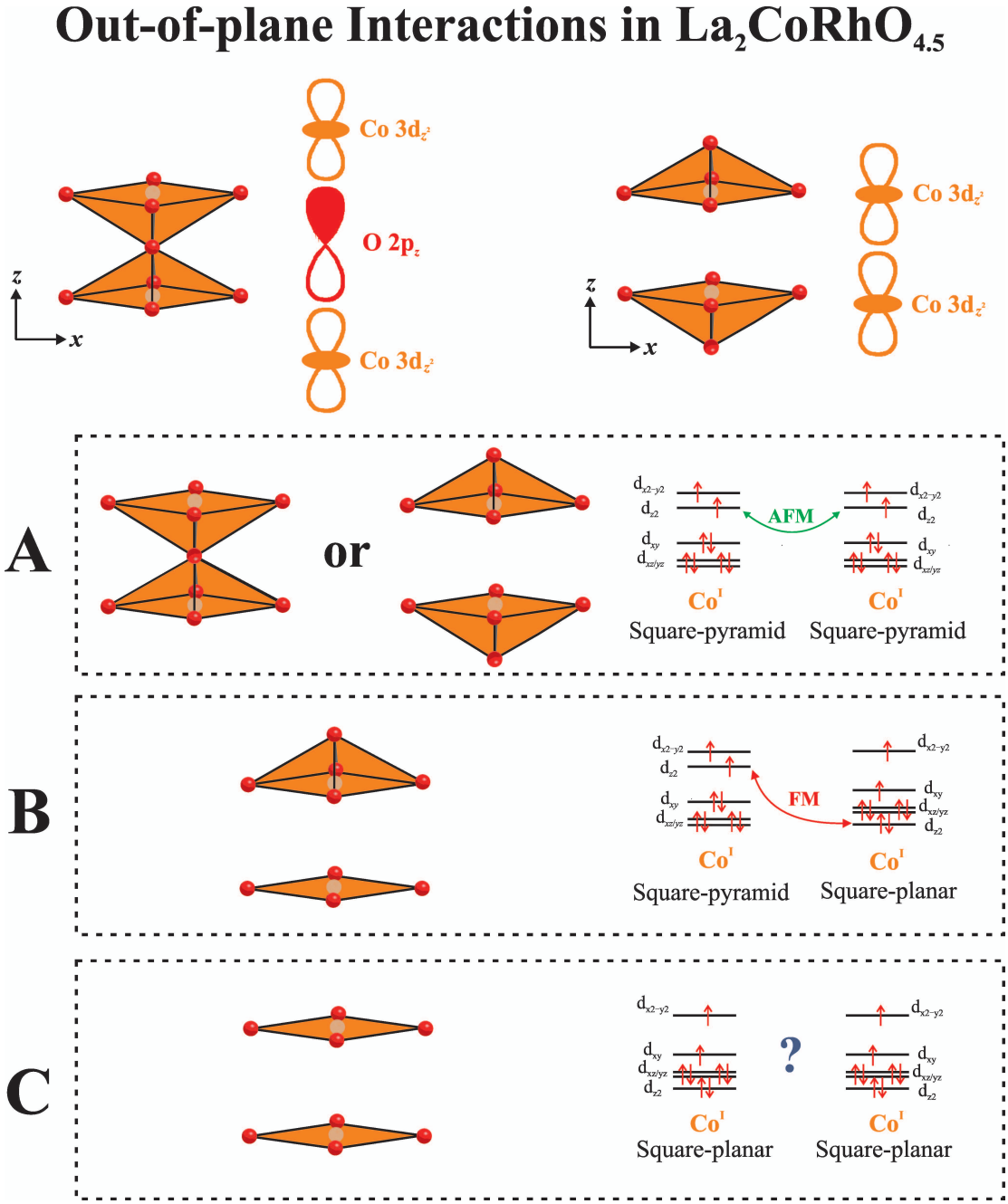


Figure 8-19 Out-of-plane magnetic interactions between Co centres in $La_2CoRhO_{4.5}$.

To further understand the competition between AFM and FM couplings along the *z*-axis, the local chemical configuration was considered. Figure 8-20 shows all the possible local arrangements of vacancies (indicated by white boxes) and anions (indicated by red boxes) which are consistent with the refined structure of $La_2CoRhO_{4.5}$. The probability that an apical anion site (indicated by pink boxes) is occupied is ¼. In addition, the formation of an octahedron is not compatible with the refined structure, which means two consecutive apical oxygen positions cannot be occupied at the same time. Thus, five configurations (A to E) are possible, as shown in Figure 8-20. Both configuration A and B represent the AFM interactions between two C_{4v} Co^{I} cations. Configuration C and D show the FM interactions between C_{4v} Co^{I} and D_{4h} Co^{I}. Configuration E shows no magnetic interaction between two D_{4h} Co^{I} sites. The calculated probability of AFM: FM: None is 16:21:27, which indicates that the number of out-of-plane FM interactions, consistent with the C-type AFM order, is greater than the number of out-of-plane AFM interactions corresponding to the G-type AFM order, indicating the couplings leading to C-type AFM order are stronger than that leading to G-type AFM order.

The variable-temperature NPD data is consistent with the inference that C-type AFM order is more favoured than G-type AFM order. Upon cooling from 300 K, C-type AFM order of $La_2CoRhO_{4.5}$ forms at some temperature above 174 K while G-type AFM order of $La_2CoRhO_{4.5}$ forms is added at around 125 K, which changes the configuration of the ordered spins as shown in Figure 8-8.

Thus, we can see that the complex magnetic structure exhibited by $La_2CoRhO_{4.5}$ arises from competition between FM and AFM couplings along the *z*-axis. However, rather than this leads to frustration, the two couplings lead to different ordered patterns for the in-plane (*xy*) and out-of-plane (*z*) components of the spins.

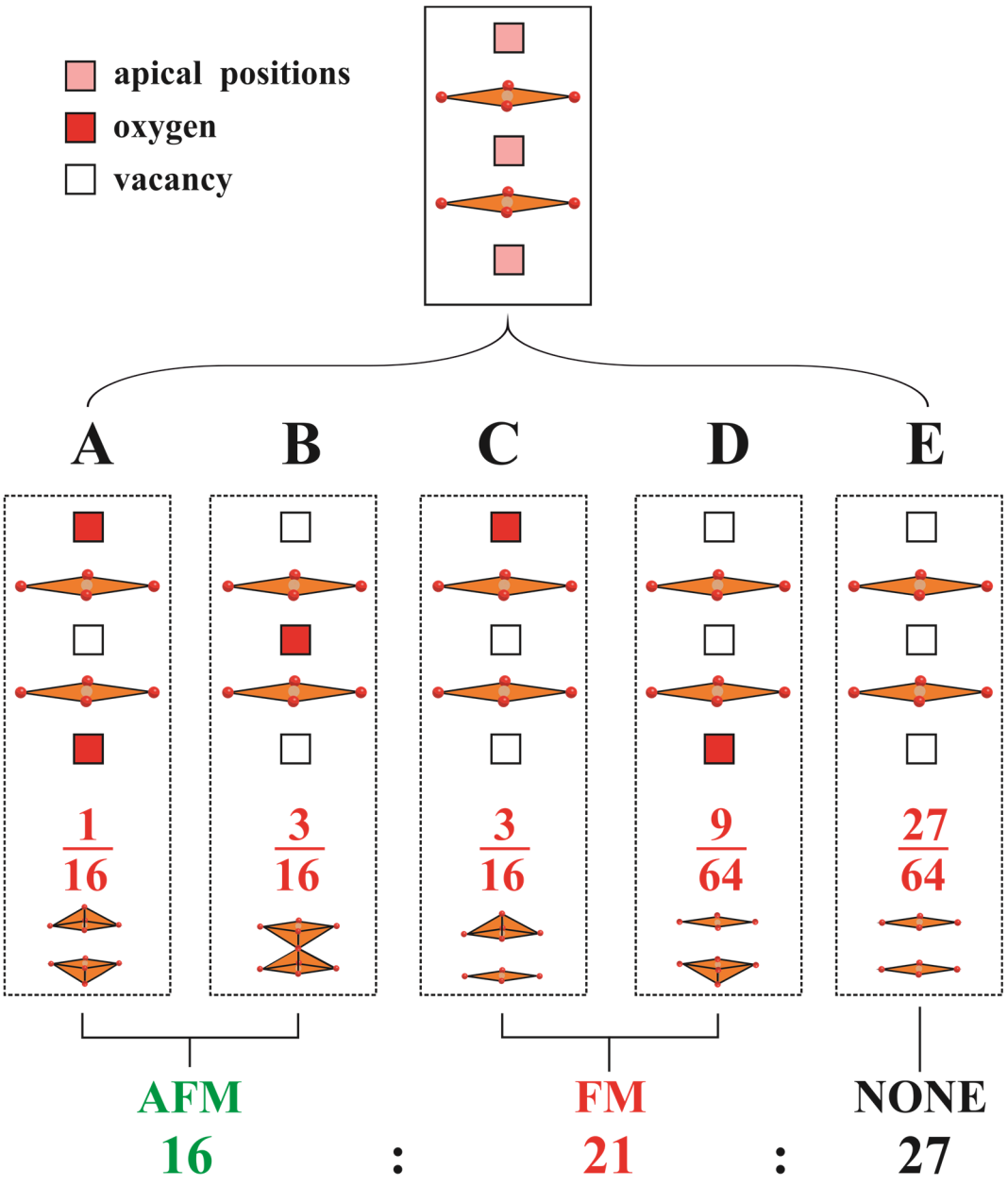


Figure 8-20 A statistical model presenting a local chemical environment for Co ions. Orange square planes with light orange spheres and red spheres present known CoO_4 sites, red squares present occupied oxygen atoms and white squares present oxygen vacancies.

8.5. Conclusion

Topochemical reduction of the solid solution phase La_2CoRhO_6 with Zr yields $La_2CoRhO_{4.5}$, which is isostructural to $La_2NiRhO_{4.5}$ and $LaSrMnRhO_{4.5}$.

A combination of variable-temperature NPD data and magnetisation data reveals that $La_2CoRhO_{4.5}$ exhibits complicated magnetic behaviour. Three magnetic regimes occurs as a function of temperature. $La_2CoRhO_{4.5}$ adopts a paramagnetic state at room temperature, an C-type AFM state below 174 K and a combination of C-type and G-type AFM state below ~ 125 K. The out-of-plane (Co $3d_{z^2}$)^1 - (Co $3d_{z^2}$)^2 direct exchange FM coupling and out-of-plane (Co $3d_{z^2}$)^1 - O $2p$ - (Co $3d_{z^2}$)^1 super-exchange AFM coupling compete with each other, leading to the formation of the two different AFM ordering patterns which coexist in the system.

Chapter 9

Conclusions

In this thesis, topochemical reactions of some rhodium-containing complex transition-metal oxides using Zr as a reducing agent were investigated and a wide range of metastable phases were made for the first time.

The initial target of the study is to form metastable oxide phases containing rhodium with unusual oxidation states such as Rh^{I} and/or Rh^{II}. Hence, a series of rhodium-containing complex oxides, which were covalently stabilized by 3d transition metal (Co, Ni, Mn, Fe), were synthesized and investigated.

As discussed in Chapter 4, in the reduction reactions of n = 1 Ruddlesden-Popper phases $LaSrM_{0.5}Rh_{0.5}O_4$ (M = Co, Ni), the 'parent' oxide phases went through the selective deintercalation of 'equatorial' oxygen atoms in transition-metal octahedra. The reactions yielded the resulting oxygen-deficient phases $LaSrM^{I}_{0.5}Rh^{I/III}_{0.5}O_{3.25}$ (M = Co, Ni), where M and Rh cations randomly and equally occupy a 1:1 ratio of square-based pyramidal sites (C_{4v}) and square-planar sites (D_{4h}). It's confirmed that instead of forming Rh^{II}, rhodium centres tend to disproportionate into a 1:1 ratio of Rh^{I}: Rh^{III} with Rh^{I} located in D_{4h} sites and Rh^{III} located in C_{4v} sites. In addition, the diamagnetic rhodium centres are regarded as suppressors of magnetic interactions between cobalt centres, leading to frustration in the system and spin glass behaviour of $LaSrM_{0.5}Rh_{0.5}O_{3.25}$ (M = Co, Ni).

The observation of these mixed valence $Rh^{I/III}$ compounds confirm the instability of Rh^{II} in complex oxides. However, disproportionation phenomenon doesn't necessarily apply to other d^7 transition metals. Unlike rhodium, analogous charge-separated $Ir^{I/III}$ oxides have not been reported yet while Ir^{II}-containing reduced oxides (Sr_2FeIrO_4[1], $Sr_2Co_{0.5}Ir_{0.5}O_3$[2]) can be found

in literature. Thus, the reduction of similar rhodium-containing oxides such as Sr_2CoRhO_4 is still worthy of further study.

The discovery of Rh^{II} disproportionation in $LaSrM_{0.5}Rh_{0.5}O_{3.25}$ (M = Co, Ni) raises a number of questions about the factors controlling the extent of anion-deintercalation. To investigate whether the metal oxidation states and oxygen deficiency are linked, A-site doping of $LaSrCo_{0.5}Rh_{0.5}O_4$ and the further reduction of this series of compounds were carried out and discussed in Chapter 5 and Chapter 6. $LaSrCo_{0.5}Rh_{0.5}O_4$ can accommodate A-site doping to form single phases in the composition range $La_xSr_{2-x}Co_{0.5}Rh_{0.5}O_4$ ($0.85 \leq x \leq 1.15$). The reduction of this series of compounds yields the reduced doped phases $La_xSr_{2-x}Co_{0.5}Rh_{0.5}O_{3.25}$ ($0.90 \leq x \leq 1.10$). The presence of a 1:1 ratio of D_{4h}:C_{4v} coordination for B-sites remains across the whole range of compositions, suggesting that the formation of this series of compounds is controlled by structural feature rather than metal oxidation states.

The topochemical reduction chemistry has been extended to cation-disordered perovskite phases La_2MRhO_6 (M = Co, Ni) and $LaSrMnRhO_6$. The successful synthesis of reduced oxide phases $La_2M^{I}Rh^{III}_{0.5}Rh^{I}_{0.5}O_{4.5}$ (M = Co, Ni) and $LaSrMn^{II}Rh^{III}_{0.5}Rh^{I}_{0.5}O_{4.5}$ further confirms the robustness of the 1:1 ratio of D_{4h}:C_{4v} B-site structural arrangement and the instability of Rh^{II} in extended oxides.

Among the three phases, $La_2NiRhO_{4.5}$ and $LaSrMnRhO_{4.5}$ exhibit canted antiferromagnetic states at 5 K while no magnetic order at low temperature is observed. However, $La_2CoRhO_{4.5}$ exhibits two different types of antiferromagnetic ordering with moments pointing at different directions (G-type antiferromagnetic order with moments pointing out-of-plane, A-type antiferromagnetic order with moments pointing in-plane) at 2 K. Each order responds separately to temperature. The strong in-plane antiferromagnetic interactions ((Co $3d_{x^2-y^2}$)^1 - O $2p$ - (Co $3d_{x^2-y^2}$)^1 super-exchange coupling) result in the antiferromagnetic state of

$La_2CoRhO_{4.5}$. The out-of-plane (Co $3d_{z^2}$)^1 - (Co $3d_{z^2}$)^2 direct exchange FM couplings and out-of-plane (Co $3d_{z^2}$)^1 - O $2p$ - (Co $3d_{z^2}$)^1 super-exchange AFM couplings compete with each other, which can explain the coexistance of two different AFM ordering patterns in the system. Analoguous to $La_2CoRhO_{4.5}$, $La_2NiRhO_{4.6}$ has strong in-plane antiferromagnetic interactions which result in short-range antiferromagnetic couplings. However, different from $La_2CoRhO_{4.5}$, the weak out-of-plane interactions in $La_2NiRhO_{4.6}$ block the three-dimensional magnetic order of the system.

Overall the projects presented in this thesis have shown a rich reduction story of rhodium in complex oxides. The chemical and magnetic properties of mentioned metastable reduced oxide phases are intimately bound up with the structures they exhibit. This thesis presents some rhodium related study but also has left some open questions and worthwhile possibilities, which needs further investigation.

Appendix 1 Table of Figures

Figure 1-1 (a) a cubic $Pm\bar{3}m$ nunit cell of $SrTiO_3$[13]; the pink dashed lines represent *A*-O, *B*-O, *A*-*B* bond distances. (b) a schematic presentation of the cooperative rotations of BO_6 octahedra to fit to $t < 1$ scenario in $CaTiO_3$ phase (Undistorted $SrTiO_3$ is plotted as a reference)[15]. ---------- 3

Figure 1-2 The ABO_3 perovskite-related structure of ($t = 1$): $SrTiO_3$ cubic $Pm\bar{3}m$ [13]; ($t < 1$): $CaTiO_3$ orthorhombic $Pbnm$[15], $LaNiO_3$ trigonal $R\bar{3}c$[17], $SrIrO_3$ monoclinic $C2/c$[18]; ($t > 1$): $BaNiO_3$ hexagonal $P6_3/mmm$[19]. ---------- 4

Figure 1-3 (a) A schematic presentation of an octahedron and its possible rotation along three 4-fold axes (shown as blue arrows). (b) A schematic presentation of in -phase uniaxial rotation (left) and out-of-phase uniaxial rotation (right). ---------- 5

Figure 1-4 Ruddlesden-Popper phases $A_{n+1}B_nO_{3n+1}$ with n = 1,2,3[29]. The red and green brackets present the perovskite slabs and the rock salt layers, respectively. The pink circles present two different *A*-site positions.---------- 8

Figure 1-5 A schematic diagram of the spin state of trivalent Co ions: (left) low spin, $t_{2g}^6e_g^0$ Co^{III} with energy of -6 J_{ex} (J_{ex}: intra-atomic exchange energy); (middle) high spin, $t_{2g}^4e_g^2$ Co^{III} with energy of 2Δ-$10J_{ex}$ (Δ: crystal field splitting energy); (right) intermediate spin, $t_{2g}^5e_g^1$ Co^{III} with energy of Δ-$7J_{ex}$. ----------10

Figure 1-6 A schematic representation of super-exchange interactions of *M*-O-*M* in 180° (left) and 90° (right) arrangements. ----------12

Figure 1-7 A schematic presentation of the Ruddlesden–Popper phase $LaSr_3NiRuO_8$ transformed topochemically into the oxide–hydride $LaSrNiRuO_4H_4$ phase by the action of CaH_2 at 450 °C. (La/Sr gray, Ni/Ru green, O red and H blue)[52].----------14

Figure 1-8 Topochemical reduction of $LaCoO_3$ with Zr getter to form reduced phases $La_nCo_nO_{3n-1}$ (n = 2,3)[53][54].----------16

Figure 2-1 A schematic graph of a sealed silica ampoule for zirconium getter reactions. ----21

Figure 2-2 A schematic graph of an argon-filled glovebox[58] ----------23

Figure 2-3 A schematic graph of an air-sensitive X-ray sample holder.----------24

Figure 2-4 Bragg's Law Reflection. The constructive interference occurs when the distance difference x between paths ABC and A'B'C' equals to an integer number of wavelengths. -25

Figure 2-5 A Schematic representation of Beamline I11 showing the main components and their approximate distances from the IVU (X-ray source)[61]. ----------28

Figure 2-6 The POLARIS diffractometer at the ISIS Facility pulsed neutron source.[65] -----31

Figure 2-7 D2B diffractometer at ILL, Grenoble, France.[66] ----------33

Figure 2-8 D1B diffractometer at ILL, Grenoble, France.[67] ----------33

Figure 2-9 A schematic representation of the principal component in a SQUID magnetometer. ----------36

Figure 2-10 A schematic representation of the principles of ferrosubtraction measurements.38

Figure 2-11 A schematic diagram of an XPS measurement system equipped with an electrostatic hemispherical analyser.[72] ----------42

Figure 3-1 Observed (red), calculated (green) and difference plots (pink) from the Rietveld structural refinement of $LaSrCo_{0.5}Rh_{0.5}O_4$ using an *I4/mmm* model against SXRD data collected at room temperature. ----------48

Figure 3-2 The crystal structure of $LaSrCo_{0.5}Rh_{0.5}O_4$ (left) with displacement ellipsoids (right). ----------49

Figure 3-3 Observed(red), calculated(green) and difference plots(pink) from the Rietveld structural refinement of $LaSrNi_{0.5}Rh_{0.5}O_4$ using an *I4/mmm* model against SXRD data collected at room temperature.----------50

Figure 3-4 The crystal Structure of $LaSrNi_{0.5}Rh_{0.5}O_4$ with displacement ellipsoids at 298 K (left) and 5 K (right). ----------51

Figure 3-5 Observed, calculated and difference plots from the refinement of $LaSrNi_{0.5}Rh_{0.5}O_4$ against NPD data collected at 298 K. ----------52

Figure 3-6 Comparison of low-angle NPD data collected from $LaSrNi_{0.5}Rh_{0.5}O_4$ at 298 K and 5 K. ----------53

Figure 3-7 Observed(red), calculated(green) and difference plots(pink) from the Rietveld structural refinement of $La_{0.5}Sr_{1.5}Fe_{0.5}Rh_{0.5}O_4$ using an *I4/mmm* model against SXRD data collected at room temperature. ----------55

Figure 3-8 The crystal Structure of $La_{0.5}Sr_{1.5}Fe_{0.5}Rh_{0.5}O_4$ with displacement ellipsoids at 298 K (left) and 5 K (right). ----------56

Figure 3-9 Observed, calculated and difference plots from the refinement of $La_{0.5}Sr_{1.5}Fe_{0.5}Rh_{0.5}O_4$ against NPD data collected at 298 K. ----------57

Figure 3-10 Comparison of low-angle NPD data collected from $La_{0.5}Sr_{1.5}Fe_{0.5}Rh_{0.5}O_4$ at 298 K and 5 K. ----------58

Figure 3-11 (left) Zero-field-cooled and field-cooled magnetisation data collected from $LaSrCo_{0.5}Rh_{0.5}RhO_4$ in an applied field of 100 Oe. Inset shows the fit to the Curie-Weiss law; (right) magnetisation data collected as a function of the applied field from $LaSrCo_{0.5}Rh_{0.5}RhO_4$. ----------61

Figure 3-12 (left) Zero-field-cooled and field-cooled magnetisation data collected field from $LaSrNi_{0.5}Rh_{0.5}O_4$ in an applied field of 100 Oe. Inset shows the fit to the Curie-Weiss law; (right) Magnetisation data collected as a function of applied field from $LaSrNi_{0.5}Rh_{0.5}RhO_4$. ----------62

Figure 3-13 (left) Zero-field-cooled and field-cooled magnetisation data collected from $La_{0.5}Sr_{1.5}Fe_{0.5}Rh_{0.5}O_4$ in an applied field of 100 Oe. Inset shows the fit to the Curie-Weiss law;

(right) Magnetisation data collected as a function of applied field from $La_{0.5}Sr_{1.5}Fe_{0.5}Rh_{0.5}O_4$. ----------63

Figure 3-14 Proposed electronic configurations of $LaSrCo_{0.5}Rh_{0.5}O_4$.----------65

Figure 3-15 Proposed electronic configurations of $LaSrNi_{0.5}Rh_{0.5}O_4$. ----------68

Figure 3-16 Proposed electronic configurations of $La_{0.5}Sr_{1.5}Fe_{0.5}Rh_{0.5}O_4$. ----------69

Figure 4-1 Topochemical reduction profile of $LaSrCo_{0.5}Rh_{0.5}O_4$ with Zr to form a compositional range of $LaSrCo_{0.5}Rh_{0.5}O_{4-\delta}$. ----------73

Figure 4-2 Reductive thermogravimetric data collected from $LaSrCo_{0.5}Sr_{0.5}O_{4-\delta}$. Top panel indicates the heating profile, bottom panel the relative mass of the sample.----------75

Figure 4-3 Reductive thermogravimetric data collected from $LaSrNi_{0.5}Rh_{0.5}O_{4-\delta}$. Top panel indicates the heating profile, bottom panel the relative mass of the sample.----------76

Figure 4-4 Observed(red), calculated(green) and difference plots(pink) from the Rietveld structural refinement of $LaSrCo_{0.5}Rh_{0.5}O_{3.25}$ using an *Immm* model against SXRD data collected at room temperature. ----------78

Figure 4-5 Observed(red), calculated(green) and difference plots(pink) from the Rietveld structural refinement of $LaSrNi_{0.5}Rh_{0.5}O_{3.25}$ using an *Immm* model against SXRD data collected at room temperature.----------78

Figure 4-6 The crystal structure of $LaSrCo_{0.5}Rh_{0.5}O_{3.25}$ with displacement ellipsoids at 298 K (left) and 5 K (right); Grey, purple, red, and pink spheres represent La/Sr, Co/Rh, O and partially occupied O positions, respectively. ----------80

Figure 4-7 Comparison of low-angle NPD data collected from $LaSrCo_{0.5}Rh_{0.5}O_{3.25}$ at 298 K and 5 K. ----------80

Figure 4-8 Observed, calculated and difference plots from the refinement of $LaSrCo_{0.5}Rh_{0.5}O_{3.25}$ against NPD data collected at 5 K. (The peak at 2.2 Å indicates the peak position of vanadium from the sample container.) ----------81

Figure 4-9 Observed, calculated and difference plots from the refinement of $LaSrCo_{0.5}Rh_{0.5}O_{3.25}$ against NPD data collected at 298 K. (The peak at 2.2 Å indicates the peak position of vanadium from the sample container.) ----------82

Figure 4-10 The crystal structure of $LaSrNi0.5Rh_{0.5}O_{3.25}$ with displacement ellipsoids at 298 K (left) and 5 K (right). ----------85

Figure 4-11 Comparison of low-angle NPD data collected from $LaSrNi_{0.5}Rh_{0.5}O_{3.25}$ at 298 K and 5 K. ----------85

Figure 4-12 Observed, calculated and difference plots from the refinement of $LaSrNi_{0.5}Rh_{0.5}O_{3.25}$ against NPD data collected at 5 K. Black tick marks indicate peak positions of the majority phase ($LaSrNi_{0.5}Rh_{0.5}O_{3.25}$, red tick marks the minority phase (SrO). ---------86

Figure 4-13 Observed, calculated and difference plots from the refinement of $LaSrNi_{0.5}Rh_{0.5}O_{3.25}$ against NPD data collected at 298 K. Black tick marks indicate peak positions of the majority phase ($LaSrNi_{0.5}Rh_{0.5}O_{3.25}$), red tick marks the minority phase (SrO). ----------87

Figure 4-14 XPS collected from $LaSrCo_{0.5}Rh_{0.5}O_{3.25}$ (top) and $LaSrNi_{0.5}Rh_{0.5}O_{3.25}$ (bottom). Peaks from the Rh $3d_{5/2}$ and Rh $3d_{3/2}$ emissions are fit by two components each, corresponding to Rh^{I} and Rh^{III}. ----------91

Figure 4-15 The paramagnetic susceptibility (top) and saturated ferromagnetic moment (bottom) of $LaSrCo_{0.5}Rh_{0.5}O_{3.25}$ collected as a function of temperature. Inset: the fit to the Curie-Weiss law in the temperature range $50 < T/K < 300$. ----------93

Figure 4-16 The paramagnetic susceptibility (top) and saturated ferromagnetic moment (bottom) of $LaSrNi_{0.5}Rh_{0.5}O_{3.25}$ collected as a function of temperature. Inset: the fit to the Curie-Weiss law in the temperature range $15 < T/K < 300$. ----------94

Figure 4-17 Magnetisation data collected as a function of applied field from $LaSrCo_{0.5}Rh_{0.5}O_{3.25}$ (left) and $LaSrNi_{0.5}Rh_{0.5}O_{3.25}$ (right). ----------95

Figure 4-18 A schematic presentation of the conversion from LaSr$M_{0.5}$Rh$_{0.5}$O$_4$ to LaSr$M_{0.5}$Rh$_{0.5}$O$_{3.25}$ (M = Co, Ni). Grey, blue, red, and pink spheres represent La/Sr, M/Rh, O, and partially occupied O positions, respectively. ----------96

Figure 4-19 Predicted Curie constants of LaSr$M_{0.5}$Rh$_{0.5}$O$_{3.25}$ (M = Co, Ni) for M^{I}/Rh^{II} oxidation-state combination. ----------98

Figure 4-20 Predicted Curie constants of LaSr$M_{0.5}$Rh$_{0.5}$O$_{3.25}$ (M = Co, Ni) for M^{II}/Rh^{I} oxidation-state combination. ----------99

Figure 4-21 Square-based pyramidal and square-planar transition-metal coordination sites in LaSr$M_{0.5}$Rh$_{0.5}$O$_{3.25}$ (M = Co, Ni) with local electronic configurations of d^6 Rh^{III} and d^8 Rh^{I} in C$_{4v}$ and D$_{4h}$ sites, respectively. ---------- 100

Figure 4-22 Predicted Curie constants of LaSr$M_{0.5}$Rh$_{0.5}$O$_{3.25}$ (M = Co, Ni) for M^{I}, Rh$^{I/III}$ oxidation-state combination. ---------- 101

Figure 5-1 Observed(red), calculated(green) and difference plots(pink) from the Rietveld structural refinement of La$_{0.85}$Sr$_{1.15}$Co$_{0.5}$Rh$_{0.5}$O$_4$ using an *I4/mmm* model against SXRD data collected at room temperature. ---------- 106

Figure 5-2 Plot (a) a, c; (b) volume against x in La$_x$Sr$_{2-x}$Co$_{0.5}$Rh$_{0.5}$O$_4$ ($0.85 \leq x \leq 1.15$) series of compounds. (Error bars for the parameters are smaller than the points plotted.)---------- 107

As shown in Figure 5-3, the differences in ionic radii of Co/Rh ions contribute to changes in the a lattice parameter and both the La^{III}/ Sr^{II} size difference and Co/Rh size difference contribute to the changes in the c lattice parameter.---------- 107

Figure 5-4 (left) Zero-field-cooled and field-cooled magnetisation data collected in an applied field of 100 Oe. Inset shows the fit to the Curie-Weiss law; (right) Magnetisation data collected as a function of applied field from La$_{0.95}$Sr$_{1.05}$Co$_{0.5}$Rh$_{0.5}$RhO$_4$. ---------- 109

Figure 5-5 Plot of (a) Curie constant, C; and (b) Weiss temperature , θ, against x in $La_xSr_{2-x}Co_{0.5}Rh_{0.5}O_4$ ($0.85 \leq x \leq 1.15$) series of compounds. (Error bars for the parameters are smaller than the points plotted.) ---------- 109

Figure 5-6 The comparison of in-plane Co-O bond length in a series of doped compounds $La_xSr_{2-x}Co_{0.5}Rh_{0.5}O_4$ ($0.85 \leq x \leq 1.15$) shown in blue markers, a series of doped compound $La_xSr_{2-x}CoO_4$ ($0.5 \leq x \leq 1.6$)[96,97] shown in red markers and $LaCoO_3$ with respect to temperature changing shown in green markers[95]. ---------- 111

Figure 6-1 Reductive thermogravimetric data collected from $La_{1.05}Sr_{0.95}Co_{0.5}Rh_{0.5}O_{3.25}$ (left) and $La_{0.90}Sr_{1.10}Co_{0.5}Rh_{0.5}O_{3.25}$ (right). Top panel indicates the heating profile, bottom panel the relative mass of the sample. ---------- 118

Figure 6-2 Observed(red), calculated(green) and difference plots(pink) from the Rietveld structural refinement of $La_{0.95}Sr_{1.05}Co_{0.5}Rh_{0.5}O_{3.25}$ using an *Immm* model against SXRD data collected at room temperature. Black tick marks indicate peak positions of the majority phase, red tick marks peak positions of the La_2O_3 phase.---------- 120

Figure 6-3 Plot (a) *a*, *b*, *c*; (b) volume against x in $La_xSr_{2-x}Co_{0.5}Rh_{0.5}O_{3.25}$ ($0.90 \leq x \leq 1.10$) series of compounds. ---------- 120

As shown in Figure 6-3 (a), the changes in the *a*, *b* lattice parameters in this series of compounds are subtle (< 0.02 Å). The unit cell shown in Figure 6-4 indicates that the differences in ionic radii of Co/Rh atoms contribute to changes in the *a* and *b* lattice parameters and both the La^{III}/ Sr^{II} size difference and Co/Rh size difference contribute to the changes in the *c* lattice parameter. Compared to the unit cell of the parent oxide $LaSrCo_{0.5}Rh_{0.5}O_4$, the selective deintercalation of oxygen atoms on 'equatorial' oxygen atoms along *a* axis makes the *a* lattice parameter shorter, while *b* and *c* remains roughly the same.---------- 121

Figure 6-5 The paramagnetic susceptibility (top) and saturated ferromagnetic moment (bottom) of $La_{0.95}Sr_{1.05}Co_{0.5}Rh_{0.5}O_{3.25}$ collected as a function of temperature. Inset: the fit to the Curie-Weiss law in the temperature range $25 < T/K < 300$. ---------- 123

Figure 6-6 Plot of (a) Curie constant, C; and (b) Weiss temperature, θ, against x in $La_xSr_{2-x}Co_{0.5}Rh_{0.5}O_{3.25}$ ($0.90 \leq x \leq 1.10$) series of compounds. ---------- 124

Figure 6-7 Magnetisation data collected as a function of applied field from (a) $La_{0.95}Sr_{1.05}Co_{0.5}Rh_{0.5}O_4$; and (b) $La_{0.95}Sr_{1.05}Co_{0.5}Rh_{0.5}O_{3.25}$.---------- 125

Figure 6-8 Predicted spin states of *B*-site transition metal cations in $LaSrCo_{0.5}Rh_{0.5}O_{3.25}$. - 127

Figure 6-9 Predicted spin states of *B*-site transition metal cations in $La_xSr_{2-x}Co_{0.5}Rh_{0.5}O_{3.25}$ ($x < 1.0$).---------- 128

Figure 6-10 Predicted spin states of *B*-site transition metal cations in $La_xSr_{2-x}Co_{0.5}Rh_{0.5}O_{3.25}$ ($x > 1.0$). ---------- 129

Figure 7-1 The crystal Structure of La_2NiRhO_6 (space group *Pbnm* with $a^+b^-b^-$ rotation). - 133

Figure 7-2 Observed(red), calculated(green) and difference plots(pink) from the Rietveld structural refinement of La_2NiRhO_6 using a *Pbnm* model against laboratory XRD data collected at room temperature. (Bruker diffractometer λ = 1.5418 Å) ---------- 134

Figure 7-3 Crystal structures of La_2MnRhO_6 (left) and $LaSrMnRhO_6$ (right) in space group *Pnma*. The bottom panel shows views down the [010] directions. Brown and green octahedra denote the Mn/Rh site. Dark grey, light grey, purple, blue spheres represent La, Sr, Mn, Rh sites respectively. ---------- 135

Figure 7-4 Observed(red), calculated(green) and difference plots(pink) from the Rietveld structural refinement of La_2MnRhO_6 using a *Pbnm* model against SXRD data collected at room temperature.---------- 136

Figure 7-5 Observed(red), calculated(green) and difference plots(pink) from the Rietveld structural refinement of $LaSrMnRhO_6$ using a *Pbnm* model against SXRD data collected at room temperature.---------- 137
Figure 7-6 Topochemical reduction profile of La_2NiRhO_6 with Zr to form a compositional range of $La_2NiRhO_{6-\delta}$. The red dashed lines represent the orthorhombic peaks from La_2NiRhO_6; the blue dashed lines represent the tetragonal peaks from $La_2NiRhO_{6-\delta}$ at 420 °C; the pink dashed line with * indexes an impurity phase. ---------- 139
Figure 7-7 Trial reduction profile of La_2MnRhO_6 with Zr---------- 140
Figure 7-8 Topochemical reduction profile of $LaSrMnRhO_6$ with Zr to form a compositional range of $LaSrMnRhO_{6-\delta}$. ---------- 141
Figure 7-9 Reductive thermogravimetric data collected from $La_2NiRhO_{6-\delta}$. Top panel indicates the heating profile, bottom panel the relative mass of the sample. ---------- 142
Figure 7-10 Reductive thermogravimetric data collected from $LaSrMnRhO_{6-\delta}$. Top panel indicates the heating profile, bottom panel the relative mass of the sample.---------- 143
Figure 7-11 Crystal structures of $La_2NiRhO_{4.6}$ in *P*4/*mmm* space group (left) and *I*4/*mcm* space group (right). The top panel shows views down the [010] directions. Blue and purple octahedra denote the Ni/Rh site. Grey, dark purple, light blue, red, pink spheres represent La, Ni, Rh, O, partially occupied O sites, respectively.---------- 145
Figure 7-12 Observed, calculated and difference plots from the refinement of $La_2NiRhO_{4.6}$ against NPD data collected at 298 K using an *I*4/*mcm* model (top) and a *P*4/*mmm* model (bottom). Upper tick marks present the peak positions of vanadium from sample containers, middle ticks mark the minority phase La_2CoRhO_6 and lower tick marks the majority phase $La_2NiRhO_{4.6}$.---------- 146
Figure 7-13 Observed, calculated and difference plots from the refinement of $LaSrMnRhO_{4.5}$ against NPD data collected at 298 K using an *I*4/*mcm* model (top) and a *P*4/*mmm* model

(bottom). Upper tick marks present the peak positions of vanadium from sample containers, lower tick marks present the peak positions of $LaSrMnRhO_{4.5}$. ---------- 147
Figure 7-14 Observed, calculated and difference plots from the refinement of $La_2NiRhO_{4.6}$ against NPD data collected at 298 K using an *I*4/*mcm* model. Upper tick marks indicate peak positions of vanadium from sample containers, middle tick marks indicate peak positions of La_2NiRhO_6 and lower tick marks indicate peak positions of $La_2NiRhO_{4.6}$. ---------- 149
Figure 7-15 Observed, calculated and difference plots from the refinement of $LaSrMnRhO_{4.5}$ against NPD data collected at 298 K using an *I*4/*mcm* model. Upper tick marks indicate peak positions of vanadium from sample containers and lower tick marks indicate peak positions of $LaSrMnRhO_{4.5}$. ---------- 149
Figure 7-16 Comparison of NPD data collected from $La_2NiRhO_{4.6}$ at 298 K (using D2B diffractometer) and 2 K (using D1B diffractometer). ---------- 151
Figure 7-17 Comparison of NPD data collected from $LaSrMnRhO_{4.5}$ at 298 K (using D2B diffractometer) and 2 K (using D1B diffractometer). ---------- 151
Figure 7-18 The paramagnetic susceptibility (top) and saturated ferromagnetic moment (bottom) of $La_2NiRhO_{4.6}$ collected as a function of temperature. Inset: the fit to the Curie-Weiss law in the temperature range $70 < T/K < 300$.---------- 153
Figure 7-19 Magnetisation data collected as a function of applied field from $La_2NiRhO_{4.6}$. 154
Figure 7-20 (left) Zero-field-cooled and field-cooled magnetisation data collected in an applied field of 100 Oe. Inset shows the fit to the Curie-Weiss law; (right) Magnetisation data collected as a function of applied field from $LaSrMnRhO_{4.5}$. ---------- 155
Figure 7-21 Electron configurations of Ni^{I} and $Rh^{I/III}$ sites in $La_2NiRhO_{4.6}$.---------- 156
Figure 7-22 In-plane magnetic interactions between Ni and Rh centres in $La_2NiRhO_{4.6}$. --- 158
Figure 7-23 Out-of-plane magnetic interactions between Ni and Rh centres in $La_2NiRhO_{4.6}$. ---------- 159

Figure 8-1 The crystal Structure of La_2CoRhO_6 (space group *Pbnm* with $a^+b^-b^-$ rotation). - 163
Figure 8-2 Observed(red), calculated(green) and difference plots(pink) from the Rietveld structural refinement of La_2CoRhO_6 using a *Pbnm* model against SXRD data collected at room temperature.---------- 163
Figure 8-3 Topochemical reduction profile of La_2CoRhO_6 with Zr to form a compositional range of $La_2CoRhO_{6-\delta}$. ---------- 165
Figure 8-4 Reductive thermogravimetric data collected from $La_2CoRhO_{6-\delta}$. Top panel indicates the heating profile, bottom panel the relative mass of the sample. ---------- 166
Figure 8-5 Observed, calculated and difference plots from the refinement of $La_2CoRhO_{4.5}$ against NPD data collected at 298 K using an *I*4*/mcm* model (top) and a *P*4*/mmm* model (bottom). Red tick marks indicate peak positions of vanadium from sample containers, black tick marks indicate peak positions of $La_2CoRhO_{4.5}$.---------- 168
Figure 8-6 Comparison of NPD data collected from $La_2CoRhO_{4.5}$ at 2 K and 298 K. Dark blue arrows index 2 additional peaks shown in 2 K data: [101] peak at 4.47Å and [100] peak at 5.64 Å.---------- 170
Figure 8-7 Simulations of NPD patterns of $La_2CoRhO_{4.5}$ using magnetic structure models $m\Gamma_1^+$, $m\mathrm{M}_3^+$ and $m\mathrm{M}_5^+$. ---------- 172
Figure 8-8 The refined magnetic unit cell ($m\Gamma_1^+/m\mathrm{M}_5^+$) of $La_2CoRhO_{4.5}$. The light purple and dark purple spheres are cobalt and rhodium, respectively. Lanthanum and oxygen in the unit cell are hidden for a better view. ---------- 173
Figure 8-9 Observed, calculated and difference plots from the refinement of $La_2CoRhO_{4.5}$ against NPD data collected at 2 K using an *I*4*/mcm* nuclear structure model and magnetic models $m\Gamma_1^+$ and $m\mathrm{M}_5^+$. The blue arrows indicate the two additional magnetic peaks: [100] peak at 25.8° and [101] peak at 32.7°. Upper tick marks indicate the peak positions for magnetic

reflections; middle tick marks indicate the peak positions of vanadium from sample containers; lower tick marks indicate the peak positions from the nuclear structure of $La_2CoRhO_{4.5}$. -- 174
Figure 8-10 Observed plots of variable temperature NPD data collected from $La_2CoRhO_{4.5}$ at 2 K, 10 K, 75 K, 100 K, 125 K and 174 K. The black arrows indicate the [100] magnetic peak ($m\Gamma_5^+$), the [101] magnetic peak ($m\Gamma_1^+$) and [110] nuclear peak. ---------- 176
Figure 8-11 The paramagnetic susceptibility (top) and saturated ferromagnetic moment (bottom) of $La_2CoRhO_{4.5}$ collected as a function of temperature. Inset: the fit to the Curie-Weiss law in the temperature range $115 < T/K < 300$. ---------- 178
Figure 8-12 Magnetisation data collected as a function of applied field from $La_2CoRhO_{4.5}$. ---------- 179
Figure 8-13 Temperature evolution of (a) *a* lattice parameter; (b) *c* lattice parameter; (c) volume of the unit cell; (d) goodness of fit for $La_2CoRhO_{4.5}$ determined from the analysis of variable temperature SXRD data at $94 \leq T/K \leq 299$. The red dashed lines in (a) and (b) show the linear fit of the *a* and *c* lattice parameters at $153 \leq T/K \leq 299$. ---------- 180
Figure 8-14 (a) The *a* and *c* lattice parameters extracted from fits to $La_2CoRhO_{4.5}$ NPD data over temperature. (b)The ordered magnetic moment M_x and M_z on Co centres extracted from fits to $La_2CoRhO_{4.5}$ NPD data over temperature. ---------- 181
Figure 8-15 A schematic diagram of the magnetic structure of $La_2CoRhO_{4.5}$ as a function of temperature.---------- 182
Figure 8-16 Observed plots of variable-temperature NPD data collected from $La_2CoRhO_{4.5}$ at 2 K and 174 K. The black arrows indicate the [100] magnetic peak ($m\Gamma_5^+$), the [101] magnetic peak ($m\Gamma_1^+$) and [110] nuclear peak. ---------- 183
Figure 8-17 Electron configurations of Co^{I} and $Rh^{I/III}$ sites in $La_2CoRhO_{4.5}$.---------- 184
Figure 8-18 In-plane magnetic interactions between Co centres in $La_2CoRhO_{4.5}$. ---------- 186
Figure 8-19 Out-of-plane magnetic interactions between Co centres in $La_2CoRhO_{4.5}$.------ 187

Figure 8-20 A statistical model presenting a local chemical environment for Co ions. Orange square planes with light orange spheres and red spheres present known CoO_4 sites, red squares present occupied oxygen atoms and white squares present oxygen vacancies. ---------- 189
Figure A2-1 Observed(red), calculated(green) and difference plots(pink) from the Rietveld structural refinement of $La_{0.90}Sr_{1.10}Co_{0.5}Rh_{0.5}O_4$ using an *I4/mmm* model against SXRD data collected at room temperature. ---------- 211
Figure A2-2 Observed(red), calculated(green) and difference plots(pink) from the Rietveld structural refinement of $La_{0.95}Sr_{1.05}Co_{0.5}Rh_{0.5}O_4$ using an *I4/mmm* model against SXRD data collected at room temperature. ---------- 212
Figure A2-3 Observed(red), calculated(green) and difference plots(pink) from the Rietveld structural refinement of $La_{1.05}Sr_{0.95}Co_{0.5}Rh_{0.5}O_4$ using an *I4/mmm* model against SXRD data collected at room temperature. ---------- 212
Figure A2-4 Observed(red), calculated(green) and difference plots(pink) from the Rietveld structural refinement of $La_{1.10}Sr_{0.90}Co_{0.5}Rh_{0.5}O_4$ using an *I4/mmm* model against SXRD data collected at room temperature. ---------- 213
Figure A2-5 Observed(red), calculated(green) and difference plots(pink) from the Rietveld structural refinement of $La_{1.15}Sr_{0.85}Co_{0.5}Rh_{0.5}O_4$ using an *I4/mmm* model against SXRD data collected at room temperature. ---------- 213
Figure A2-6 Zero-field-cooled and field-cooled magnetisation data collected in an applied field of 100 Oe. Inset shows fit to the Curie-Weiss law (left); Magnetisation data collected as a function of applied field (right) from $La_{0.85}Sr_{1.15}Co_{0.5}Rh_{0.5}RhO_4$. ---------- 214
Figure A2-7 Zero-field-cooled and field-cooled magnetisation data collected in an applied field of 100 Oe. Inset shows fit to the Curie-Weiss law (left); Magnetisation data collected as a function of applied field (right) from $La_{0.90}Sr_{1.10}Co_{0.5}Rh_{0.5}RhO_4$. ---------- 214

Figure A2-8 Zero-field-cooled and field-cooled magnetisation data collected in an applied field of 100 Oe. Inset shows fit to the Curie-Weiss law (left); Magnetisation data collected as a function of applied field (right) from $LaSrCo_{0.5}Rh_{0.5}RhO_4$. ---------- 215
Figure A2-9 Zero-field-cooled and field-cooled magnetisation data collected in an applied field of 100 Oe. Inset shows fit to the Curie-Weiss law (left); Magnetisation data collected as a function of applied field (right) from $La_{1.05}Sr_{0.95}Co_{0.5}Rh_{0.5}RhO_4$. ---------- 215
Figure A2-10 Zero-field-cooled and field-cooled magnetisation data collected in an applied field of 100 Oe. Inset shows fit to the Curie-Weiss law (left); Magnetisation data collected as a function of applied field (right) from $La_{1.10}Sr_{0.90}Co_{0.5}Rh_{0.5}RhO_4$. ---------- 216
Figure A2-11 Zero-field-cooled and field-cooled magnetisation data collected in an applied field of 100 Oe. Inset shows fit to the Curie-Weiss law (left); Magnetisation data collected as a function of applied field (right) from $La_{1.15}Sr_{0.85}Co_{0.5}Rh_{0.5}RhO_4$. ---------- 216
Figure A2-12 Reductive thermogravimetric data collected from $La_{0.95}Sr_{1.05}Co_{0.5}Rh_{0.5}O_{3.25}$. Top panel indicates the heating profile, bottom panel the relative mass of the sample.---------- 217
Figure A2-13 Reductive thermogravimetric data collected from $La_{1.10}Sr_{0.90}Co_{0.5}Rh_{0.5}O_{3.25}$. Top panel indicates the heating profile, bottom panel the relative mass of the sample.---------- 218
Figure A2-14 Reductive thermogravimetric data collected from $La_{1.15}Sr_{0.85}Co_{0.5}Rh_{0.5}O_{3.64}$. Top panel indicates the heating profile, bottom panel the relative mass of the sample.---------- 219
Figure 2A-15 Observed(red), calculated(green) and difference plots(pink) from the Rietveld structural refinement of $La_{0.90}Sr_{1.10}Co_{0.5}Rh_{0.5}O_{3.25}$ using an *Immm* model against SXRD data collected at room temperature. ---------- 220
Figure 2A-16 Observed(red), calculated(green) and difference plots(pink) from the Rietveld structural refinement of $La_{1.05}Sr_{0.95}Co_{0.5}Rh_{0.5}O_{3.25}$ using an *Immm* model against SXRD data collected at room temperature. Lower tick marks indicate peak positions of the majority phase, upper tick marks indicate peak positions of La_2O_3. ---------- 221

Figure 2A-17 Observed(red), calculated(green) and difference plots(pink) from the Rietveld structural refinement of $La_{1.10}Sr_{0.90}Co_{0.5}Rh_{0.5}O_{3.25}$ using an *Immm* model against SXRD data collected at room temperature. ---------- 221

Figure 2A-18 Observed(red), calculated(green) and difference plots(pink) from the Rietveld structural refinement of $La_{1.15}Sr_{0.85}Co_{0.5}Rh_{0.5}O_{3.25}$ using an *Immm* model against SXRD data collected at room temperature. ---------- 222

Figure 2A-19 The paramagnetic susceptibility (top) and saturated ferromagnetic moment (bottom) of $La_{0.90}Sr_{1.10}Co_{0.5}Rh_{0.5}O_{3.25}$ collected as a function of temperature. Inset: the fit to the Curie-Weiss law in the temperature range $60 < T/K < 300$. ---------- 223

Figure A2-20 The paramagnetic susceptibility (top) and saturated ferromagnetic moment (bottom) of $La_{01.05}Sr_{0.95}Co_{0.5}Rh_{0.5}O_{3.25}$ collected as a function of temperature. Inset: the fit to the Curie-Weiss law in the temperature range $70 < T/K < 300$. ---------- 224

Figure A2-21 The paramagnetic susceptibility (top) and saturated ferromagnetic moment (bottom) of $La_{0.95}Sr_{1.05}Co_{0.5}Rh_{0.5}O_{3.25}$ collected as a function of temperature. Inset: the fit to the Curie-Weiss law in the temperature range $70 < T/K < 300$. ---------- 225

Figure A2-22 Magnetisation data collected as a function of applied field from $La_{0.90}Sr_{1.10}Co_{0.5}Rh_{0.5}O_{3.25}$. ---------- 226

Figure A2-23 Magnetisation data collected as a function of applied field from $La_{1.05}Sr_{0.95}Co_{0.5}Rh_{0.5}O_{3.25}$. ---------- 226

Figure 2A-24 Magnetisation data collected as a function of applied field from $La_{1.10}Sr_{0.90}Co_{0.5}Rh_{0.5}O_{3.25}$. ---------- 227

Figure 2A-25 (left) Zero-field-cooled and field-cooled magnetisation data collected from La_2NiRhO_6 in an applied field of 100 Oe; (right) magnetisation data collected as a function of applied field from La_2NiRhO_6 (The error bars for magnetisation data is too small to be visible). ---------- 227

Figure 2A-26 (left) Zero-field-cooled and field-cooled magnetisation data collected from $LaSrMnRhO_6$ in an applied field of 100 Oe; (right) magnetisation data collected as a function of applied field from $LaSrMnRhO_6$ (The error bars for magnetisation data is too small to be visible.). ---------- 228
Figure 2A-27 (left) Zero-field-cooled and field-cooled magnetisation data collected from La_2CoRhO_6 in an applied field of 100 Oe. Inset shows fit to the Curie-Weiss law; (right) Magnetisation data collected as a function of applied field from La_2CoRhO_6 (The error bars for magnetisation data is too small to be visible.). ---------- 228

Appendix 2

Additional Data for Chapter 5 - 8

Appendix 2.1 Synchrotron X-ray Diffraction (SXRD) Data of $La_xSr_{2-x}Co_{0.5}Rh_{0.5}O_4$ ($0.85 \leqslant x \leqslant 1.15$)

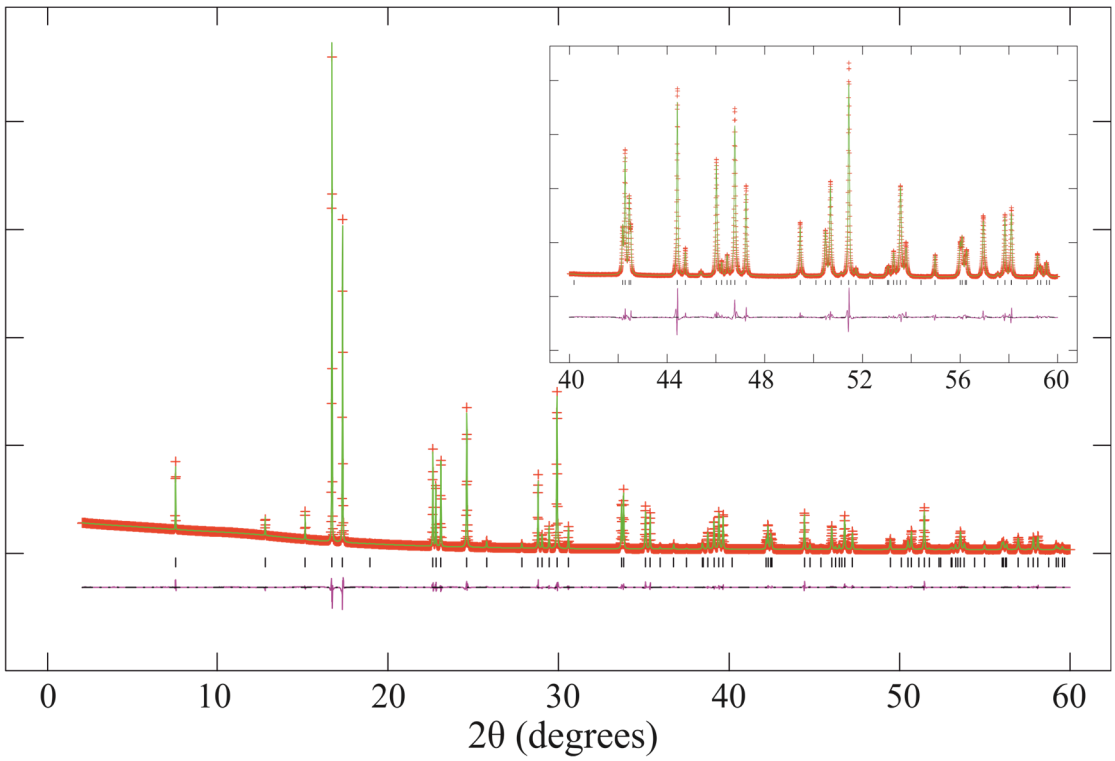


Figure A2-1 Observed(red), calculated(green) and difference plots(pink) from the Rietveld structural refinement of $La_{0.90}Sr_{1.10}Co_{0.5}Rh_{0.5}O_4$ using an *I4/mmm* model against SXRD data collected at room temperature.

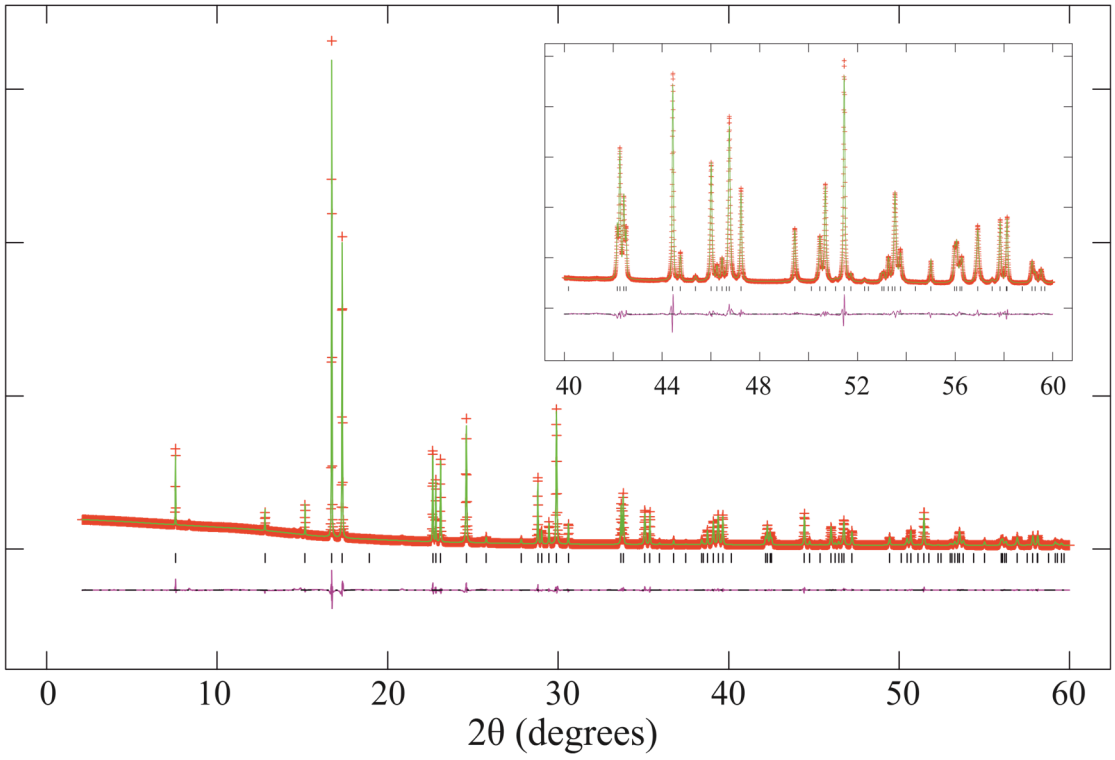


Figure A2-2 Observed(red), calculated(green) and difference plots(pink) from the Rietveld structural refinement of $La_{0.95}Sr_{1.05}Co_{0.5}Rh_{0.5}O_4$ using an *I4/mmm* model against SXRD data collected at room temperature.

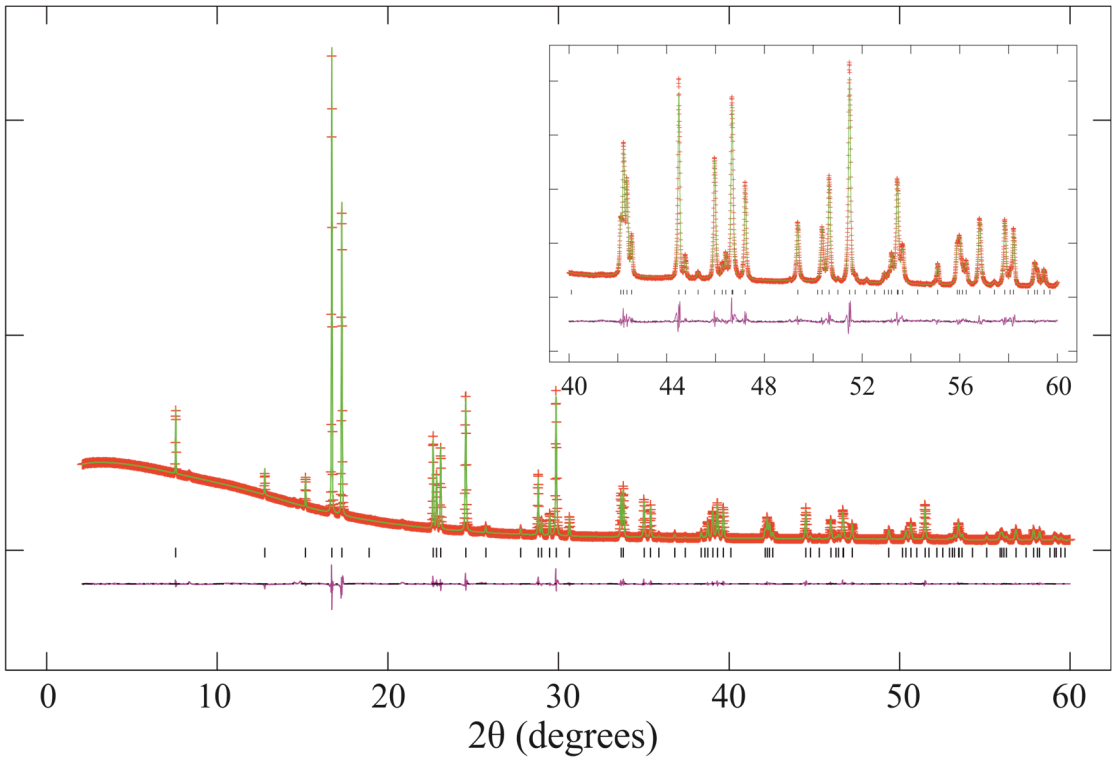


Figure A2-3 Observed(red), calculated(green) and difference plots(pink) from the Rietveld structural refinement of $La_{1.05}Sr_{0.95}Co_{0.5}Rh_{0.5}O_4$ using an *I4/mmm* model against SXRD data collected at room temperature.

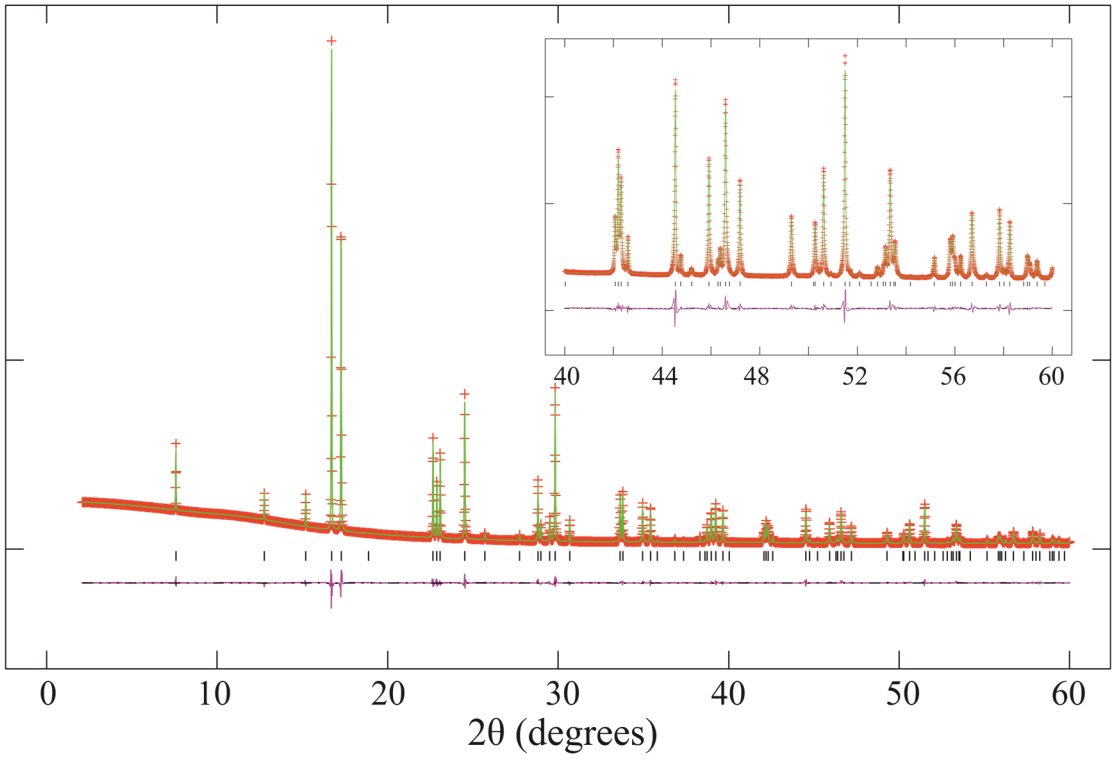


Figure A2-4 Observed(red), calculated(green) and difference plots(pink) from the Rietveld structural refinement of $La_{1.10}Sr_{0.90}Co_{0.5}Rh_{0.5}O_4$ using an *I4/mmm* model against SXRD data collected at room temperature.

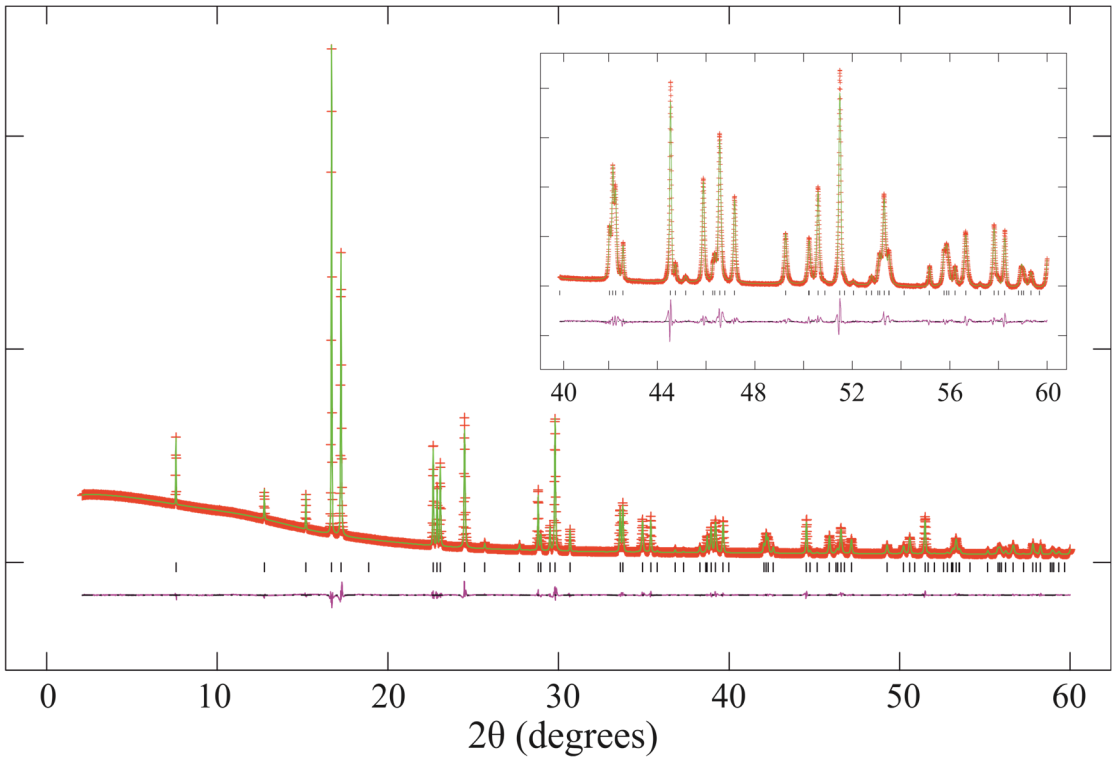


Figure A2-5 Observed(red), calculated(green) and difference plots(pink) from the Rietveld structural refinement of $La_{1.15}Sr_{0.85}Co_{0.5}Rh_{0.5}O_4$ using an *I4/mmm* model against SXRD data collected at room temperature.

Appendix 2.2 Magnetisation Data of $La_xSr_{2-x}Co_{0.5}Rh_{0.5}O_4$ ($0.85 \leq x \leq 1.15$)

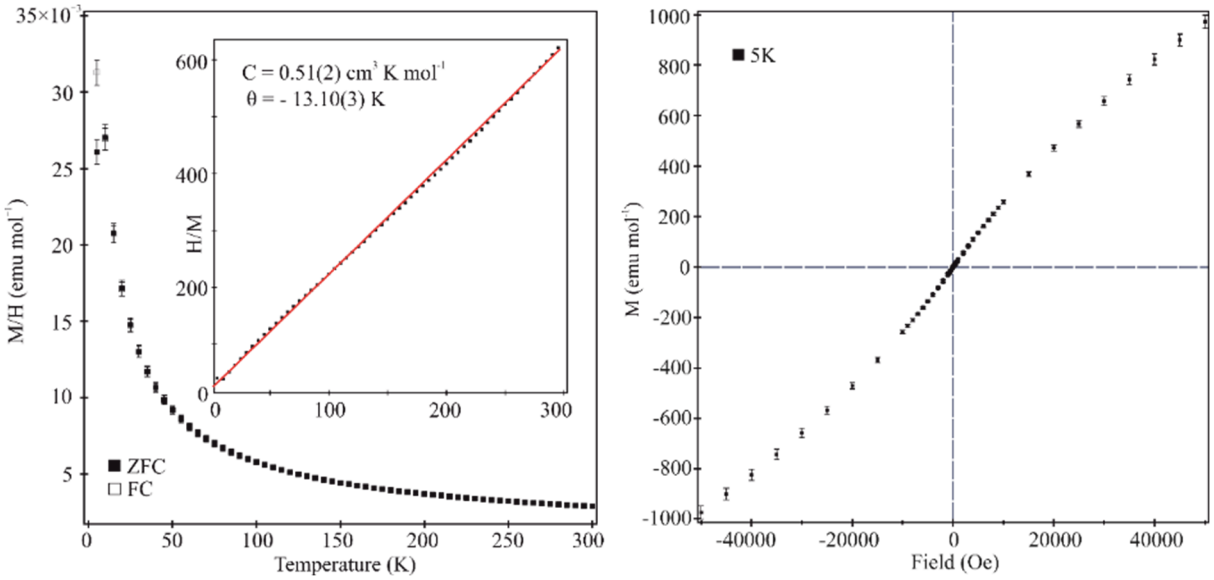


Figure A2-6 Zero-field-cooled and field-cooled magnetisation data collected in an applied field of 100 Oe. Inset shows fit to the Curie-Weiss law (left); Magnetisation data collected as a function of applied field (right) from $La_{0.85}Sr_{1.15}Co_{0.5}Rh_{0.5}RhO_4$.

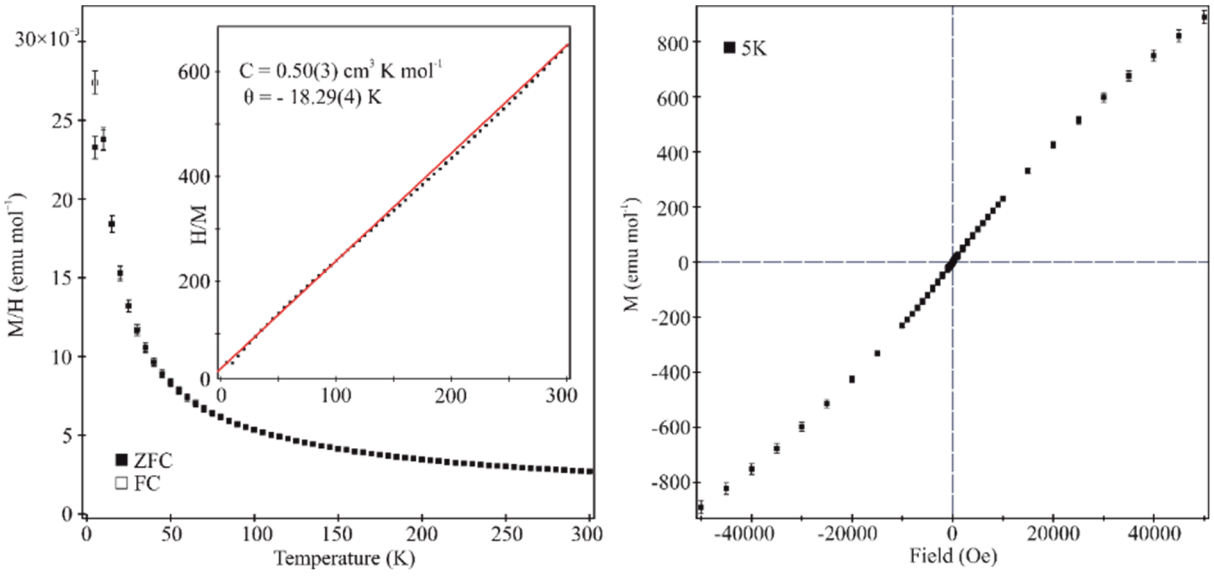


Figure A2-7 Zero-field-cooled and field-cooled magnetisation data collected in an applied field of 100 Oe. Inset shows fit to the Curie-Weiss law (left); Magnetisation data collected as a function of applied field (right) from $La_{0.90}Sr_{1.10}Co_{0.5}Rh_{0.5}RhO_4$.

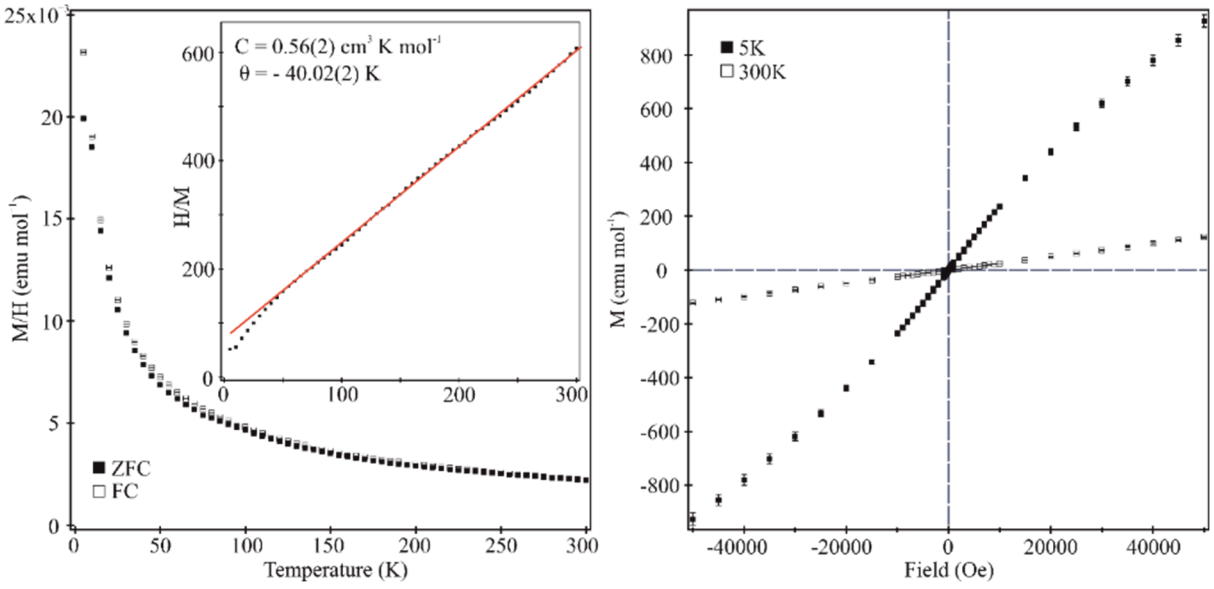


Figure A2-8 Zero-field-cooled and field-cooled magnetisation data collected in an applied field of 100 Oe. Inset shows fit to the Curie-Weiss law (left); Magnetisation data collected as a function of applied field (right) from $LaSrCo_{0.5}Rh_{0.5}RhO_4$.

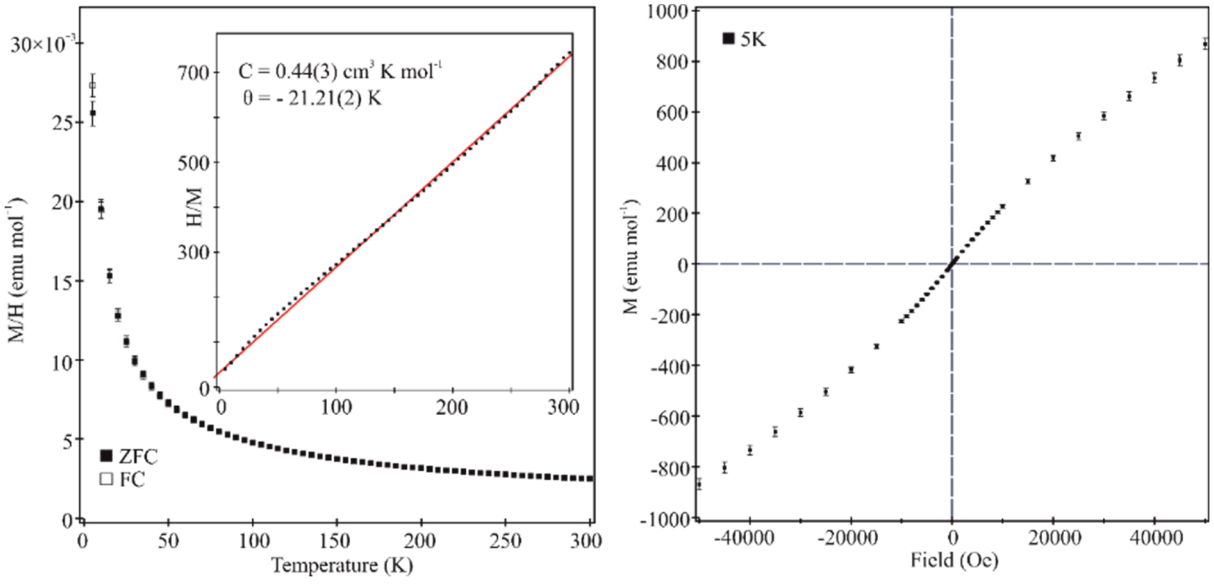


Figure A2-9 Zero-field-cooled and field-cooled magnetisation data collected in an applied field of 100 Oe. Inset shows fit to the Curie-Weiss law (left); Magnetisation data collected as a function of applied field (right) from $La_{1.05}Sr_{0.95}Co_{0.5}Rh_{0.5}RhO_4$.

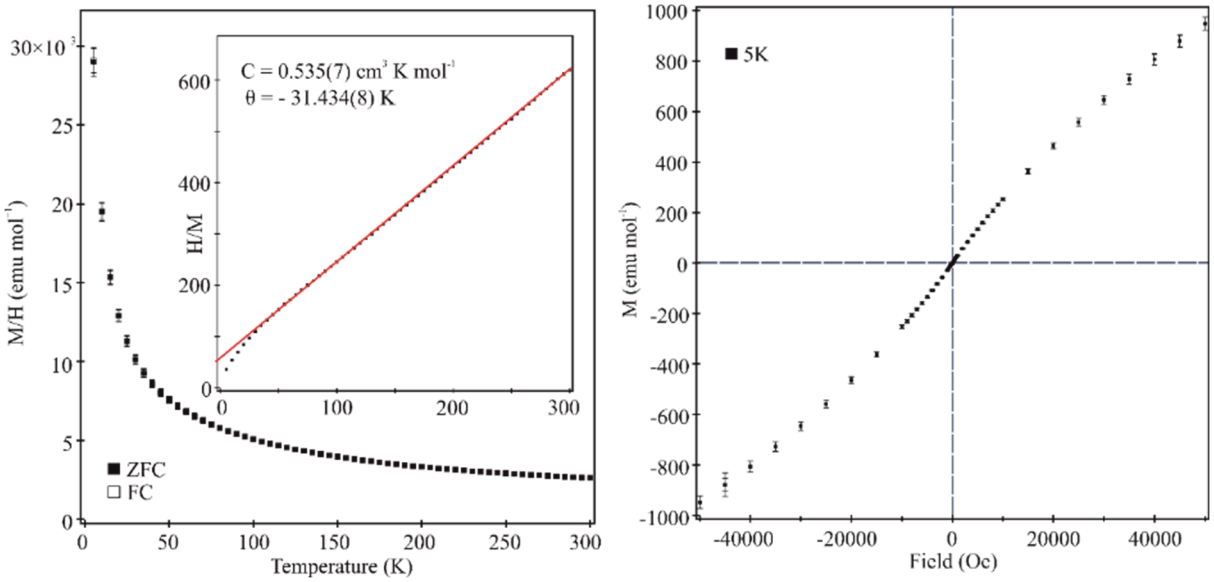


Figure A2-10 Zero-field-cooled and field-cooled magnetisation data collected in an applied field of 100 Oe. Inset shows fit to the Curie-Weiss law (left); Magnetisation data collected as a function of applied field (right) from $La_{1.10}Sr_{0.90}Co_{0.5}Rh_{0.5}RhO_4$.

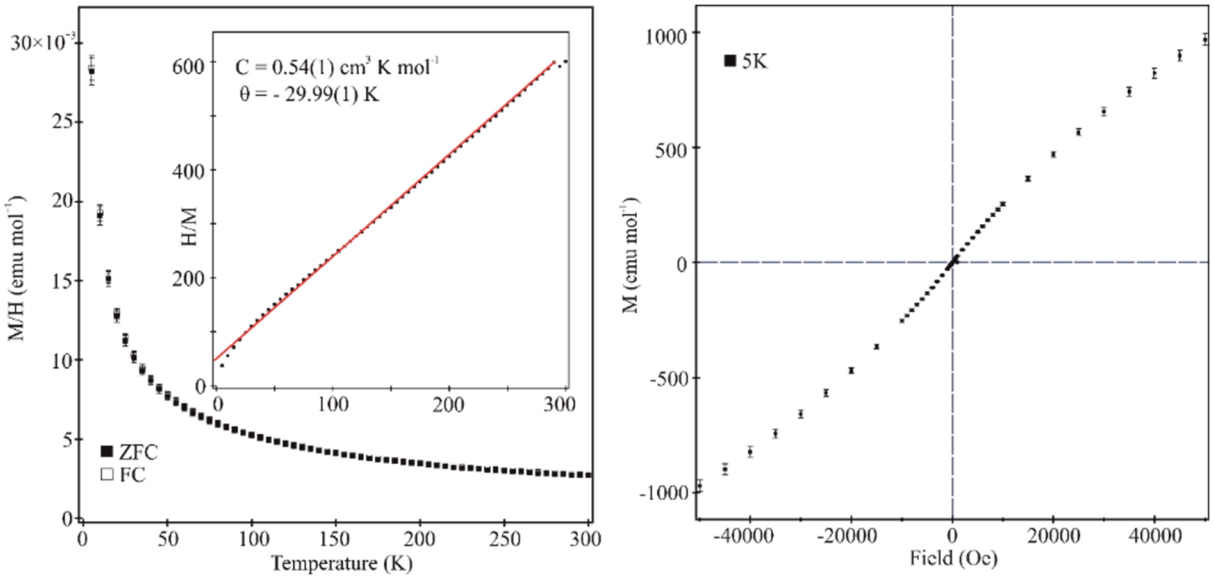


Figure A2-11 Zero-field-cooled and field-cooled magnetisation data collected in an applied field of 100 Oe. Inset shows fit to the Curie-Weiss law (left); Magnetisation data collected as a function of applied field (right) from $La_{1.15}Sr_{0.85}Co_{0.5}Rh_{0.5}RhO_4$.

Appendix 2.3 Thermogravimetric Data of $La_xSr_{2-x}Co_{0.5}Rh_{0.5}O_{4-\delta}$ ($0.90 \leq x \leq 1.15$)

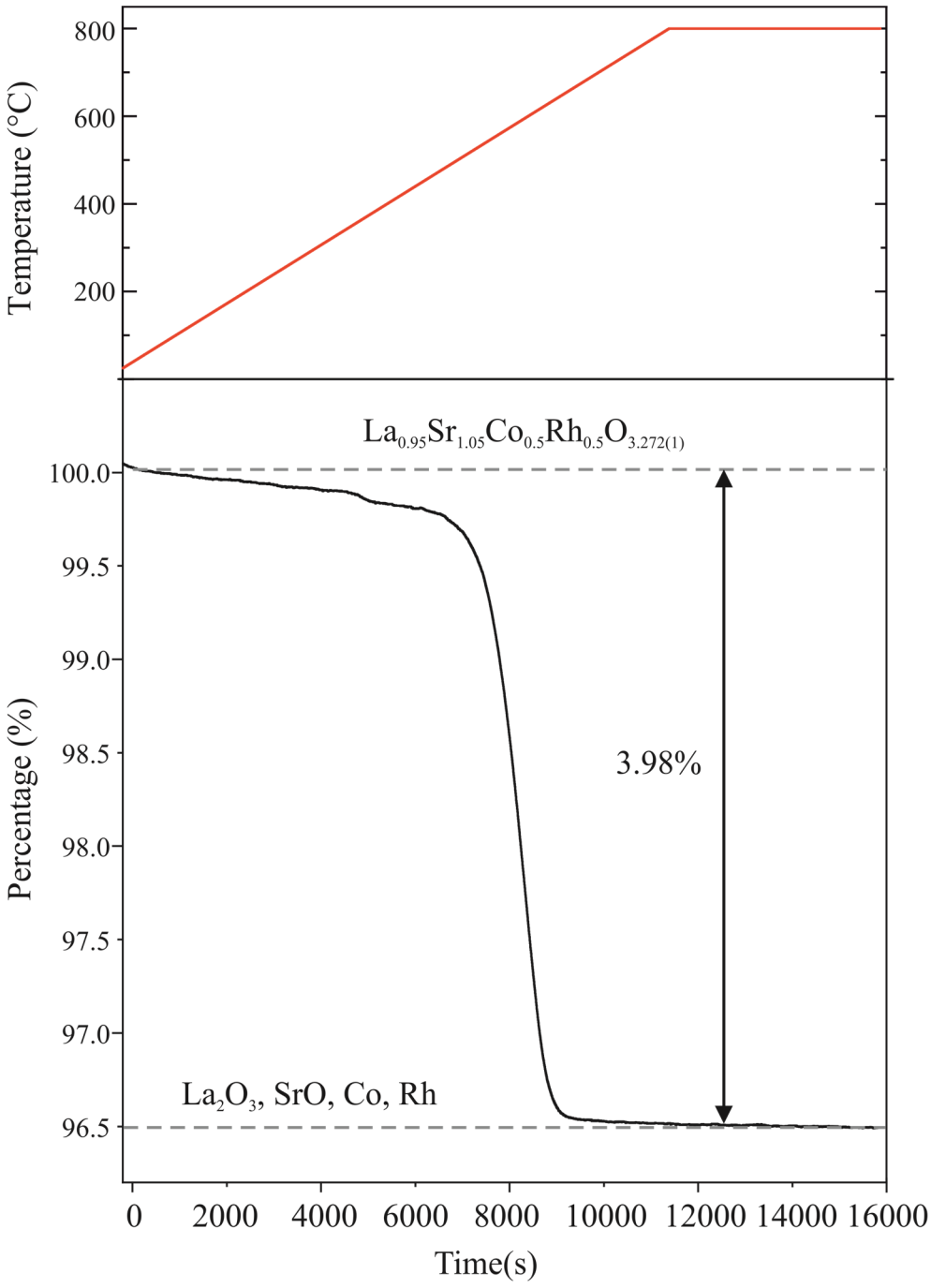


Figure A2-12 Reductive thermogravimetric data collected from $La_{0.95}Sr_{1.05}Co_{0.5}Rh_{0.5}O_{3.25}$. Top panel indicates the heating profile, bottom panel the relative mass of the sample.

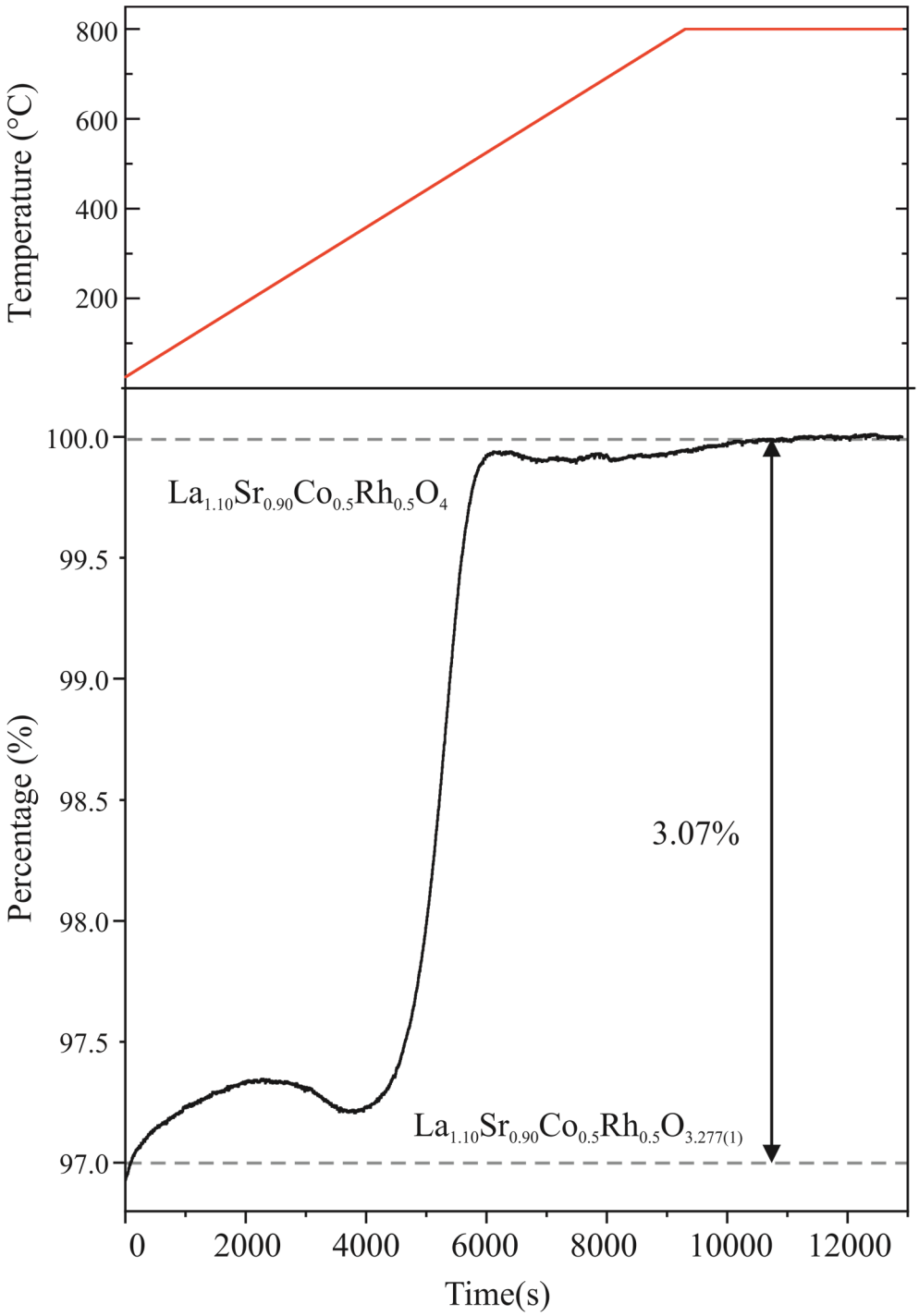


Figure A2-13 Reductive thermogravimetric data collected from $La_{1.10}Sr_{0.90}Co_{0.5}Rh_{0.5}O_{3.25}$. Top panel indicates the heating profile, bottom panel the relative mass of the sample.

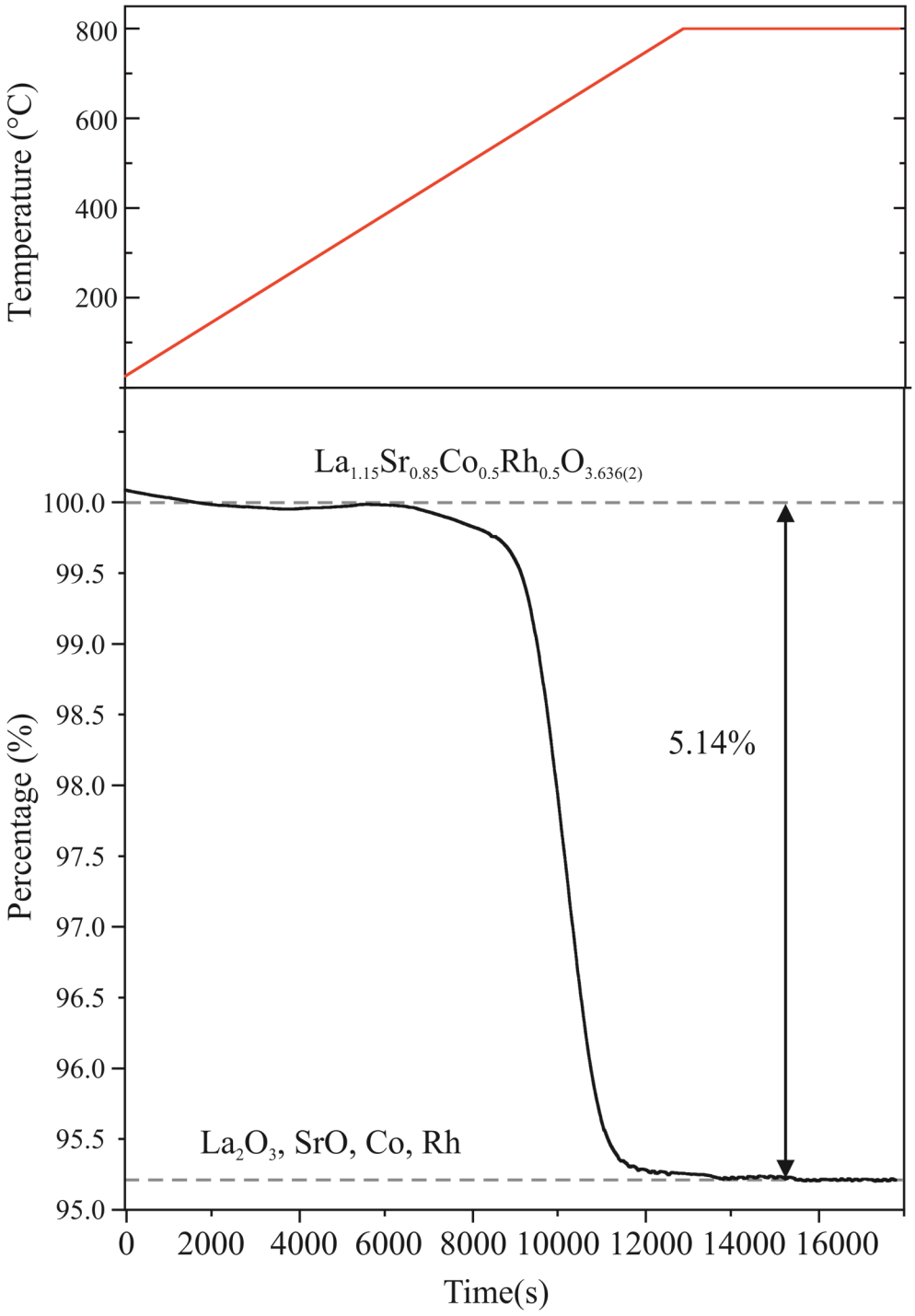


Figure A2-14 Reductive thermogravimetric data collected from $La_{1.15}Sr_{0.85}Co_{0.5}Rh_{0.5}O_{3.64}$. Top panel indicates the heating profile, bottom panel the relative mass of the sample.

Appendix 2.4 SXRD Data of $La_xSr_{2-x}Co_{0.5}Rh_{0.5}O_{3.25}$ ($0.90 \leq x \leq 1.15$)

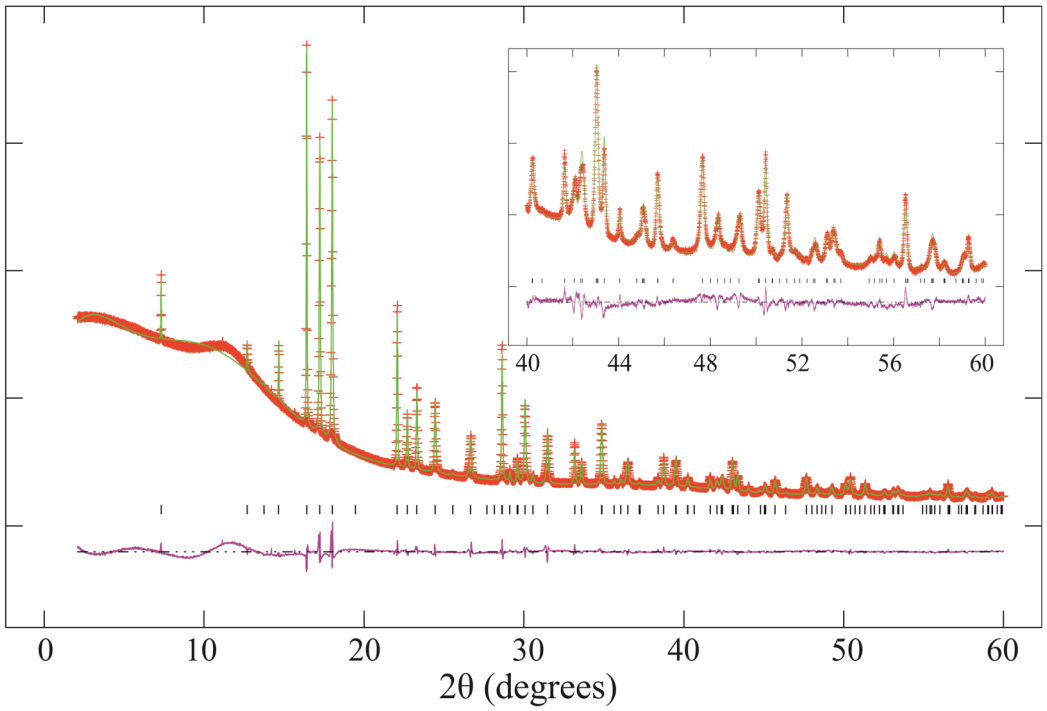


Figure 2A-15 Observed(red), calculated(green) and difference plots(pink) from the Rietveld structural refinement of $La_{0.90}Sr_{1.10}Co_{0.5}Rh_{0.5}O_{3.25}$ using an *Immm* model against SXRD data collected at room temperature.

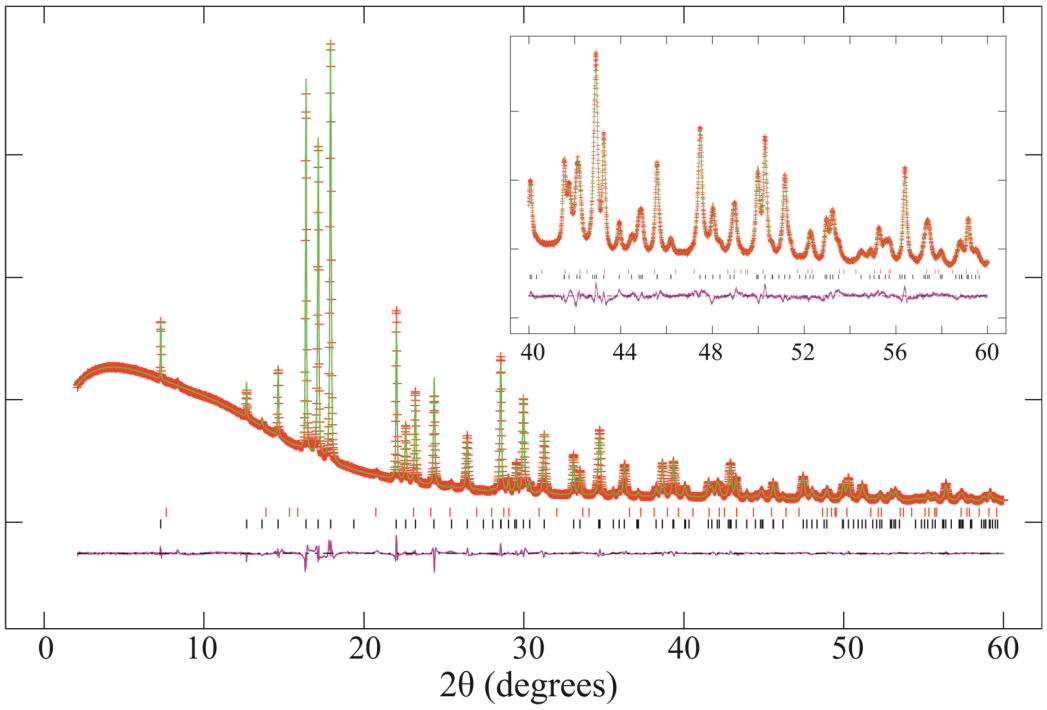


Figure 2A-16 Observed(red), calculated(green) and difference plots(pink) from the Rietveld structural refinement of $La_{1.05}Sr_{0.95}Co_{0.5}Rh_{0.5}O_{3.25}$ using an *Immm* model against SXRD data collected at room temperature. Lower tick marks indicate peak positions of the majority phase, upper tick marks indicate peak positions of La_2O_3.

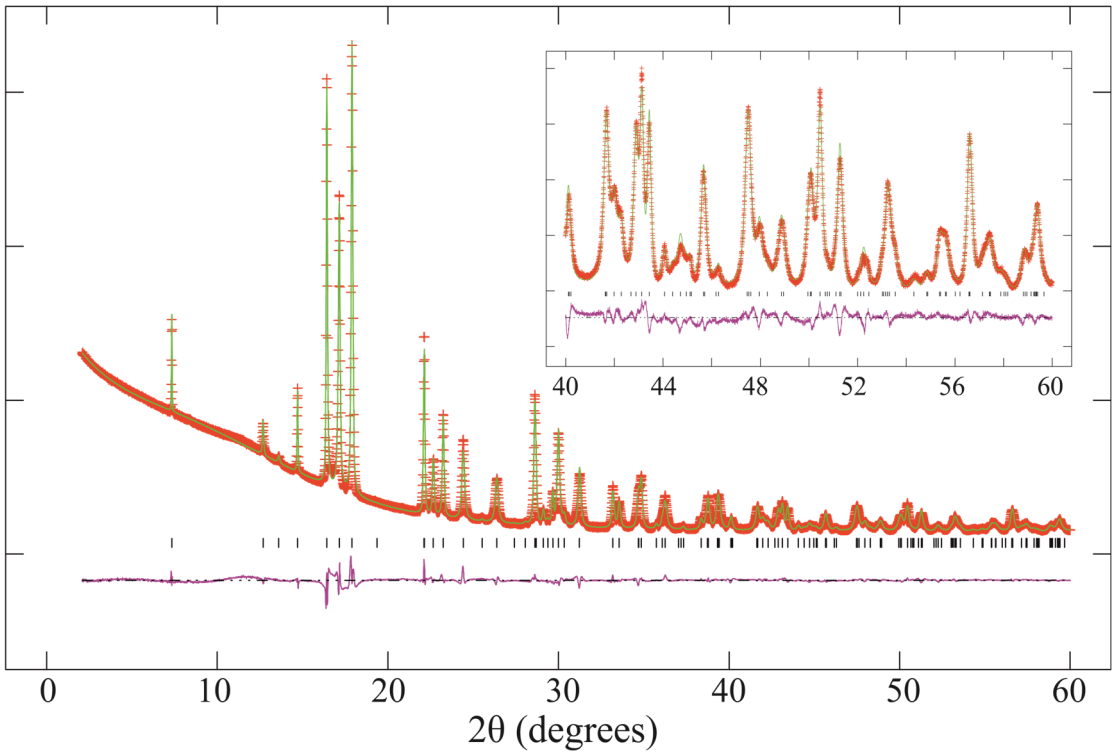


Figure 2A-17 Observed(red), calculated(green) and difference plots(pink) from the Rietveld structural refinement of $La_{1.10}Sr_{0.90}Co_{0.5}Rh_{0.5}O_{3.25}$ using an *Immm* model against SXRD data collected at room temperature.

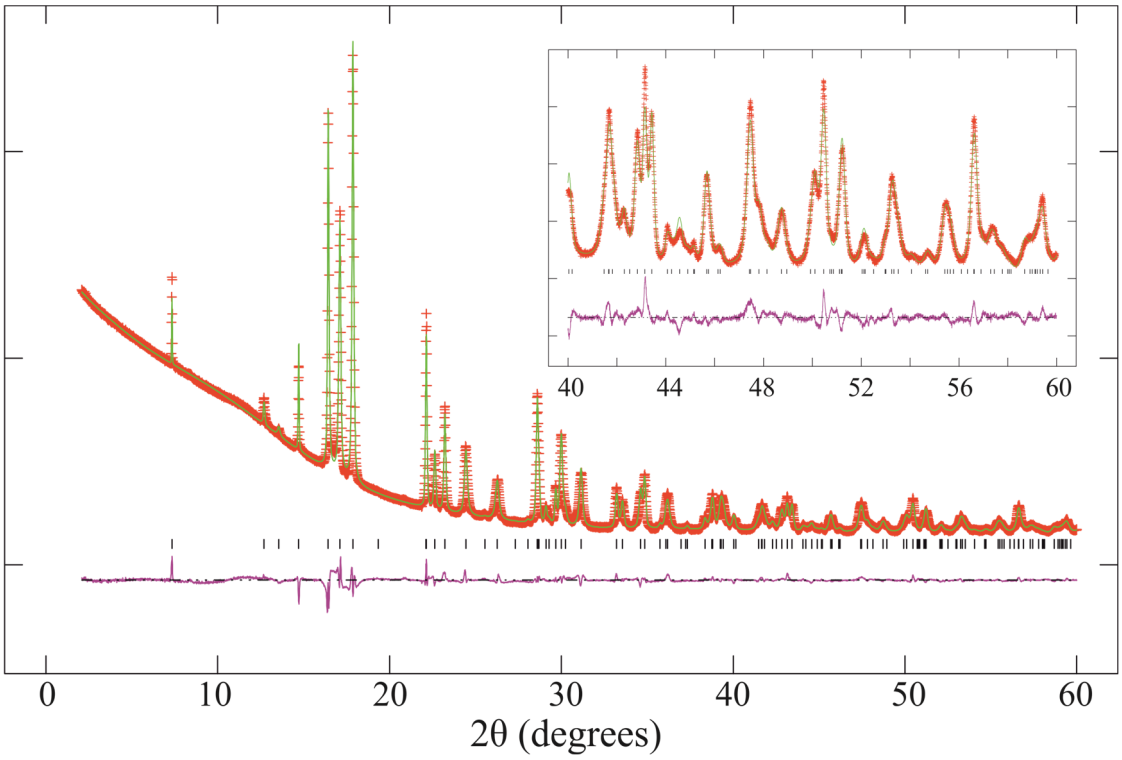


Figure 2A-18 Observed(red), calculated(green) and difference plots(pink) from the Rietveld structural refinement of $La_{1.15}Sr_{0.85}Co_{0.5}Rh_{0.5}O_{3.25}$ using an *Immm* model against SXRD data collected at room temperature.

Appendix 2.5 Magnetisation Data of $La_xSr_{2-x}Co_{0.5}Rh_{0.5}O_{3.25}$ ($0.90 \leq x \leq 1.10$)

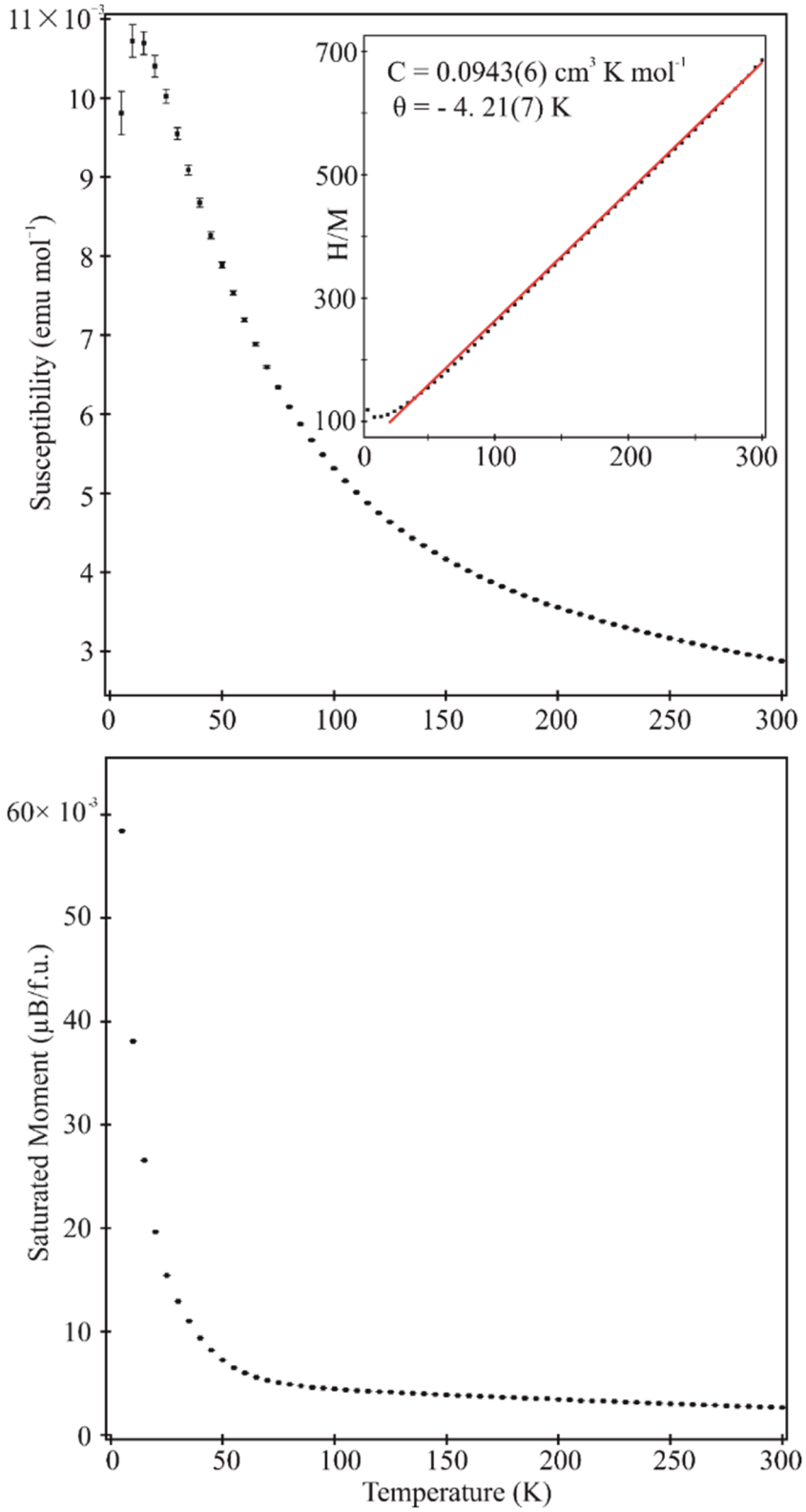


Figure 2A-19 The paramagnetic susceptibility (top) and saturated ferromagnetic moment (bottom) of $La_{0.90}Sr_{1.10}Co_{0.5}Rh_{0.5}O_{3.25}$ collected as a function of temperature. Inset: the fit to the Curie-Weiss law in the temperature range $60 < T/K < 300$.

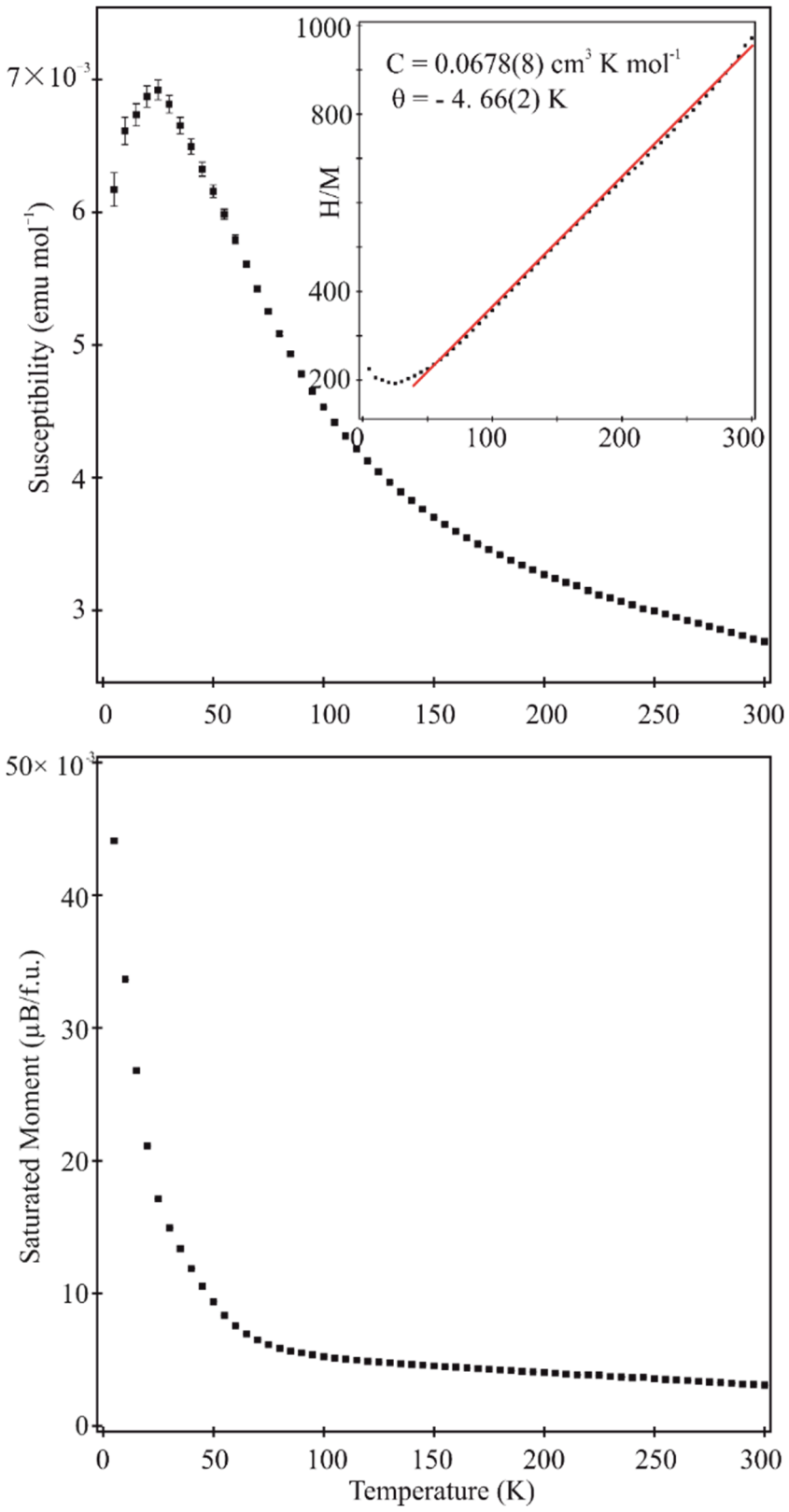


Figure A2-20 The paramagnetic susceptibility (top) and saturated ferromagnetic moment (bottom) of $La_{1.05}Sr_{0.95}Co_{0.5}Rh_{0.5}O_{3.25}$ collected as a function of temperature. Inset: the fit to the Curie-Weiss law in the temperature range $70 < T/K < 300$.

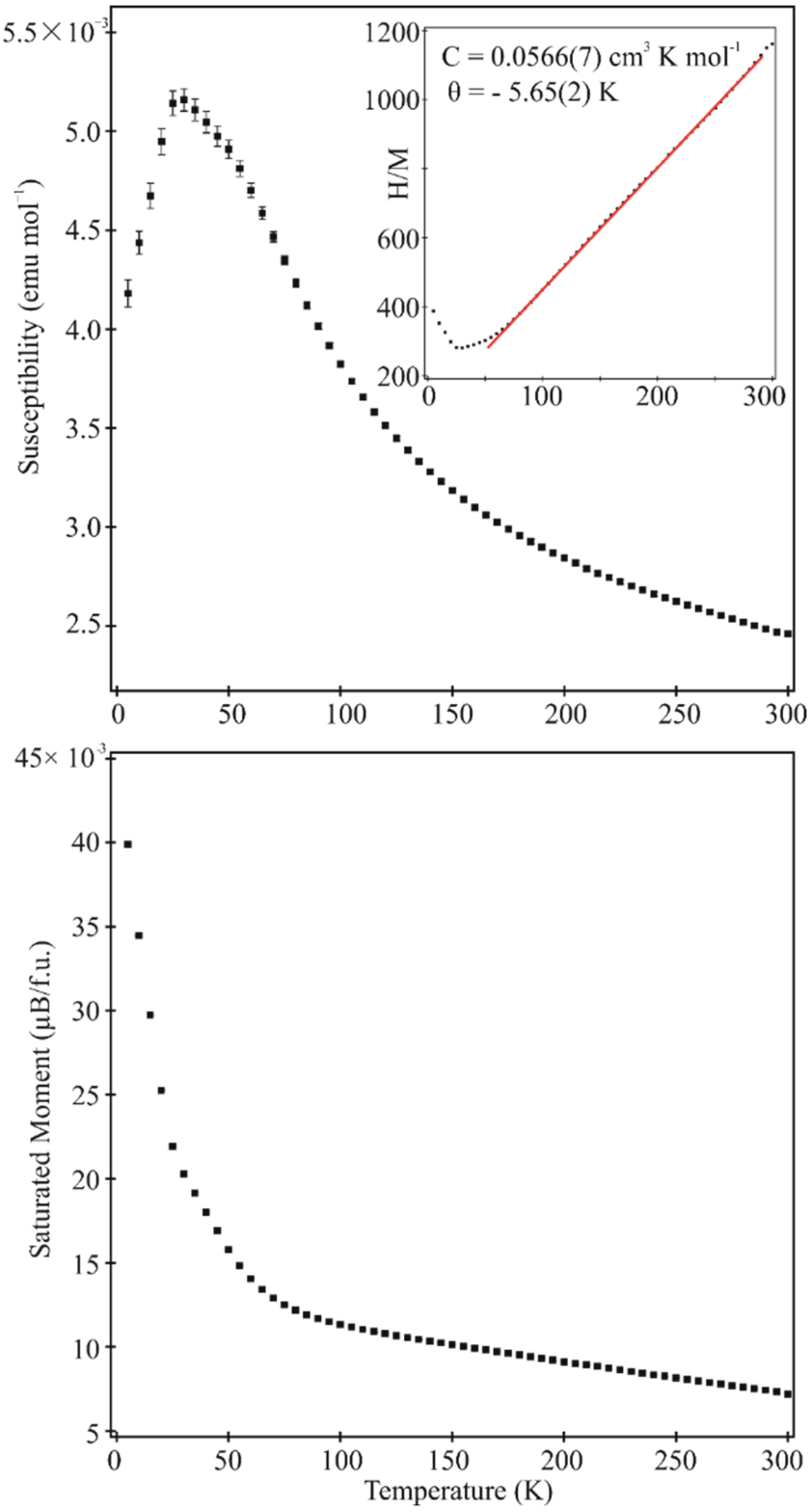


Figure A2-21 The paramagnetic susceptibility (top) and saturated ferromagnetic moment (bottom) of $La_{1.10}Sr_{0.90}Co_{0.5}Rh_{0.5}O_{3.25}$ collected as a function of temperature. Inset: the fit to the Curie-Weiss law in the temperature range 70 < *T*/K < 300.

Appendix 2.6 Magnetisation-field Data of $La_xSr_{2-x}Co_{0.5}Rh_{0.5}O_{3.25}$ ($0.90 \leq x \leq 1.10$)

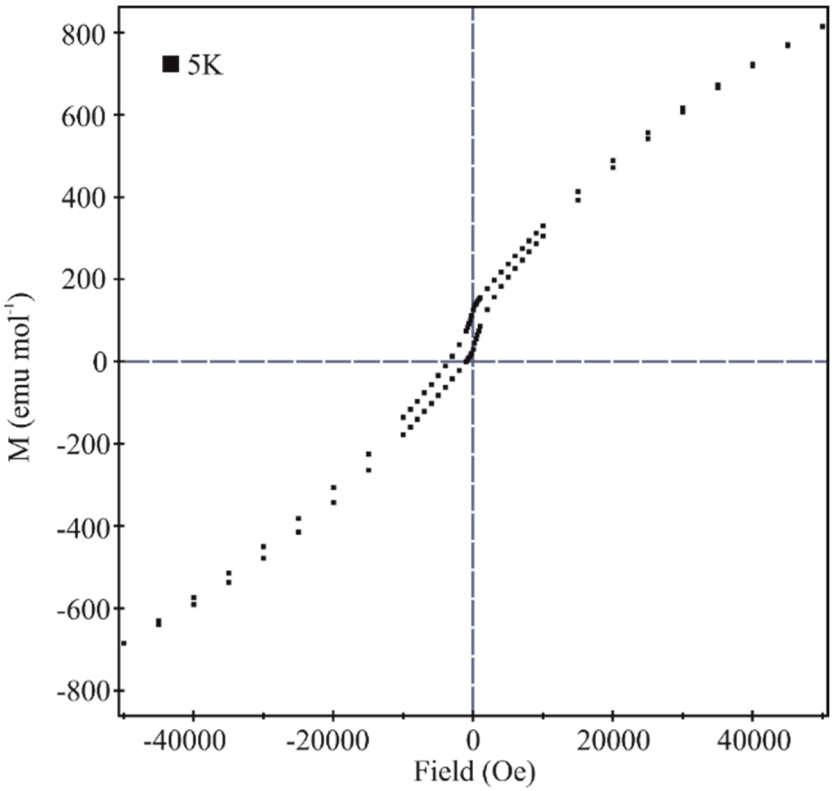


Figure A2-22 Magnetisation data collected as a function of applied field from $La_{0.90}Sr_{1.10}Co_{0.5}Rh_{0.5}O_{3.25}$.

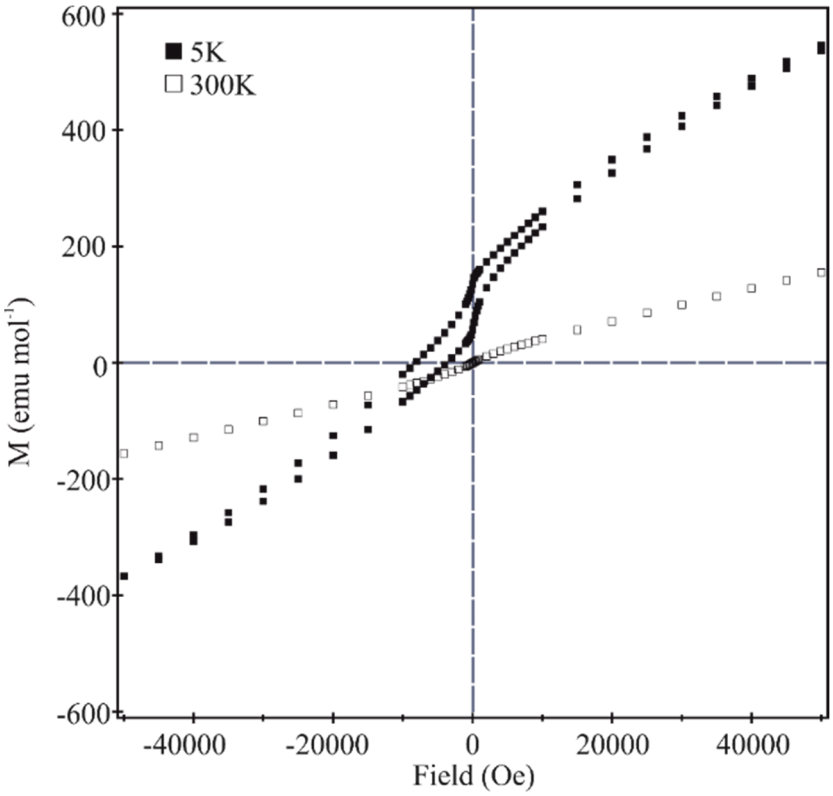


Figure A2-23 Magnetisation data collected as a function of applied field from $La_{1.05}Sr_{0.95}Co_{0.5}Rh_{0.5}O_{3.25}$.

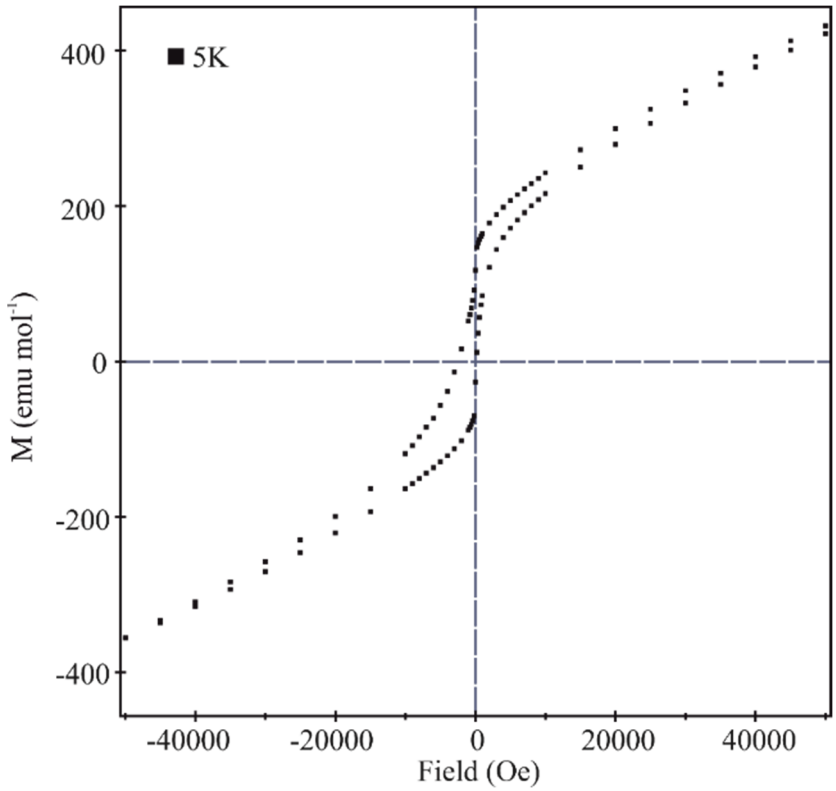


Figure 2A-24 Magnetisation data collected as a function of applied field from $La_{1.10}Sr_{0.90}Co_{0.5}Rh_{0.5}O_{3.25}$.

Appendix 2.7 Magnetisation Data of La_2MRhO_6 (M = Co, Ni) and $LaSrMnRhO_6$

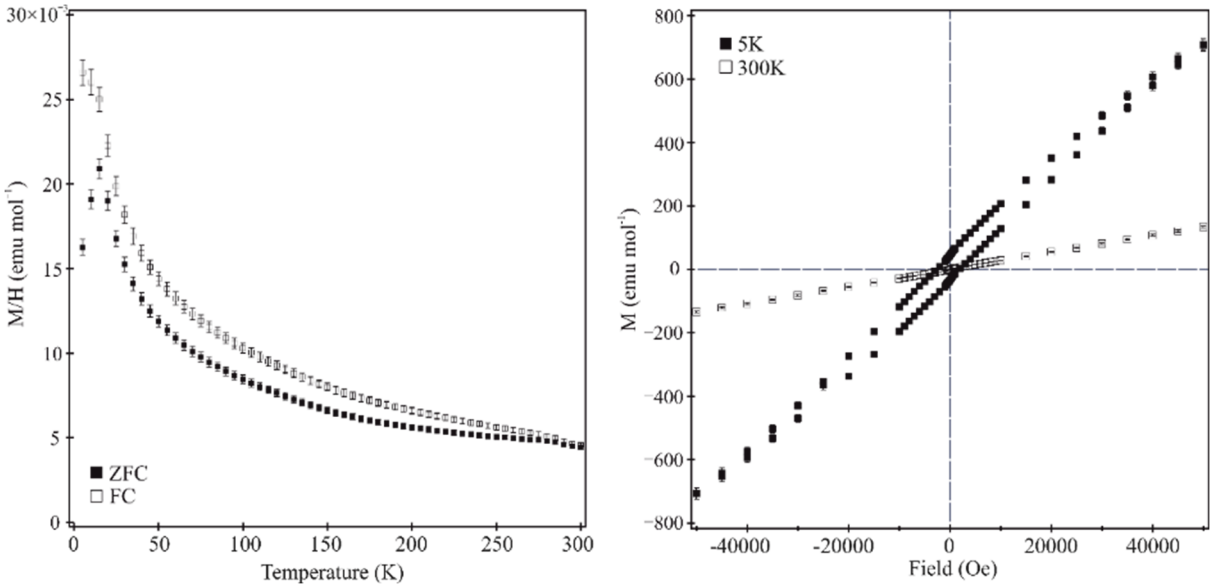


Figure 2A-25 (left) Zero-field-cooled and field-cooled magnetisation data collected from La_2NiRhO_6 in an applied field of 100 Oe; (right) magnetisation data collected as a function of applied field from La_2NiRhO_6 (The error bars for magnetisation data is too small to be visible).

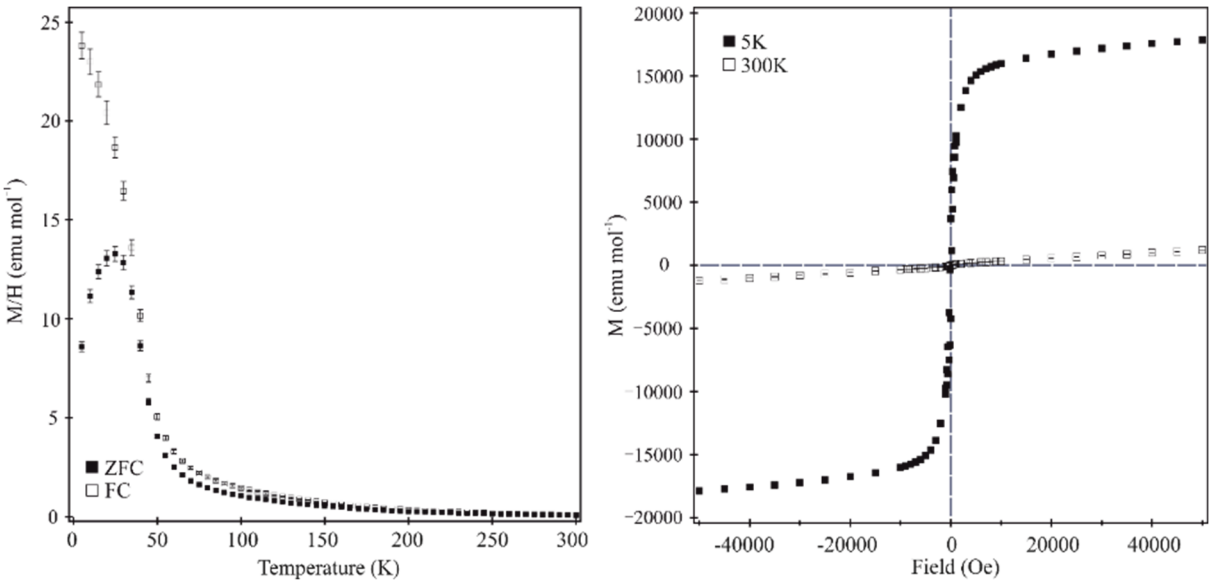


Figure 2A-26 (left) Zero-field-cooled and field-cooled magnetisation data collected from $LaSrMnRhO_6$ in an applied field of 100 Oe; (right) magnetisation data collected as a function of applied field from $LaSrMnRhO_6$ (The error bars for magnetisation data is too small to be visible.).

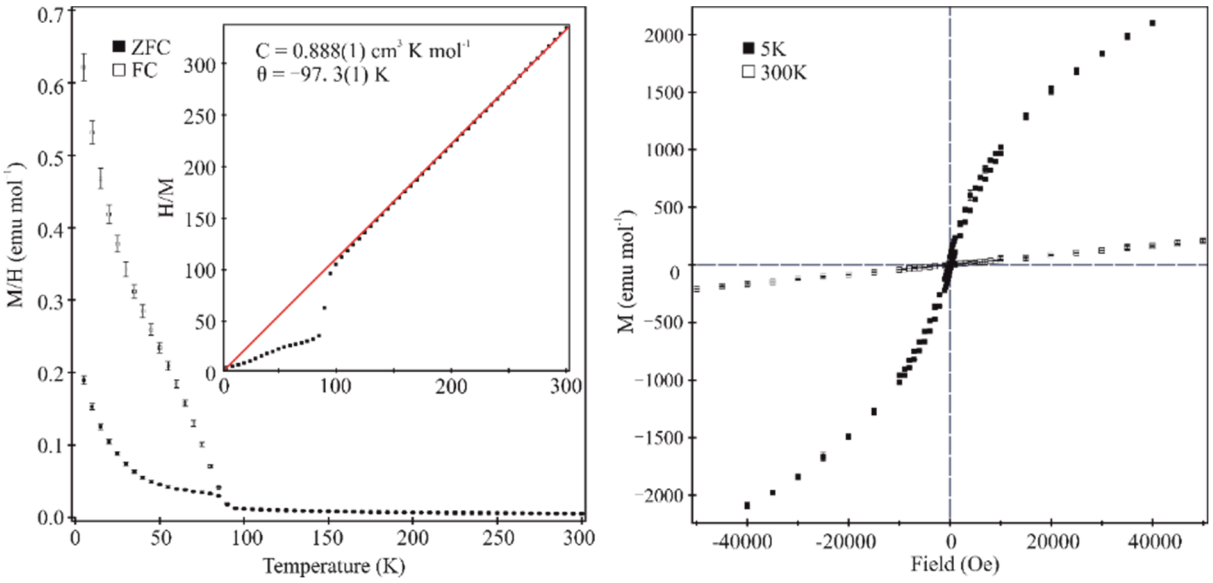


Figure 2A-27 (left) Zero-field-cooled and field-cooled magnetisation data collected from La_2CoRhO_6 in an applied field of 100 Oe. Inset shows fit to the Curie-Weiss law; (right) Magnetisation data collected as a function of applied field from La_2CoRhO_6 (The error bars for magnetisation data is too small to be visible.).

Appendix 3 Bibliography

[1] N. A. Spaldin, *Magnetic Materials: Fundamentals and Applications*, Cambridge University Press, Cambridge, **2010**.

[2] P. Schiffer, A. P. Ramirez, W. Bao, S. W. Cheong, *Phys. Rev. Lett.* **1995**, *75*, 3336–3339.

[3] K.-I. Kobayashi, T. Kimura, Y. Tomioka, H. Sawada, K. Terakura, Y. Tokura, *Phys. Rev. B - Condens. Matter Mater. Phys.* **1999**, *59*, 159–162.

[4] J. G. B. Miiller, K.A., *Z. Phys. B - Condens. Matter* **1986**, *64*, 189–193.

[5] M. R. Norman, C. Pépin, *Reports Prog. Phys.* **2003**, *66*, 1547–1610.

[6] M. Dawber, *Rev. Mod. Phys.* **2005**, *77*, 1083–1130.

[7] W. Eerenstein, N. D. Mathur, J. F. Scott, *Nature* **2006**, *442*, 759–765.

[8] R. E. Cohen, *Nature* **1992**, *358*, 136–138.

[9] J. M. Moreau, C. Michel, R. Gerson, W. J. James, *J. Phys. Chem. Solids* **1971**, *32*, 1315–1320.

[10] R. Asahi, T. Morikawa, T. Ohwaki, K. Aoki, Y. Taga, *Science* **2001**, *293*, 269–271.

[11] M. A. Peña, J. L. G. Fierro, *Chem. Rev.* **2001**, *101*, 1981–2017.

[12] J. B. Goodenough, J. S. Zhou, *Chem. Mater.* **1998**, *10*, 2980–2993.

[13] Y. A. Abramov, V. G. Tsirelson, V. E. Zavodnik, S. A. Ivanov, I. D. Brown, *Acta Crystallogr. Sect. B* **1995**, *51*, 942–951.

[14] V. M. Goldschmidt, *Naturwissenschaften* **1926**, *14*, 477.

[15] R. H. Buttner, E. N. Maslen, *Acta Crystallogr. Sect. B* **1992**, *48*, 644–649.

[16] H. D.Megau, C.N.W.Darlington, *Acta Crystallogr. Sect. A* **1975**, *31*, 161–173.

[17] A. K. Norman, M. A. Morris, *J. Mater. Process. Technol.* **1999**, *92–93*, 91–96.

[18] I. Qasim, B. J. Kennedy, M. Avdeev, *J. Mater. Chem. A* **2013**, *1*, 3127–3132.

[19] Y. Takeda, F. Kanamaru, S. Masahiko, K. Mitsue, *Acta Crystallogr.* **1976**, *B32*, 2464–2466.

[20] A. M. Glazer, *Acta Crystallogr. Sect. B Struct. Crystallogr. Cryst. Chem.* **1972**, *28*, 3384–3392.

[21] P. M. Woodward, *Acta Crystallogr. Sect. B Struct. Sci.* **1997**, *53*, 32–43.

[22] M. T. Anderson, K. B. Greenwood, G. A. Taylor, K. R. Poeppelmeier, *Prog. Solid State Chem.* **1993**, *22*, 197–233.

[23] G. King, P. M. Woodward, *J. Mater. Chem.* **2010**, *20*, 5785–5796.

[24] D. Iwanaga, Y. Inaguma, M. Itoh, *Mater. Res. Bull.* **2000**, *35*, 449–457.

[25] M. Cernea, F. Vasiliu, C. Bartha, C. Plapcianu, I. Mercioniu, *Ceram. Int.* **2014**, *40*, 11601–11609.

[26] R. J. D. Tilley, *Perovskites: Structure–Property Relationships*, Cambridge University Press, **2016**.

[27] S. N. Ruddlesden, P. Popper, *Acta Crystallogr.* **1957**, *10*, 538–539.

[28] S. N. Ruddlesden, P. Popper, *Acta Crystallogr.* **1958**, *11*, 54–55.

[29] M. Malvestuto, E. Carleschi, R. Fittipaldi, E. Gorelov, E. Pavarini, M. Cuoco, Y. Maeno,

F. Parmigiani, A. Vecchione, *Phys. Rev. B - Condens. Matter Mater. Phys.* **2011**, *83*, 3–7.

[30] S. Yamaguchi, Y. Okimoto, Y. Tokura, *Phys. Rev. B - Condens. Matter Mater. Phys.* **1997**, *55*, R8666–R8669.

[31] M. Oku, *J. Solid State Chem.* **1978**, *23*, 177–185.

[32] Z. Hu, C. Mazumdar, G. Kaindl, F. M. F. De Groot, S. A. Warda, D. Reinen, *Chem. Phys. Lett.* **1998**, *297*, 321–328.

[33] Z. Hu, H. Wu, M. W. Haverkort, H. H. Hsieh, H. J. Lin, T. Lorenz, J. Baier, A. Reichl, I. Bonn, C. Felser, A. Tanaka, C. T. Chen, L. H. Tjeng, *Phys. Rev. Lett.* **2004**, *92*, 3–6.

[34] A. A. Belik, S. Iikubo, K. Kodama, N. Igawa, S. Shamoto, E. Takayama-Muromachi, *Chem. Mater.* **2008**, *20*, 3765–3769.

[35] C. Martin A Maignan, D. Pelloquin, N. Nguyen, B. Raveau, *Appl. Phys. Lett.* **1997**, *71*, 1421–1423.

[36] W. Kobayashi, S. Ishiwata, I. Terasaki, M. Takano, I. Grigoraviciute, H. Yamauchi, M. Karppinen, *Phys. Rev. B - Condens. Matter Mater. Phys.* **2005**, *72*, 1–5.

[37] K. Knížek, J. Hejtmánek, M. Maryško, Z. Jirák, J. Buršík, *Phys. Rev. B - Condens. Matter Mater. Phys.* **2012**, *85*, 1–7.

[38] J. Li, A. E. Smith, K. S. Kwong, C. Powell, A. W. Sleight, M. A. Subramanian, *J. Solid State Chem.* **2010**, *183*, 1388–1393.

[39] H. Guo, K. Manna, H. Luetkens, M. Hoelzel, A. C. Komarek, *Phys. Rev. B* **2016**, *94*, 3–9.

[40] M. W. Haverkort, Z. Hu, J. C. Cezar, T. Burnus, H. Hartmann, M. Reuther, C. Zobel, T. Lorenz, A. Tanaka, N. B. Brookes, H. H. Hsieh, H. J. Lin, C. T. Chen, L. H. Tjeng, *Phys. Rev. Lett.* **2006**, *97*, 38–41.

[41] J. B. Goodenough, P. M. Raccah, *J. Appl. Phys.* **1965**, *36*, 1031–1032.

[42] J. B. Goodenough, *Magnetism and the Chemical Bond*, John Wiley & Sons, Ltd, **1964**.

[43] P. W. Anderson, *Phys. Rev.* **1950**, *79*, 350–356.

[44] M. A. Hayward, M. A. Green, M. J. Rosseinsky, J. Sloan, *J. Am. Chem. Soc.* **1999**, *121*, 8843–8854.

[45] H. Kageyama, K. Hayashi, K. Maeda, J. P. Attfield, Z. Hiroi, J. M. Rondinelli, K. R. Poeppelmeier, *Nat. Commun.* **2018**, *9*, DOI 10.1038/s41467-018-02838-4.

[46] N. N. Greenwood, A. Earnshaw, *Chemistry of the Elements (Second Edition)*, Butterworth-Heinemann, Oxford, **1997**.

[47] F. D. Romero, S. J. Burr, J. E. McGrady, D. Gianolio, G. Cibin, M. A. Hayward, *J. Am. Chem. Soc.* **2013**, *135*, 1838–1844.

[48] Z. Xu, L. Jin, J.-K. Backhaus, F. Green, M. A. Hayward, *Inorg. Chem.* **2021**, *60*, 14904–14912.

[49] Y. Tsujimoto, C. Tassel, N. Hayashi, T. Watanabe, H. Kageyama, K. Yoshimura, M. Takano, M. Ceretti, C. Ritter, W. Paulus, *Nature* **2007**, *450*, 1062–1065.

[50] Y. Kobayashi, O. J. Hernandez, T. Sakaguchi, T. Yajima, T. Roisnel, Y. Tsujimoto, M. Morita, Y. Noda, Y. Mogami, A. Kitada, M. Ohkura, S. Hosokawa, Z. Li, K. Hayashi, Y. Kusano, J. E. Kim, N. Tsuji, A. Fujiwara, Y. Matsushita, K. Yoshimura, K. Takegoshi, M. Inoue, M. Takano, H. Kageyama, *Nat. Mater.* **2012**, *11*, 507–511.

[51] F. D. Romero, A. Leach, J. S. Möller, F. Foronda, S. J. Blundell, M. A. Hayward, *Angew. Chemie - Int. Ed.* **2014**, *53*, 7556–7559.

[52] L. Jin, M. Lane, D. Zeng, F. K. K. Kirschner, F. Lang, P. Manuel, S. J. Blundell, J. E. McGrady, M. A. Hayward, *Angew. Chemie - Int. Ed.* **2018**, *57*, 5025–5028.

[53] O. H. Hansteen, H. Fjellvåg, B. C. Hauback, *J. Solid State Chem.* **1998**, *141*, 411–417.

[54] O. H. Hansteen, *J. Mater. Chem.* **1998**, *8(9)*, 2081–2088.

[55] T. Moriga, O. Usaka, T. Imamura, I. Nakabayashi, I. Matsubara, T. Kinouchi, S. Kikkawa, F. Kanamaru, *Bull. Chem. Soc. Jpn.* **1994**, *67*, 687–693.

[56] T. Moriga, O. Usaka, I. Nakabayashi, T. Kinouchi, S. Kikkawa, F. Kanamaru, *Solid State Ionics* **1995**, *79*, 252–255.

[57] F. D. Romero, P. A. Bingham, S. D. Forder, M. A. Hayward, *Inorg. Chem.* **2013**, *52, 19,* 10920 - 10928.

[58] Gloveox-Manual-MB20-200_Labmaster_TP700_V4.1_MBI.pdf, *MBRAUN Inc.* **2014**.

[59] W. Clegg, A. J. Blake, *Crystal Structure Analysis : Principles and Practice*, Oxford University Press, Oxford, **2009**.

[60] C. Wu, K. H. Mess, T. Maury, F. Zimmermann, *Handbook of Accelerator Physics and Engineering*, World Scientific, **1999**.

[61] S. P. Thompson, J. E. Parker, J. Potter, T. P. Hill, A. Birt, T. M. Cobb, F. Yuan, C. C. Tang, *Rev. Sci. Instrum.* **2009**, *80*, 075107.

[62] N. Tartoni, S. P. Thompson, C. C. Tang, B. L. Willis, G. E. Derbyshire, A. G. Wright, S.C. Jaye, J. M. Homer, J. D. Pizzey, A. M. T. Bell, *J. Synchrotron Radiat.* **2007**, *15*, 43-49.

[63] V. F. Sears, *Neutron News* **1992**, *3*, 26–37.

[64] J. Rodríguez-Carvajal, *Phys. B Phys. Condens. Matter* **1993**, *192*, 55–69.

[65] "https://www.isis.stfc.ac.uk/pages/polaris-technical-information.aspx," **2022**.

[66] "https://www.ill.eu/users/instruments/instruments-list/d2b/description/instrument-layout," **2022**.

[67] *https://www.ill.eu/users/instruments/instruments-list/d1b/description/instrument-layout* **2022**.

[68] H. M. Rietveld, *J. Appl. Crystallogr.* **1969**, *2*, 65–71.

[69] A. C. Larson, R. B. Von Dreele, *GSAS MANUAL, Los Alamos Natl. Lab. Rep. LAUR* **1994**, 86–748.

[70] J. Clarke, *Sci. Am.* **1994**, *271*, 46–53.

[71] J. Bardeen, L. N. Cooper, R. Schrieffer, *Phys. Rev.* **1957**, *108*, *5*, 1175.

[72] H. Seyama, M. Soma, B. K. G. Theng, *X-Ray Photoelectron Spectroscopy*, Elsevier Inc., **2013**.

[73] N. Hasanli, A. Scrimshire, P. A. Bingham, R. G. Palgrave, M. A. Hayward, *Dalt. Trans.* **2020**, *49*, 11346–11353.

[74] D. J. Gallon, P. D. Battle, S. J. Blundell, A. I. Coldea, M. J. Rosseinsky, C. Steer, *J. Mater. Chem.* **2003**, *13*, 1166–1172.

[75] L. Awin, B. J. Kennedy, M. Avdeev, *Ceram. Int.* **2013**, *39*, 233–237.

[76] A. E. Smith, A. W. Sleight, M. A. Subramanian, *Mater. Res. Bull.* **2010**, *45*, 460–463.

[77] M. T. Haque, H. Satoh, N. Kamegashira, *J. Alloys Compd.* **2005**, *390*, 115–121.

[78] S. Asai, R. Okazaki, I. Terasaki, Y. Yasui, W. Kobayashi, A. Nakao, K. Kobayashi, R. Kumai, H. Nakao, Y. Murakami, N. Igawa, A. Hoshikawa, T. Ishigaki, O. Parkkima, M. Karppinen, H. Yamauchi, *J. Phys. Soc. Japan* **2013**, *82*.

[79] P. D. Battle, J. F. Vente, *J. Solid State Chem.* **1999**, *146*, 163–167.

[80] H. Hsu, Y. G. Yu, R. M. Wentzcovitch, *Earth Planet. Sci. Lett.* **2012**, *359–360*, 34–39.

[81] M. Hayward, *Soft Chem. Synth. oxides Compr. Inorg. Chem.* **2013**, 417–453.

[82] F. D. Romero, D. Gianolio, G. Cibin, P. A. Bingham, J. Hollander, S. D. Forder, M. A. Hayward, *J. Am. Chem. Soc.* **2013**, *135*, 1838−1844.

[83] D. Coster, R. De L. Kronig, *Physica* **1935**, *2*, 13–24.

[84] Y. Abe, K. Kato, M. Kawamura, K. Sasaki, *Surf. Sci. Spectra* **2001**, *8*, 117–125.

[85] M. Carvalho, L. F. Wieserman, D. M. Hercules, *Appl. Spectrosc.* **1982**, *36*, 290–296.

[86] A. V. Naumkin, A. Kraut-Vass, S. W. Gaarenstroom, C. J. Powell, *NIST X-Ray Photoelectron Spectroscopy (XPS) Database, Version 3*, **2012**.

[87] R. V. Panin, N. R. Khasanova, C. Bougerol, W. Schnelle, G. Van Tendeloo, E. V. Antipov, *Inorg. Chem.* **2010**, *49*, 1295–1297.

[88] W. Yi, Y. Matsushita, M. Tanaka, A. A. Belik, *Inorg. Chem.* **2012**, *51*, 7650–7656.

[89] J. A. Barth, C. P. Von R, I. Viii, C. Co, G. Beuter, A. Brodbeck, M. Holzer, S. M. J. Striihle, *Zeitschrift fur Anorg. und Allg. Chemie* **1992**, *616*, 27–34.

[90] C. T. Prewitt, K. B. Schwartz, R. D. Shannon, *Acta Crystallogr. Sect. C Cryst. Struct. Commun.* **1983**, *39*, 519–521.

[91] K. B. Schwartz, J. B. Parise, C. T. Prewitt, R. D. Shannon, *Acta Crystallogr. Sect. B* **1983**, *39*, 217–226.

[92] J. E. Page, M. A. Hayward, *Inorg. Chem.* **2019**, *58*, 6336–6343.

[93] J. E. Page, H. W. T. Morgan, D. Zeng, P. Manuel, J. E. McGrady, M. A. Hayward, *Inorg. Chem.* **2018**, *57*, 13577–13585.

[94] L. Jin, M. A. Hayward, *Chem. Commun.* **2019**, *55*, 4861–4864.

[95] P. G. Radaelli, S. W. Cheong, *Phys. Rev. B* **2002**, *66*, 094408.

[96] Y. Moritomo, K. Higashi, K. Matsuda, A. Nakamura, *Phys. Rev. B* **1997**, *55*, R14725–R14728.

[97] Y. Shimada, S. Miyasaka, R. Kumai, Y. Tokura, *Phys. Rev. B* **2006**, *73*, 134424.

[98] Z. Xu, L. Jin, J. K. Backhaus, F. Green, M. A. Hayward, *Inorg. Chem.* **2021**, *60*, 14904–14912.

[99] A. Pabst, *J. Chem. Phys.* **1943**, *11*, 145–149.

[100] B. J. Campbell, H. T. Stokes, D. E. Tanner, D. M. Hatch, *J. Appl. Crystallogr.* **2006**, *39*, 607–614.

[101] H. T. Stokes, D. M. Hatch, B. J. Campbell, *ISODISTORT, ISOTROPY Software Suite*, **2022**.